Control of Dual Active Bridge for DC Distribution Systems on More Electric Aircrafts

Linglin Chen (BSc, MSc)

Submitted to the University of Nottingham
for the degree of Doctor of Philosophy

January 2020

Abstract

DC-DC power converters are key equipment in DC distribution systems on more electric aircrafts. The Dual-Active-Bridge (DAB) DC-DC converter topology has been widely considered in such application. In this thesis, the DAB topology is studied particularly from the perspective of the control.

Fundamentals of the DAB power converter are introduced, including the switching patterns, modulations, modelling and control. Common control methods for the DAB converters, including feedback control, feedforward control, transformer current control, linearization control and sliding mode control are also addressed in depth. The relevant advantages and drawbacks of each of those control methods have been analysed. In the application of the DAB converters in the on-board DC distribution system, multiple control objectives are often required. However, none of the control methods mentioned above can easily provide good overall performance and flexibility.

Therefore, a Moving Discretised Control Set – Model Predictive Control (MDCS-MPC) is introduced. Circuit parameters, terminal voltages and operating modes of DAB are embedded in the prediction model. Control parameters designed for MDCS-MPC can provide good performance throughout the power and terminal voltage range. The proposed approach enables flexible multi-objective control. In this thesis three control scenarios have been investigated:

- In the first case study, the DAB converter is required to regulate the load voltage and ganrantee large signal stability. A phase portrait based stability analysis approach has been proposed for the assessment of large signal stability. The DAB converter stability has been evaluated with the MDCS-MPC, the results of which have shown insights into factors that stabilize or destabilize the converter operation.
- The MDCS-MPC has been extended into two-dimensional operation where the DAB converter is responsible for both efficiency maximization and load current regulation. The load current regulation demands fast dynamic while the efficiency often is only at stake in

the steady state. The two-dimensional MDCS-MPC brings in freedom to trade-off between the two control-objectives.

- Stabilization of the DC distribution system has been incorporated as another control objective alongside the load current regulation with MDCS-MPC. The system impedance information is not required for the implementation of MDCS-MPC based stabilization control. Fast stabilization while maintaining reasonably good load regulation performance can be achieved. The proposed MDCS-MPC can inherently incorporate multi-objective control without the risk of losing the controllability to any of its control objectives. Parameters associated with MDCS-MPC have direct physical influence. Therefore, the design and tuning of the MDCS-MPC are more straightforward than multi-loop PI control structures.

Acknowledgement

It has been a great adventure for me to complete my Ph.D program at the University of Nottingham over the past three years. There are a number of people who have been so important to me in this journey, and I would like to express my deepest gratitude to them.

First of all, I would like to thank my main supervisor Prof. Patrick Wheeler for enabling all my research activities, and Dr. Alessandrio Costabeber for his great support. He showed to me what it takes to be a proper researcher. Special thanks to Dr. Luca Tarisciotti. As a supervisor, he had not only lead and guided me in research, but also taught me about the western culture. I could not possibly have come this far without his sterling efforts.

I would like to express my sincere appreciation to Prof. Tomislav Dragicevic from Aalborg University, Prof. Fei Gao from Shanghai Jiao Tong University and Prof. Shuai Shao from Zhejiang University. They have provided professional critiques and insights to my works which constantly pushed my limits.

In addition, I would like to thank many PEMC group members including: Dr. Tao Yang for investment in my prototype, Dr. Con Ahumada for all the encouragement and tasty chilean wines, Dr. Constantina Panayiotou for PEMC gourp activities, Dr. Xuchen Wang for laughter, Dr. Zhenyu Wang for professional discussions, Dr. Zhen Huang for Chinese group activities, Dr. Jiawei Zhang for personal consultancy, Dr. Xiaochen Zhang for life-job advices, Mr. Patrick Xie for his kindness, Mr. Davide Gottatrdo for top-tier hand-made pizza. Last but not least, I would like to thank my friends Mr. Chen Li and Mr. David Dewar for their company.

Thanks to the University of Nottingham for rewarding me the “Faculty of Engineering Research Excellence PhD Scholarship” which economically enabled this Ph.D program.

I would like to express my heartfelt appreciation to my wife Jie Zhang for her love, emotional support and encouragement.

List of Publications

Following is a list of papers that have been submitted, accepted or published during the course of my Ph.D in peer-reviewed journal articles and conference proceedings:

Journal Articles

[J1] **L. Chen**, L. Tarisciotti, A. Costabeber, Q. Guan, P. Wheeler and P. Zanchetta, "Phase-Shift Modulation for a current-fed isolated DC-DC converter in More Electric Aircraft," in IEEE Transactions on Power Electronics, vol. 34, no. 9, pp. 8528-8543, Sept. 2019.

[J2] **L. Chen**, S. Shao, Q. Xiao, L. Tarisciotti, T. Dragicevic and P. Wheeler, "Model-Predictive-Control for Dual-Active-Bridge Converters Supplying Pulsed Power Loads in Naval DC Micro-grids," in IEEE Transactions on Power Electronics, vol. 35, no. 2, pp. 1957-1966, Feb. 2020

[J3] **L. Chen**, L. Tarisciotti, A. Costabeber, F. Gao, P. Wheeler and P. Zanchetta, "Advanced modulations for a current-fed isolated DC-DC converter with wide voltage operating ranges," in IEEE Journal of Emerging and Selected Topics in Power Electronics, vol. 7, no. 4, pp. 2540-2552, Dec. 2019.

[J4] **L. Chen**, F. Gao, K. Shen, Z. Wang, L. Tarisciotti, P. Wheeler and T. Dragicevic , "Predictive Control based DC Micro-grid Stabilization with the Dual-Active-Bridge Converter," in IEEE Transactions on Industrial Electronics. doi: 10.1109/TIE.2020.2965460.

[J5] **L. Chen**, L. Lin, S. Shao, F. Gao, Z. Wang, P. Wheeler and T. Dragicevic, "Moving Discretized Control Set — Model Predictive Control for Dual-Active-Bridge with Triple Phase Shift," in IEEE Transactions on Power Electronics. doi: 10.1109/TPEL.2019.2962838.

[J6] Q. Xiao, **L. Chen**, H. Jia, P. Wheeler and T. Dragicevic, " Model Predictive Control for Dual-Active-Bridge in Naval DC Micro-grids Supplying Pulsed Power Loads Featuring Fast

Transition and Online Transformer Current Minimization," in IEEE Transactions on Industrial Electronics. DOI: 10.1109/TIE.2019.2934070.

[J7] Q. Xiao, **L. Chen**, Y. Jin, Y. Mu, A. Cupertino, H. Jia, Y. Neyshabouri, T. Dragicevic and R. Teodorescu, "An Improved Fault-Tolerant Control Scheme for Cascaded H-bridge STATCOM with Higher Attainable Balanced Line-to-line Voltage," in IEEE Transactions on Industrial Electronics. DOI: 10.1109/TIE.2020.2978716

[J8] L. Tarisciotti, A. Costabeber, **L. Chen**, A. Walker and M. Galea, "Current-Fed Isolated DC/DC Converter for Future Aerospace Micro-grids," in IEEE Transactions on Industry Applications, vol. 55, no. 3, pp. 2823-2832, May-June 2019.

[J9] B. Zhang, S. Shao, **L. Chen**, X. Wu and J. Zhang, "Steady State and Transient DC Magnetic Flux Bias Suppression Methods for a Dual Active Bridge Converter," in IEEE Journal of Emerging and Selected Topics in Power Electronics. DOI: 10.1109/JESTPE.2019.2947299

[J10] Qian Xiao, Yu Jin, **Linglin Chen**, Xiaodan Yu, Hongjie Jia, Huiqiao Liu, Remus Teodorescu, Frede Blaabjerg, " A Simple Operation Approach for Modular Multilevel Converter under Grid Voltage Swell in Medium-Voltage Microgrids," in IEEE Access, vol. 7, pp. 147280-147291, 2019

[J11] Qian Xiao, Jinyu Wang, Yu Jin, **Linglin Chen**, Hongjie Jia, T. Dragicevic and Remus Teodorescu, "A Novel Operation Scheme for Modular Multilevel Converter with Enhanced Ride-Through Capability of Submodule Faults," in IEEE Journal of Emerging and Selected Topics in Power Electronics. DOI: 10.1109/JESTPE.2020.2967576

[J12] Q. Xu, N. Vafamand, **L. Chen** and T. Dragicevic, "Review on Advanced Control Technologies for Bidirectional DC/DC Converters in DC Microgrids," in IEEE Journal of Emerging and Selected Topics in Power Electronics. DOI: 10.1109/JESTPE.2020.2978064

[J13] S. Shao, **L. Chen**, Z. Shan, F. Gao, H. Chen, D. Sha and T. Dragicevic, "Modeling and Advanced Control of Dual Active Bridge DC-DC Converters: A Review," in IEEE Transactions on Power Electronics. (under peer review)

Conference Papers

[C1] **L. Chen**, L. Tarisciotti, A. Costabeber, P. Wheeler and P. Zanchetta, "Model Predictive Control for Isolated DC/DC Power Converters with Transformer Peak Current Shaving," 2018 IEEE Energy Conversion Congress and Exposition (ECCE), Portland, OR, 2018, pp. 5954-5960.

[C2] **L. Chen**, L. Tarisciotti, A. Costabeber, P. Zanchetta and P. Wheeler, "Parameters mismatch analysis for the Active-Bridge-Active-Clamp (ABAC) converter," 2017 IEEE Southern Power Electronics Conference (SPEC), Puerto Varas, 2017, pp. 1-6.

[C3] D. Gottardo, L. De Lillo, L. Empringham, A. Costabeber and **L. Chen**, "Single Stage Dual Active Bridge AC-DC Converter with Active Power Decoupling," 2018 International Symposium on Power Electronics, Electrical Drives, Automation and Motion (SPEEDAM), Amalfi, 2018, pp. 497-501.

[C4] **L. Chen**, L. Tarisciotti, A. Costabeber, P. Zanchetta and P. Wheeler, "Advanced modulation for the Active-Bridge-Active-Clamp (ABAC) converter," 2017 IEEE Southern Power Electronics Conference (SPEC), Puerto Varas, 2017, pp. 1-6.

[C5] Q. Xiao, Y. Jin, J. Wang, S. Wang, **L. Chen**, H. Jia, Y. Mu, T. Dragicevic and R. Teodorescu, "A Novel Fault-Tolerant Control Method for Modular Multilevel Converter with an Improved Phase Disposition Level-Shifted PWM," IECON 2019 - 45th Annual Conference of the IEEE Industrial Electronics Society, Lisbon, Portugal, 2019, pp. 3839-3844.

Book Chapter

[B1] **Linglin Chen**, Tao Yang, Fei Gao, Serhiy Bozhko, and Patrick Wheeler, “DC micro-grid control principles – hierarchical control diagram”. The first chapter of the book "DC Distribution Systems and Micro-grids" (https://www2.theiet.org/resources/books/pow-en/dc-systms.cfm)

Table of Content

Abstract 3
Acknowledgement 5
List of Publications 6
Journal Articles 6
Conference Papers 8
Book Chapter 8
Table of Content 9
List of Figures 13
List of Tables 21
Chapter 1 Introduction 22
1.1 The More Electric Aircraft (MEA) concept 23
1.2 DC power distribution system 25
1.3 DC-DC power converters 27
1.4 Objectives and contributions 30
1.5 Thesis outline 31
Chapter 2 The Fundamentals of the Dual-Active-Bridge 34
2.1 Switching patterns 36
2.2 Modulation techniques 39
2.3 Analysis on Single-Phase-Shift (SPS) modulation 43
2.3.1 Power transmission 43
2.3.2 Zero Voltage Switching (ZVS) 46
2.3.3 Dead-band effect 48
2.3.4 Considerations for the choice of L_p 50
2.3.5 Capacitive filtering 55
2.4 Triple-Phase-Shift (TPS) modulation optimization 56
2.4.1 Operating modes 56
2.4.2 Current stress minimization 59
2.5 Modelling 61
2.5.1 Average model 61
2.5.2 Ideal small signal model 62

2.5.3 Practical switching model 64
2.6 PI controller design 67
2.7 Practical results 69
2.7.1 Transient and steady state results 71
2.7.2 Efficiency measurements 73
2.8 Chapter summary 73
Chapter 3 Control methods for Dual Active Bridge 75
3.1 PI only control 76
3.2 Feedforward control 78
3.2.1 Hybrid Control 79
3.2.2 Virtual Direct Power Control 83
3.3 Transformer current control 89
3.3.1 Feedforward current control 89
3.3.2 Predictive current control 94
3.3.3 Stationary current control 98
3.4 Linearization control 102
3.5 Sliding mode control 107
3.6 Model predictive control 112
3.7 Comparisons of control methods 113
3.8 Chapter summary 117
Chapter 4 Mono-dimensional MDCS-MPC 119
4.1 Control introduction 120
4.1.1 Discretized model 120
4.1.2 Operating principle 123
4.1.3 Dynamic enhancement 126
4.1.4 Cost function 130
4.1.5 Steady state error 133
4.1.6 Algorithm flow chart 137
4.2 Large signal stability analysis 139
4.2.1 Phase portrait analysis method 139
4.2.2 Benchmark control 141
4.2.3 Analysis on I_{HV2} saturation 148
4.2.4 Analysis on MDCS-MPC 149
4.3 Small signal analysis 156

4.4 Practical results 160
4.4.1 Stability 160
4.4.2 Steady state 162
4.4.3 Dynamic 163
4.4.4 Computation burden 165
4.5 Chapter summary 165
Chapter 5 Multi-dimensional MDCS-MPC 167
5.1 Online v.s. offline optimization 168
5.2 Mathematical model 171
5.2.1 Challenge with PI 172
5.2.2 Error correction 173
5.3 Operating principle 174
5.4 Cost function 177
5.5 Algorithm flow chart 180
5.6 Performance evaluations 182
5.6.1 Steady state performance 182
5.6.2 Dynamic performance 185
5.6.3 Effectiveness of G_2 187
5.7 Chapter summary 189
Chapter 6 Stabilization of the DC distribution system 191
6.1 Stability criteria 192
6.2 Passive damping 193
6.3 Active Damping 195
6.3.1 PI based stabilization 196
6.3.2 Co-ordinated integration 206
6.4 Chapter summary 209
Chapter 7 MDCS-MPC based system stabilization 211
7.1 Operating principle 213
7.2 Phase margin assessment 216
7.3 Current regulation performance 219
7.4 Time domain assessments 221
7.5 Practical results 224
7.5.1 Stabilization 225
7.5.2 Current regulation 226

7.6 Chapter summary 227
Chapter 8 Conclusion and future works 229
8.1 Conclusion 229
8.2 Future works 231
References 233

List of Figures

Fig. 1.1 Constant speed constant frequency generation system 24
Fig. 1.2 Variable speed constant frequency generation system 24
Fig. 1.3 Variable speed variable frequency generation system 25
Fig. 1.4 MEA DC distribution system[22]. 27
Fig. 1.5 The diagram of a current-fed DAB converter 29
Fig. 1.6 The diagram of the interleaved current-fed DAB converter 29
Fig. 1.7 Thesis outline 32
Fig. 2.1 The diagram of the DAB converter under investigation. 34
Fig. 2.2 Generic waveforms of the DAB. 35
Fig. 2.3 Relationship between the switching pattern, the modulation and the control. 36
Fig. 2.4 Two possible switching patterns for DAB converters where HS stands for hard switching and SS stands for soft switching. 37
Fig. 2.5 Idea switching waveforms with inductive loads 38
Fig. 2.6 Conceptual waveform demonstrations on existing modulations. (a) D_1=0.5, D_2=0.5, D_3 is controlled; (b) D_2=0.5, D_1 and D_3 are controlled or D_1=0.5, D_2 and D_3 are controlled; (c) D_1=D_2=D, D and D_3 are controlled; (d) D_3=0, D_1 and D_2 are controlled to achieve ZCS and ZVS; (e) D_1, D_2 and D_3 are controlled to achieve ZCS and ZVS and (f) D_1, D_2 and D_3 are controlled. 40
Fig. 2.7 Relationship between modulations 41
Fig. 2.8 Conceptual waveforms to show the back and forth power in (a) SPS modulation. (b) EPS modulation. 43
Fig. 2.9 DAB with both terminals connected to DC sources. 44
Fig. 2.10 Conceptual waveforms for SPS (a) V_{HV1}>V_{HV2} and (b) V_{HV1}<V_{HV2}. 44
Fig. 2.11 Unified transmission power characterization of SPS. 46
Fig. 2.12 The ideal ZVS region of a DAB with SPS modulation. 47
Fig. 2.13 Transformer current with different outer phase shift values under the terminal voltage condition (a) M<1 and (b) M>1. 48
Fig. 2.14 Voltage ringing example with (a) the operation point in M>1 ZVS region and its corresponding (b) waveforms comparing phenomena with/without dead-band. 49
Fig. 2.15 Phase drift example with (a) the operation point M<1 in ZVS region and its corresponding (b) waveforms comparing phenomena with/without dead-band. 50
Fig. 2.16 Overlapping of the ZVS region and the contour plot of reactive power ratio r_Q. 52

Fig. 2.17 The diagram of the DAB converter under investigation. 53
Fig. 2.18 Implications of k to the ZVS region and reactive power ratio r_Q. 54
Fig. 2.19 Illustration on the DC terminal currents and voltage 55
Fig. 2.19 Transformer peak current comparison between SPS and TPS 60
Fig. 2.20 The reduced order model of the DAB. 61
Fig. 2.21 Transfer function AC sweeping diagram with the average model. 63
Fig. 2.22 Comparison between the AC swept ideal model and the mathematical model in Table 2.8. 64
Fig. 2.23 Transfer function AC sweeping diagram for the switching model. 65
Fig. 2.24 Comparisons on the transfer function between the ideal model and the switching model under different equilibrium points. 66
Fig. 2.25 Transfer function comapirson under differnet power and terminal voltages 66
Fig. 2.26 The control and TPS modulation diagram. 67
Fig. 2.27 The control block diagram using the PI controller considering delays. 67
Fig. 2.28 Plots of $G_o(s)$ for different equilibrium points. Control parameters are set as K_p=0.05, K_i=89.6. 69
Fig. 2.29 The schematic of the prototype 70
Fig. 2.29 The experiment prototype converter. 70
Fig. 2.30 Transition with the PI controller 71
Fig. 2.31 Steady state waveforms 72
Fig. 2.32 Reference tracking performance with the designed PI controller. 72
Fig. 2.33 Efficiency measurement. 73
Fig. 3.1 The diagram of the DAB converter under investigation. 75
Fig. 3.2 Transformer terminal voltages and current waveform of SPS. 76
Fig. 3.3 PI control diagram with resistive load R_L [78]. 77
Fig. 3.4 PI control diagram with load current I_{load} perturbation. 77
Fig. 3.5 (a) $G_{R2O}(s)$ and (b) $Z_o(s)$ under 1kW are plotted according to models in (3. 5) and (3. 6) 78
Fig. 3.6 The hybrid control with resistive load R_L [73]. 79
Fig. 3.7 Hybrid control diagram with resistive load R_L. 80
Fig. 3.8 Hybrid control diagram with load current I_{load} perturbation. 81
Fig. 3.9 Plot of (a) $G_{R2O}(s)$ and (b) $Z_o(s)$ with the hybrid control under 1kW. 82
Fig. 3.10 Plot of (a) $G_{R2O}(s)$ and (b) $Z_o(s)$ with the hybrid control under 270V/270V 1kW. 83
Fig. 3.11 The VDPC control with resistive load R_L [79]. 85

Fig. 3.12 The VDPC control block diagram with resistive load R_L. 87
Fig. 3.13 VDPC control diagram with load current I_{load} perturbation. 88
Fig. 3.14 The VDPC control with different resistive load R_L 89
Fig. 3.15 Transformer terminal voltages and current waveform of SPS. 90
Fig. 3.16 The control diagram of the FFCC [80]. 91
Fig. 3.17 The control block diagram of the FFCC with resistive load R_L. 92
Fig. 3.18 FFCC control diagram with load current I_{load} perturbation. 93
Fig. 3.19 Plot of (a) $G_{R2O}(s)$ and (b) $Z_o(s)$ with the FFCC under 1kW. 94
Fig. 3.20 Transformer terminal voltages and current waveform of SPS. 94
Fig. 3.21 The predictive current control with resistive load R_L [81]. 95
Fig. 3.22 The predictive current control block diagram with resistive load R_L. 96
Fig. 3.23 Predictive current control diagram with load current I_{load} perturbation. 97
Fig. 3.24 Plot of (a) $G_{R2O}(s)$ and (b) $Z_o(s)$ with the predictive current control under 1kW. 98
Fig. 3.25 DAB transformer stage (a) full harmonic and (b) FHA circuits. 98
Fig. 3.26 The stationary current control with resistive load R_L [82], [83]. 100
Fig. 3.27 The stationary current control block diagram with resistive load R_L. 101
Fig. 3.28 The stationary current control block diagram with load disturbance I_{load}. 101
Fig. 3.29 Plot of (a) $G_{R2O}(s)$ and (b) $Z_o(s)$ with the stationary current control under 1kW. 102
Fig. 3.30 Linearization control diagram with resistive load R_L [84]. 103
Fig. 3.31 Equivalent linearization control block diagram with resistive load R_L. 103
Fig. 3.32 Plot of (a) $G_{R2O}(s)$ and (b) $Z_o(s)$ with the linearization control under 1kW. 104
Fig. 3.33 Linearization control block diagram with resistive load R_L [84]. 105
Fig. 3.34 Plot of (a) $G_{R2O}(s)$ and (b) $Z_o(s)$ with the linearization control under 270V/270V 1kW. 106
Fig. 3.35 Plot of (a) $G_{R2O}(s)$ and (b) $Z_o(s)$ with the linearization control under 270V/270V 1kW and α=2. 107
Fig. 3.36 Double integral sliding mode control diagram with resistive load R_L [86]. 110
Fig. 3.37 Double integral sliding mode control block diagram with resistive load R_L. 110
Fig. 3.38 Double integral sliding mode control block diagram with load current disturbance I_{load}. 111
Fig. 3.39 Plot of (a) $G_{R2O}(s)$ and (b) $Z_o(s)$ with the double integral sliding mode control under 1kW. 112
Fig. 3.40 Plot of (a) $G_{R2O}(s)$ and (b) $Z_o(s)$ under 270V/270V 1kW with consistant inductance in control and circuit. 114

Fig. 3.41 Plot of (a) $G_{R2O}(s)$ and (b) $Z_o(s)$ under 270V/270V 1kW with inductance in control 10% larger than in hardware circuit. 116

Fig. 4.1 The reduced order model of the DAB. 120

Fig. 4.2 Generic waveforms of SPS and TPS. 121

Fig. 4.3 Prediction error assessment circuit 122

Fig. 4.4 Voltage prediction error evaluation. 123

Fig. 4.5 Demonstration of the smallest phase shift value in PWM modules. 124

Fig. 4.6The operating principle of the mono-dimensional MDCS-MPC for DAB. μ is set to be 3 for illustration. 125

Fig. 4.7 Simulation results with constant load current I_{load} = 3.3A. μ = 3, V_{HV1}=300V,V_{HV2_ref}=300V. 126

Fig. 4.8 Simulation results with constant load R_L = 90ohm. μ = 3, V_{HV1}=300V, V_{HV2_ref}=300V. 126

Fig. 4.9 R_L decreases from 900ohm to 90ohm at time instance 0.05s with μ = 3, V_{HV1}=300V, V_{HV2_ref}=300V. 127

Fig. 4.10 R_L decreases from 900ohm to 90ohm at time instance 0.05s with μ = 11, V_{HV1}=300V, V_{HV2_ref}=300V. 128

Fig. 4.11 R_L decreases from 900ohm to 90ohm at time instance 0.05s with μ = 21, V_{HV1}=300V, V_{HV2_ref}=300V. 128

Fig. 4.12 R_L decreases from 900ohm to 90ohm at time instance 0.05s with μ = 201, V_{HV1}=300V, V_{HV2_ref}=300V. 129

Fig. 4.13 Block diagram of the adaptive step. 129

Fig. 4.14 R_L decreases from 900ohm to 90ohm at time instance 0.05s with μ = 11, V_{HV1}=300V, V_{HV2_ref}=300V, and λ=1. 130

Fig. 4.15 R_L decreases from 900ohm to 90ohm at time instance 0.05s with μ = 11, V_{HV1}=300V, V_{HV2_ref}=300V, λ=1 and α_2=1.2. 131

Fig. 4.16 R_L decreases from 900ohm to 90ohm at time instance 0.05s with μ = 11, V_{HV1}=300V, V_{HV2_ref}=300V, and λ=1 and α_2=2.5. 132

Fig. 4.17 R_L decreases from 900ohm to 90ohm at time instance 0.05s with μ = 11, V_{HV1}=300V, V_{HV2_ref}=300V, and λ=1 and α_2=4. 132

Fig. 4.18 I_{load} increases from 0.3A to 3.3A at time instance 0.05s with μ = 11, V_{HV1}=300V, V_{HV2_ref}=300V, and λ=1 and α_2=4. 133

Fig. 4.19 The compensation diagram for the prediction error 134

Fig. 4.20 Illustration of the steady state error 135

Fig. 4.21 The flow chart of MDCS-MPC 138

Fig. 4.22 The general phase portrait of DAB 140

Fig. 4.23 Different control behaviours. 142

Fig. 4.24 DAB with constant current load 142
Fig. 4.25 Control behaviours. 143
Fig. 4.26 Four quadrant for constant current load 144
Fig. 4.27 Phase portrait with constant current load using the benchmark control. 145
Fig. 4.28 DAB with constant resistive loads. 146
Fig. 4.29 Four quadrants with resistive loads. 146
Fig. 4.30 Phase portrait with constant resistive load using the benchmark control. 148
Fig. 4.31 Phase portrait with I_{HV2} saturation using the benchmark control. 148
Fig. 4.32 mono-dimensional MDCS-MPC behaviours. 149
Fig. 4.33 Explaination on the mono-dimensional MDCS-MPC behaviours. 151
Fig. 4.34 Phase portrait in blue line with constant current load using the MDCS-MPC. Phase portrait in grey line with constant current load using the benchmark control. 152
Fig. 4.35 Simulation results with constant load current I_{load} = 3.3A. μ = 3, V_{HV1}=300V,V_{HV2_ref}=300V. 153
Fig. 4.36 Explaination on the mono-dimensional MDCS-MPC behaviour with adaptive step. 154
Fig. 4.37 Mono-dimensional MDCS-MPC control behaviours. 155
Fig. 4.38 Explaination on the mono-dimensional MDCS-MPC behaviours with G_2. 156
Fig. 4.39 Frequency response sweeping circuit. 157
Fig. 4.40 Sweeping results for $G_{R2O}(f)$ in (4. 76) under equilibrium point 260V/300V 1kW 158
Fig. 4.41 Frequency response with different input voltages in TPS 159
Fig. 4.42 Load voltage reference tracking. 160
Fig. 4.43 Load step up response with μ=7 and α_2=0 161
Fig. 4.44 Load step up with adaptive step, μ=7 and α_2=0. 161
Fig. 4.45 Load step up with adaptive step, μ=7 and α_2=4. 161
Fig. 4.46 MDCS-MPC controlled DAB loaded with load variations @20Hz. Prediction compensation disabled. V_{HV1}=300V, V_{HV2_ref}=300V. 162
Fig. 4.47 Compensation for the prediction error. Operation under V_{HV1}=300V, V_{HV2_ref}=300V over the whole power range. 163
Fig. 4.48 Load step up/down using MDCS-MPC in TPS 163
Fig. 4.49 Load step up/down using the PI controller in TPS 164
Fig. 4.50 Change of voltage reference V_{HV2_ref} with MDCS-MPC 164
Fig. 4.51 Change of voltage reference V_{HV2_ref} with PI 165
Fig. 4.52 Measurement of computational time. 165

Fig. 5.1 Mono-dimensional and multi-dimensional MDCS-MPC. 167
Fig. 5.2 Two-dimensional MDCS-MPC with DPS 168
Fig. 5.3 Generic waveforms for predominant operating modes in DPS. 169
Fig. 5.4 Minimum transformer current stress trajectories with different terminal voltage ratio M. 170
Fig. 5.5 Tracking trajectory comparison 171
Fig. 5.6 The reduced order model. 171
Fig. 5.7 Sweeping diagram of the transfer function $G_{DPS}(s)=i_{HV2}(s)/D_f(s)$. 172
Fig. 5.8 Sweeping results of two equilibrium points. The transfer function $G_{DPS}(s)=i_{HV2}(s)/D_f(s)$ is tested under 250V/270V terminal voltage condition. 173
Fig. 5.9 Discretised control variables in DPS. 175
Fig. 5.10 A conceptual process of the 2D MDCS-MPC 175
Fig. 5.11 The two-dimensional moving discretised control set. 176
Fig. 5.12 Power 3D plot and its contour plot. 178
Fig. 5.13 Transformer peak current 3D and its contour plot 179
Fig. 5.14 Overlapping of power and peak current contour plots 179
Fig. 5.15 The flow chart of 2-D MDCS-MPC 181
Fig. 5.16 Evaluated circuit 182
Fig. 5.17 Comparisons on the transformer peak current between SPS and DPS under terminal voltage 150V/320V. 183
Fig. 5.18 Time domain waveforms comparison under 150V/320V 600W. 183
Fig. 5.19 Comparisons on the transformer peak current between SPS and DPS under terminal voltage 270V/300V. 184
Fig. 5.20 Time domain waveforms comparison under 270V/300V 600W. 185
Fig. 5.21 Transition from 0W to 1kW Two-dimensional DPS with 3*3 points are calculated in one switching period. α_1=1, α_2=0.1. V_{HV1}=150V, V_{HV2}=300V. 185
Fig. 5.22 Transition from 0W to 1kW Two-dimensional DPS with 7*7 points are calculated in one switching period. α_1=1, α_2=0.1. V_{HV1}=150V, V_{HV2}=300V. 186
Fig. 5.23 Transition from 0W to 1kW Two-dimensional DPS with 21*21 points are calculated in one switching period. α_1=1, α_2=0.1. V_{HV1}=150V, V_{HV2}=300V. Adaptive step disabled. 186
Fig. 5.24 Two-dimensional DPS with 7*7 points calculated in one switching period. Transition from 0W to 600W. α_1=1, α_2=0.1. V_{HV1}=250V, V_{HV2}=270V. 187
Fig. 5.25 Two-dimensional DPS with 7*7 points calculated in one switching period. G_2 enabled at 0.05s. α_1=1, α_2=0.1. V_{HV1}=250V, V_{HV2}=270V 188

Fig. 5.26 Two-dimensional DPS with 7*7 points calculated in one switching period. Transition from 0W to 600W. α_1=1, α_2=10. V_{HV1}=250V, V_{HV2}=270V. 189

Fig. 6.1 (a) System configuration. (b) Circuit diagram of DAB. (c) Single Phase Shift (SPS) waveforms 191

Fig. 6.2 (a) Simplified system. (b) Impedance model 192

Fig. 6.3 Equivalent close-loop system to (6. 1) 193

Fig. 6.4 (a) Bode plot and (b) Nyquist plot of the impedance ratio in (6. 1) where v_1=300V, L_p=283uH, C_f=380uF and L_f=11mH. 194

Fig. 6.5 A general illustration on the increase of PM by using active damping approaches. Blue line represents Z_{out}. Green line stands for Z_{in} 195

Fig. 6.6 An active damping approach based on the PI controller. 196

Fig. 6.7 The reduced order model of the DAB. 197

Fig. 6.8 Intuitive explanation on the stabilization. (a) DAB controls only battery current control. (b) Stabilization control is enabled 198

Fig. 6.9 Control diagram without *LC* input filter and stabilization control loop. 199

Fig. 6.10 Bode plots of (a) Z_{in} and Z_{out}. (b) $G_{R2O}(s)$ without stabilization control and input *LC* filter. 199

Fig. 6.11 Comparison between the ideal Z_{in} from (6. 3) and calculated Z_{in} from (6. 11). . 200

Fig. 6.12 Control diagram without the input *LC* filter. 201

Fig. 6.13 Bode plots of (a) Z_{in} and (b) $G_{R2O}(s)$ with stabilization control but without input *LC* filter. 202

Fig. 6.14 Signal-flow graph model of the control block diagram in Fig. 6.6. 203

Fig. 6.15 Bode plot of $G_{R2O}(s)$ with stabilization control and *LC* filter. k_{p2} and k_{i2} are set as 0.02 and 100. 204

Fig. 6.16 (a) Saturation issue with PI controllers where k_{p1}=0.02, k_{i1}=100, k_{p2}=0.003 and k_{i2}=5. Circuit parameters in Table 7.2 are used. (b) Alleviation of the saturation with a slower stabilization loop where k_{p1}=0.02, k_{i1}=100, k_{p2}=0.001 and k_{i2}=0.1. Circuit parameters are listed in Table 7.2. 206

Fig. 6.17 PI based active stabilization methods 207

Fig. 6.18 Stabilization with co-ordinated control where PI controllers are set as k_{p1}=0.02, k_{i1}=100, k_{p2}=0.003 and k_{i2}=5. Circuit parameters in Table 7.2 are used 209

Fig. 7.1 The operating principle of the MDCS-MPC for DAB. μ is set to be 3 for illustration. 214

Fig. 7.2 The control block of the MDCS-MPC 216

Fig. 7.3 The measurement diagram for the input impedance Z_{in}. 217

Fig. 7.4 Stability assessment with mono-dimensional MDCS-MPC α_2=0 @1kW 270V/270V. Circuit and control parameters in Table 7.2 and Table 7.3 are used. 218

Fig. 7.5 Stabilization with mono-dimensional MDCS-MPC α_2=0.1 @1kW 270V/270V. Circuit and control parameters in Table 7.2 and Table 7.3 are used. 218

Fig. 7.6 Stabilization with mono-dimensional MDCS-MPC α_2=0.3 @1kW 270V/270V. Circuit and control parameters in Table 7.2 and Table 7.3 are used. 219

Fig. 7.7 The measurement diagram for the close loop transfer function 219

Fig. 7.8 Stabilization with mono-dimensional MDCS-MPC α_2=0.1 @1kW 270V/270V. Circuit parameters in Table 7.1, Table 7.2 and Table 7.3 are used. 220

Fig. 7.9 Time domain stabilization waveforms under different values of L_f. 222

Fig. 7.10 Transition between -1kW and 1kW 223

Fig. 7.11 The DAB hardware setup. 225

Fig. 7.12 Stabilization comparisons 226

Fig. 7.13 Load step down transition comparisons with stabilization control enabled 227

List of Tables

Table 1.1 recent civil and military mea with ac electrical power system [10] 25
Table 2.1 switching loss comparison based on Fig. 2.4 38
Table 2.2 modulation techniques 41
Table 2.3 dead-band effect in different scenarios 49
Table 2.4 operating modes for tps modulation of a dab 56
Table 2.5 transformer current at switching instance unified at $1/(4f_sL_p)$ 58
Table 2.6 optimization table 60
Table 2.7 the controlled current in the reduced order model 62
Table 2.8 control to output transfer function 62
Table 2.9 circuit & control parameters 70
Table 2.10 hardware components 71
Table 3.1 circuit parameters 75
Table 3.2 control parameters with the same crossover frequency @ 600hz 113
Table 3.3 summary of the control methods in DAB 117
Table 4.1 the controlled current in the reduced order model with TPS 122
Table 5.1 the average model of DPS 172
Table 7.1 control parameters for time domain assessment 221
Table 7.2 circuit parameters 224
Table 7.3 mdcs-mpc control parameters 224
Table 7.4 hardware components 224
Table 8. 1 Summary of the relative advantages and drawbacks 231

Chapter 1 Introduction

Climate change is one of the most pressing issues facing the world. Human greenhouse gas emissions have pushed global temperatures up by around 1℃ since pre-industrial times. A changing climate may have negative impacts in ecological, physical and health, including extreme weather events (such as floods, droughts, storms, and heatwaves); sea-level rise; altered crop growth; and disrupted water systems [1]. To mitigate climate change, United Nations member parties have set a target, in the Paris Agreement, of limiting average warming to 2℃ above pre-industrial temperatures [2].

CO_2 emissions and the environmental impact they pose has moved to the forefront of public attention. As there are a variety of renewable sources available for electricity generation eg. solar, wind, tide and geothermal heat. The reduction of CO_2 becomes one of the driving forces in leading electric vehicle adoption. The advert of lithium-ion batteries and electric propulsion technologies are igniting a revolution in transportation. Everything from cars to trucks and buses is going electric. Due to policy incentives and relatively low barriers to entry, the automotive industry has shown great enthusiasm in the electrification revolution. Technological advances including renewable generation, storage, distribution and utilization have been accumulated, especially battery technologies. Electrification attempts in other sectors of transportation including aviation, marine, and rail have also been set forth in recent decades.

The aviation industry is one of the fastest growing sources of greenhouse gas emissions, And unlike cars, aviation is often excluded from national climate plans because it often operates across borders. According to a report in 2018 [3], commercial aviation has experienced a 32% increase in CO_2 emission over the past five years. If expansion trends in aviation industry progress at the current pace, airplanes will be a significant source of pollution in the future.

1.1 The More Electric Aircraft (MEA) concept

The invention of flight has been one of the most profound technologies in history. In the past century, it has functioned pretty much the same way. There are three revolutions in the history for the aviation industry. The first revolution was the use of piston engine that enabled the Wright brothers to launch their flight [4]. The second was the use of the jet engine, which was only applied to larger planes [5]. The third revolution is widely believed to be the electric propulsion [6].

In some light sports and trainer aircrafts for short haul flying, all electric products have already been seen on the market. However, large portion of the aviation industries emissions come from long haul and that is where battery-powered electric planes hit the buffers. A fundamental problem with electric aircraft has been that a typical lithium-ion battery cell (1MJ/kg) has only 1/40 of the energy density of jet fuel (43MJ/kg). Therefore, with a battery powered airplane, the mileage is considerably shorter compared to the conventionally fueled planes. In this respect, hydrogen is an extremely good candidate with around 130MJ/kg energy density. However, at the moment, opinion is split in the industry mainly due to the much higher cost associated with producing the hydrogen and the infrastructure required. The hydrogen is a gas so it has to be cryogenically chilled to get it into liquid form and that requires a massive amount of energy which our current renewable infrastructure is not yet set up to handle.

However, until lithium-ion and fuel cell battery technologies improve, hybrid electric aircraft is the solution what will be utilized for larger capacity flights over longer distances. The current trend is to make the aircraft more electric rather than all electric for large planes. In the MEA, the utilization of hydraulic, mechanical, and pneumatic power sources are replaced by electrical systems [7], resulting in reductions on the overall weight, operating cost, energy losses and environmental impact [8].

One of the challenges for the development of MEA is the design of its electrical power systems capable of managing power in the range from few kW to MW. There are typically three types of generation system for the electrical power:

- Constant speed constant frequency (CSCF) shown in Fig. 1.1. Speed gearboxes are connected between the gas turbine and the electrical generator, converting the input shaft rotating at a wide range of speeds to an output shaft that rotates at a constant speed. Electrical generators can then be fed with a constant input speed shaft.

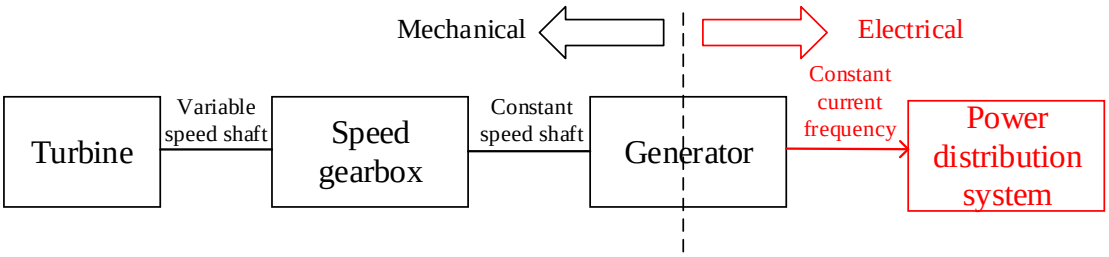


Fig. 1.1 Constant speed constant frequency generation system

- Variable speed constant frequency (VSCF) shown in Fig. 1.2. Electrical generators mounted on the turbine produce three phase alternating currents at variable frequencies due to the changes in revolutions per minute of the shaft. Three phase alternating currents are then passed to a power converter unit that converts them to a constant frequency-400 Hz.

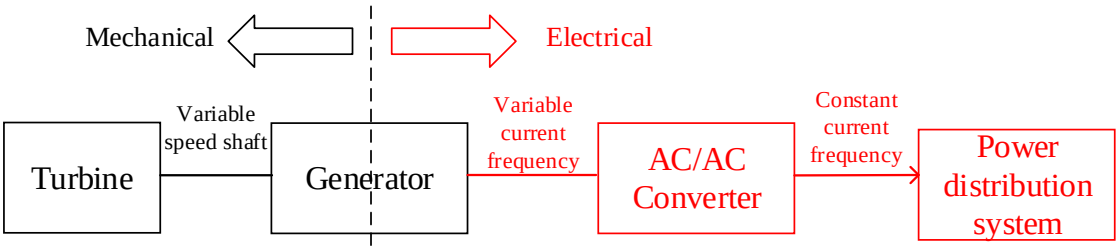


Fig. 1.2 Variable speed constant frequency generation system

- Variable speed variable frequency (VSVF) shown in Fig. 1.3. Generators with controllable excitations are connected to variable-speed shafts supplied by the main turbine engines. Closed loop control of the excitation allows a constant amplitude of the voltage, with frequency in the range of 350–800 Hz [9].

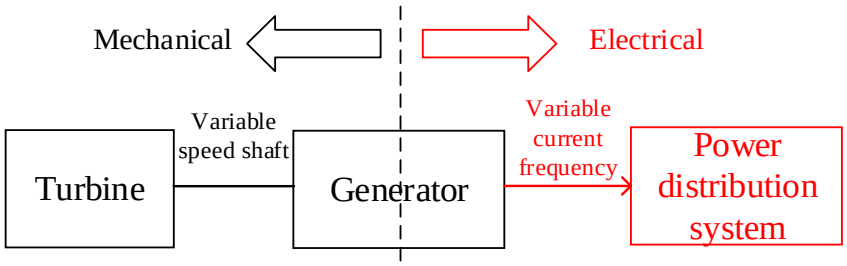


Fig. 1.3 Variable speed variable frequency generation system

The above mentioned electrical power generation systems have already been applied in a number of civil and military aircrafts as listed in Table 1.1.

TABLE 1.1 RECENT CIVIL AND MILITARY MEA WITH AC ELECTRICAL POWER SYSTEM [10]

Generation type	Civil aircrafts	Military aircrafts
CSCF	B777 2*120kVA A340 4*90kVA MD-12 4*120kVA B747-X 4*120kVA B717 2*40kVA B737NG 2*90kVA B767-400 2*120kVA	Eurofighter Typhoon
VSCF (Cycloconverter) 115VAC		F-18C/D 2*40/45kVA F-18E/F 2*60/65kVA
VSCF (DC link) 115VAC	B777 2*20kVA MD-90 2*75kVA	
VSVF 115VAC/380-760Hz	Horizon 2*20/25 kVA A380 4*150kVA	Boeing JSF 2*50kVA
VSVF 230VAC	B787 4*250kVA A350 4*100kVA	

1.2 DC power distribution system

The main purpose of the electrical power distribution system onboard an aircraft is to distribute electricity to the loads on the aircraft. The challenges with new aircraft is that they now have multiple power sources similar to renewable micro-grids. The electrical power distribution system has to manage those sources and provide power to each of its loads. Technologies are required to help design equipment that can work at high voltages, which reduces the current flowing through and helps to reduce the wire gauge needed to distribute power to the loads. Equipment also needs to be designed for operation at lower temperatures so that the units may

be placed in distributed locations of the aircraft where climate control may not be able to reach. The most important role for the electrical power distribution system is to keep the aircraft safe from short circuits. Conventionally, this has been done with circuit breakers and fuses. Today, as technology moves forward, solid state distribution systems are used to provide better and safer control of the systems.

According to MIL-STD-704F, the AC voltage standard is 115VAC (RMS) with frequency 360-800Hz. The high AC frequency leads to high reactive power and skin effects on the power line which reduces the power transmitting efficiency. In this respect, with a higher DC voltage standard 270VDC and zero frequency, the power line can transmit energy more efficiently. Another reason to use DC distribution is that the avionic loads are mainly of the DC type, using DC distribution reduces conversion stages along the power chain, boosting the power transmitting efficiency again. Therefore, the DC approach leads to higher efficiency, lower weight and costs [9], [11], [12].

Fig. 1.4 shows a typical MEA DC distribution structure which comprises a Low Voltage Direct Current (LVDC) network and a High Voltage Direct Current (HVDC) network. On the LVDC network, typically, Low Voltage (LV) emergency batteries and other energy storage elements, such as Electro-Mechanical Batteries (EMB), are connected to the Electrical Power Unit (EPU) which supplies avionics circuitry [13]. On the HVDC network, High Voltage (HV) generators [14], [15] provide the required voltage and power, together with HV batteries [13] and other electrical power units [16], which supply electric actuators, de-icing systems and other equipment [17]–[19]. Moreover, Starter Generator (S/G) systems [20], [21], with their Electrical Control Unit (ECU) are able to provide the required power to start the aircraft engines, and generate additional power during flight, on the HVDC or LVDC network.

In this distribution structure, the DC-DC converters plays roles in power conversion and management. Some DC-DC converters are essentially solid state transformers in the system converting voltage level between 270V and 28V. Another functionality for DC-DC converters is to manage the power from/to batteries.

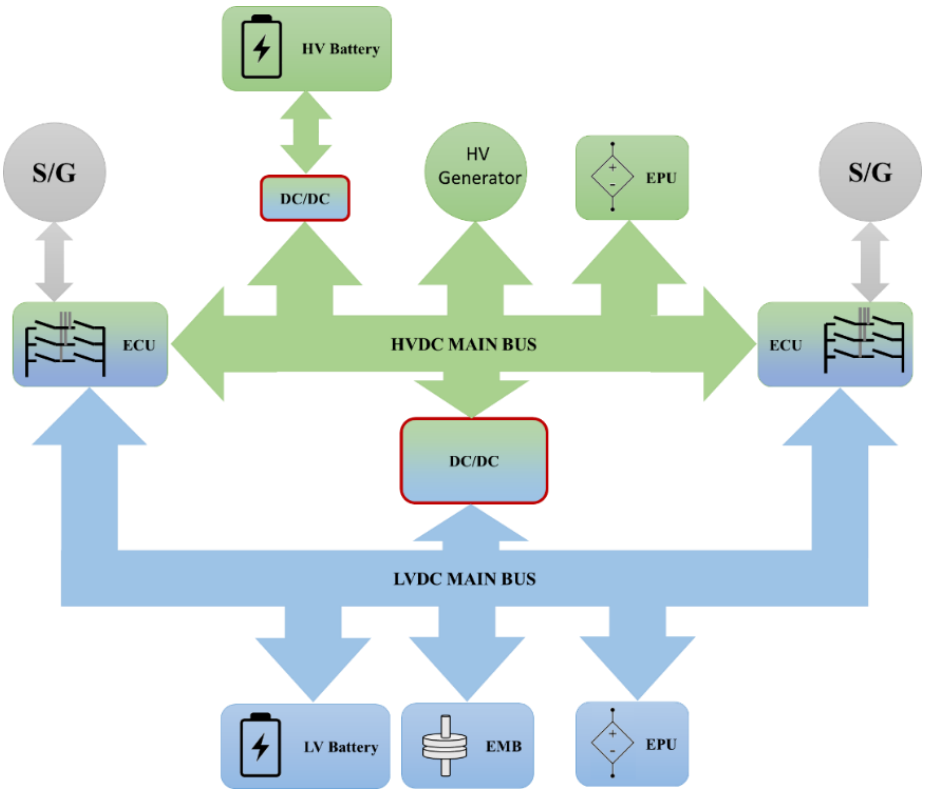


Fig. 1.4 MEA DC distribution system[22].

1.3 DC-DC power converters

As shown in Fig. 1.4, bidirectional DC/DC converters are necessary equipment in the DC distribution system to provide active interfaces between the DC networks [23], [24] and energy storage elements. The DC-DC converters are required to have high power density and high efficiency, to be integrated in the aircraft structure with minimum impact on volume, weight and heat management. At the same time, they must provide reliable and flexible operation, also to be capable of responding to fault events or other abnormal operating conditions with controlled and predictable behaviour, while minimising the impact on power generation. In particular, the reliability of the DC-DC converter is crucial during “emergency flight” operation, as it will supply the essential equipment to guarantee flight safety. The converter will also need to operate in a stringent and harsh environment, including limited cooling capabilities; pressure drops, mechanical vibrations and possible EMC or lightning interference, and their operation should have minimum effect on the environment. In order to achieve these challenging

requirements, it is clear that cutting-edge technological innovations, innovative design approaches and extensive reliability tests will be required. As a starting point, efforts have been made by researchers to find or innovate suitable DC-DC topologies for MEA applications.

Transformer isolation and solid state circuit breakers are two main approaches to prevent fault propagation. In the high current applications, the solid state circuit breaker needs to have several semiconductor switches in parallel to reduce the voltage drop and enough snubber to absorb the remaining energy on the power line when cutting off. These lead to increased cost and size/weight of the converter. In this regard, the transformer provides magnetic coupling between DC terminals with no electric connection. No extra devices are needed to put in series on the power line. The transformer also provides voltage step up/down capability.

A number of isolated DC/DC converter topologies have been found in existing literature. Flyback, Forward, and Forward-Flyback converters are investigated in [25], [26]. These topologies require a minimal number of active devices, however, the inefficient use of transformer results in their low efficiency. Resonant converters, such as isolated *LLC* resonant DC/DC converter and Series Resonant (SR) converter [27] can also be considered for this application. They take advantage of resonant networks in order to achieve Zero Voltage Switching (ZVS) or Zero Current Switching (ZCS) commutations, providing highly efficient power conversion. A series resonant DC/DC converter is analysed in [28], where all the switches can achieve both ZVS and ZCS. A hybrid between a LLC resonant and a DAB converter is proposed in [29], where the LLC is responsible for low power operation while the DAB contributes to the high power range. Tapped transformer and resonant tanks are employed in [30] to widen ZVS range. A fixed-frequency controlled series-resonant converter and its centre aligned modulation are studied in [31], which decouples the voltage gain from the operating power and frequency. However, additional passive components are needed in those converters. Moreover, converter design becomes challenging when a wide operating voltage is required due to large switching frequency variation.

To cope with the stringent power quality requirement in More-Electric-Aircraft (MEA), an inductor can be put on the DC side before the capacitor [32] to suppress the current ripple as shown in Fig. 1.5. However, this poses difficulties in current commutation.

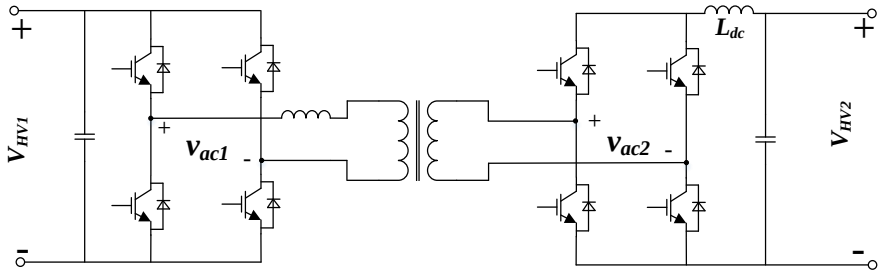


Fig. 1.5 The diagram of a current-fed DAB converter

Therefore, instead of configuring the inductor in series to the LV bus, it can be placed between AC terminal of the LV bridge and LV source/load as shown in Fig. 1.6.

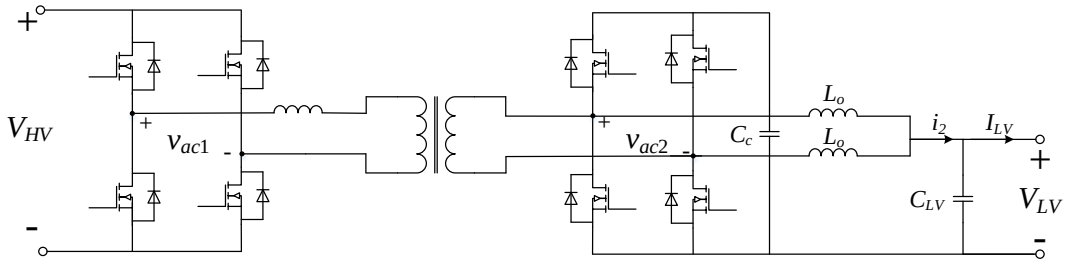


Fig. 1.6 The diagram of the interleaved current-fed DAB converter

A soft-switched bidirectional half-bridge DC-DC converter is proposed in [33]. This configuration not only can reduce the current ripple on the LV terminal, but can also increase the voltage step up/down capability, making the transformer easier to design. However, capacitors in the half bridge circuit need to handle the current flowing through the transformer. This requires capacitors with large current rating, thus making the topology less attractive in high power applications. Additionally, two inductors can be placed between LV source/load and LV bridge poles, and they are interleaved at the LV terminal [22], [34], [35]. This type of current-fed DAB converter can provide interleaved current paths on the LV terminal, reducing the requirement for passive filtering. The S-DAB topology proposed in [36] also features an interleaved structure, which incorporates two half bridges on the LV side. Diodes are used to achieve zero current switching (ZCS). In this configuration, DC transformer bias can be naturally suppressed without applying active controls [37], [38].

Dual-Active-Bridge (DAB) is the origin of lots of the derived topologies mentioned above. DAB presents a good capability for regulating the terminal voltage [39]. Reasonably high

efficiency can be achieved with low switching losses due to their natural capability of achieving ZVS commutation when the devices are turned on [40]. Understanding the characteristic of the DAB with sufficient depth can help with the derivation, design and assessment of other relevant isolated DC-DC power converters.

1.4 Objectives and contributions

The aim of this work is to look at the control strategy for a typical isolated DC-DC power converter – DAB in the on-board DC distribution system. Objectives of this work are listed as follows:

- Understand the characteristics of the DAB. The DAB topology is the origin of many others. Sufficient depth of understanding in DAB can help with the derivation, design and assessment of other relevant isolated DC-DC power converters. Knowledge in the operation principles of DAB also underpins the design of its control algorithm.
- Look into the converter level control strategy for the DAB. Conventional linear controllers are often designed based on a single equilibrium point which presents deteriorated performance in the global power and voltage operating ranges. Alternative control solutions need to be investigated to enable fast transition and stable operation of the DC-DC power converters with additional embedded flexibility in multi-objectives control.
- Address the stability in both converter and system levels. In the practical DC distribution system, DC-DC power converters may be subjected to erratic load and terminal voltages. Conventional small signal based converter stability analysis has limitations in the applicability of non-linear controllers, large converter model variations and significant load disruptions. Stability of the DAB converter itself and DAB enabled DC distribution systems need to be analysed.

The main contributions of this work are:

- A Moving Discretised Control Set – Model Predictive Control (MDCS-MPC) inspired from the well-known Finite Control Set – Model Predictive Control (FCS-MPC) is proposed. Circuit parameters, terminal voltages and operating modes of DAB are

embedded in the prediction model. Therefore, control parameters designed for MDCS-MPC can provide good performance throughout the power and terminal voltage range. The proposed approach enables flexible multi-objective optimization. Compared with previous applications of FSC-MPC in DC-DC converters [41], [42], MDCS-MPC utilizes only two prediction horizons and a small number of calculating points in each switching period. The computational burden is relatively low so the MDCS-MPC can be implemented in commercial control platforms. Fixed switching frequency is also obtained which eases passive components design.

- A phase portrait based stability analysis approach has been proposed for the assessment of large signal stability of the DAB converter. The DAB converter stability has been analysed with the MDCS-MPC, the results of which has shown insights into factors that stabilize or destabilize the converter operation. This analysis approach is also applicable for stability analysis with other linear and non-linear control methods.
- The MDCS-MPC has been extended into two-dimensional operation where the DAB converter is responsible for both efficiency maximization and load current regulation. The load current regulation demands fast transition while the efficiency is only at stake in the steady state. The two-dimensional MDCS-MPC brings benefits in adjusting the priorities between the two control objectives.
- The stability control of the DC distribution system has been incorporated as another control objective alongside the load current regulation. The proposed MDCS-MPC presents adaptive performance with uncertain grid impedance. Fast stabilization while maintaining reasonably good load regulation performance can be achieved. The proposed MDCS-MPC inherently can incorporate multi-objective control without the risk of losing the controllability of any of its control objectives. Parameters associated with MDCS-MPC have direct physical influence. Therefore, the design and tuning of the MDCS-MPC are more straightforward than multi-loop PI controllers.

1.5 Thesis outline

The thesis outline is summarized as shown in Fig. 1.7. Details of each chapter are described as follows:

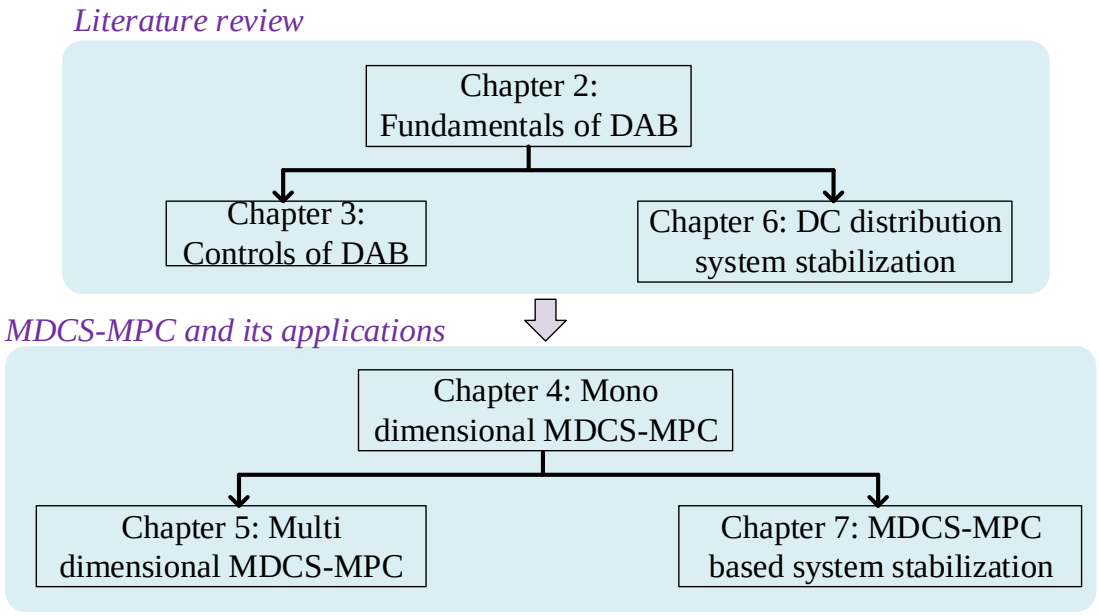


Fig. 1.7 Thesis outline

Chapter 2 provides the fundamentals of the DAB power converter, including the switching patterns, modulations, modelling and control. Two switching patterns – the phase shifting pattern and the pulse modulating pattern have been introduced. Modulations are implemented on top of the switching pattern. Two techniques, single phase shift modulation and triple phase shift modulation, have been introduced and analysed in detail. The modelling of DAB is also addressed. The ideal small signal models of triple phase shift have been developed, based on which the PI controller is designed. Issues with the PI controller are observed.

Chapter 3 gives an in-depth literature review on the control methods for the DAB converters, including feedback control, feedforward control, transformer current control, linearization control and sliding mode control. The load disturbance rejection and voltage tracking capabilities have been assessed. Based on the analysis, remarks on those control methods are given.

The mono-dimensional MDCS-MPC which provides fast transition and large signal stability is presented in Chapter 4. The introduction of the mono-dimensional MDCDS-MPC begins with the basic operating principle. Two approaches to enhance the transition performance of MDCS-MPC are discussed. A cost function which provides both reference racking and stability is derived. A compensation approach has been proposed to compensate for the steady state error.

The stability analysis is carried out for MDCS-MPC. The phase portrait has been used as the main analysis tool. For an easy start, a benchmark control is assumed where stability with current/resistive loads are analysed and proofed. The instability when the control saturates is explained. Based on all the above analysis, the stability with MDCS-MPC is addressed.

Chapter 5 introduces a two-dimensional MDCS-MPC. The advantage of the online over the offline optimization has been addressed. The implementation of the online optimization with two-dimensional MDCS-MPC is introduced. The two dimensional discretised control set and the search method have been illustrated and distinguished from the mono-dimensional MDCS-MPC. A cost function is proposed which, on one hand, regulates the load current. On the other hand, it reduces the transformer peak current value. The dynamic performance of the introduced two-dimensional MDCS-MPC has been assessed. The effectiveness of the transformer peak current reduction term in the cost function has been validated.

Another scenario is investigated where the DAB converter is responsible for both load current regulation and DC system stabilization in Chapter 6. The impedance stability criteria has been developed. Based on the criteria, the system stability is determined by the impedance ratio. Theoretical analysis on the passive damping has been performed. Active stabilization methods are looked into as alternatives to passive damping approaches. Active stabilization methods are achieved by control algorithm without inducing physical components. The conventional PI based stabilization control presents a critical problem with control loop saturation which has been addressed. A solution named co-ordination integration with a few changes to the conventional PI control is proposed.

An alternative active damping control is established based on the mono-dimensional MDCS-MPC in Chapter 7. The cost function has been modified and incorporates a system stabilization term. The impedance based stability analysis has been carried out using the describing function for the proposed MDCS-MPC. Comparisons between the PI and MDCS-MPC based stabilization control techniques are presented in both time and frequency domain. Experiments are also conducted to verify the theoretical claims.

Chapter 2 The Fundamentals of the Dual-Active-Bridge

A diagram of the Dual-Active-Bridge (DAB) converter is shown in Fig. 2.1. The transformer ratio is set as 1 for 270V-270V application. Two H-bridges, H_1 and H_2, one each side of the high frequency transformer, generate quasi-square wave voltages v_{ac1} and v_{ac2} with a fundamental frequency of f_s. Voltages v_{ac1} and v_{ac2} are applied across the power transferring inductor L_p, producing a transformer current i_{ac2}.

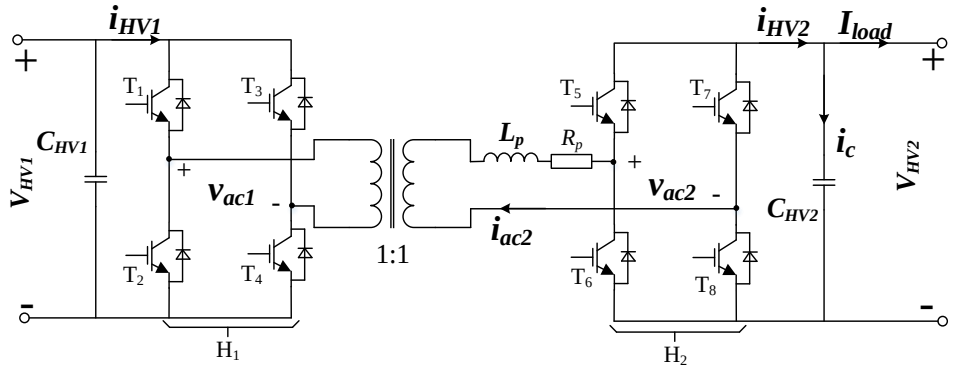


Fig. 2.1 The diagram of the DAB converter under investigation.

There are three states for each transformer terminal voltages v_{ac1} and v_{ac2} as shown in Fig. 2.2. The transformer primary terminal voltage v_{ac1} can be V_{HV1}, 0 or $-V_{HV1}$ during any switching period T_s, while transformer secondary terminal voltage v_{ac2} can be V_{HV2}, 0 or $-V_{HV2}$. During one switching cycle, active states V_{HV1} and $-V_{HV1}$ in v_{ac1} must have the same time period T_1 to avoid transformer primary DC bias. Active states V_{HV2} and $-V_{HV2}$ in v_{ac2} must also have the time period T_2 to avoid transformer secondary DC bias. D_1 and D_2 are termed as active states duties. D_1 and D_2 are defined as:

$$D_1 = \frac{T_1}{T_s} \tag{2. 1}$$

$$D_2 = \frac{T_2}{T_s} \tag{2. 2}$$

where T_3 is the period between the rising edges of transformer terminal voltages v_{ac1} and v_{ac2}. If T_1 leads T_5, T_3 is positive otherwise negative. T_f represents the time shift between the centres

of the two transformer voltages v_{ac1} and v_{ac2}. D_3 and D_f are termed as phase shift duties. D_3 and D_f are defined as:

$$D_3 = \frac{T_3}{T_s} \tag{2. 3}$$

$$D_f = \frac{T_f}{T_s} \tag{2. 4}$$

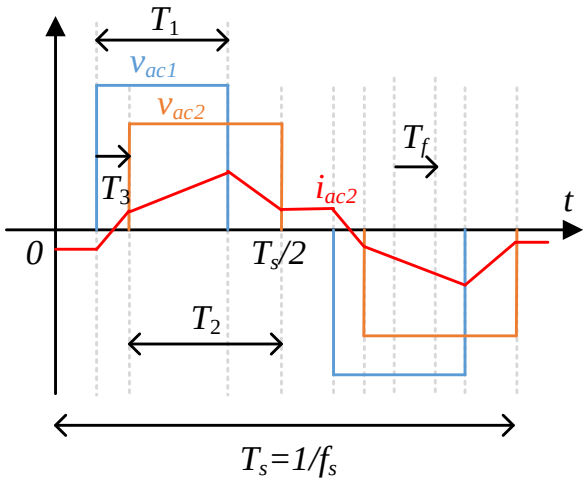


Fig. 2.2 Generic waveforms of the DAB.

In this chapter, switching patterns, modulations, modelling and control for DAB are introduced. The switching patterns in section 2.1 describe two different ways to generate the quasi-square wave voltages v_{ac1} and v_{ac2}. Modulations are responsible for the converter steady state optimizations. The relationships between D_1, D_2 and D_3 are derived as optimizing outcomes. Prevailing modulation techniques are introduced in section 2.2. In section 2.3, analysis is carried out with the most straightforward and popular modulation technique on DAB named Single Phase Shift (SPS). The optimization with the most complex modulation technique named Triple Phase Shift (TPS) is addressed in section 2.4. Modelling and control are discussed in section 2.5. The relationship between the switching pattern, the modulation and the control are shown in Fig. 2.3.

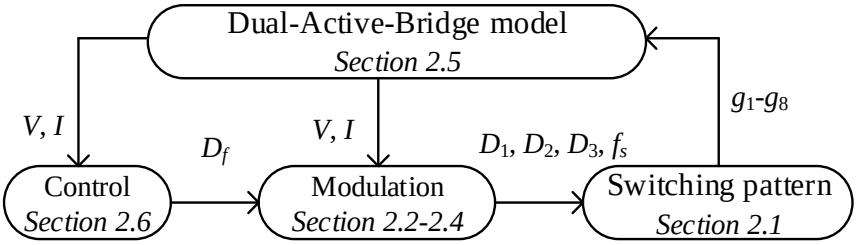
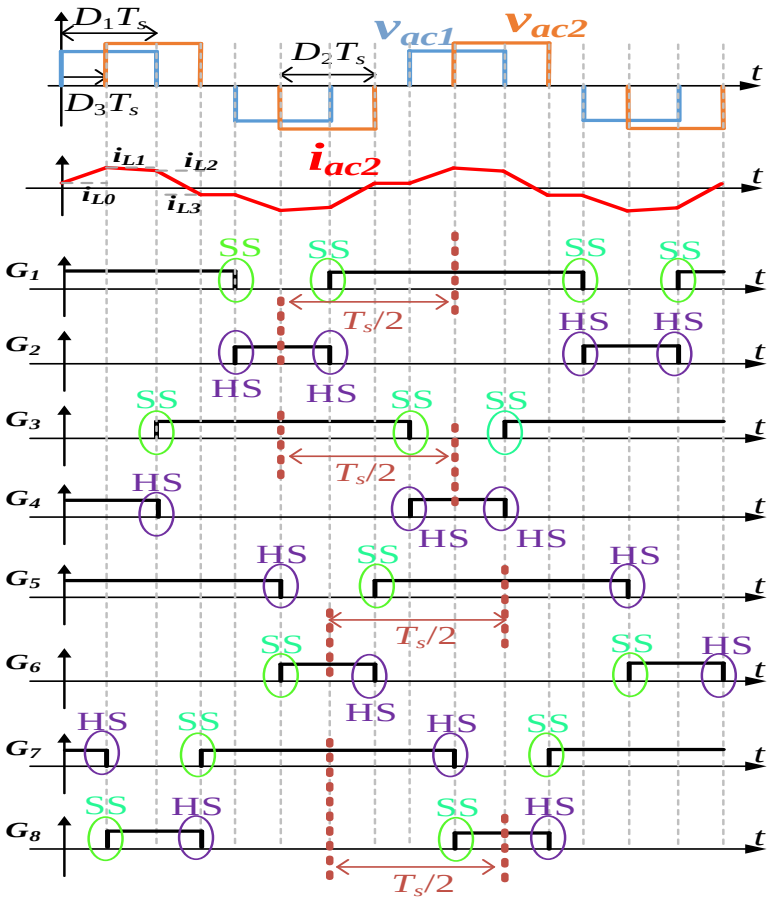


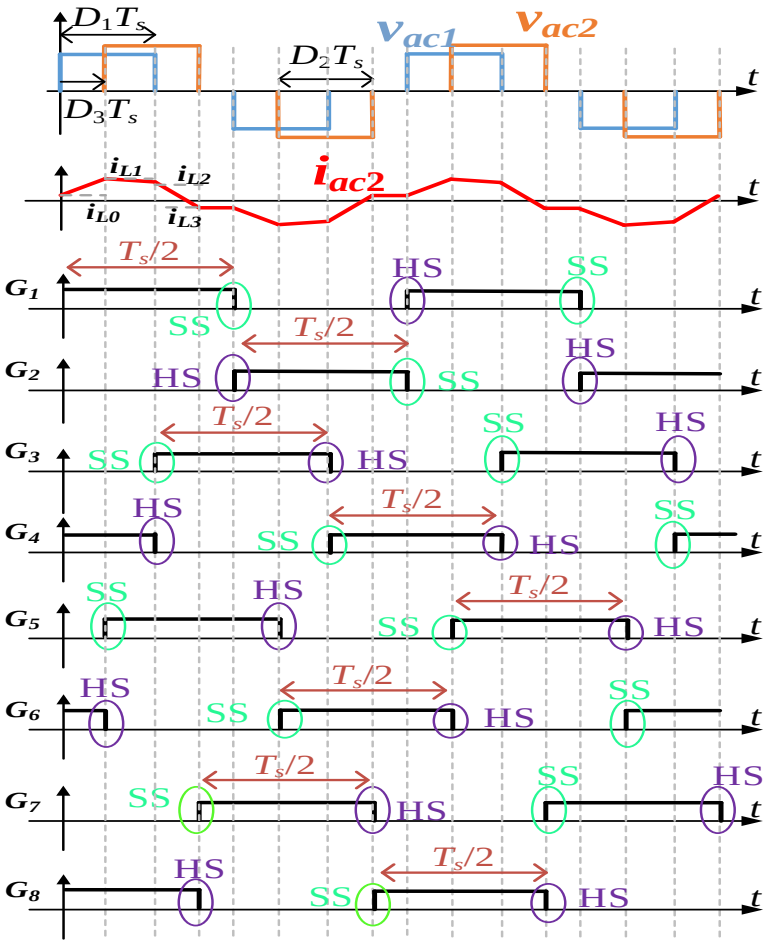
Fig. 2.3 Relationship between the switching pattern, the modulation and the control.

2.1 Switching patterns

There are two basic ways to generate the quasi-square wave voltages v_{ac1} and v_{ac2} –pulse width modulating pattern Fig. 2.4(a) [43] and phase shifting pattern Fig. 2.4(b) [44]. The phase shifting pattern is the most used method. In the phase shifting pattern, duty cycles are fixed at 50% for all of the switches as shown in Fig. 2.4 (b).



(a) pulse width modulating pattern

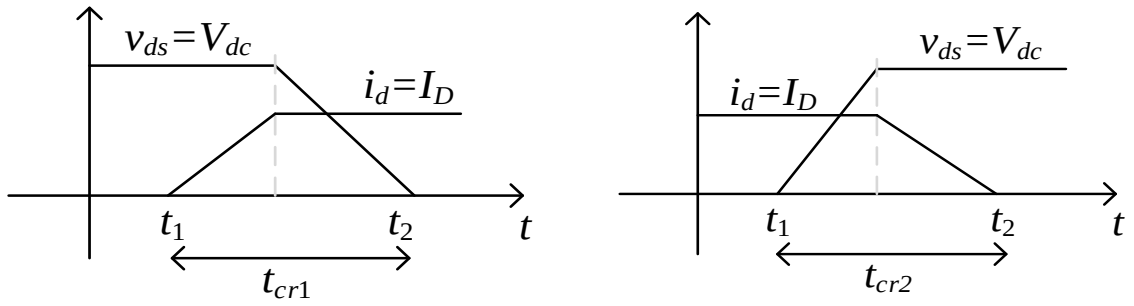


(b) phase shifting pattern

Fig. 2.4 Two possible switching patterns for DAB converters where HS stands for hard switching and SS stands for soft switching.

The pulse width modulating pattern is shown in Fig. 2.4 (a). Compared with the phase shifting pattern, the pulse width modulating pattern defines a fixed 180 degree phase shift between bridge legs within the same H bridge. Duty cycles of switches are controlled to generate the quasi-square wave voltages v_{ac1} and v_{ac2}.

Assuming that the same switching devices are used for T_1-T_8, and the ideal hard switching process is shown in Fig. 2.5.



(a) on (b) off

Fig. 2.5 Idea switching waveforms with inductive loads

The Switching losses can be calculated as:

$$P_{on} = f_s \int_{t_1}^{t_2} v_{ds} i_d dt = \frac{1}{2} t_{cr1} f_s V_{dc} I_D = k_{on} V_{dc} I_D \tag{2. 5}$$

$$P_{off} = f_s \int_{t_1}^{t_2} v_{ds} i_d dt = \frac{1}{2} t_{cr2} f_s V_{dc} I_D = k_{off} V_{dc} I_D \tag{2. 6}$$

$$P_{sw} = P_{on} + P_{off} = V_{dc} I_D (k_{on} + k_{off}) \tag{2. 7}$$

Comparisons of the switching loss P_{sw} between the two switching patterns are listed below in Table 2.1. One observation is that when the phase shifting pattern is used, losses are evenly distributed between switches in the same bridge leg. When pulse width modulating pattern is used, although the overall losses are the same to that of its counterpart, the switching losses are not evenly distributed between the switches in the same bridge leg. This phenomena in the pulse width modulating pattern, on one hand, would cause difficulty in choosing switching devices; On the other hand, if properly utilized, this phenomena potentially provides extra degree of freedom to implement active thermal control of the device junction temperature [45]. Conventionally, phase shifting pattern is often used rather than pulse width modulating pattern in DAB.

TABLE 2.1 SWITCHING LOSS COMPARISON BASED ON FIG. 2.4

	Phase shift pattern	Pulse width modulating pattern
T_1	$2k_{on}V_{HV1}i_{L0}$	0
T_2	$2k_{on}V_{HV1}i_{L0}$	$2V_{HV1}$ ($k_{on}i_{L0}$+ $k_{off}i_{L2}$)

T_3	$2k_{off}V_{HV1}i_{L2}$	0
T_4	$2k_{off}V_{HV1}i_{L2}$	$2V_{HV1}\ (k_{on}i_{L0}+ k_{off}i_{L2})$
T_5	$2k_{off}V_{HV2}i_{L1}$	$2k_{off}V_{HV2}i_{L1}$
T_6	$2k_{off}V_{HV2}i_{L1}$	$2k_{off}V_{HV2}i_{L3}$
T_7	$2k_{off}V_{HV2}i_{L3}$	$2k_{off}V_{HV2}i_{L1}$
T_8	$2k_{off}V_{HV2}i_{L3}$	$2k_{off}V_{HV2}i_{L3}$
Sum	$4(k_{on}V_{HV1}i_{L0}+ k_{off}V_{HV1}i_{L2}+ k_{off}V_{HV2}i_{L1}+ k_{off}V_{HV2}i_{L3})$	$4(k_{on}V_{HV1}i_{L0}+ k_{off}V_{HV1}i_{L2}+ k_{off}V_{HV2}i_{L1}+ k_{off}V_{HV2}i_{L3})$

2.2 Modulation techniques

Prevailing modulation techniques for DAB converters are Single-Phase-Shift (SPS) modulation [46], Extended-Phase-Shift (EPS) modulation [47], Dual-Phase-Shift (DPS) modulation [48], Triple-Phase-Shift (TPS) modulation [49], TRiangular current Manipulation (TRM) modulation [50] and TrapeZoidal current Manipulation (TZM) modulation [51]. Conceptual waveforms of those modulation techniques are shown in Fig. 2.6.

In the Single Phase Shift (SPS) modulation Fig. 2.6(a), D_3 and D_f are equal, while D_1 and D_2 are fixed at 0.5. When SPS modulation is used, there is only one control variable that is D_f. D_f is therefore used to achieve the main control objective such as the regulation of power, terminal voltage or current. However, when the other modulation techniques, shown in Fig. 2.6(b)-(f), are used, more control variables can be made available. There is a maximum of four control variables, D_1, D_2, D_f (or D_3) and f_s. The existence of an extra degree of freedom in control provides the possibility for optimizing the steady state operation of DAB converters for a range of objectives. The transformer peak current optimization for the TPS will be addressed in section 2.4.

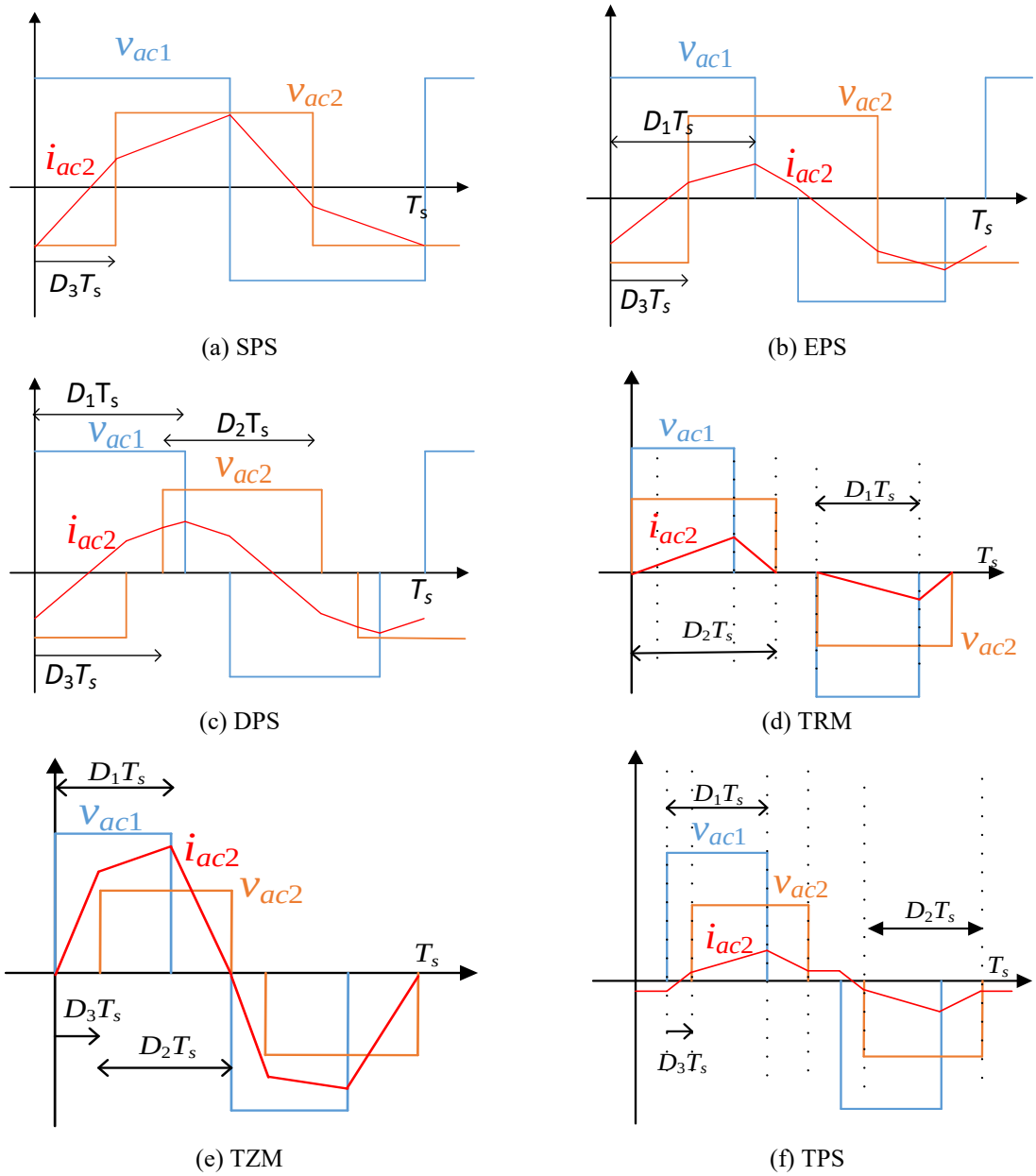


Fig. 2.6 Conceptual waveform demonstrations on existing modulations. (a) D_1=0.5, D_2=0.5, D_3 is controlled; (b) D_2=0.5, D_1 and D_3 are controlled or D_1=0.5, D_2 and D_3 are controlled; (c) D_1=D_2=D, D and D_3 are controlled; (d) D_3=0, D_1 and D_2 are controlled to achieve ZCS and ZVS; (e) D_1, D_2 and D_3 are controlled to achieve ZCS and ZVS and (f) D_1, D_2 and D_3 are controlled.

Relationships between those techniques are shown in Fig. 2.7. The overlap between DPS and EPS is SPS. The transformer current in TRM has a triangular shape while the shape for TZM is trapezoidal. Therefore, there also exists an overlap between DPS and TZM, and the same between EPS and TRM. As illustrated in Fig. 2.6(f), TPS is the universal modulation which comprises all of the modulations illustrated in Fig. 2.6.

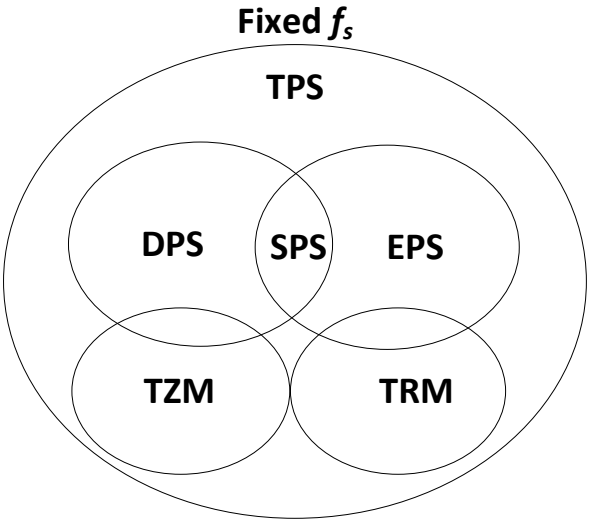


Fig. 2.7 Relationship between modulations

Switching frequency can also be considered as another control variable in addition to the phase shift duty (D_3) and active states duties (D_1, D_2) [52]. Four control variables D_1-D_3 and f_s collectively determine the power transfer in DAB converters. However, due to the difficulty in the design of passive components and the complexity in the optimization, variable frequency modulations pose less attraction to practical engineers. Typical works on the above mentioned modulation techniques are classified in Table 2.2.

TABLE 2.2 MODULATION TECHNIQUES

Variables	D_3	D_1 D_2	f_s	Degree of Freedom
SPS [53]	Controlled	Const. (D_1=D_2=0.5)	Const.	1
EPS [47]	Controlled	Controlled (D_1 or D_2)	Const.	2
DPS [48]	Controlled	Controlled (D_1=D_2)	Const.	2
TPS [54]	Controlled	Controlled	Const.	3
TRM [50]	Controlled	Calculated from D_3	Const.	1
TZM [51]	Controlled	Controlled	Const.	3
Variable f_s [52]	Controlled	Const. (D_1=D_2=0.5)	Controlled	2

The advantage of the SPS modulation is its simplicity. Only a single control variable - the duty D_3, is required to adjust the DAB power level. SPS is the most popular modulation technique in DAB[39], [46], [53], [55]. However, there are a few major drawbacks:

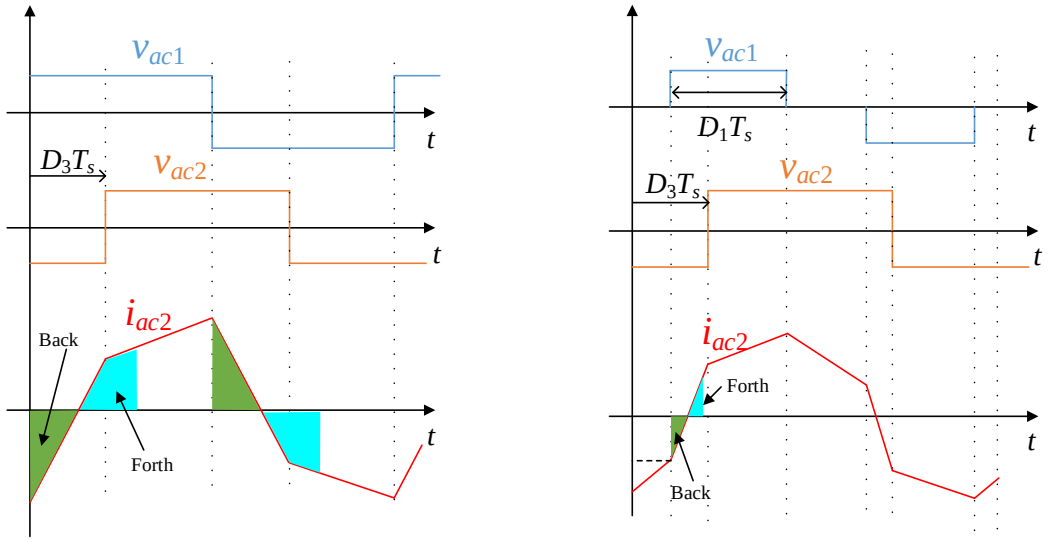
- The back and forth power flowing through the inductor results in extra unnecessary conduction loss. This will be discussed in section 2.3.4.

- SPS cannot achieve ZVS across the whole power range when terminal voltages vary from their nominal values. Therefore, switching loss could be high in partial loads, and efficiency would be greatly reduced. Detailed discussions are provided in section 2.3.2.

The disadvantages of SPS give motivation towards investigating alternatives which take advantages of the full bridges by not only adjusting the phase shift duty but by also changing the active state duties in order to reduce the circulating current and to achieve low switching losses.

In EPS modulation, the cross-connected switch pairs in one full bridge are alternatively switched generating a 50% duty square wave pole voltage, while switch pairs in another bridge are operated with an inner phase-shift ratio [47]. This results in a three-level quasi-square wave pole voltage. During the time intervals of the zero voltage of the three-level wave, the current flows within the full bridge without passing through the voltage source or loads, and the instantaneous power is 0. So the circulating power decreases. An intuitive back and forth power comparison between SPS and EPS is given in Fig. 2.8. Note that the figure is drawn conceptually to illustrate the possibility of using EPS to reduce the reactive power in the inductor and transformer. Detailed explanations can be found in the literature [47]. As illustrated in Fig. 2.6(b), there are two degrees of freedom for the EPS, therefore, there are possibilities to improve the efficiency of the converter. However, the accurate loss model of the DAB converter is complex due to the existence of the high frequency transformer, which makes the optimization problem complicated. Therefore, indirect optimization objectives are introduced such as the switching and conduction losses [56], the transformer Root-Mean-Square (RMS) value [57], [58], the transformer peak current value [59] and reactive power [52], [54], [60]. Similar features also apply to both DPS and TPS.

There are also some works which look into the combinations of standard modulations to achieve better results over the whole power range. A combination between TRM, TZM and SPS is proposed in [61] while model predictive control is introduced to estimate the optimal modulation between SPS and TRM in real time [62]. It can be concluded that TRM has advantages in efficiency under light load due to the fact that the transformer current is discontinuous and ZCS can be achieved while SPS is always used in high load power because it has a wider power operation range.



(a) (b)

Fig. 2.8 Conceptual waveforms to show the back and forth power in (a) SPS modulation. (b) EPS modulation

TPS modulation typically provides the best optimization results, however, the complexity of the TPS modulation hinders its application in practice. Therefore, in order to enhance the efficiency when switching losses are dominant, the TRM and TZM illustrated in Fig. 2.6 are typically considered. As shown in Fig. 2.6(d), TRM allows the secondary side H-bridge switching at zero current when both on and off. Furthermore, compared to SPS, a considerable reduction of the RMS current could also be achieved at partial loads [63]. Compared to the TRM, the TZM shown in Fig. 2.6(e) can extend the power range [64], [65].

2.3 Analysis on Single-Phase-Shift (SPS) modulation

The existence of the high frequency transformer makes the DAB converters very different from the conventional non-isolated DC-DC power converters. Characteristics such as the power transmission, zero voltage switching and dead-band effect are addressed in this section. In order to simplify the analysis, only SPS is considered, however, the same analysis methods also apply for DAB using other modulations, as shown in Fig. 2.6.

2.3.1 Power transmission

The DAB converter is extensively used to manage the power flow in applications, for energy storage systems, renewable sources integration and electrical vehicles. In most cases, DAB is

controlled in the power/current mode where both DC sides have their own independent voltage sources.

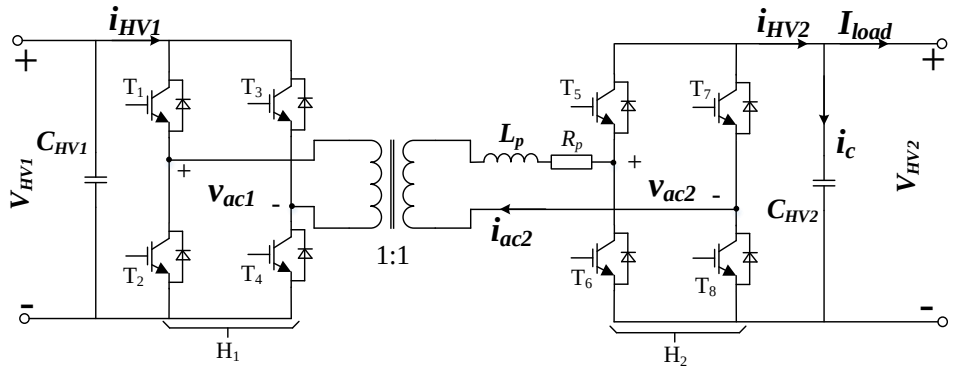


Fig. 2.9 DAB with both terminals connected to DC sources.

For a 270V/270V power conversion, the transformer turn ratio N is set as 1. The conceptual waveforms for SPS under two different terminal voltage conditions are shown in Fig. 2.10.

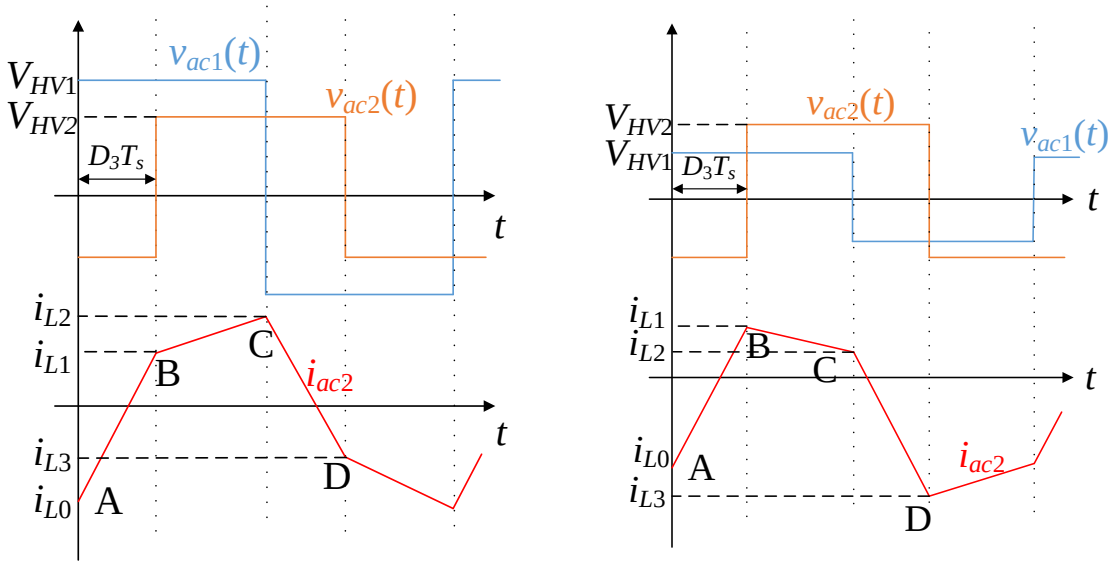


Fig. 2.10 Conceptual waveforms for SPS (a) $V_{HV1}>V_{HV2}$ and (b) $V_{HV1}<V_{HV2}$.

Only a half cycle is needed to calculate the transferred power due to the symmetry waveform, thus the expression of power is:

$$P_{DC}=\frac{2}{T_s}\int_0^{\frac{T_s}{2}} v_{ac2}(t)\bullet i_{ac2}(t)dt=\frac{2}{T_s}V_{HV2}\int_0^{\frac{T_s}{2}} i_{ac2}(t)dt \tag{2. 8}$$

In order to calculate the power, the initial current value i_{L0} in Fig. 2.10 must firstly be calculated. (2. 9) and (2. 10) hold true regardless of the terminal voltage condition for SPS.

$$i_{L0} = -i_{L2} \tag{2. 9}$$

$$i_{L2} = i_{L0} + \frac{V_{HV1} + V_{HV2}}{L_p} D_3 T_s + \frac{V_{HV1} - V_{HV2}}{L_p} (0.5 - D_3) T_s \tag{2. 10}$$

Therefore, the initial current can be calculated as:

$$i_{L0} = \frac{(V_{HV2} - V_{HV1}) - 4D_3 V_{HV2}}{4 f_s L_p} \tag{2. 11}$$

Substituting (2. 11) into (2. 8), the transferred power is obtained:

$$P_{DC} = \frac{V_{HV1} V_{HV2}}{f_s L_p} D_3 (1 - 2|D_3|) \tag{2. 12}$$

, where D_3>0 stands for the power transferred from V_{HV1} to V_{HV2}, and D_3<0 means the opposite. Maximum power can be achieved when D_3=0.25.

$$P_{\max} = \frac{V_{HV1} V_{HV2}}{8 f_s L_p} \tag{2. 13}$$

Hence the relative power as a function of D_3 is:

$$P_{SPS}^{(pu)} = \frac{P_{DC}}{P_{\max}} = 8D_3 (1 - 2D_3) \tag{2. 14}$$

According to formula (2. 14), the transmission power characterization is shown in Fig. 2.11. The power increases with D_3 in the range from -0.5 to 0.5. If D_3 exceeds this range of operation, the power is going to decrease with D_3. Therefore, from the PI control perspective, the operating range of D_3 is set within [-0.5, 0.5]. From the perspective of operating efficiency, when D_3 exceeds the operating range [-0.5, 0.5], the ratio between reactive power to active power increases, leading to efficiency drop. This will be discussed later in the chapter.

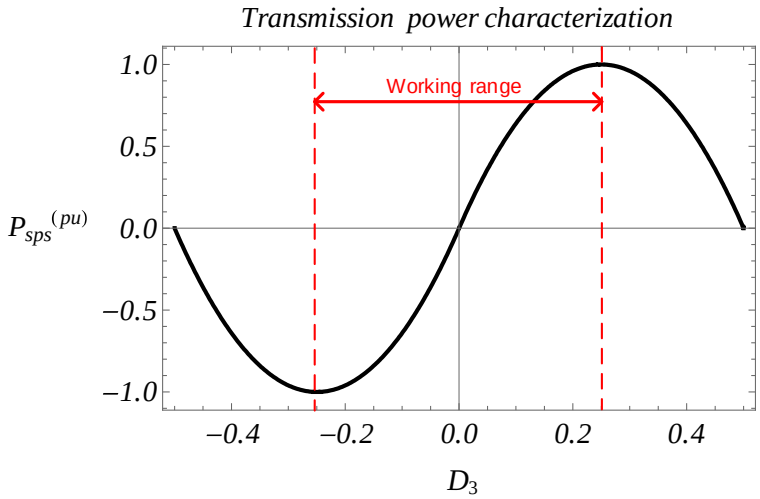


Fig. 2.11 Unified transmission power characterization of SPS.

2.3.2 Zero Voltage Switching (ZVS)

ZVS is a term to describe the condition when the voltage stress drops to zero before a switch is turned on. There would be no turn-on loss under ZVS conditions. Typically, when ZVS is achieved in the DAB, the switching losses would be small resulting in high power conversion efficiency. DAB converters can lose ZVS when terminal voltages vary from their nominal values. In order to appreciate this phenomena, the ZVS region is analysed in this section. The constraints which define the ZVS can be specified for the two H-bridges as

$$i_{L0} < 0 \tag{2. 15}$$

$$i_{L1} > 0 \tag{2. 16}$$

, where i_{L0} and i_{L1} are calculated as:

$$i_{L0} = \frac{(V_{HV2} - V_{HV1}) - 4D_3 V_{HV2}}{4 f_s L_p} \tag{2. 17}$$

$$i_{L1} = \frac{V_{HV2} + V_{HV1}(4D_3 - 1)}{4 f_s L_p} \tag{2. 18}$$

Therefore, ZVS constraints are derived as:

$$\frac{(1-M)}{4} < D_3, \text{ if } M < 1 \tag{2. 19}$$

$$\frac{(M-1)}{4M} < \mathrm{D}_3, \text{ if } M > 1 \tag{2. 20}$$

, where M is the voltage ratio defined as:

$$M = \frac{V_{HV2}}{V_{HV1}} \tag{2. 21}$$

According to (2. 19) and (2. 20), the ZVS region can be plotted in Fig. 2.12. When M equals 1, ZVS for both H_1 and H_2 can always be achieved independentlt from the phase shift duty D_3. This is why the DAB is often preferred to be operated under ideally fixed nominal terminal voltages. The more M deviates from 1, the smaller the ZVS region will be.

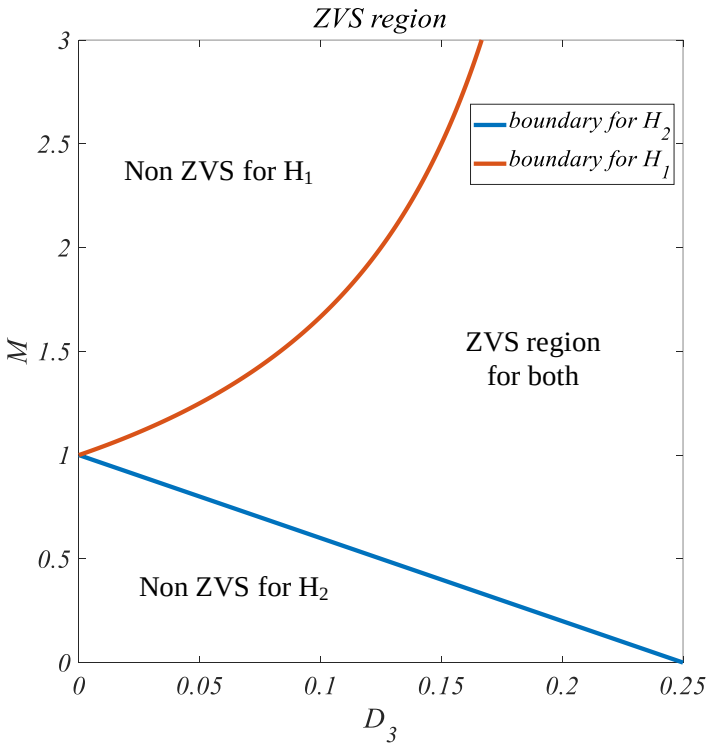


Fig. 2.12 The ideal ZVS region of a DAB with SPS modulation.

An intuitive way to understand Fig. 2.12 is shown in Fig. 2.13. With the increasing of load power, D_3 also increases as per (2. 12). According to (2. 17), (2. 18) and Fig. 2.13, with the increasing of D_3, i_{L0} decreases while i_{L1} increases. When M<1 as in Fig. 2.13 (a), i_{L0} is always smaller than zero, therefore ZVS can always be achieved for the H_1 bridge. However, with the decreasing of D_3, i_{L1} could be smaller than zero. ZVS cannot be guaranteed for the H_2 bridge

within the full power range when M is not equal to 1. Similar phenomena happens when M>1 in Fig. 2.13 (b), where the role of H_1 and H_2 changes.

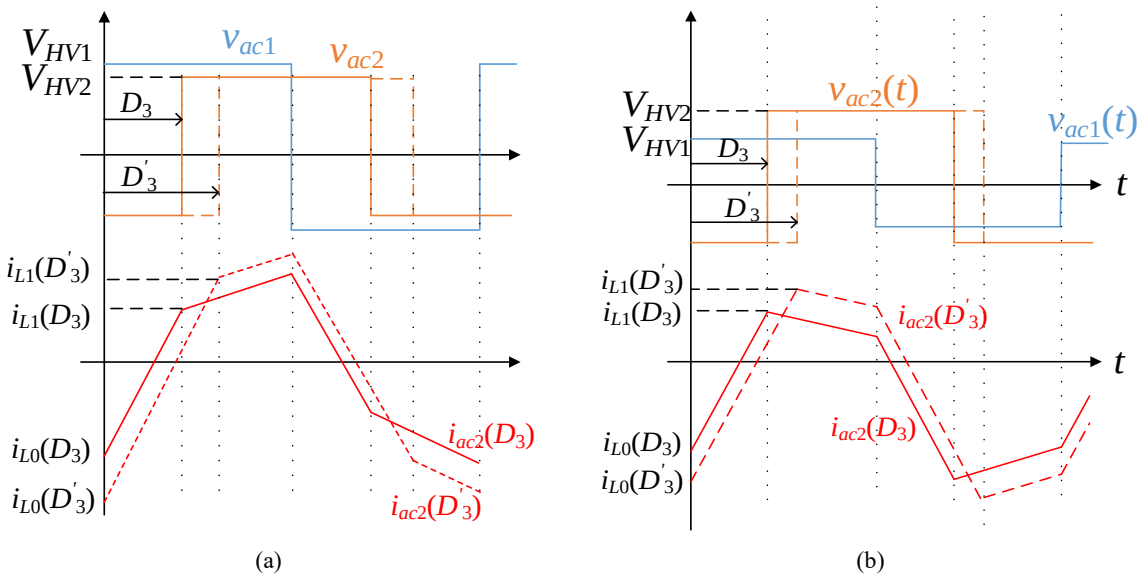


Fig. 2.13 Transformer current with different outer phase shift values under the terminal voltage condition (a) M<1 and (b) M>1.

Note that the ideal ZVS region is only relevant to the voltage ratio M and the phase shift duty D_3. In practice, other parameters such as the transformer magnetising inductance and the snubber capacitance have also impact on the ZVS region [66].

2.3.3 Dead-band effect

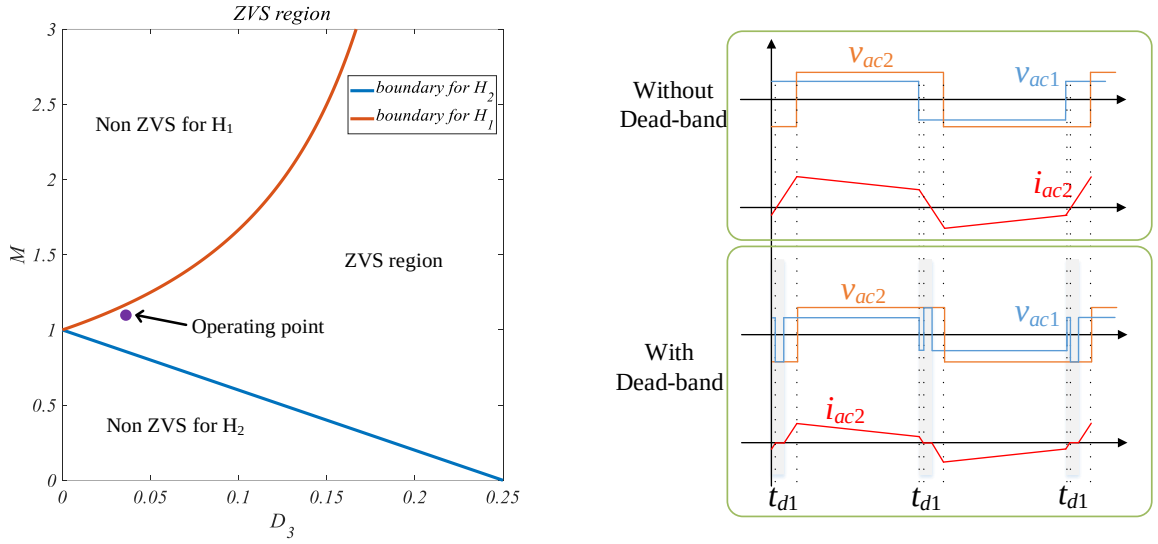
To avoid the shoot-through of the bridge in the commutating process, a dead-band is inserted between the interlocked switches in the same bridge. The dead-band is crucial to guarantee the reliability of the converter operations. However, the dead-band will cause waveform distortion and other unexpected short-timescale phenomena in SPS.

In this section, many of the dead-band effects have been analysed in different operating scenarios of the DAB converter. The results are summarized in Table 2.3. t_{d1} and t_{d2} are the dead-band time for H_1 and H_2 bridges, respectively. It has been shown in the table that when the operating point is within the ZVS region shown in Fig. 2.12, the only possible dead-band phenomena is the ringing in the primary pole voltage v_{ac1} while ZVS is not achieved for either H_1 or H_2, phenomena such as phase drift or ringing in the secondary pole voltage v_{ac2} can occur.

TABLE 2.3 DEAD-BAND EFFECT IN DIFFERENT SCENARIOS

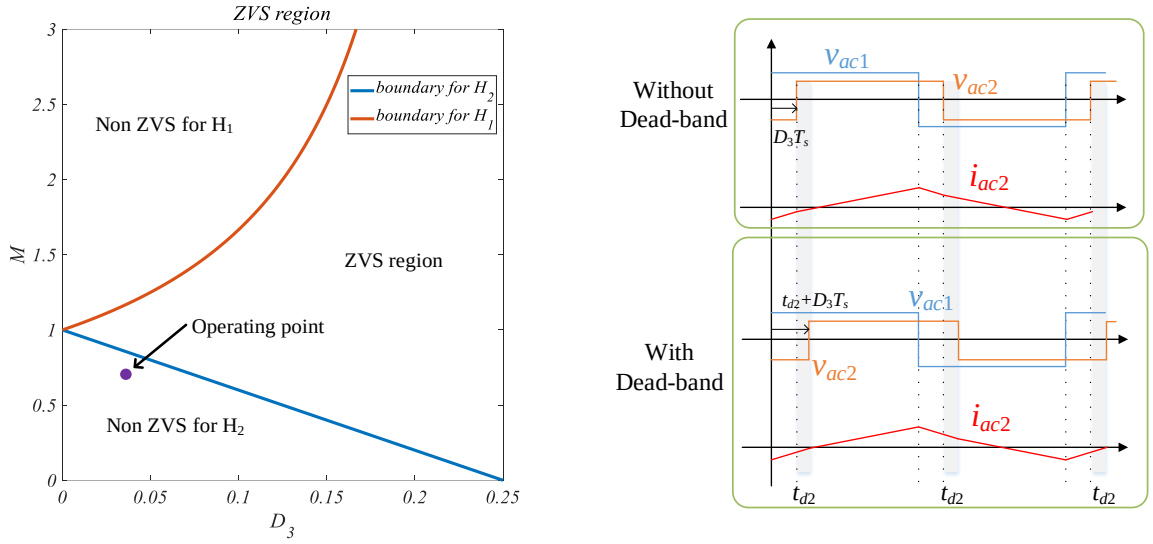
ZVS	M	Current polarity change		Phenomena
		during t_{d1}	during t_{d2}	
Yes	M<1	No	No	No effect
		Yes	No	v_{ac1} ringing [67], [68]
	M>1	Yes	No	v_{ac1} ringing (Fig. 2.14) [46], [53]
		No	No	No effect
No	M<1	No	Yes	v_{ac2} ringing [69]
		No	No	v_{ac2} phase drift (Fig. 2.15) [69]
	M>1	No	Yes	v_{ac2} ringing [69]
		No	No	v_{ac1} phase drift [69]

The typical waveforms for operation under M>1 are shown in Fig. 2.14 where the transformer current changes its direction within the dead-band time for bridge H_1. The primary pole voltage v_{ac1} changes its polarity during the dead-band time causing voltage ringing in the practice where parasitic components are included in the circuit. When compared with the ideal case without dead-band time, the transformer current reduces, indicating that less power is transferred. Another example showing the phase drift phenomena is shown in Fig. 2.15. The outer phase shift is increased by t_{d2} due to the dead-band effect.



(a) (b)

Fig. 2.14 Voltage ringing example with (a) the operation point in M>1 ZVS region and its corresponding (b) waveforms comparing phenomena with/without dead-band.



(a) (b)

Fig. 2.15 Phase drift example with (a) the operation point M<1 in ZVS region and its corresponding (b) waveforms comparing phenomena with/without dead-band.

The changes of polarity in the pole voltages are caused by the change of transformer current direction during the dead-band time. The ringing in the pole voltage could potentially cause increased energy loss and electromagnetic interference (EMI) problems [53]. Apart from these issues, both phenomena could cause an error in power transfer with respect to the calculation in (2. 12). This indicates the fact that when power is zero, the phase shift duty D_3 is not necessarily zero. When PI control is implemented, this error can be easily compensated, however, D_3 should be allowed to change its polarity even in unidirectional applications.

2.3.4 Considerations for the choice of L_p

The inductor L_p in the circuit shown in Fig. 2.1 is utilized to transfer power between two H bridges on each side of transformer. Inductance L_p is often designed to match the maximum power P_{max} calculated in (2. 13) to the required power P_r.

$$L_p = \frac{V_{HV1} V_{HV2}}{8 f_s P_r} \tag{2. 22}$$

However, the value of L_p calculated by (2. 22) requires the phase shift duty D_3 to be 0.25 at full power. This design approach considers only the power transferring capability and does not consider reactive power consumption or take the soft switching region into account. In this section, design considerations for L_p are addressed.

2.3.4.1 Reactive power

Reactive power is a parameter of interest to investigate in a DAB converter. By reducing reactive power in the high frequency transformer stage, RMS value of the transformer current could be minimised at partial power. As a result, this reduces conduction and copper losses. Different definitions of the reactive power for DAB are found in [48], [60], [70]. *H. Bai et al.* defined reactive power as back and forth power, as shown in Fig. 2.8 [48]. If no negative power flow exists, the converter has zero reactive power consumption. However, this is inaccurate since a DAB always has reactive power due to the existence of the power transferring inductance L_p. Another definition is given by the authors of [70] as a product of the inductor voltage RMS value and current RMS value to represent the reactive power for non-sinusoidal voltage and current. *B. Zhao et al.* [60] adopted Fourier transformation to calculate reactive power in each frequency the same way as how reactive power is calculated in a conventional AC power system. This last definition is used in this section where the Fourier transformation of the transformer pole voltages are:

$$v_{ac1}(t) = \frac{4V_{HV1}}{\pi} \sum_{n=1}^{\infty} \frac{1}{2n-1} \sin(2n-1)\omega t \tag{2. 23}$$

$$v_{ac2}(t) = \frac{4V_{HV2}}{\pi} \sum_{n=1}^{\infty} \frac{1}{2n-1} \sin[(2n-1)\omega t - 2\pi D_3] \tag{2. 24}$$

Note n is not the order of the harmonic but $2n$-1. Therefore, the phasor current of the transformer can be calculated as:

$$\dot{i}_{ac2}^{(2n-1)} = \frac{\dot{v}_{ac1}^{(2n-1)} - \dot{v}_{ac2}^{(2n-1)}}{j(2n-1)\omega L_p} \tag{2. 25}$$

, where

$$\dot{v}_{ac1}^{(2n-1)} = \frac{4V_{HV1}}{\pi(2n-1)} \angle 0 \tag{2. 26}$$

$$\dot{v}_{ac2}^{(2n-1)} = \frac{4V_{HV2}}{\pi(2n-1)} \angle \frac{-2\pi D_3}{2n-1} \tag{2. 27}$$

Therefore, the $(2n\text{-}1)^{th}$ order reactive power is calculated as:

$$Q^{(2n-1)} = \left| \dot{i}_{ac2}^{(2n-1)} \right|^2 (2n-1)\omega L_p = \frac{1+M^2-2M\cos(2\pi D_3)}{(2n-1)\omega L_p}\left[\frac{4V_{HV1}}{\pi(2n-1)}\right]^2 \quad (2.\ 28)$$

The apparent power from square wave source v_{ac1} is calculated as:

$$\left|S^{(2n-1)}\right| = \left| \dot{v}_{ac1}^{(2n-1)} \dot{i}_{ac2}^{(2n-1)} \right| = \frac{\sqrt{1+M^2-2M\cos(2\pi D_3)}}{(2n-1)\omega L_p}\left[\frac{4V_{HV1}}{\pi(2n-1)}\right]^2 \quad (2.\ 29)$$

Therefore, the ratio between the reactive power and the apparent power is:

$$r_Q = \frac{\sum_{n=1}^{\infty} Q^{(2n-1)}}{\sum_{n=1}^{\infty} \left|S^{(2n-1)}\right|} = \sqrt{1+M^2-2M\cos(2\pi D_3)} \quad (2.\ 30)$$

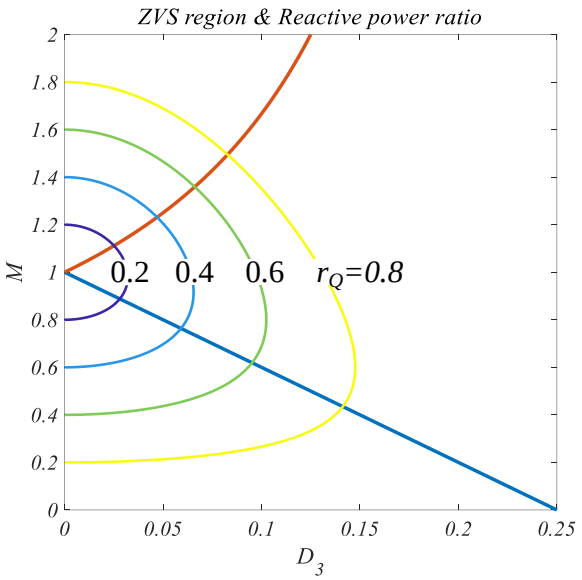


Fig. 2.16 Overlapping of the ZVS region and the contour plot of reactive power ratio r_Q.

As indicated in (2. 30), the ratio r_Q reflects the relative reactive power consumption of the power transfer inductor L_p. It depends only on the voltage ratio M and the phase shift duty D_3. The contour plot of the r_Q overlaps with the ZVS region shown in Fig. 2.16. Under the same value of M, larger D_3 induces larger reactive power ratio. It is worth emphasizing that both the ZVS region and the reactive ratio relate to only D_3 and M. This conclusion will be used in the section 2.3.4.2 to aid the design of inductor L_p

2.3.4.2 Load characteristic

When the DAB is connected with a resistive load as in Fig. 2.17, the load current is dependent on the load terminal voltage and resistor R_L.

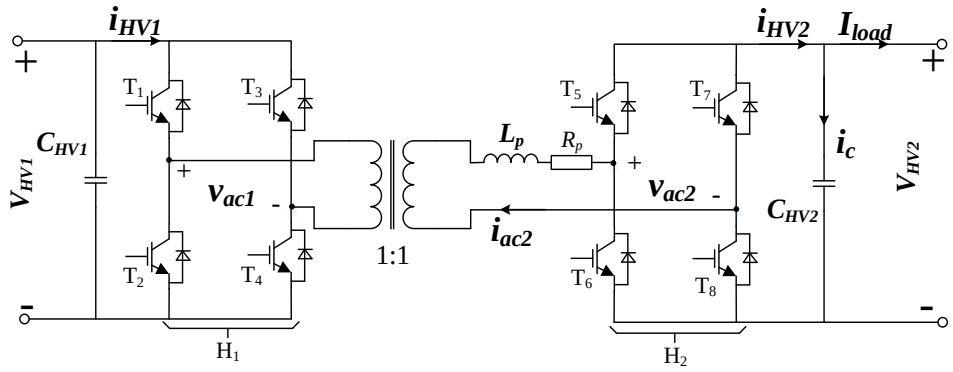


Fig. 2.17 The diagram of the DAB converter under investigation.

According to (2. 12), the bridge current i_{HV2} can be calculated as:

$$i_{HV2} = \frac{V_{HV1}}{f_s L_p} D_3 (1 - 2|D_3|) \tag{2. 31}$$

Substituting (2. 31) into (2. 21):

$$M = \frac{V_{HV2}}{V_{HV1}} = \frac{i_{HV2} R_L}{V_{HV1}} = k D_3 (1 - 2|D_3|) \tag{2. 32}$$

, where f_s is the fixed switching frequency, k relates to load resistance R_L and inductance L_p as shown in (2. 33). The value of L_p is inversely correlated to the power, hence, when designing the value of L_p, full load power is assumed. Under such an assumption, k only relates to L_p.

$$k = \frac{R_L}{f_s L_p} \tag{2. 33}$$

Plot equations (2. 19), (2. 20), (2. 30) and (2. 32) together in Fig. 2.18. In the figure, assume the terminal voltage ratio is 1.11 in the steady state. The intersection of the load characteristic and the fixed voltage ratio lines are the operating point at full power. When k is increased from 12.15 to 14.58, the full power operating point moves from A to B. As illustrated in the figure, the operation at point A presents larger reactive power ratio than point B. However, point B is

closer to the ZVS boundary compared to point A. At the intersected point between the horizontal voltage ratio line M=1.11 and the ZVS boundary, with a larger vale of k, the power is larger. This means that with a larger value of k, the power threshold to achieve ZVS gets higher. It can be concluded that a larger k can reduce the consumption of reactive power, but it also makes the ZVS region smaller. The reactive power relates to conduction losses while the ZVS region relates to switching losses. Therefore, a compromise should be made between ZVS region and reactive power when designing L_p.

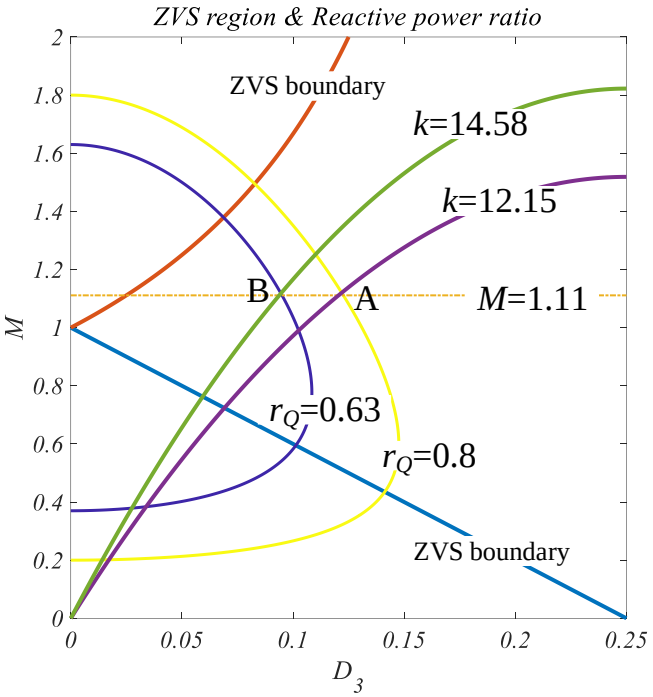


Fig. 2.18 Implications of k to the ZVS region and reactive power ratio r_Q.

For example, assuming the switching frequency f_s is selected as 20kHz, and the power rating is 1kW. Assume also that the nominal input voltage V_{HV1} is 270V and the output voltage V_{HV2} is 170V-300V. Therefore, M varies from 0.62-1.11. A predefined maximum reactive power ratio value r_Q is set to 0.8, then k is equal to 12.15 at full load. L_p can then be calculated from (2. 33) as 300μH. According to (2. 13), the maximum power P_{max} is now 1.5kW.

2.3.5 Capacitive filtering

The DC capacitors on both DC terminals are responsible for absorbing the AC component of the rectified currents i_{HV1} and i_{HV2}. An illustration is shown in Fig. 2.19 where V_{HV1} equals V_{HV2}, the current i_c flows into the output capacitor causing voltage variations ΔV_{HV2}.

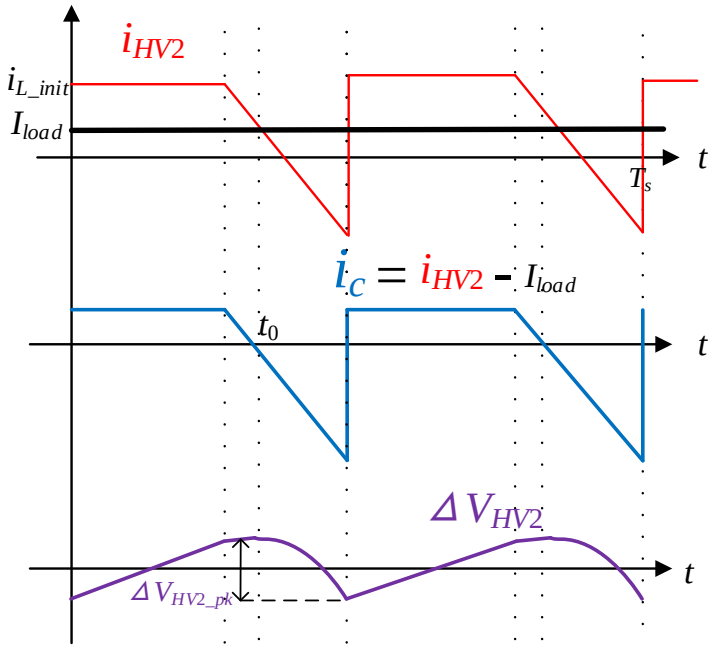


Fig. 2.19 Illustration on the DC terminal currents and voltage

The principle to design the capacitance to ensure 1% terminal voltage variation to its nominal value. The detailed design process of the capacitance can be found in literature [53]. It will not be repeated here. According to [53], the formular for calculating the capacitance is given as follows:

$$C_{HV2} = \frac{[2D_3(1-2D_3)R_L - 2(1-8D_3^2)f_s L_p]^2}{32 f_s^2 L_p r_p [4D_3^2(1-2D_3)^2 R_L^2 - 4 f_s L_p D_3(1-2D_3)R_L]} \quad (2.\ 34)$$

Assuming f_s=20kHz, L_p=300uH, r_p=0.01, R_L=72.5ohm, and D_3= 0.1, according to (2. 34), the output capacitance for filtering purpose is 92uF. The output capacitor is ofter made by the combination of paralleled film and ceramic capacitors. However, the pratical capacitance could be larger than 92uF for the dynamic performace purpose.

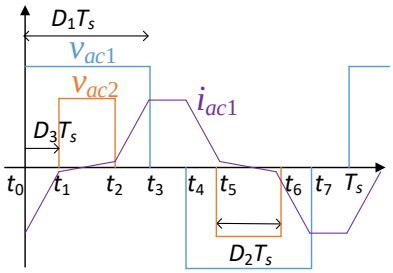
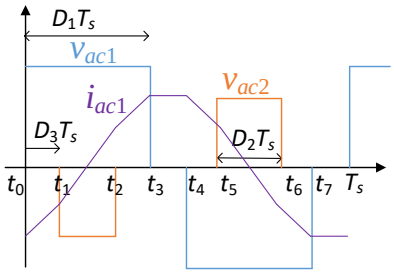
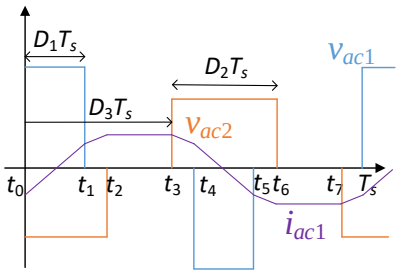
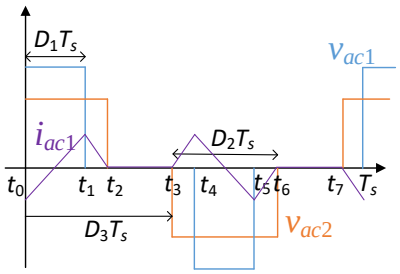
2.4 Triple-Phase-Shift (TPS) modulation optimization

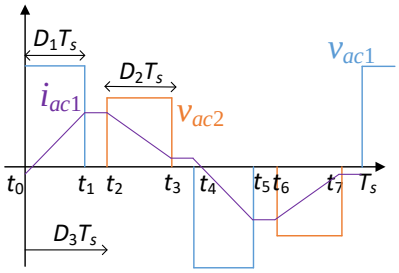
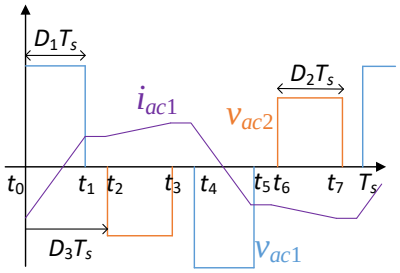
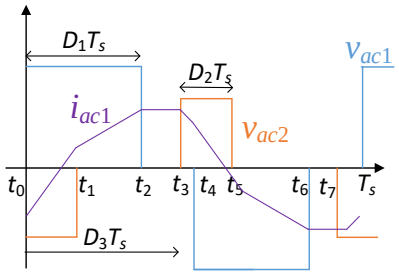
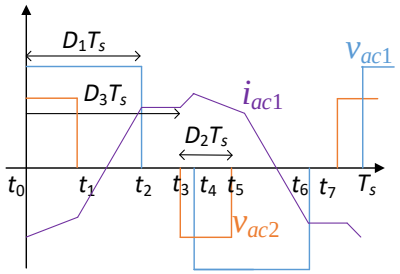
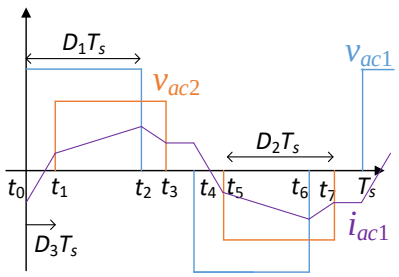
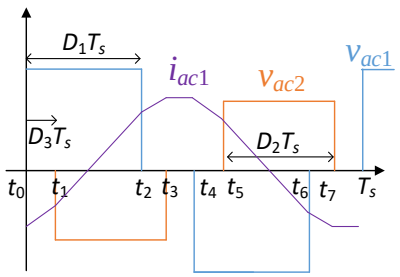
Triple Phase Shift (TPS) is the universal modulation which comprises of all the modulation techniques illustrated in Fig. 2.6. In the constant switching frequency category, TPS is recognized as the most effective approach to maximize the efficiency of a DAB converter [54], [58]. The offline optimization of TPS modulation is presented in this section.

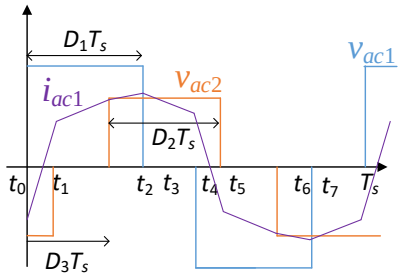
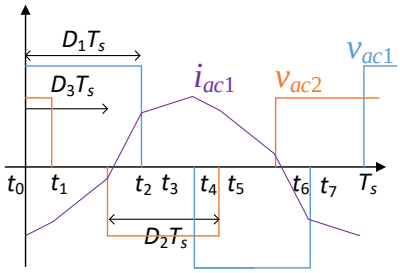
2.4.1 Operating modes

In TPS modulation, D_1, D_2 and D_3 are regarded as three independent control variables. TPS can be further divided into twelve different operating modes depending on the expressions for power and the constraints on D_1, D_2 and D_3. All of the operating modes are listed in Table 2.4 with illustrative transformer terminal voltage and current waveforms. The expression for power is calculated using the same method as in section 2.3.1 (2. 8). The power is unified at P_{max} as defined in (2. 13):

TABLE 2.4 OPERATING MODES FOR TPS MODULATION OF A DAB

Mode	**Mode 1**	**Mode 1'**
Waveforms		
	t_0=0, t_1=D_3T_s, t_2=$(D_2+D_3)T_s$, t_3=D_1T_s, t_4=0.5T_s	
Mode constraints	$D_1 \geq D_2$, $D_1-D_2 \geq D_3 \geq 0$	
Power	$P_{pu}=8(D_2^2-D_1D_2+2D_2D_3)$	$P_{pu}=-8(D_2^2-D_1D_2+2D_2D_3)$
Range	0.5pu < P_{pu} < 0.5pu	0.5pu < P_{pu} < 0.5pu
Mode	**Mode 2**	**Mode 2'**
Waveforms		

	t_0=0, t_1=D_1T_s, t_2=(D_2+D_3-0.5)T_s, t_3=D_3T_s, t_4=0.5T_s	
Mode constraints	D_2≥D_1, 0.5≥D_3≥(0.5+D_1-D_2)	
Power	P_{pu}=8(D_1^2-D_1D_2+D_1-2D_2D_3)	P_{pu}=-8(D_1^2-D_1D_2+D_1-2D_2D_3)
Range	0.5pu < P_{pu} < 0.5pu	0.5pu < P_{pu} < 0.5pu
Mode	**Mode 3**	**Mode 3'**
Waveforms		
	t_0=0, t_1=D_1T_s, t_2=D_3T_s, t_3=(D_2+ D_3)T_s, t_4=0.5T_s	
Mode constraints	0.5-D_1≥D_2, 1-D_2≥D_3≥D_1	
Power	P_{pu}=8D_1D_2	P_{pu}=-8D_1D_2
Range	0pu < P_{pu} < 0.5pu	-0.5pu < P_{pu} < 0pu
Mode	**Mode 4**	**Mode 4'**
Waveforms		
	t_0=0, t_1=(D_2+D_3-0.5)T_s, t_2= D_1T_s, t_3=D_3T_s, t_4=0.5T_s	
Mode constraints	0.5≥D_2≥D_1, (0.5+D_1-D_3)≥D_2≥0.5-D_3	
Power	P_{pu}=2(-4D_2^2-4D_3^2+4D_2+4D_3-8D_2D_3+4D_1D_2-1)	P_{pu}=-2(-4D_2^2-4D_3^2+4D_2+4D_3-8D_2D_3+4D_1D_2-1)
Range	0pu < P_{pu} < 0.67pu	-0.67pu < P_{pu} < 0pu
Mode	**Mode 5**	**Mode 5'**
Waveforms		
	t_0=0, t_1=D_3T_s, t_2= D_1T_s, t_3=(D_2+D_3)T_s, t_4=0.5T_s	
Mode constraints	D_1≥D_3≥0, (0.5-D_3)≥D_2≥D_1-D_3	
Power	P_{pu}=8(-D_1^2-D_3^2+D_1D_2+2D_1D_3)	P_{pu}=-8(-D_1^2-D_3^2+D_1D_2+2D_1D_3)
Range	0pu < P_{pu} < 0.667pu	-0.667pu < P_{pu} < 0pu

Mode	**Mode 6**	**Mode 6'**
Waveforms		
	t_0=0, t_1=(D_2+D_3-0.5)T_s, t_2=D_3T_s, t_3=D_1T_s, t_4=0.5T_s	
Mode constraints	D_1≥0.5-D_2, D_1≥D_3≥(0.5-D_2)	
Power	P_{pu}=2(-4D_1^2-4D_2^2-8D_3^2+8D^3-8D_2D_3+4D_1D_2+8D_1D_3+4D_2-1)	P_{pu}=-2(-4D_1^2-4D_2^2-8D_3^2+8D^3-8D_2D_3+4D_1D_2+8D_1D_3+4D_2-1)
Range	0pu < P_{pu} < 1pu	-1pu < P_{pu} < 0pu

The same method as in (2. 9) and (2. 11) is used to calculate the transformer current at the switching instance. The results are listed in Table 2.5 where the current is unified at $1/(4f_sL_p)$.

TABLE 2.5 TRANSFORMER CURRENT AT SWITCHING INSTANCE UNIFIED AT $1/(4F_SL_P)$

Mode	$i_{ac1}(t_0)$	$i_{ac1}(t_1)$
1	$2NV_{HV2}D_2$-$2V_{HV1}D_1$	-$2V_{HV1}D_1$+$4V_{HV1}D_3$+$2NV_{HV2}D_2$
1'	-$2NV_{HV2}D_2$-$2V_{HV1}D_1$	-$2V_{HV1}D_1$+$4V_{HV1}D_3$-$2NV_{HV2}D_2$
2	2NV_{HV2}-$2V_{HV1}D_1$-$2NV_{HV2}D_2$-$4NV_{HV2}D_3$	$2V_{HV1}D_1$+4N$V_{HV2}D_1$-$2NV_{HV2}D_2$+$2NV_{HV2}$-$4NV_{HV2}D_3$
2'	$2NV_{HV2}D_2$+$4NV_{HV2}D_3$-$2V_{HV1}D_1$-2NV_{HV2}	$2V_{HV1}D_1$-4N$V_{HV2}D_1$+$2NV_{HV2}D_2$-$2NV_{HV2}$+$4NV_{HV2}D_3$
3	-$2V_{HV1}D_1$+$2NV_{HV2}D_2$	$2V_{HV1}D_1$+$2NV_{HV2}D_2$
3'	-$2V_{HV1}D_1$-$2NV_{HV2}D_2$	$2V_{HV1}D_1$-$2NV_{HV2}D_2$
4	2NV_{HV2}-$2V_{HV1}D_1$-$2NV_{HV2}D_2$-$4NV_{HV2}D_3$	-$2V_{HV1}D_1$-$2V_{HV1}$+$4V_{HV1}D_2$+$2NV_{HV2}D_2$+$4V_{HV1}D_3$
4'	$2NV_{HV2}D_2$+$4NV_{HV2}D_3$-$2V_{HV1}D_1$-2NV_{HV2}	-$2V_{HV1}D_1$-$2V_{HV1}$+$4V_{HV1}D_2$-$2NV_{HV2}D_2$+$4V_{HV1}D_3$
5	-$2V_{HV1}D_1$+$2NV_{HV2}D_2$	-$2V_{HV1}D_1$+$4V_{HV1}D_3$+$2NV_{HV2}D_2$
5'	-$2V_{HV1}D_1$-$2NV_{HV2}D_2$	-$2V_{HV1}D_1$+$4V_{HV1}D_3$-$2NV_{HV2}D_2$
6	-$2V_{HV1}D_1$-$2NV_{HV2}D_2$-$4NV_{HV2}D_3$+$2NV_{HV2}$	$4V_{HV1}D_2$-$2V_{HV1}D_1$+$4V_{HV1}D_3$+$2NV_{HV2}D_2$-$2V_{HV1}$
6'	$2NV_{HV2}D_2$-$2V_{HV1}D_1$+$4NV_{HV2}D_3$-$2NV_{HV2}$	$4V_{HV1}D_2$-$2V_{HV1}D_1$+$4V_{HV1}D_3$-$2NV_{HV2}D_2$-$2V_{HV1}$
Mode	$i_{ac1}(t_2)$	$i_{ac1}(t_3)$
1	$4V_{HV1}D_2$-$2V_{HV1}D_1$+$4V_{HV1}D_3$-2N$V_{HV2}D_2$	$2V_{HV1}D_1$-2N$V_{HV2}D_2$
1'	$4V_{HV1}D_2$-$2V_{HV1}D_1$+$4V_{HV1}D_3$+2N$V_{HV2}D_2$	$2V_{HV1}D_1$+2N$V_{HV2}D_2$
2	$2V_{HV1}D_1$+2N$V_{HV2}D_2$	$2V_{HV1}D_1$+2N$V_{HV2}D_2$
2'	$2V_{HV1}D_1$-2N$V_{HV2}D_2$	$2V_{HV1}D_1$-2N$V_{HV2}D_2$
3	$2V_{HV1}D_1$+2N$V_{HV2}D_2$	$2V_{HV1}D_1$-2N$V_{HV2}D_2$
3'	$2V_{HV1}D_1$-2N$V_{HV2}D_2$	$2V_{HV1}D_1$+2N$V_{HV2}D_2$

4	$2V_{HV1}D_1+2NV_{HV2}D_2$	$2V_{HV1}D_1+2NV_{HV2}D_2$
4’	$2V_{HV1}D_1-2NV_{HV2}D_2$	$2V_{HV1}D_1-2NV_{HV2}D_2$
5	$2V_{HV1}D_1-4NV_{HV2}D_1+2NV_{HV2}D_2+4NV_{HV2}D_3$	$2V_{HV1}D_1-2NV_{HV2}D_2$
5’	$2V_{HV1}D_1+4NV_{HV2}D_1-2NV_{HV2}D_2-4NV_{HV2}D_3$	$2V_{HV1}D_1+2NV_{HV2}D_2$
6	$-2V_{HV1}D_1+4V_{HV1}D_3+2NV_{HV2}D_2$	$2V_{HV1}D_1-4NV_{HV2}D_1+2NV_{HV2}D_2+4NV_{HV2}D_3$
6’	$-2V_{HV1}D_1+4V_{HV1}D_3-2NV_{HV2}D_2$	$2V_{HV1}D_1+4NV_{HV2}D_1-2NV_{HV2}D_2-4NV_{HV2}D_3$

2.4.2 Current stress minimization

In a DAB converter with a high switching frequency, considerable losses are produced on the high frequency transformer. Accurate mathematical models to describe the core losses and copper losses of a high frequency transformer can be complicated. Therefore, direct optimization on the operating efficiency is difficult [47]. Indirect metrics are often chosen as the optimization objectives such as transformer current stress [71], ZVS region [56], transformer current Root-Mean-Square (RMS) value [51], [57] and reactive power [48], [60]. Among those objectives, optimization on transformer current stress can result in analytical expressions while many of others require large look-up tables.

In this section, minimization on transformer current stress for a DAB converter modulated with TPS has been introduced as in (2. 35). Twelve operating modes for TPS listed in Table 2.4 are considered. The current stress value can be obtained from Table 2.5. The minimization results are shown in Table 2.6. Phase shift duties D_1, D_2 and D_3 are in linear relationships with D_f. D_f is typically generated from the controllers. Those linear relationships are only relavent to the terminal voltage ratio and are independent from the circuit parameters.

$$Minimize\ i_{ac2_peak} = Max[i_{ac2}(t)] \tag{2. 35}$$

s.t.

$$0 < D_1 < 0.5\ \&\ 0 < D_2 < 0.5\ \&\ 0 < D_3 < 0.5 \tag{2. 36}$$

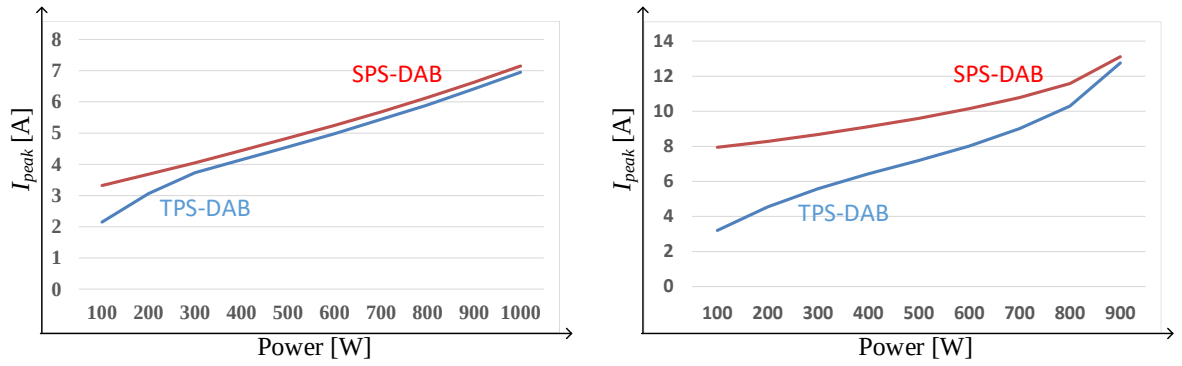
With the optimized TPS, the number of independent control variables is reduced from three to one (D_f). With the information of values D_f and M, Table 2.6 can be used to produce control variables D_1, D_2 and D_3.

TABLE 2.6 OPTIMIZATION TABLE

Gain	D_f range	Relationships	Mode
M<1	$[0, \frac{1-M}{4}]$	$D_1=\frac{2M}{1-M}D_f,\ D_2=\frac{2}{1-M}D_f,\ D_3=0$	I
	$(\frac{1-M}{4}, \frac{1}{4}]$	$D_1=\frac{2M-1}{2M}+\frac{1-M}{M}D_f,\ D_2=0.5,\ D_3=\frac{M+4D_f-1}{4M}$	II
M>1	$[0, \frac{M-1}{4M}]$	$D_1=\frac{2M}{M-1}D_f,\ D_2=\frac{2}{M-1}D_f,\ D_3=2D_f$	III
	$(\frac{M-1}{4M}, \frac{1}{4}]$	$D_1=0.5,\ D_2=1-0.5M+2(M-1)D_f,$ $D_3=(2-M)D_f+0.25(M-1)$	IV

The optimized TPS modulation indirectly improves the efficiency by minimizing the current stress value especially under partial load when the terminal voltages of the DAB vary from their nominal values [54], [58]. This is the major benefit of using the TPS modulation compared to SPS modulation.

Simulations have been carried out in order to validate the effectiveness of the optimized TPS modulation. Circuit parameters in Table 2.9 are used, and results are shown in Fig. 2.20 for a comparison of the transformer peak current between SPS modulation and TPS modulation.



(a)260V/300V (b)150V/300V

Fig. 2.20 Transformer peak current comparison between SPS and TPS

When comparing Fig. 2.20(a) and (b), it can be seen that with the increasing deviation of the terminal voltage ratio from unity, the reduction of transformer peak current is more significant with TPS modulation. The reduction of the transformer peak current results in improvement of the operating efficiency. The efficiency measurements with practical lab protoype are given in Fig. 2.35 from Section 2.7.2.

2.5 Modelling

Mathematic models are fundamental to control design. Conventionally, when linear controls are used, small signal models are required to aid the controller design. In this section, the average model and small signal model of the DAB topology modulated with TPS are described. The DAB load voltage PI control design is also presented.

2.5.1 Average model

The switching average modelling technique has been widely used for power electronics modelling and analysis [72]. The switching average models of the DAB have also been investigated by researchers. Modelling methods such as reduced order model [39], [73], improved reduced order model [74], generalized average models [75] and discrete time model [76] have been proposed. Among those methods, the reduced order model presents the best compromise between complexity and accuracy [39], [73]. Therefore, in this section, the reduced order model is used. The reduced order model of the DAB is shown in Fig. 2.21.

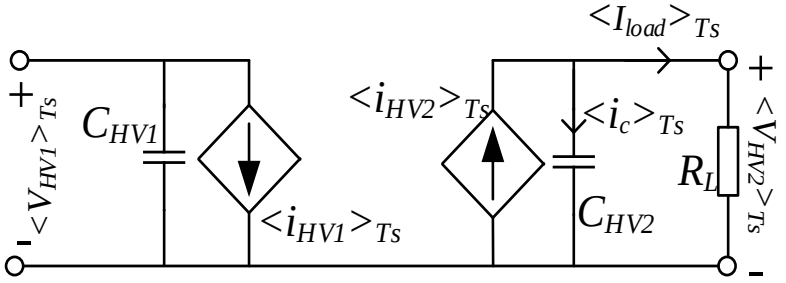


Fig. 2.21 The reduced order model of the DAB.

The secondary transformer current i_{ac2} is rectified by H_2 to current i_{HV2} as shown in Fig. 2.17. The value of i_{HV2} at each switching instance can be also obtained from Table 2.5. The controlled current $<i_{HV2}>_{Ts}$ is the switching average value of i_{HV2}. It can be calculated as shown in equation (2. 37).

$$< i_{HV2} >_{Ts} = \frac{1}{T_s} \int_0^{T_s} i_{HV2} dt \tag{2. 37}$$

Substituting values from Table 2.5 and Table 2.6 into equation (2. 37), the controlled current for each mode can be derived as shown in Table 2.7, where the currents are unified at:

$$I_c^* = \frac{V_{HV1}}{8 f_s L_p} \tag{2. 38}$$

The differential equation of the output voltage can be developed from Fig. 2.21:

$$\frac{d < V_{HV2} >_{Ts}}{dt} = \frac{< i_{HV2} >_{Ts}}{C_{HV2}} - \frac{< V_{HV2} >_{Ts}}{R_L C_{HV2}} \tag{2. 39}$$

TABLE 2.7 THE CONTROLLED CURRENT IN THE REDUCED ORDER MODEL

Mode	$<i_{HV2}>_{Ts}$
I	$\frac{32MD_f^{\,2}}{1-M}$
II	$\frac{-8(M^2+1)D_f^{\,2}+4(2M^2-M+1)D_f-(M-1)^2}{M^2}$
III	$\frac{32D_f^{\,2}}{M-1}$
IV	$-16(M^2-2M+2)D_f^{\,2}+8(M^2-2M+2)D_f-(M-1)^2$

2.5.2 Ideal small signal model

The small signal model is derived by superimposing small perturbations about an equilibrium point. The control to output transfer functions for a TPS modulated DAB converter are shown in Table 2.8 , where the notation with a bar $\bar{X}$ denotes the equilibrium points.

TABLE 2.8 CONTROL TO OUTPUT TRANSFER FUNCTION

Mode	$G_{TPS}(s) = V_{HV2}(s)/D_f(s)$
I	$G_{TPS_I}(s) = \frac{8\overline{D_f}\,\overline{V_{HV1}}\,\overline{r_V}R_L(1-\overline{r_V})}{C_{HV2}f_s L_p R_L(1-\overline{r_V})^2 s - 4R_L\overline{D_f}^{\,2} + f_s L_p(\overline{r_V}^{\,2}-\overline{r_V}+1)}$
II	$G_{TPS_II}(s) = -\frac{2R_L\overline{V_{HV1}}\,\overline{r_V}(4\overline{D_f}+\overline{r_V}+4\overline{D_f}\,\overline{r_V}^{\,2}-2\overline{r_V}^{\,2}-1)}{4C_{HV2}f_s L_p R_L\overline{r_V}^{\,3}s - 8R_L\overline{D_f}^{\,2} - 2R_L\overline{D_f}\,\overline{r_V} + 4R_L\overline{D_f} + 4f_s L_p\overline{r_V}^{\,3} + R_L\overline{r_V} - R_L}$
III	$G_{TPS_III}(s) = \frac{8\overline{D_f}\,\overline{V_{HV1}}R_L(\overline{r_V}-1)}{sC_{HV2}f_s L_p R_L(1-\overline{r_V})^2 + 4R_L\overline{D_f}^{\,2} + f_s L_p(1-\overline{r_V})^2}$

IV	$G_{TPS_IV}(s)=\dfrac{-4R_L\overline{V_{HV1}}(4\overline{D_f}-1)(\overline{r_V}^2-2\overline{r_V}+2)}{4C_{HV2}f_sL_pR_Ls+4f_sL_p-R_L+R_L\overline{r_V}-16\overline{D_f}^2R_L+8\overline{D_f}R_L-8\overline{D_f}\,\overline{r_V}R_L+16\overline{D_f}^2\overline{r_V}R_L}$

In order to verify the accuracy of model $G_{TPS}(s)$ listed in Table 2.8, comparisons between the model and the AC swept transfer functions $G_{TPS}(s)$ based on the ideal reduced order model shown in Fig. 2.21 are carried out. Simulations have been conducted using the software PLECS Block Set 3.6.1 built in MATLAB SIMULINK 2017a. The circuit and controller parameters are as shown in Table 2.9, unless otherwise specified.

The AC sweeping diagram with the ideal reduced order model is shown in Fig. 2.22. Small sinusoidal perturbations are injected and superimposed on the steady state value of $\overline{D_f}$. Correspondent frequency components of the output voltage are measured. The control to output transfer function can be then calculated based on the simulated data.

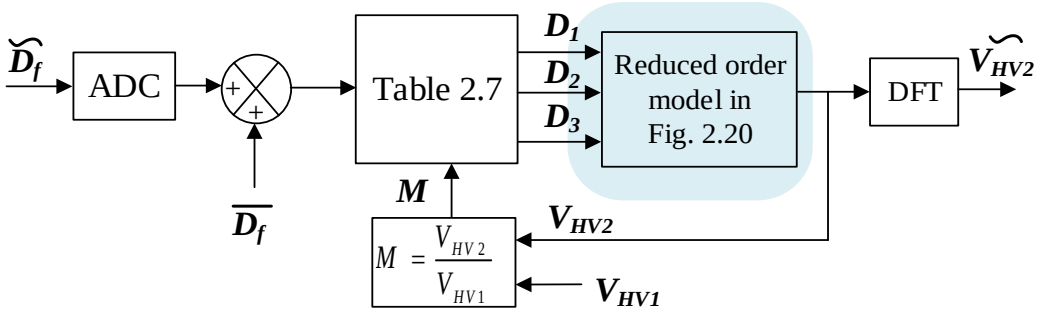
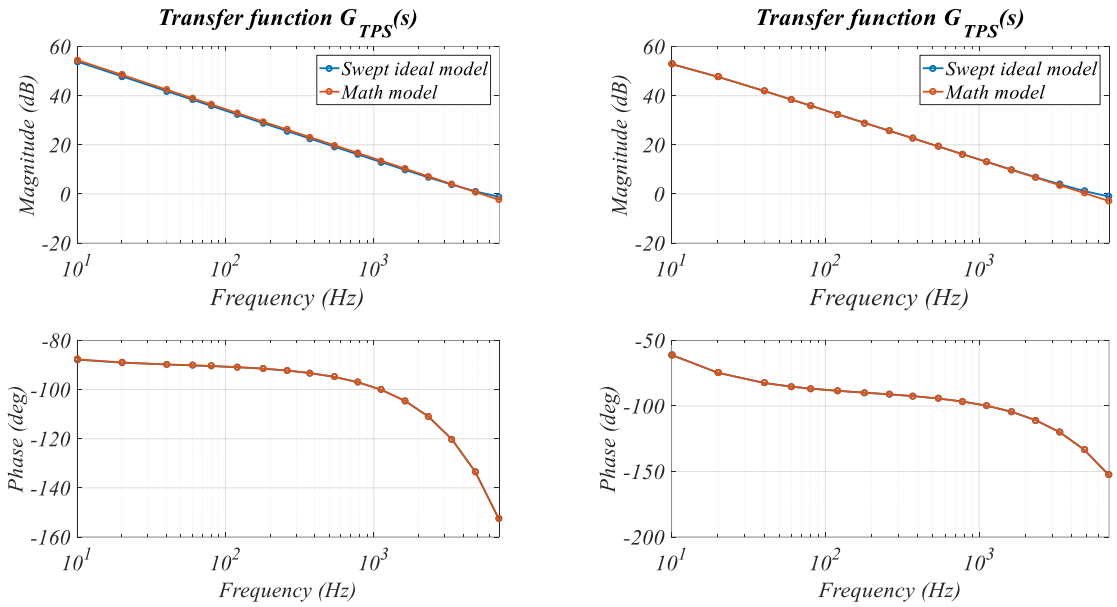


Fig. 2.22 Transfer function AC sweeping diagram with the average model.

The results are shown in Fig. 2.23. The mathematical model agrees quite well with the AC swept ideal model. This confirms the accuracy of the mathematical model in Table 2.8. It is worth mentioning that the ideal model is a first order system. Ideally, the phase should be always negative 90 degrees. However, as shown in the figure, the phase is larger than negative 90 degrees in low frequency due to the impact from R_L. The phase is smaller than negative 90 degrees in high frequency due to the digital sampling delay reflected as $e^{-s/2fs}$ in multiplication to transfer functions from Table 2.8.



(a) 260V/300V 10W Mode III (b) 180V/300V 1kW Mode IV

Fig. 2.23 Comparison between the AC swept ideal model and the mathematical model in Table 2.8.

2.5.3 Practical switching model

The reduced order model shown in Fig. 2.21 has neglected the dynamic and losses in the high frequency transformer stage. In order to identify the impact of the high frequency transformer, this sub-section compares the AC sweeping transfer functions $G_{TPS}(s)$ between the switching model shown in Fig. 2.17 and the ideal reduced order model shown in Fig. 2.21 are conducted.

The AC sweeping diagram for the switching model are depicted in Fig. 2.24. The inclusion of the body capacitors of the switching devices will drastically increase the computation burden for the simulation software which makes the parallel computing in MATLAB slow to run. The accurate modelling of the core and skin effect are also quite complicated. For simplicity, in the switching model, only dead time t_d and DC transformer primary parasitic resistance R_p are implemented. The body capacitors affect only microscopic transition. Core and winding models only have implications in the overall loss, the switching model shown in Fig. 2.17 is considered reasonable. The circuit parameters shown in Table 2.9 are used for these simulations.

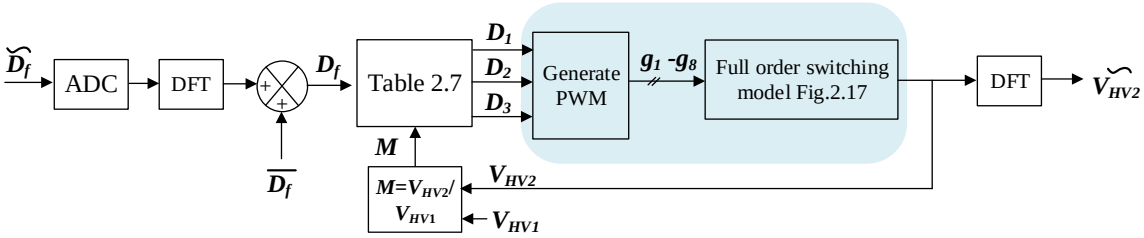
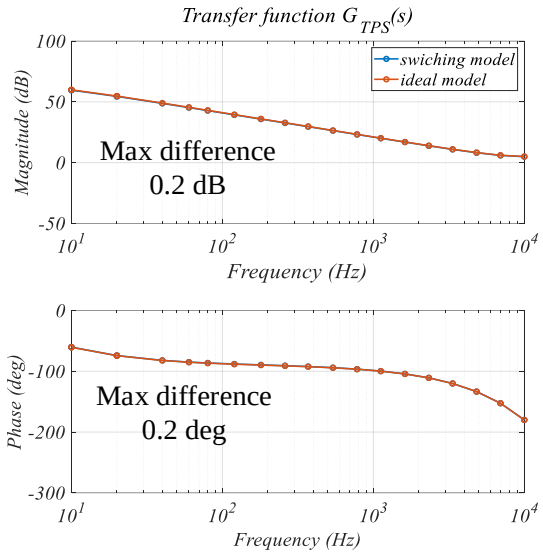
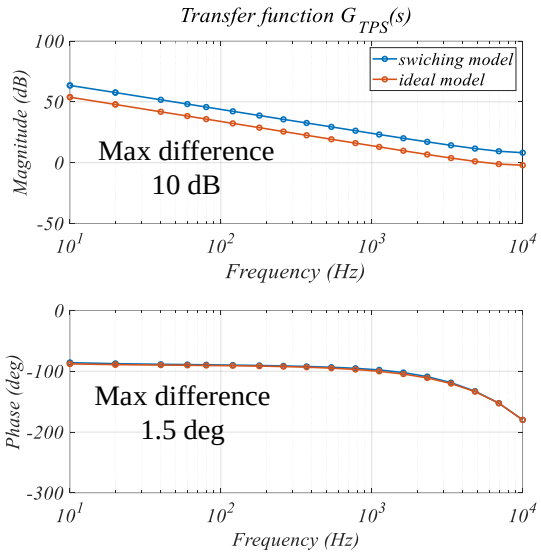


Fig. 2.24 Transfer function AC sweeping diagram for the switching model.

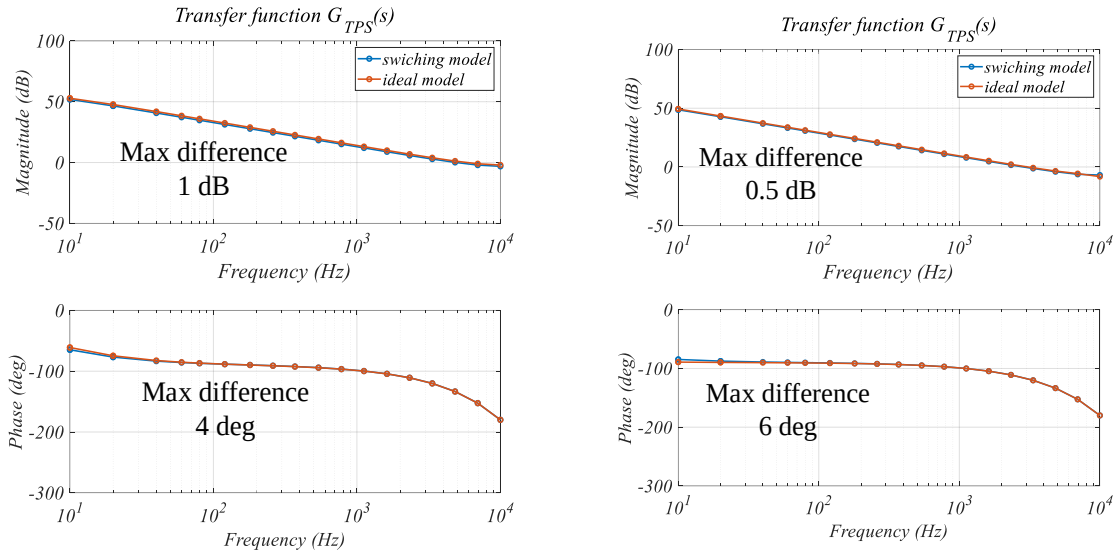
At this point, the first comparison is carried out under the equilibrium condition where the input voltage is 260V, load voltage reference is set as 300V and power is 1kW. The TPS works in mode IV in both switching and ideal models. The results are given in Fig. 2.25 (a). The amplitude curves show a good match between the two models when the equilibrium power point decreases down to 10W. Due to the losses of the converter, the switching model works in mode IV while the ideal model works in mode III. The comparison between two models under the condition where the input voltage is 260V, load voltage reference is 300V and power is 10W is provided in Fig. 2.25 (b). There is a significant mismatch in the amplitude curves due to operation in different modes. The switching model and ideal model show good agreement with the equilibrium points where the input voltage is 180V, load voltage reference is 300V and the power is 10W and 1kW in Fig. 2.25 (c) and Fig. 2.25 (d), respectively.



(a) 260V/300V 1kW



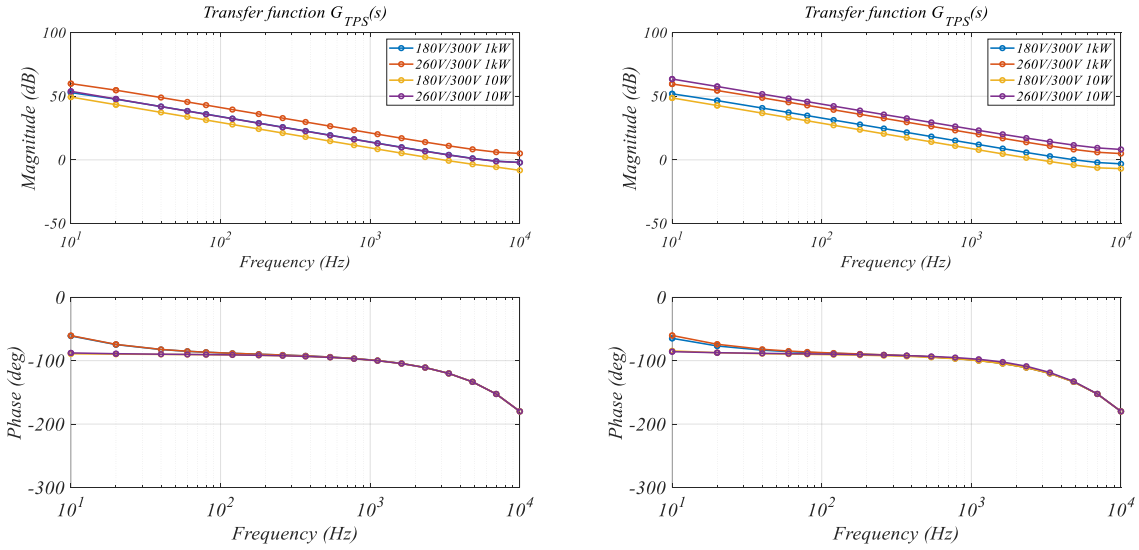
(b) 260V/300V 10W



(c) 180V/300V 1kW (d) 180V/300V 10W

Fig. 2.25 Comparisons on the transfer function between the ideal model and the switching model under different equilibrium points.

Fig. 2.25 is rearranged and shown in Fig. 2.26. On the observation of both figures in Fig. 2.26, terminal voltages and power are two factors that have influence over the small signal model of TPS. Power has impact on the phase in the low frequency range while the terminal voltages do not. The terminal voltages and power both have impact on the magnitude of the small signal model $G_{TPS}(s)$. These influences render a single set of PI parameters working in a wide voltage and power range with good performance, which is going to be addressed in the next sub-section.



(a) Ideal model (b) Switching model

Fig. 2.26 Transfer function comapirson under differnet power and terminal voltages

2.6 PI controller design

With the above developed transfer function, a PI based voltage controller is used as a comparison benchmark to the control method proposed in the next chapter. The transfer function $G_{TPS}(s)$ varies under different operating terminal voltages and load power. Moreover, due to the co-existence of four operating modes, the PI controller parameter design becomes challenging. PI parameters K_p and K_i are defined in equation (2. 40).

$$G_v(s) = K_p + \frac{K_i}{s} \tag{2. 40}$$

The PI control diagram for the TPS is shown in Fig. 2.27. Sampling of the output voltage V_{HV2} is required.

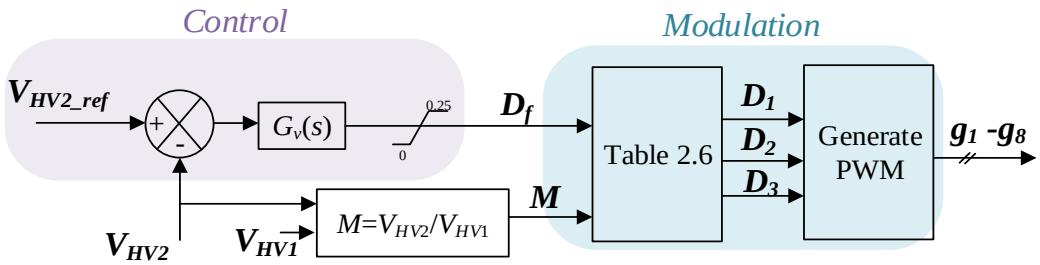


Fig. 2.27 The control and TPS modulation diagram.

The control block diagram considering the sampling and digital control delays [77] is shown in Fig. 2.28.

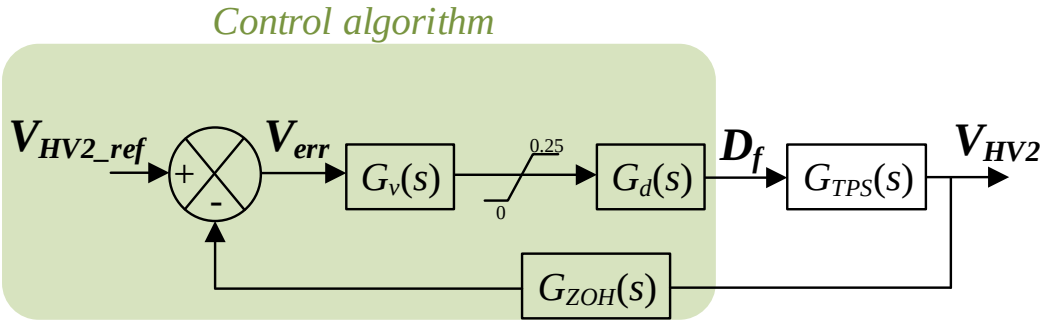


Fig. 2.28 The control block diagram using the PI controller considering delays.

The expressions for $G_d(s)$ and $G_{ZOH}(s)$ are presented as:

$$G_d(s) = e^{-s/f_s} \tag{2. 41}$$

$$G_{ZOH}(s)=\frac{\ell[\varepsilon(t)]-\ell[\varepsilon(t-\frac{1}{f_s})]}{A}=\frac{1}{A}(\frac{1}{s}-\frac{1}{s}e^{-s/f_s}) \tag{2. 42}$$

, where A is a constant to balance the gain. The Zero Order Hold (ZOH) in frequency domain is thus written as:

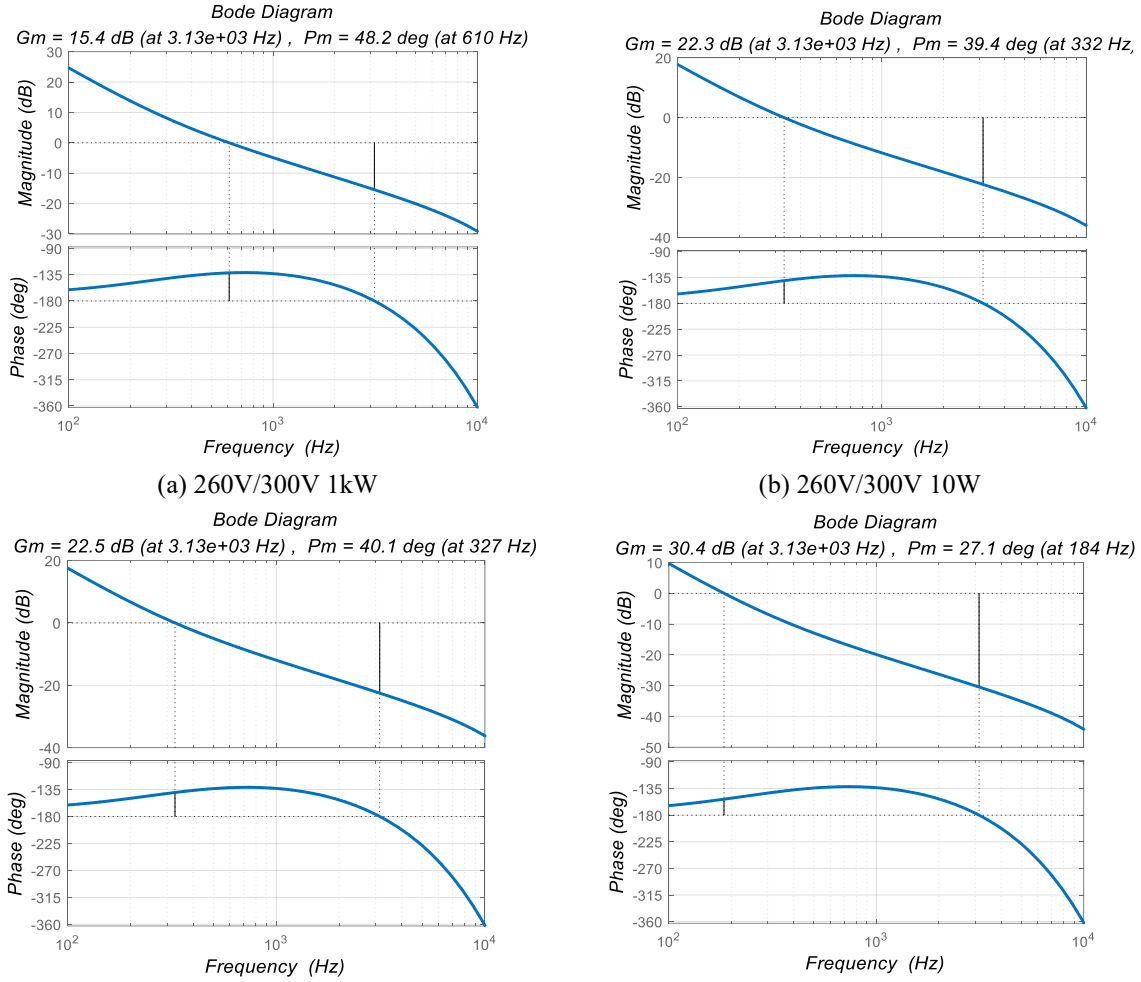
$$G_{ZOH}(j\omega)=\frac{1}{Af_s}\frac{\sin\frac{\omega}{2fs}}{\frac{\omega}{2fs}}e^{-s/2f_s}=\frac{1}{Af_s}\frac{\sin\frac{\omega}{2fs}}{\frac{\omega}{2fs}}e^{-s/2f_s} \tag{2. 43}$$

When ω=0, it is easy to find out that A should be equals to $1/f_s$. For a first order capacitive system such as the one shown in Fig. 2.21, ideally, the controller can be designed with high bandwidth without the worry for the stability issue. However, in practice, two things have to be taken into account. The mathematical models in Table 2.8 should take also $e^{-s/fs}$ and $e^{-0.5s/fs}$ into account for digital control and sampling delays, thus causing phase degradation in the high frequency range as shown in Fig. 2.23. Another consideration is the analogue to digital sampling noise. Because the sampling noise is blended into the feedback variables and it cannot be rejected by the control loops. If the control bandwidth is set high, the load voltage and transformer current could end up dithering due to the sampling noise in V_{HV2}.

The loop transfer function $G_o(s)$ is defined in equation (2. 44) and plotted in Fig. 2.26 with different equilibrium points.

$$G_o(s)=G_v(s)G_{TPS}(s)G_d(s)G_{ZOH}(s) \tag{2. 44}$$

Note that the PI control parameters are designed to achieve a crossover frequency of 610Hz under the equilibrium ponint: V_{HV1}=260V/V_{HV2}=300V P=1kW. The change of power and terminal voltages affects the small signal model $G_{TPS}(s)$. With fixed PI control parameters, $G_o(s)$ will also be affected. As a consequence, the crossover frequencies are 610Hz, 332Hz, 327Hz and 184Hz for equilibrium points V_{HV1}=260V/V_{HV2}=300V P=1kW, V_{HV1}=260V/V_{HV2}=300V P=10W, V_{HV1}=180V/V_{HV2}=300V P=1kW and V_{HV1}=180V/V_{HV2}=300V P=10W, respectively. Therefore, the dynamic performance cannot be retained with one set of PI parameters.



(a) 260V/300V 1kW (b) 260V/300V 10W

(c) 180V/300V 1kW (d) 180V/300V 10W

Fig. 2.29 Plots of $G_o(s)$ for different equilibrium points. Control parameters are set as K_p=0.05, K_i=89.6.

2.7 Practical results

The optimized TPS modulation and the PI voltage controller has been implemented on a 1kW 20kHz laboratory prototype. Bench power supply EA-PS 9360-40 3U is connected directly to the primary side of the DAB converter providing a stiff input voltage V_{HV1}. The DAB converter is required to regulate the secondary terminal voltage V_{HV2} to the reference value V_{HV2_ref}. The experiment prototype is shown in Fig. 2.30 and Fig. 2.31. A TMS320F2837xD evaluation board from Texas Instruments has been used as the digital control platform and communicates with a host computer. IGBT device SKM75GB128D is used for the full bridge switches with a 1.6us programmable software dead time. Two 380uF 400V polypropylene capacitors from KEMET are utilized for each DC terminal. The integrated transformer and inductor (L_p=300uH)

are made using MnZn ferrites with 3.9mm^2 litzs wire. The magnetizing inductance is L_m=3mH. The main components used in the prototype are summarized in Table 2.10.

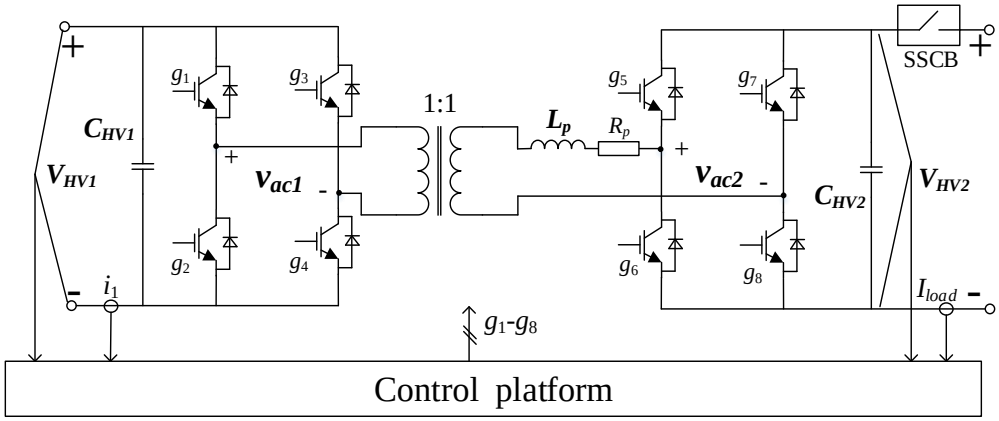


Fig. 2.30 The schematic of the prototype

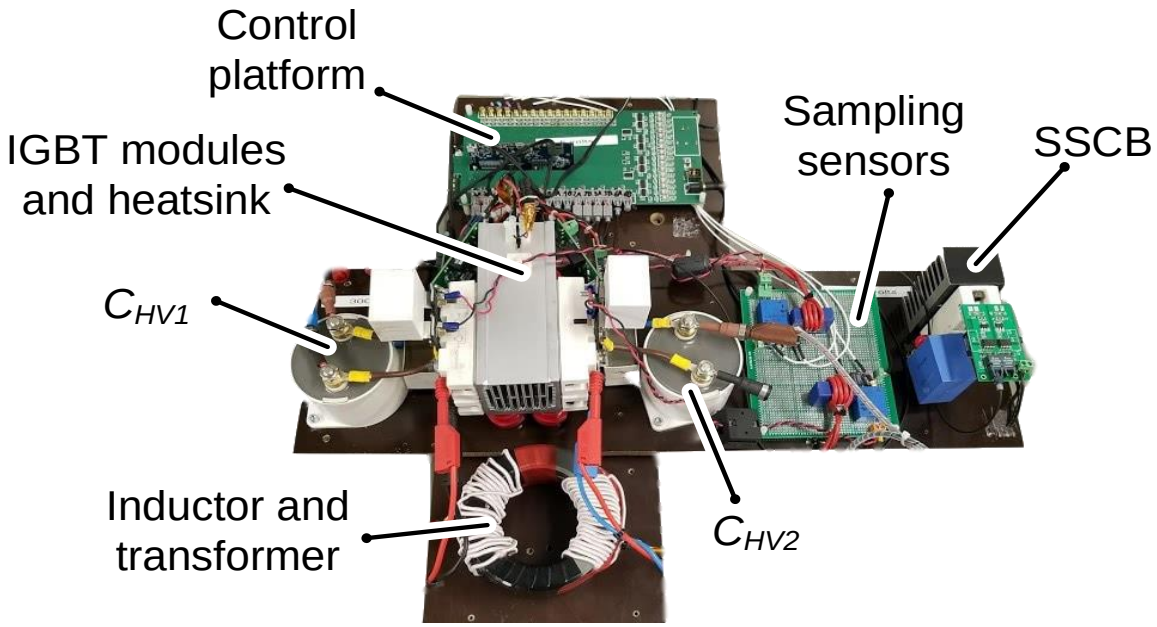


Fig. 2.31 The experiment prototype converter.

TABLE 2.9 CIRCUIT & CONTROL PARAMETERS

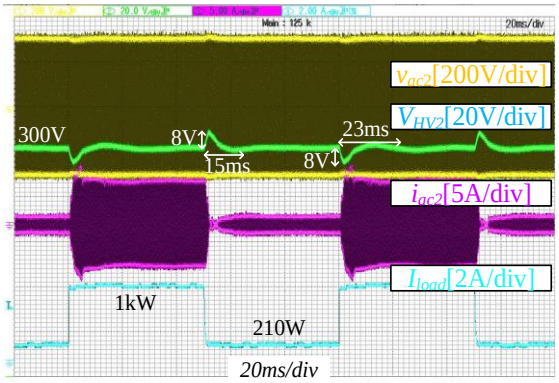
Description	Value	Units
Switching frequency f_s	20	kHz
Dead time t_d	1.6	μS
Transformer turn ratio	20:20	/
Power inductor L_p	283	μH
Parasitic resistance R_p	50	mΩ
DC capacitor C_{HV1} C_{HV2}	384	μF
Rated/Max power	1 / 1.5	kW
Proportional coefficient K_p	0.01	/
Integral coefficient K_i	3.57	/

TABLE 2.10 HARDWARE COMPONENTS

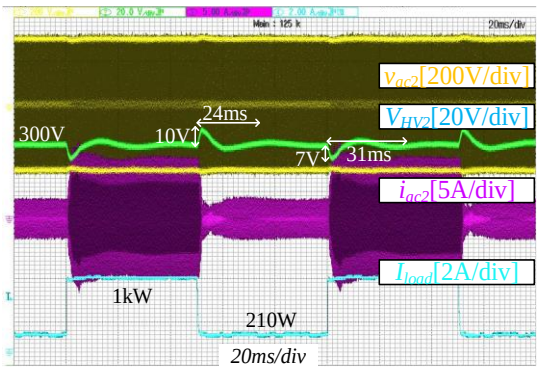
Component	Description	Parameters
Switching devices	SKM75GB128D	V_{CES}=1200V; I_c=100A
Pri/Sec capacitors	C4DEFPQ6380A8TK, Polypropylene	380uF; 400V
Magnetic components	MnZn Ferrites; 3.9mm^2 litz wire	L_m=3mH; L_p=0.3mH
Voltage sensors	LV 25-P	t_r=40us
Current sensors	LA 55-p	BW(-1dB) 200kHz

2.7.1 Transient and steady state results

The experiment results with load variations are shown in Fig. 2.32. The input voltage is set to 300V and 260V in Fig. 2.32(a) and Fig. 2.32(b), respectively. The output voltage reference is set to 300V. The load power transits between 1kW and 210W at a frequency of 20Hz. In Fig. 2.32(a), the load voltage sees the largest variation in the reference value by 8V during transition while the value is 10V in Fig. 2.32(b). The settling times in Fig. 2.32(b) have also deteriorated from Fig. 2.32(a). These phenomena agree with the results in Fig. 2.26. This showcases one of the issues associated with the PI controller. Conventionally, PI control parameters are designed and tuned at a single operating point. A good global performance cannot be guaranteed. The steady state waveforms of Fig. 2.32 are shown in Fig. 2.33. When terminal voltages stay at unity, TPS operates the same as SPS. However, when voltage deviates, TPS operates the converter with varying active state duties.

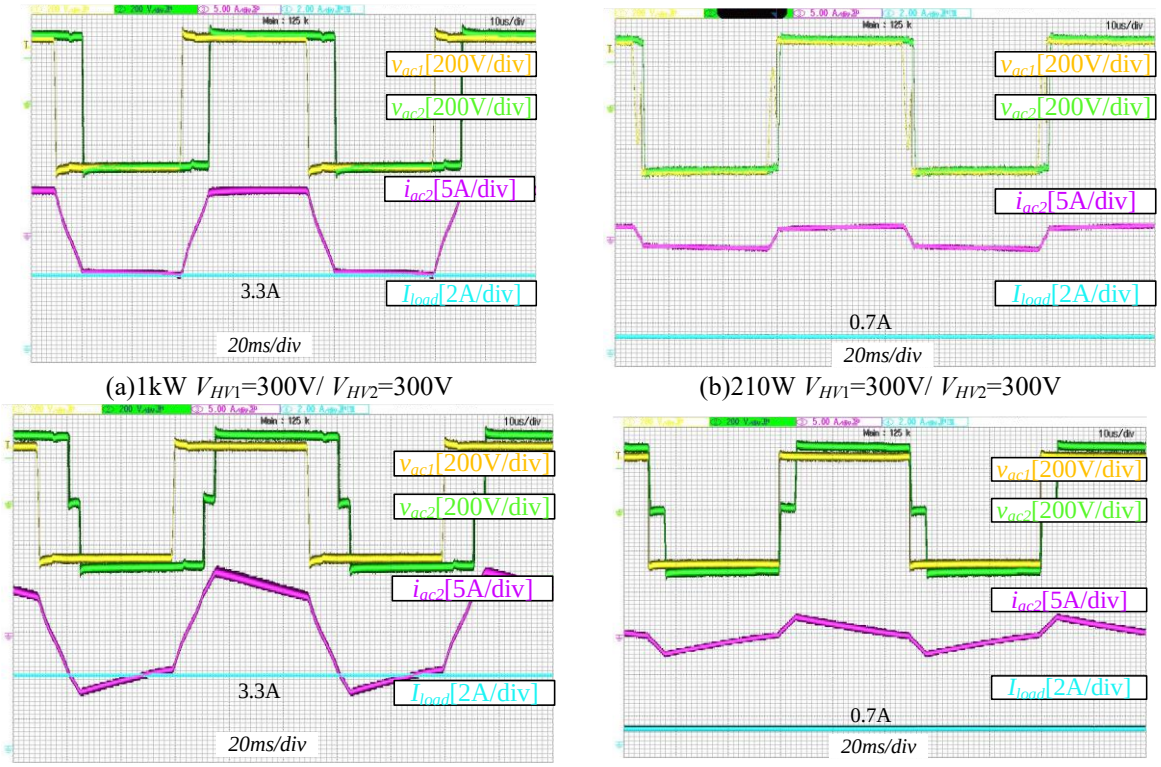


(a) V_{HV1}=300V/ V_{HV2}=300V



(b) V_{HV1}=260V/ V_{HV2}=300V

Fig. 2.32 Transition with the PI controller

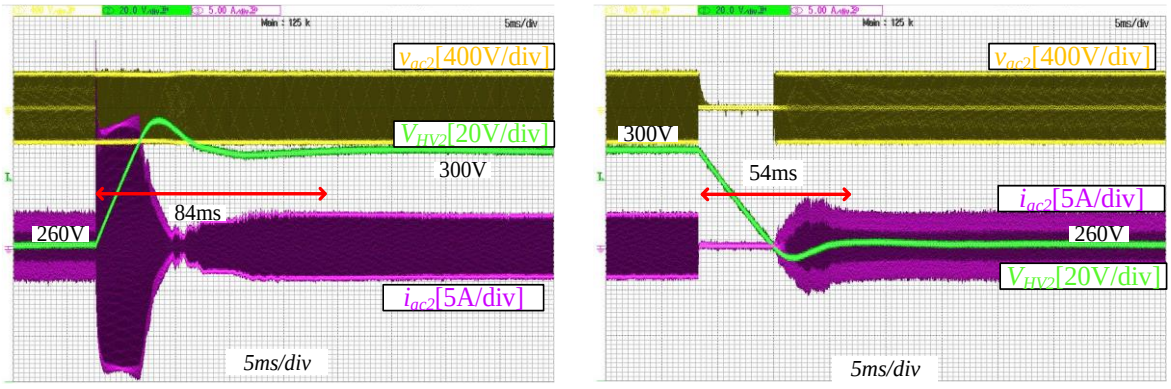


(a)1kW V_{HV1}=300V/ V_{HV2}=300V (b)210W V_{HV1}=300V/ V_{HV2}=300V

(c)1kW V_{HV1}=260V/ V_{HV2}=300V (d)210W V_{HV1}=260V/ V_{HV2}=300V

Fig. 2.33 Steady state waveforms

Experiments on the step change of the reference voltage are also conducted. The output voltage references are changed between 260V and 300V. The transition results are presented in Fig. 2.34. In the experiment, settling times of 84ms and 54ms are achieved for reference step up/down respectively.



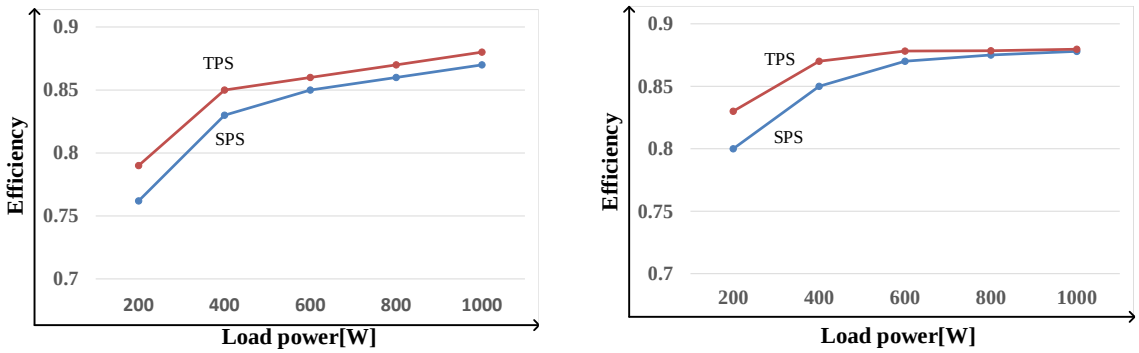
(a) V_{HV2_ref} from 260V to 300V (b) V_{HV2_ref} from 300V to 260V

Fig. 2.34 Reference tracking performance with the designed PI controller.

It is worth mentioning that the absolute dynamic of the PI controller is not the fastest due to the slow control parameters. The controller can be tunned faster if the hardware design is improved. Notwithstanding, the relative comparisons can still support the claims.

2.7.2 Efficiency measurements

The efficiency is measured by a PPA4500 power analyser from Newtons4th Ltd. When the DAB converter is modulated with SPS and TPS under two different terminal voltage conditions, the efficiency curves are shown in Fig. 2.35(a) and (b). Although the absolute value of the efficiency is low as the DAB prototype hardware is not optimal, the TPS still shows its advantage over SPS in efficiency boosting particularly in partial load [54].



(a) Boost mode 260V/300V (b) Buck mode 300V/260V

Fig. 2.35 Efficiency measurement.

The boost mode (260V/300V) has lower efficiency than the buck mode (300V/260V). In boost mode, the peak transformer current is the turn-off current for IGBT devices. In contrast, for buck mode operation, the transformer peak current is the turn-on current. For IGBT devices, the minority carrier stored in the junction causes the characteristic "tail" in the current waveform of an IGBT at turn-off, which increases the loss. A second observation is that in partial load, the efficiency of TPS is higher than SPS due to the employment of two other phase shift variables and offline optimization on efficiency can be carried out, however, the efficiency curves have trends to converge with the increasing of load power. This has a correlation with the increasing of active state duty values D_1 and D_2. When using TPS at full power, both active state duties are close to 0.5. TPS eventually converges to the SPS.

2.8 Chapter summary

The fundamentals of the DAB have been introduced in this chapter, including switching patterns, modulations, modelling and control. Two switching patterns – the phase shifting

pattern and the pulse modulating pattern have been introduced. Both switching patterns demonstrate the same overall switching loss. However, the phase shifting pattern is often used due to its property of even switching loss distribution between devices in the same H bridge leg.

Modulation techniques are implemented on top of the switching pattern. Amongst existing modulation techniques, SPS is the most straightforward approach in DAB converters. SPS has a higher power transfer capability compared to other modulation techniques. However, it presents a few drawbacks. The ZVS region gets smaller when the terminal voltage ratio varies from unity, thus the efficiency will drop, and also the deadtime effect causes EMI problems and error in the power transfer in light load. The problems can be alleviated through proper design of the power transfer inductance. When designing the value of L_p, a trade-off between the reactive power (conduction loss) and ZVS region (switching loss) should be taken into account. In order to boost the efficiency of the DAB converter when the terminal voltage ratio varies from unity using SPS, TPS has been analysed with its twelve operating modes. Transformer peak current has been chosen as an indirect esteem indicator for the efficiency. Thus, minimization of the transformer peak current has been conducted with closed-form expressions. The improvement of efficiency with optimized TPS has been verified using experimental results.

The modelling of a DAB converter is different from that of non-isolated DC-DC converters such as buck, boost and Ćuk. The existence of the high frequency transformer poses a difficulty in developing the average model of the DAB converter. One of the modelling methods, called the reduced order model, neglects the dynamic on the transformer, thus reducing one order of the converter and hence the name. This method has been widely used for its simplicity and reasonably high accuracy to describe the average model of DAB. In this chapter, the reduced order average models have been derived for TPS. The ideal small signal models of TPS have been also developed. It has been demonstrated in both analysis and experimental that the performance of the DAB converter varies with different operating points with one set of PI parameters.

Chapter 3 Control methods for Dual Active Bridge

In this chapter, the main control objective of the DAB is the load voltage regulation. Existing control methods found in the literature includes feedback control [78], feedforward control [73], [79], transformer current control [80]–[83], linearization control [84] and sliding mode control[85], [86]. The load disturbance rejection and voltage tracking capabilities have been assessed. Based on the analysis, remarks on those control methods are given.

All the control methods are assessed under the same circuit where the DAB converter is loaded with a resistor R_L as in Fig. 3.1.

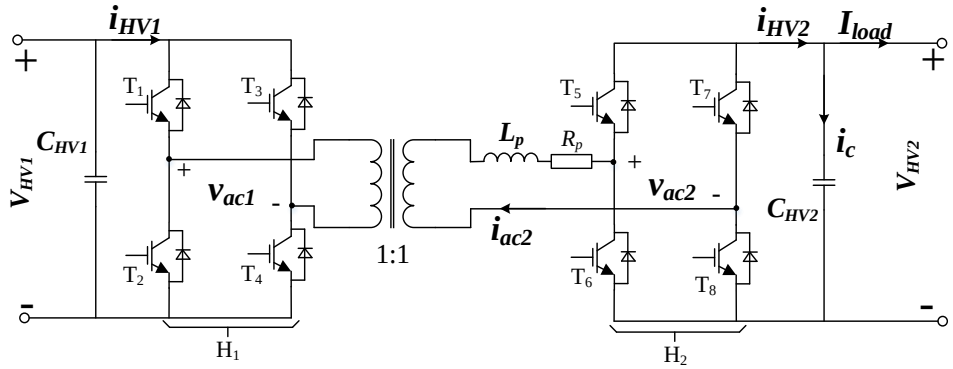


Fig. 3.1 The diagram of the DAB converter under investigation.

The circuit parameters are listed in Table 3.1.

TABLE 3.1 CIRCUIT PARAMETERS

Description	Value	Units
Switching frequency f_s	20	kHz
Transformer turn ratio	20:20	/
Primary power inductor L_p	283	μH
Parasitic resistance R_p	50	mΩ
Secondary DC capacitor C_{HV2}	384	μF

It is worth pointing out that the term “control method” here designates algorithms or circuits that take only the sampling of the voltages and/or currents as inputs to generate the phase shift duties or active state duties of the DAB. By this definition, the so called “control” in the literature [47], [51], [54], [59], [87]–[89] is classified as the optimization of advanced modulations rather than the control methods discussed here. By the above definition of control,

most methods found in the literature are proposed based on SPS shown in Fig. 3.2 due to its simplicity. Except for the PI and stationary current controls, the rest of the control methods show considerable difficulty for being extended with advanced modulations that typically present more than one operating modes. Therefore, only SPS is considered in this chapter.

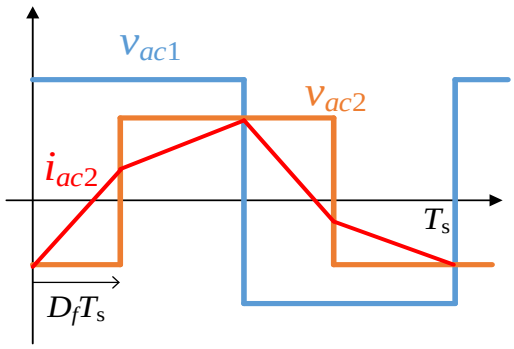


Fig. 3.2 Transformer terminal voltages and current waveform of SPS.

3.1 PI only control

The PI load voltage control scheme is presented in Fig. 3.3, where the phase shift duty D_f between the primary and secondary bridges is modified dependent on the error between the load voltage and its reference [78]. A proportional-integral compensator $G_{vI}(s)$ defined in (3. 1) can be used to minimize the steady state error.

$$G_{v1}(s) = k_{p1} + \frac{k_{i1}}{s} \tag{3. 1}$$

Based on Chapter 2 section 2.3.1, the phase shift duty ratio D_f to i_{HV2} transfer function $G_{SPS}(s)$ can be written as (3. 2).

$$G_{SPS}(s) = \frac{< i_{HV2} >_{T_s}(s)}{D_f(s)} = \frac{\overline{V_{HV1}}(1-4\overline{D_f})}{f_s L_p} \tag{3. 2}$$

, where $\overline{D_f}$ is the phase shift duty ratio at the equilibrium point. The phase shift duty ratio D_f to load voltage V_{HV2} transfer function $G_{SPS}(s)$ can be written as

$$G_{DAB}(s)=\frac{V_{HV2}(s)}{D_f(s)}=G_{SPS}(s)Z_L(s) \tag{3. 3}$$

, where

$$Z_L(s)=\frac{R_L}{1+R_L C_{HV2}s} \tag{3. 4}$$

$G_{SPS}(s)$, R_L and C_{HV2} are constants under a fixed equilibrium point. The transfer function $G_{DAB}(s)$ is a first order system.

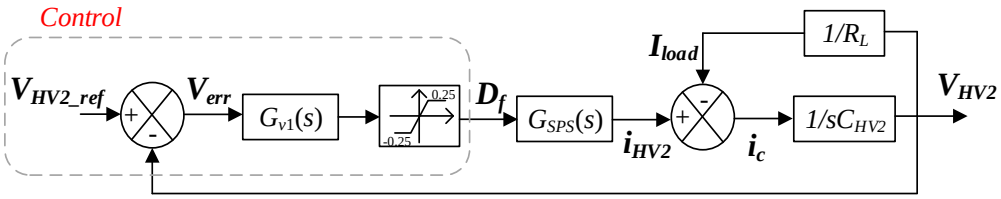


Fig. 3.3 PI control diagram with resistive load R_L [78].

Therefore, the close-loop control to output transfer function is derived based on Fig. 3.3 as

$$G_{R2O}(s)=\frac{V_{HV2}}{V_{HV2_ref}}=\frac{G_{v1}(s)G_{SPS}(s)Z_L(s)}{1+G_{v1}(s)G_{SPS}(s)Z_L(s)} \tag{3. 5}$$

Aiming to derive the expression of the output impedance $Z_o(s)$, the resistive load R_L is replaced by a current disturbance I_{load} in the main circuit Fig. 3.1. The control diagram becomes Fig. 3.4.

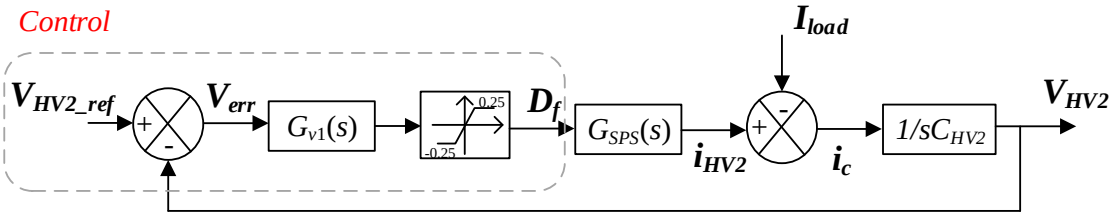
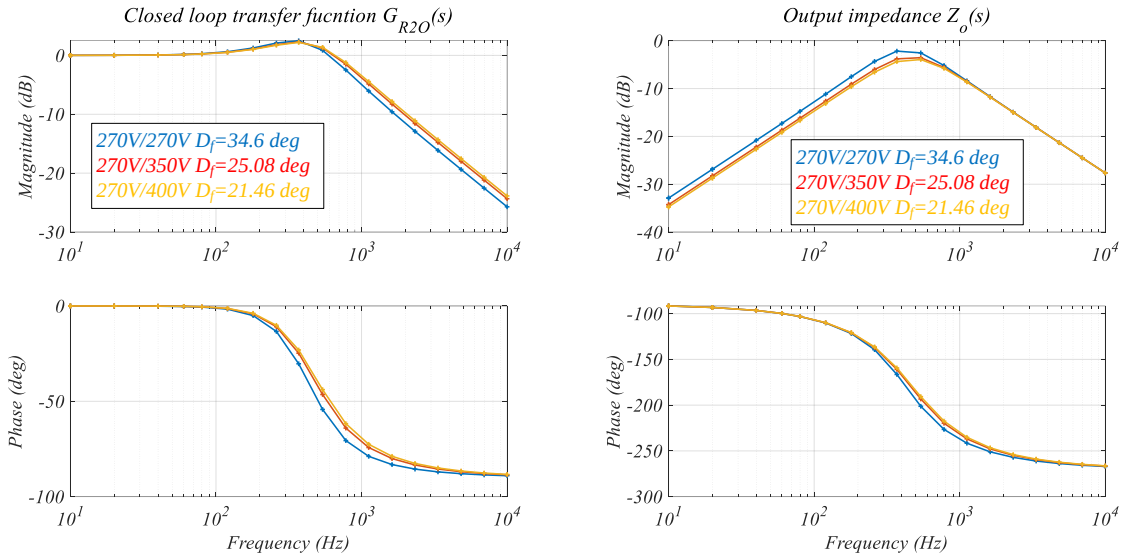


Fig. 3.4 PI control diagram with load current I_{load} perturbation.

Based on the control diagram in Fig. 3.4, the output impedance can be developed as

$$Z_o(s) = \frac{V_{HV2}}{I_{load}} = -\frac{1/sC_{HV2}}{1 + G_{v1}(s)G_{SPS}(s)\ 1/sC_{HV2}} \tag{3. 6}$$

$G_{R2O}(s)$ reflects the ability of the PI control to track the load voltage reference while $Z_o(s)$ indicates the ability to regulate the load voltage under load disturbance. The PI control parameters are set as $k_{p1} = 0.0425$, $k_{i1} = 94.4536$ to make the crossover frequency 600Hz at the equilibrium point 270V270V 1kW. The plots of $G_{R2O}(s)$ and $Z_o(s)$ are shown in Fig. 3.5 for various terminal voltages. It can be observed that there exists insignificant discrepencies.



(a) (b)

Fig. 3.5 (a) $G_{R2O}(s)$ and (b) $Z_o(s)$ under 1kW are plotted according to models in (3. 5) and (3. 6)

3.2 Feedforward control

The feedforward controls draw on the information of the load current and generate the phase shift duty close to its steady state. The feedforward controls are not applied independently. PI controllers are often employed to eliminate the steady state error. Combined feedforward plus PI control can improve performance over PI control as the load disturbance can be measured and counterbalanced before it affects the load voltage. Two typical feedforward controls, hybrid control and the virtual direct power control, for DAB converters found in the exsiting literatures are introduced. Small signal models of the two controllers are developed for comparison purpose.

3.2.1 Hybrid Control

A feedforward control strategy is proposed based on the relationship between the phase shift duty ratio D_f and operating power [73]. At steady state, the operating power can be expressed as (3. 7).

$$P = \frac{V_{HV1}V_{HV2}}{f_s L_p}\overline{D_f}\left(1-2\left|\overline{D_f}\right|\right) = V_{HV2}I_{load} \tag{3. 7}$$

Based on (3. 7), the phase shift duty at steady state can be calculated as (3. 8). Alternatively D_f^* can be also generated using a lookup table to avoid the computation [90].

$$D_f^* = \begin{cases} \frac{1}{4} - \sqrt{\frac{1}{16} - \frac{f_s L_p I_{load}}{2V_{HV1}}} & I_{load} \geq 0 \\ \frac{1}{4} + \sqrt{\frac{1}{16} - \frac{f_s L_p I_{load}}{2V_{HV1}}} & I_{load} < 0 \end{cases} \tag{3. 8}$$

Fig. 3.6 shows the control diagram, which is termed as a hybrid control method in [73]. The value D_f^* calculated from (3. 8) is superimposed on the output of the PI controller $G_{v2}(s)$. Due to the non-linearity of the equation (3. 8), classic control theory to assess the control performance cannot be applied directly. Local linearization of the equation (3. 8) is the antecedent of the small signal based analysis.

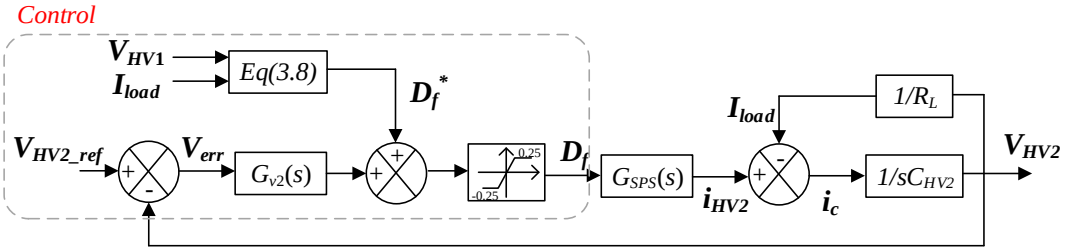


Fig. 3.6 The hybrid control with resistive load R_L [73].

Assuming the input voltage remains constant, in order to conduct small signal analysis, local linearization of the equation (3. 8) results in the expression in (3. 9).

$$G_i(s)=\frac{dD_f^{*}}{dI_{load}}=\begin{cases}\dfrac{f_sL_p}{4V_{HV1}}\left(\dfrac{1}{16}-\dfrac{f_sL_p\overline{I_{load}}}{2V_{HV1}}\right)^{-\frac{1}{2}} & I_{load}\geq 0\\ -\dfrac{f_sL_p}{4V_{HV1}}\left(\dfrac{1}{16}-\dfrac{f_sL_p\overline{I_{load}}}{2V_{HV1}}\right)^{-\frac{1}{2}} & I_{load}<0\end{cases} \tag{3. 9}$$

, where $\overline{I_{load}}$ is the equilibrium value calculated as:

$$\overline{I_{load}}=\frac{V_{HV1}}{f_sL_p}\overline{D_f}(1-2\overline{D_f}) \tag{3. 10}$$

Based on equations (3. 2) and (3. 9), for unidirectional power flow, it can be concluded that (3. 11) holds true when the inductance L_p keeps the same value in both control and circuit.

$$G_i(s)G_{SPS}(s)=1 \tag{3. 11}$$

With the feedforward gain $G_i(s)$, the control block diagram becomes Fig. 3.7.

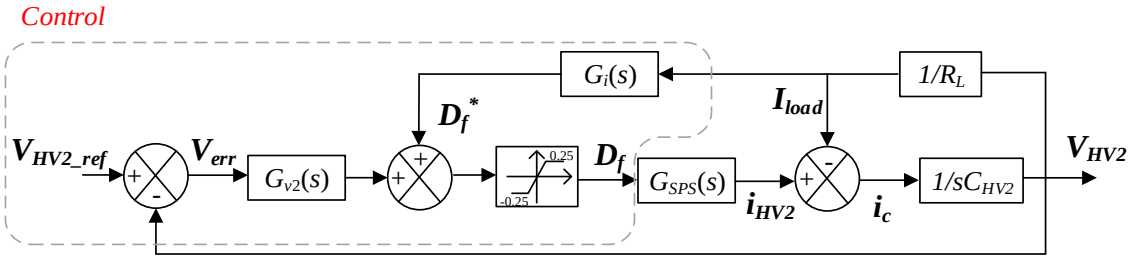


Fig. 3.7 Hybrid control diagram with resistive load R_L.

The close-loop control to output transfer function $G_{R2O}(s)$ is derived based on Fig. 3.7 as

$$G_{R2O}(s)=\frac{V_{HV2}}{V_{HV2_ref}}=\frac{G_{v2}(s)G_{SPS}(s)\,{}^{1}\!/\!_{sC_{HV2}}}{1-T_1(s)-T_2(s)-T_3(s)} \tag{3. 12}$$

, where loop gains are calculated as:

$$T_1(s)=-G_{v2}(s)G_{SPS}(s)\,{}^{1}\!/\!_{sC_{HV2}} \tag{3. 13}$$

$$T_2(s)=-\frac{1}{sC_{HV2}R_L} \tag{3. 14}$$

$$T_3(s) = \frac{G_i(s)G_{SPS}(s)}{sC_{HV2}R_L} \tag{3. 15}$$

Substituting (3. 13) - (3. 15) into (3. 12) yields:

$$G_{R2O}(s) = \frac{V_{HV2}}{V_{HV2_ref}} = \frac{G_{v2}(s)G_{SPS}(s)R_L}{1-G_i(s)G_{SPS}(s)+sC_{HV2}R_L+G_{v2}(s)G_{SPS}(s)R_L} \tag{3. 16}$$

Substituting (3. 11) into (3. 16) yields:

$$G_{R2O}(s) = \frac{V_{HV2}}{V_{HV2_ref}} = \frac{G_{v2}(s)G_{SPS}(s)}{sC_{HV2}+G_{v2}(s)G_{SPS}(s)} \tag{3. 17}$$

In light of the comparison between (3. 16) and (3. 17), it can be concluded that the feedforward gain $G_i(s)$ has eliminated the influence of R_L on the transfer function $G_{R2O}(s)$. Aiming to derive the expression of the output impedance $Z_o(s)$, the resistive load R_L is replaced by a current source I_{load}. The control diagram becomes Fig. 3.8.

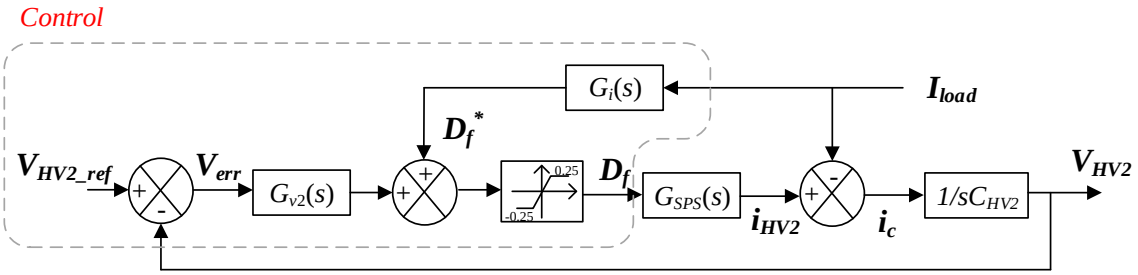


Fig. 3.8 Hybrid control diagram with load current I_{load} perturbation.

Based on the control diagram in Fig. 3.8, the output impedance can be developed as

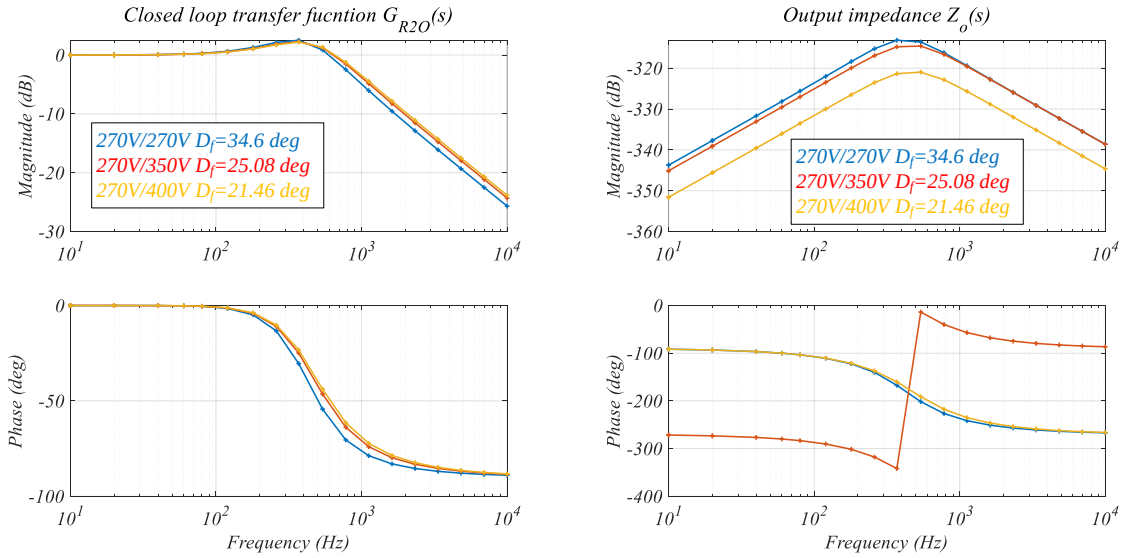
$$Z_o(s) = \frac{V_{HV2}}{I_{load}} = \frac{G_i(s)G_{SPS}(s)-1}{1+G_{v1}(s)G_{SPS}(s)\,\frac{1}{sC_{HV2}}}\,\frac{1}{sC_{HV2}} \tag{3. 18}$$

Substituting (3. 11) into (3. 18) yields:

$$Z_o(s) = 0 \tag{3. 19}$$

The output impedance becomes zero with the feedforward gain $G_i(s)$. However, the result is valid only when the inductance in the circuit equals the value in the control. The same as PI

control, the $G_{v2}(s)$ control parameters are set as k_{p2} = 0.0427, k_{i2} = 92.9285 to make the crossover frequency at 600Hz for 270V/270V 1kW. The plot of $G_{R2O}(s)$ and $Z_o(s)$ are shown in Fig. 3.9. Comparing Fig. 3.5 and Fig. 3.9, it can be seen that the feedforward gain $G_i(s)$ has little influence over the transfer function. However, $G_i(s)$ reduces the output impedance significantly.



(a) (b)

Fig. 3.9 Plot of (a) $G_{R2O}(s)$ and (b) $Z_o(s)$ with the hybrid control under 1kW.

In practice, the inductance L_p can hardly keep consistent with the value in control. Assuming the inductance value in the circuit L_{p_p} is α times larger than the value in control algorithm L_{p_c}:

$$L_{p_p} = \alpha L_{p_c} \tag{3. 20}$$

Therefore, the feedforward gain becomes:

$$G_i(s) = \frac{dD_f^*}{dI_{load}} = \begin{cases} \dfrac{f_s L_{p_c}}{4V_{HV1}}\left(\dfrac{1}{16} - \dfrac{f_s L_{p_c}\overline{I_{load}}}{2V_{HV1}}\right)^{-\frac{1}{2}} & I_{load} \geq 0 \\ -\dfrac{f_s L_{p_c}}{4V_{HV1}}\left(\dfrac{1}{16} - \dfrac{f_s L_{p_c}\overline{I_{load}}}{2V_{HV1}}\right)^{-\frac{1}{2}} & I_{load} < 0 \end{cases} \tag{3. 21}$$

The equilibrium point value $\overline{I_{load}}$ is calculated as:

$$\overline{I_{load}} = \frac{V_{HV1}}{f_s L_{p_p}}\overline{D_f}(1-2\overline{D_f}) \tag{3. 22}$$

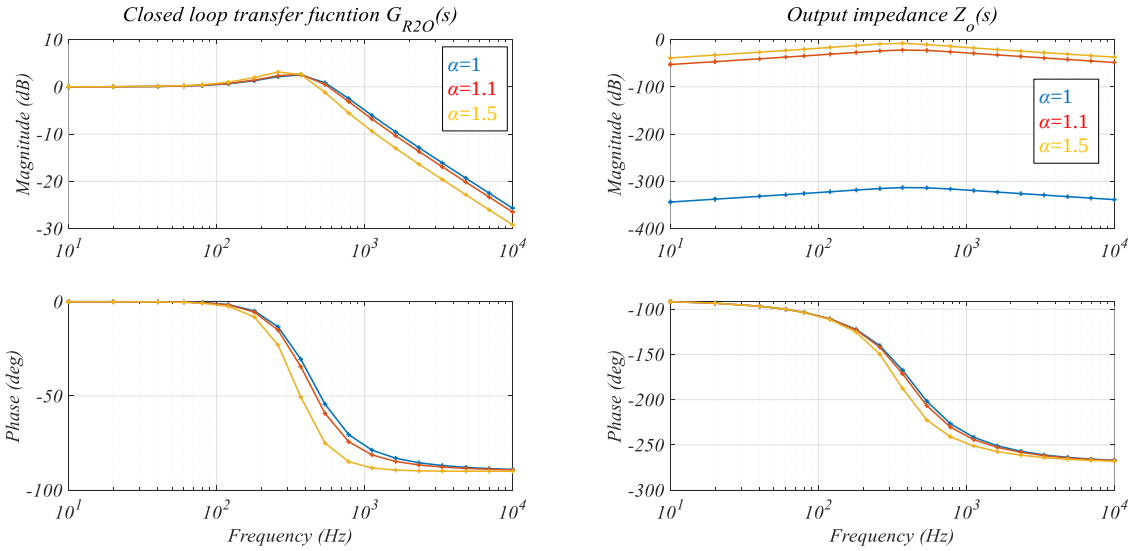
The model of the DAB circuit becomes:

$$G_{SPS}(s)=\frac{V_{HV1}(1-4\overline{D_f})}{f_s L_{p_p}}=\frac{V_{HV1}(1-4\overline{D_f})}{\alpha f_s L_{p_c}} \tag{3. 23}$$

The product of $G_i(s)$ and $G_{SPS}(s)$ becomes (3. 24). Therefore, according to the expression for the output impedance (3. 18), $Z_o(s)$ will not be zero.

$$G_{SPS}(s)G_i(s)=\frac{(1-4\overline{D_f})}{4\alpha}\frac{1}{\sqrt{\frac{1}{16}-\frac{\overline{D_f}(1-2\overline{D_f})}{2\alpha}}}\neq 1 \quad (\alpha\neq 1) \tag{3. 24}$$

The transfer function expression (3. 16) and output impedance expression (3. 18) are utilized for the plot Fig. 3.10. The output impedance $Z_o(s)$ gets larger when α increases. This shows that the hybrid control needs accurate acquisition of the inductance value L_p in order to achieve good load disturbance rejection. The accurate inductance value may be challenging to calculate for an inductor that operates under high fundamental frequency. The practical performance of the hybrid control may not be as good as designed.



(a) (b)

Fig. 3.10 Plot of (a) $G_{R2O}(s)$ and (b) $Z_o(s)$ with the hybrid control under 270V/270V 1kW.

3.2.2 Virtual Direct Power Control

Another feedforward control termed as Virtual Direct Power Control (VDPC) has been proposed by *W.Song et al.* [79]. The advantage of the VDPC is that it eliminates the necessity of using the information of the inductance L_p by using the unified power to calculate for D_f^*. In this method, a virtual power reference P^* is defined:

$$P^* = U_v^* I_{load}^* \tag{3. 25}$$

, where U_v^* is named the virtual desired load voltage, the output value of a PI compensator. Assuming a resistive load is connected to the secondary terminal of DAB, the desired output current I_{load}^* can be described as:

$$\frac{I_{load}}{V_{HV2}} = \frac{I_{load}^*}{V_{HV2_ref}} \tag{3. 26}$$

Substituting (3. 26) to (3. 25) yields:

$$P^* = \frac{U_v^* V_{HV2_ref}}{V_{HV2}} I_{load} \tag{3. 27}$$

On the other hand, the unified power is expressed as:

$$P_{pu} = V_{HV1} V_{HV2} D_f (1 - 2D_f) \tag{3. 28}$$

, where the unity base is:

$$P_{base} = 1/f_s L_p \tag{3. 29}$$

At steady state, U_v^* is equal to:

$$\overline{U_v^*} = \overline{V_{HV2}} / P_{base} \tag{3. 30}$$

Solving P_{pu}=P*. The expression of D_f^* is derived free from inductance L_p as in (3. 31).

$$D_f^* = \begin{cases} \frac{1}{4} - \sqrt{\frac{1}{16} - \frac{V_{HV2_ref} I_{load}}{2 V_{HV1} V_{HV2}^2} U_v^*} & I_{load} \geq 0 \\ \frac{1}{4} + \sqrt{\frac{1}{16} - \frac{V_{HV2_ref} I_{load}}{2 V_{HV1} V_{HV2}^2} U_v^*} & I_{load} < 0 \end{cases} \tag{3. 31}$$

In essence, the VDPC utilized the unified power (3. 28) for the calculation of the phase shift duty D_f^* to avoid involving the value of L_p. The sampling values of the load voltage V_{HV2} and current I_{load} are included in the calculation for D_f^* to enhance the disturbance rejection ability. The control diagram of the VDPC is shown in Fig. 3.11.

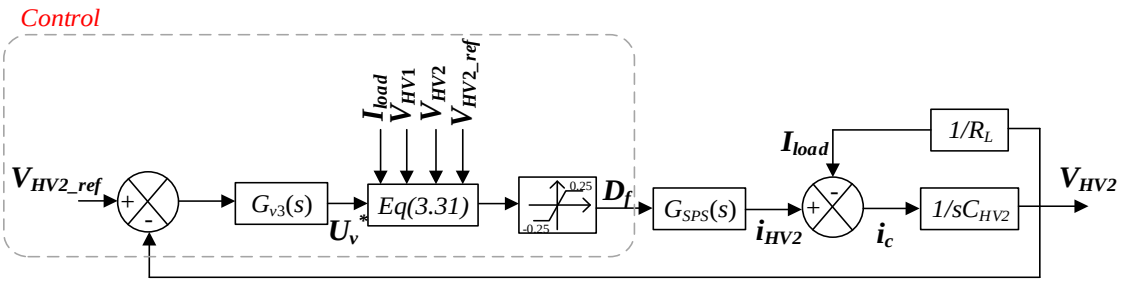


Fig. 3.11 The VDPC control with resistive load R_L [79].

Assuming the input terminal voltage V_{HV1} and the load voltage reference V_{HV2_ref} remain constant. The partial derivatives of D_f^* to load current I_{load}, load voltage V_{HV2} and the output value of PI U_v^* are:

$$G_I(s) = \frac{\partial D_f^*}{\partial I_{load}} = \begin{cases} \frac{1}{\sqrt{\frac{1}{16} - \frac{V_{HV2_ref} \overline{I_{load}}}{2 \overline{V_{HV1}} \overline{V_{HV2}}^2} \overline{U_v^*}}} \frac{V_{HV2_ref} \overline{U_v^*}}{4 \overline{V_{HV1}} \overline{V_{HV2}}^2} & I_{load} \geq 0 \\ -\frac{1}{\sqrt{\frac{1}{16} - \frac{V_{HV2_ref} \overline{I_{load}}}{2 \overline{V_{HV1}} \overline{V_{HV2}}^2} \overline{U_v^*}}} \frac{V_{HV2_ref} \overline{U_v^*}}{4 \overline{V_{HV1}} \overline{V_{HV2}}^2} & I_{load} < 0 \end{cases} \tag{3. 32}$$

$$G_V(s)=\frac{\partial D_f^{\ *}}{\partial V_{HV2}}=\begin{cases}-\dfrac{1}{\sqrt{\dfrac{1}{16}-\dfrac{V_{HV2_ref}\overline{I_{load}}}{2\overline{V_{HV1}}\overline{V_{HV2}}^{\,2}}\overline{U_v^{\,*}}}}\dfrac{V_{HV2_ref}\overline{I_{load}}}{2\overline{V_{HV1}}\overline{V_{HV2}}^{\,3}}\overline{U_v^{\,*}} & I_{load}\geq 0\\ \dfrac{1}{\sqrt{\dfrac{1}{16}-\dfrac{V_{HV2_ref}\overline{I_{load}}}{2\overline{V_{HV1}}\overline{V_{HV2}}^{\,2}}\overline{U_v^{\,*}}}}\dfrac{V_{HV2_ref}\overline{I_{load}}}{2\overline{V_{HV1}}\overline{V_{HV2}}^{\,3}}\overline{U_v^{\,*}} & I_{load}<0\end{cases} \tag{3. 33}$$

$$G_U(s)=\frac{\partial D_f^{\ *}}{\partial U_v^{\ *}}=\begin{cases}\dfrac{1}{\sqrt{\dfrac{1}{16}-\dfrac{V_{HV2_ref}\overline{I_{load}}}{2\overline{V_{HV1}}\overline{V_{HV2}}^{\,2}}\overline{U_v^{\,*}}}}\dfrac{V_{HV2_ref}\overline{I_{load}}}{4\overline{V_{HV1}}\overline{V_{HV2}}^{\,2}} & I_{load}\geq 0\\ -\dfrac{1}{\sqrt{\dfrac{1}{16}-\dfrac{V_{HV2_ref}\overline{I_{load}}}{2\overline{V_{HV1}}\overline{V_{HV2}}^{\,2}}\overline{U_v^{\,*}}}}\dfrac{V_{HV2_ref}\overline{I_{load}}}{4\overline{V_{HV1}}\overline{V_{HV2}}^{\,2}} & I_{load}<0\end{cases} \tag{3. 34}$$

, where the equilibrium point value $\overline{U_v^{\,*}}$ can be calculated from (3. 30); Value $\overline{V_{HV2}}$ equals the load voltage reference V_{HV2_ref}; Value $\overline{I_{load}}$ is calculated as:

$$\overline{I_{load}}=\frac{V_{HV1}}{f_s L_{p_p}}\overline{D_f}(1-2\overline{D_f}) \tag{3. 35}$$

Therefore, for unidirectional power flow, the products are:

$$G_{SPS}(s)G_I(s)=1 \tag{3. 36}$$

$$G_{SPS}(s)G_V(s)=-\frac{2\overline{I_{load}}}{\overline{V_{HV2}}}=-\frac{2}{R_L} \tag{3. 37}$$

$$G_{SPS}(s)G_U(s)=\frac{P_{base}}{R_L} \tag{3. 38}$$

Based on the small signal models in (3. 32) - (3. 34), the control block diagram of the VDPC is shown in Fig. 3.12 where the VDPC essentially equals to the PI control with load voltage and current feedforward.

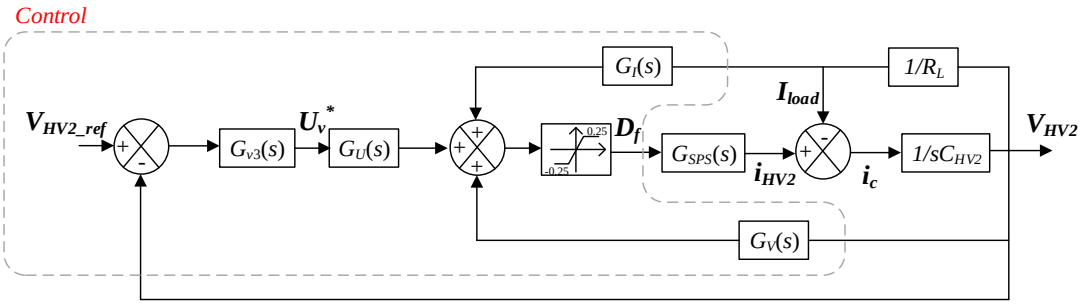


Fig. 3.12 The VDPC control block diagram with resistive load R_L.

The closed-loop control to output transfer function is derived based on Fig. 3.12 as:

$$G_{R2O}(s)=\frac{V_{HV2}}{V_{HV2_ref}}=\frac{G_{v3}(s)G_U(s)G_{SPS}(s)\,{}^{1}\!/_{sC_{HV2}}}{1-T_1(s)-T_2(s)-T_3(s)-T_4(s)} \tag{3. 39}$$

, where loop gains are calculated as:

$$T_1(s)=-G_{v3}(s)G_U(s)G_{SPS}(s)\,{}^{1}\!/_{sC_{HV2}} \tag{3. 40}$$

$$T_2(s)=-\frac{1}{sC_{HV2}R_L} \tag{3. 41}$$

$$T_3(s)=\frac{G_I(s)G_{SPS}(s)}{sC_{HV2}R_L} \tag{3. 42}$$

$$T_4(s)=\frac{G_V(s)G_{SPS}(s)}{sC_{HV2}} \tag{3. 43}$$

Substituting (3. 40) - (3. 43) into (3. 39) yields:

$$G_{R2O}(s)=\frac{V_{HV2}}{V_{HV2_ref}}=\frac{R_LG_{v3}(s)G_U(s)G_{SPS}(s)}{sC_{HV2}R_L+R_LG_{v3}(s)G_U(s)G_{SPS}(s)+1-G_I(s)G_{SPS}(s)-R_LG_V(s)G_{SPS}(s)} \tag{3. 44}$$

Substituting (3. 36) - (3. 38) into (3. 44) yields the simplified transfer function:

$$G_{R2O}(s)=\frac{G_{v3}(s)P_{base}}{sC_{HV2}R_L+P_{base}G_{v3}(s)+2}=\frac{1}{1+\dfrac{sC_{HV2}R_L+2}{G_{v3}(s)P_{base}}} \tag{3. 45}$$

Aiming to derive the expression of the output impedance $Z_o(s)$, the resistive load R_L is replaced by a current source I_{load}. The control diagram becomes Fig. 3.13.

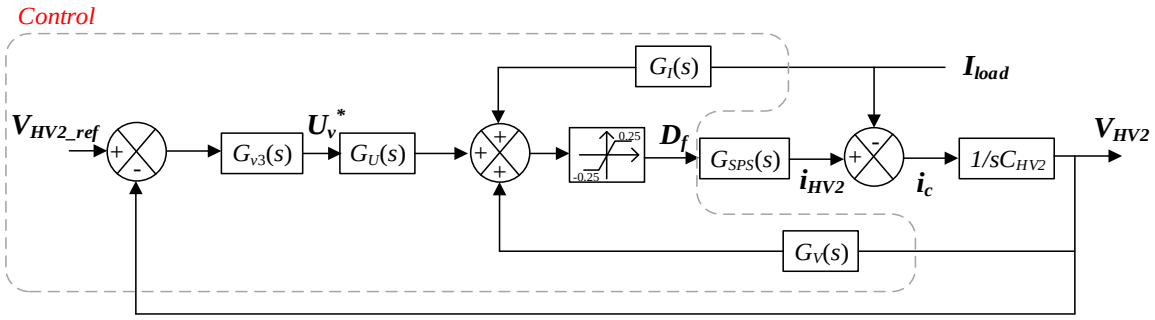


Fig. 3.13 VDPC control diagram with load current I_{load} perturbation.

Based on the control diagram in Fig. 3.13, the output impedance can be developed as:

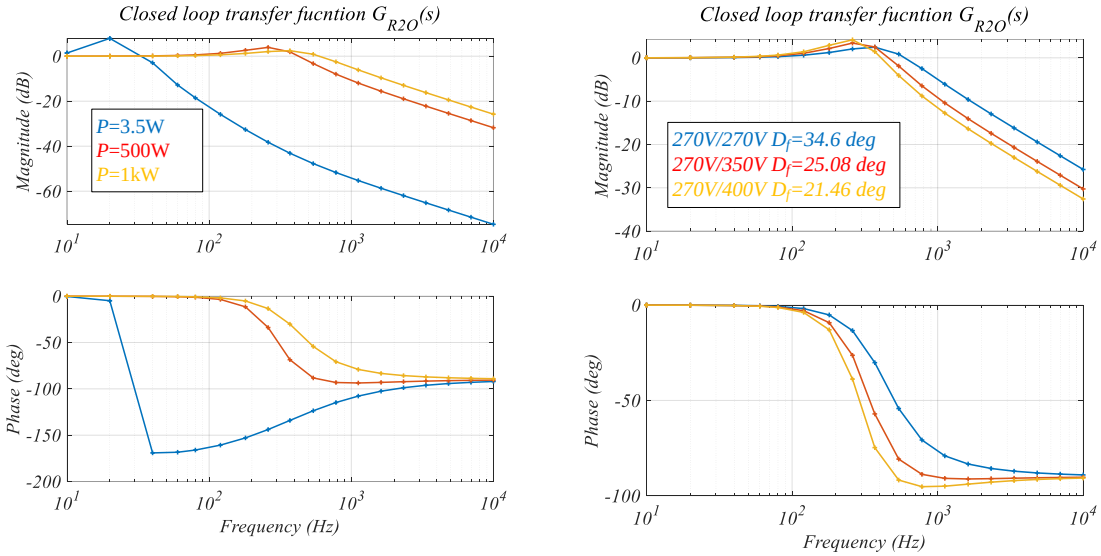
$$Z_o(s)=\frac{V_{HV2}}{I_{load}}=\frac{G_I(s)G_{SPS}(s)-1}{1-T_1(s)-T_4(s)}\Big/\frac{1}{sC_{HV2}} \tag{3. 46}$$

Substituting (3. 36) into (3. 46) yields:

$$Z_o(s)=\frac{V_{HV2}}{I_{load}}=0 \tag{3. 47}$$

Theoretically, it can be concluded that when the load voltage V_{HV2} is well regulated at its reference V_{HV2_ref}, the output impedance $Z_o(s)$ of the VDPC is zero. However, due to sampling errors, the condition (3. 36) is hard to achieve. Apart from this, the most pressing issue with the VDPC is that the inclusion of gain $G_U(s)$ on the reference to output path causes a large variation in the model with load current, posing challenges on the design of the voltage compensator $G_{v3}(s)$. For instance, if the PI parameters for $G_{v3}(s)$ are set as k_{p3} = 511.6613, k_{i3} = 1.1629*10^6 to make the crossover frequency at 600Hz for 270V/270V 1kW, the bode plot of the transfer function $G_{R2O}(s)$ becomes as in Fig. 3.14(a) under different loads. The transfer function $G_{R2O}(s)$ shows considerable differences under power 3.5W and 1kW. Therefore, the compensator $G_{R2O}(s)$ has to be adaptive with the power. The VDPC also shows variant transfer

function $G_{R2O}(s)$ with changing terminal voltages as shown in Fig. 3.14(b). The greatest advantage of the VDPC is that the output impedance can keep at zero irrelevant to the power, load voltage and circuit parameter L_p.



(a) different power 270V/270V (b) different load voltage 1kW

Fig. 3.14 The VDPC control with different resistive load R_L

3.3 Transformer current control

The common feature of this category is that the transformer current is involved in the control. Either high bandwidth current sensors are required or state observers are employed for obtaining the transformer current instant values.

3.3.1 Feedforward current control

A Feed-Forward Current Control (FFCC) is proposed by *Z. Shan et al.* [80] with the transformer instant current being regulated similarly to the peak current control described in [91]. The reduced order average model shows good agreement with the full order switching model even when the dynamic on the transformer current has been neglected [92]. Therefore, this premise is also assumed in FFCC. Typical waveforms of the transformer terminal voltages and current are shown as in Fig. 3.15.

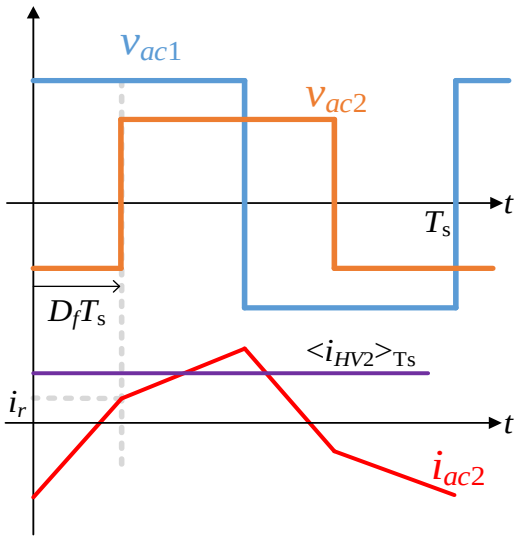


Fig. 3.15 Transformer terminal voltages and current waveform of SPS.

Transformer current value at the switching instance of the secondary side bridge is denoted as i_r. According to the Chapter 2 section 2.3.1, the expression of i_r is:

$$i_r = \frac{V_{HV2} - V_{HV1} + 4V_{HV1}D_f}{4 f_s L_p} \tag{3. 48}$$

$<i_{HV2}>_{Ts}$ is the switching average value of the secondary bridge DC side current. According to Chapter 2 section 2.3.1, $<i_{HV2}>_{Ts}$ is expressed as in (3. 49). In the steady state, the load current I_{load} equals to $<i_{HV2}>_{Ts}$.

$$< i_{HV2} >_{T_s} = \frac{V_{HV1}}{f_s L_p} D_f (1 - 2|D_f|) \tag{3. 49}$$

Therefore, the relationship between i_r and I_{load} is:

$$i_r = \frac{2I_{load}}{1 + \sqrt{1 - \frac{8I_{load}L_p f_s}{V_{HV1}}}} - \frac{V_{HV1} - V_{HV2}}{4 f_s L_p} \tag{3. 50}$$

Since the term $(V_{HV1}\text{-}V_{HV2})/(4f_sL_p)$ has slower variation and can be compensated by the PI controller, the simplified relationship of (3. 50) is:

$$i_r = \frac{2I_{load}}{1+\sqrt{1-\frac{8I_{load}L_p f_s}{V_{HV1}}}} \tag{3. 51}$$

, the derivative of i_r to the load current I_{load} is:

$$G_{ir}(s) = \frac{\partial i_r}{\partial I_{load}} = \frac{1}{1-4\overline{D_f}} \tag{3. 52}$$

The control block diagram of FFCC is shown in Fig. 3.16. With a SR flip-flop, the secondary bridge is commutated at the time instant when the transformer current is equal to a reference i_r. Reference i_r is the sum of the feedforward output i_r^* and the feedback output Δi_r.

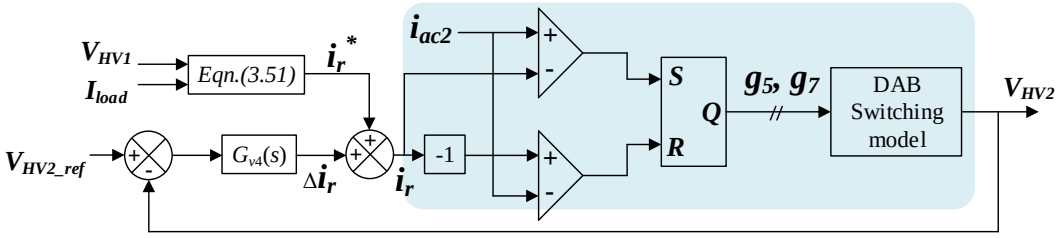


Fig. 3.16 The control diagram of the FFCC [80].

According to equations (3. 48) and (3. 49), current $<i_{HV2}>_{Ts}$ can be expressed by i_r as:

$$< i_{HV2} >_{T_s} = (i_r - \frac{V_{HV2}-V_{HV1}}{4 f_s L_p})[1-2(i_r - \frac{V_{HV2}-V_{HV1}}{4 f_s L_p})\frac{f_s L_p}{V_{HV1}}] \tag{3. 53}$$

Therefore, the partial derivatives are:

$$G_p(s) = \frac{\partial < i_{HV2} >_{T_s}}{\partial i_r} = 1 - \frac{\overline{V_{HV2}} - \overline{V_{HV1}} + 4\overline{V_{HV1}}\,\overline{D_f}}{\overline{V_{HV1}}} \tag{3. 54}$$

$$G_q(s) = \frac{\partial < i_{HV2} >_{T_s}}{\partial V_{HV2}} = \frac{4\overline{D_f} - 1}{4 f_s L_p} \tag{3. 55}$$

According to the derived small signal models (3. 52), (3. 54) and (3. 55), the control block diagram of the FFCC is illustrated in:

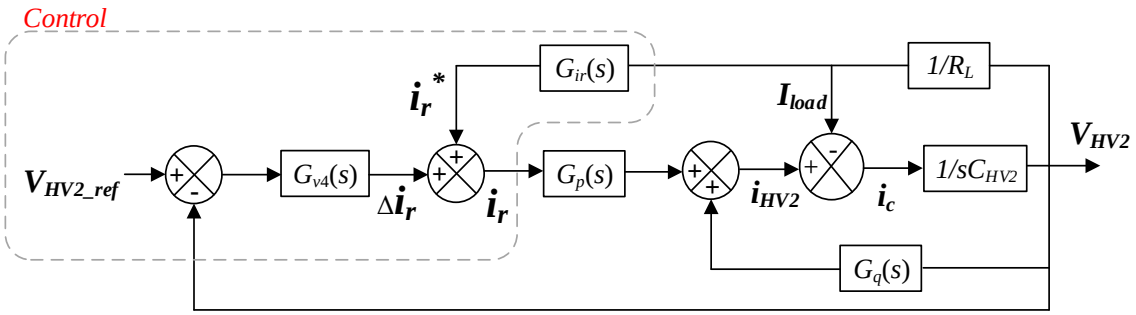


Fig. 3.17 The control block diagram of the FFCC with resistive load R_L.

Based on the control block diagram Fig. 3.17, the closed loop reference to load voltage transfer function $G_{R2O}(s)$ can be written as:

$$G_{R2O}(s)=\frac{V_{HV2}}{V_{HV2_ref}}=\frac{G_{v4}(s)G_p(s)\,{}^{1}\!/_{sC_{HV2}}}{1-T_1(s)-T_2(s)-T_3(s)-T_4(s)} \tag{3. 56}$$

, where loop gains are calculated as:

$$T_1(s)=-G_{v4}(s)G_p(s)\,{}^{1}\!/_{sC_{HV2}} \tag{3. 57}$$

$$T_2(s)=-\frac{1}{sC_{HV2}R_L} \tag{3. 58}$$

$$T_3(s)=\frac{G_q(s)}{sC_{HV2}} \tag{3. 59}$$

$$T_4(s)=\frac{G_{ir}(s)G_p(s)}{sC_{HV2}R_L} \tag{3. 60}$$

Substituting (3. 40) - (3. 43) into (3. 39) yields:

$$\begin{aligned}G_{R2O}(s)&=\frac{V_{HV2}}{V_{HV2_ref}}\\&=\frac{G_{v4}(s)G_p(s)R_L}{1+sC_{HV2}R_L+G_{v4}(s)G_p(s)R_L-G_q(s)R_L-G_{ir}(s)G_p(s)}\end{aligned} \tag{3. 61}$$

Aiming to derive the expression of the output impedance $Z_o(s)$, the resistive load R_L is replaced by a current disturbance I_{load}. The control diagram becomes Fig. 3.18.

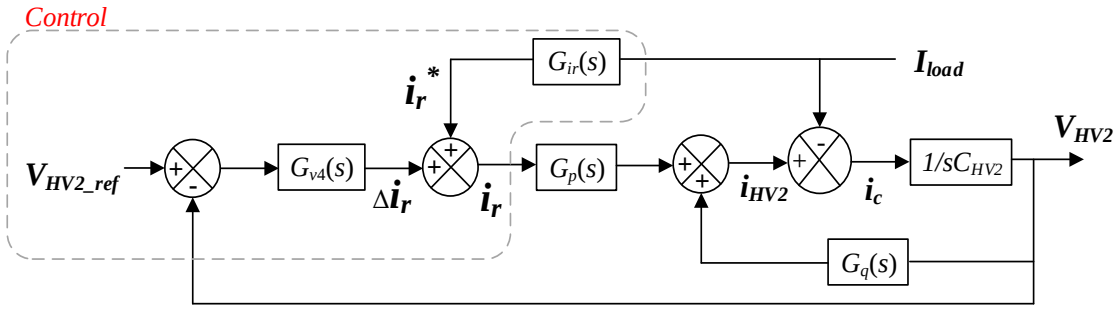


Fig. 3.18 FFCC control diagram with load current I_{load} perturbation.

Based on the control diagram in Fig. 3.18, the output impedance can be developed as:

$$Z_o(s)=\frac{V_{HV2}}{I_{load}}=\frac{G_{ir}(s)G_p(s)-1}{1-T_1(s)-T_3(s)}\Big/_{sC_{HV2}} \tag{3. 62}$$

According to equations (3. 52) and (3. 54), if the terminal voltage ratio equals unity, (3. 63) holds true.

$$G_{ir}(s)G_p(s)=1 \tag{3. 63}$$

Substituting (3. 63) back to (3. 61) and (3. 62) yield:

$$G_{R2O}(s)=\frac{V_{HV2}}{V_{HV2_ref}}=\frac{G_p(s)}{\dfrac{sC_{HV2}-G_q(s)}{G_{v4}(s)}+G_p(s)} \tag{3. 64}$$

$$Z_o(s)=0 \tag{3. 65}$$

If the PI parameters for $G_{v4}(s)$ are set as k_{p4} = 1.2135, k_{i4} = 9.8*10^3, the transfer function expression (3. 56) and output impedance expression (3. 62) are utilized for the plot Fig. 3.19.The output impedance is zero due to the unity terminal voltage ratio. However, when the load voltage varies from the nominal value, the disturbance rejection performances cannot be well retained as shown in Fig. 3.19(b).

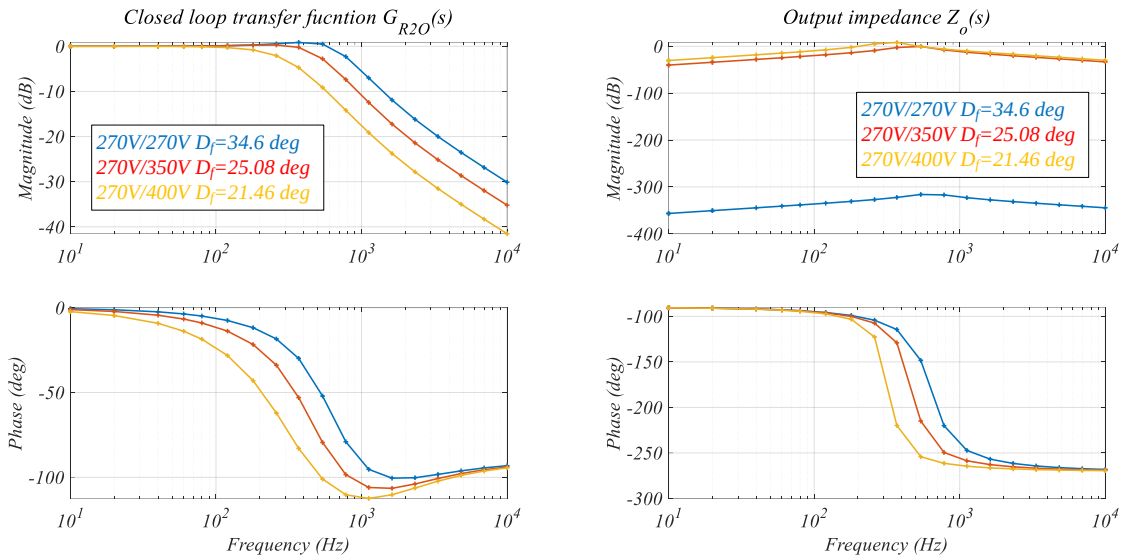


Fig. 3.19 Plot of (a) $G_{R2O}(s)$ and (b) $Z_o(s)$ with the FFCC under 1kW.

3.3.2 Predictive current control

As discussed above, the load disturbance rejection ability gets worse when the terminal voltage ratio is not at unity with FFCC. To address the issue, another digital predictive transformer current control is proposed by *S. Dutta et al.* [81].

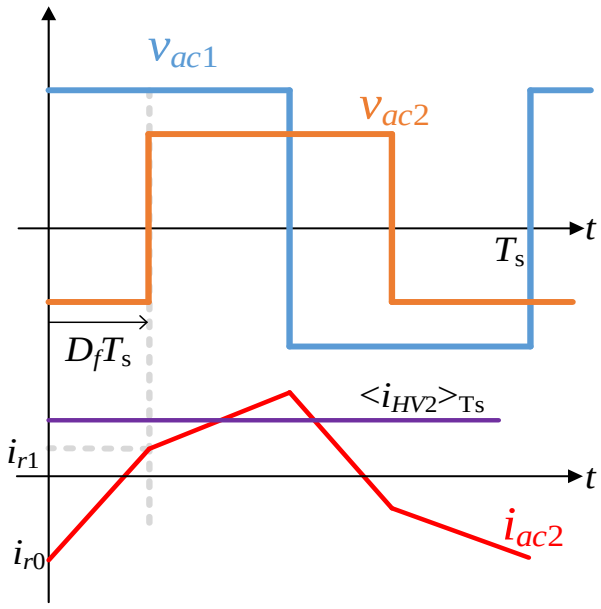


Fig. 3.20 Transformer terminal voltages and current waveform of SPS.

According to Chapter 2 section 2.3.1, current values i_{r0} and i_{r1} at the switching instances 0 and D_fT_s shown in Fig. 3.20 are calculated as:

$$i_{r0} = \frac{(V_{HV2} - V_{HV1}) - 4D_f V_{HV2}}{4 f_s L_p} \tag{3. 66}$$

$$i_{r1} = i_{r0} + \frac{V_{HV2} + V_{HV1}}{L_p} D_f T_s \tag{3. 67}$$

According to (3. 67), D_f can be calculated as:

$$D_f = \frac{i_{r1} - i_{r0}}{T_s} \frac{L_p}{V_{HV2} + V_{HV1}} \tag{3. 68}$$

Therefore, the control diagram of the predictive current control is illustrated in Fig. 3.21.

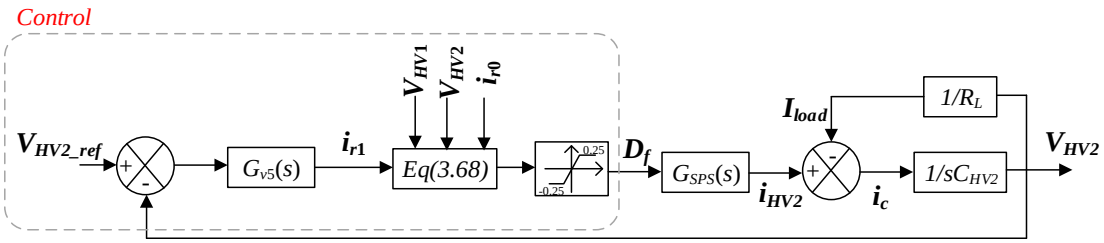


Fig. 3.21 The predictive current control with resistive load R_L [81].

Solving a pair of simultaneous equations (3. 49) and (3. 66) for i_{r0}:

$$i_{r0} = \frac{(V_{HV2} - V_{HV1}) - 4D_f V_{HV2}}{4 f_s L_p} \tag{3. 69}$$

Substituting (3. 8) into (3. 66) yields:

$$i_{r0} = \frac{V_{HV2}\sqrt{1 - \frac{8 f_s L_p < i_{HV2} >_{T_s}}{V_{HV1}}} - V_{HV1}}{4 f_s L_p} \tag{3. 70}$$

In order to conduct small signal analysis, assume the input terminal voltage V_{HV1} remains constant. Equations (3. 68) and (3. 70) are linearized as:

$$G_{ir1}(s)=\frac{\partial D_f}{\partial i_{r1}}=\frac{f_s L_p}{\overline{V_{HV2}}+\overline{V_{HV1}}} \tag{3. 71}$$

$$G_{ir0}(s)=\frac{\partial D_f}{\partial i_{r0}}=-\frac{f_s L_p}{\overline{V_{HV2}}+\overline{V_{HV1}}} \tag{3. 72}$$

$$G_{vo}(s)=\frac{\partial D_f}{\partial V_{HV2}}=-\frac{\overline{D_f}}{\overline{V_{HV1}}+\overline{V_{HV2}}} \tag{3. 73}$$

$$G_{ii}(s)=\frac{\partial i_{r0}}{\partial <i_{HV2}>_{T_s}}=-\frac{\overline{V_{HV2}}}{\overline{V_{HV1}}}\frac{1}{1-4\overline{D_f}} \tag{3. 74}$$

$$G_{vi}(s)=\frac{\partial i_{r0}}{\partial V_{HV2}}=\frac{1-4\overline{D_f}}{4 f_s L_p} \tag{3. 75}$$

The control block diagram of the predictive current control is therefore drawn as in Fig. 3.22.

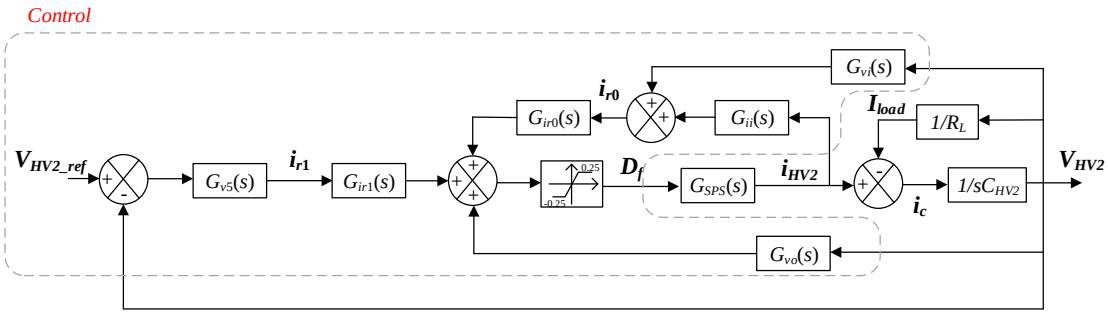


Fig. 3.22 The predictive current control block diagram with resistive load R_L.

Based on the control block diagram Fig. 3.22. The closed loop reference to load voltage transfer function $G_{R2O}(s)$ can be written as:

$$G_{R2O}(s)=\frac{V_{HV2}}{V_{HV2_ref}}=\frac{G_{v5}(s)G_{ir1}(s)G_{SPS}(s)\ {}^{1}\!/\!_{sC_{HV2}}}{1-T_1(s)-T_2(s)-T_3(s)-T_4(s)-T_5(s)} \tag{3. 76}$$

, where loop gains are calculated as:

$$T_1(s) = -G_{v5}(s)G_{ir1}(s)G_{SPS}(s)\,{}^{1}\!/_{sC_{HV2}} \tag{3. 77}$$

$$T_2(s) = -\frac{1}{sC_{HV2}R_L} \tag{3. 78}$$

$$T_3(s) = G_{vo}(s)G_{SPS}(s)\,{}^{1}\!/_{sC_{HV2}} \tag{3. 79}$$

$$T_4(s) = G_{ir0}(s)G_{ii}(s)G_{SPS}(s) \tag{3. 80}$$

$$T_5(s) = G_{vi}(s)G_{ir0}(s)G_{SPS}(s)\,{}^{1}\!/_{sC_{HV2}} \tag{3. 81}$$

Aiming to derive the expression of the output impedance $Z_o(s)$, the resistive load R_L is replaced by a current source I_{load}. The control diagram becomes Fig. 3.23.

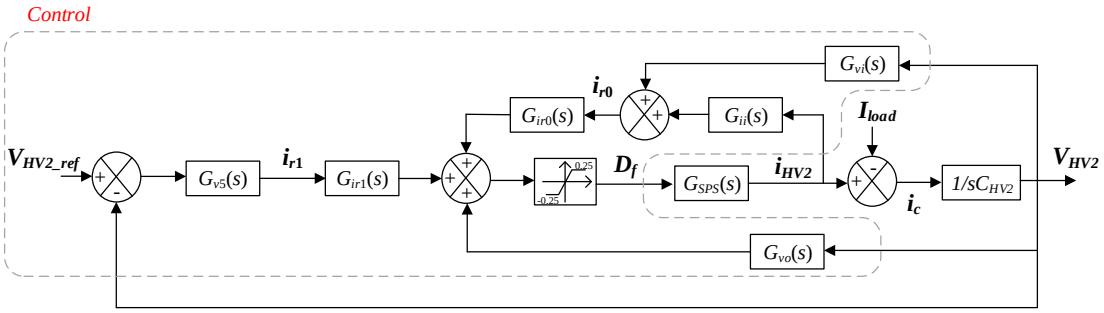


Fig. 3.23 Predictive current control diagram with load current I_{load} perturbation.

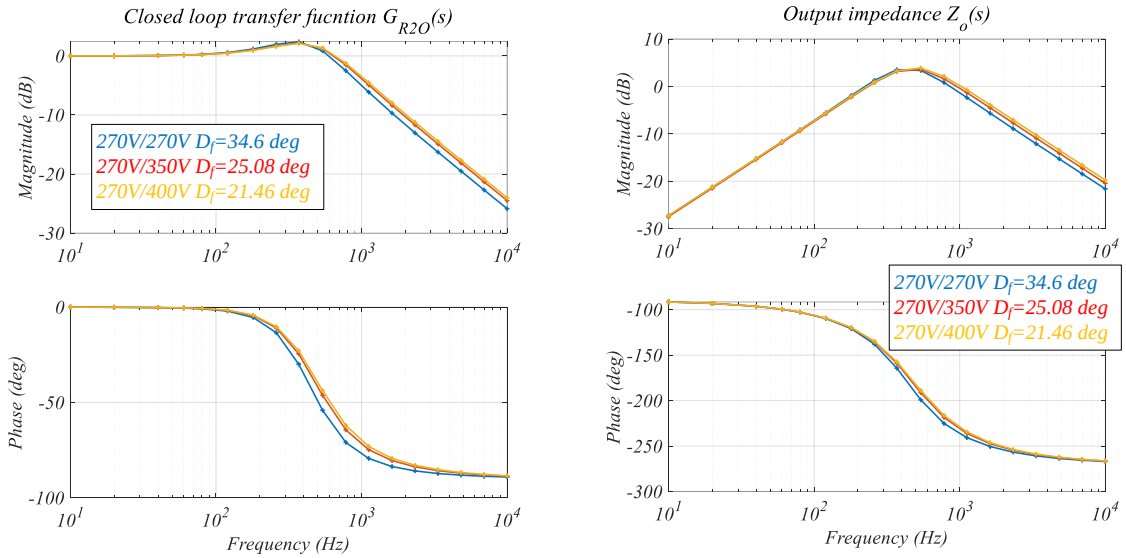
Based on the control diagram, the output impedance can be developed as:

$$Z_o(s) = \frac{V_{HV2}}{I_{load}} = \frac{-\,{}^{1}\!/_{sC_{HV2}}}{1 - T_1(s) - T_3(s) - T_4(s) - T_5(s)} \tag{3. 82}$$

Let the PI parameters for $G_{v5}(s)$ be set the same as FFCC where k_{p5} = 1.9923, k_{i5} = 4.7*10^3. Input voltage is 270V while the load voltage varies from 270V to 400V. The load power stays at 1kW. The transfer function expression (3. 72) and output impedance expression (3. 82) are utilized for the plot Fig. 3.24 where both show comparatively smaller changes with terminal voltage variations to FFCC.

This is an ideal case analysis with predictive control. However, in practical implementation, the prediction error occurs in the calculation for D_f with (3. 68). Compensation has been typically achieved by introducing extra PI controllers [81], which deteriorate the performance.

Furthermore, the predictive current control requires intensive computation in one switching period. For DAB converters with wide bandgap devices where switching frequency could range from 100kHz – 1MHz [93]–[95], it is challenging to implement the predictive current control.

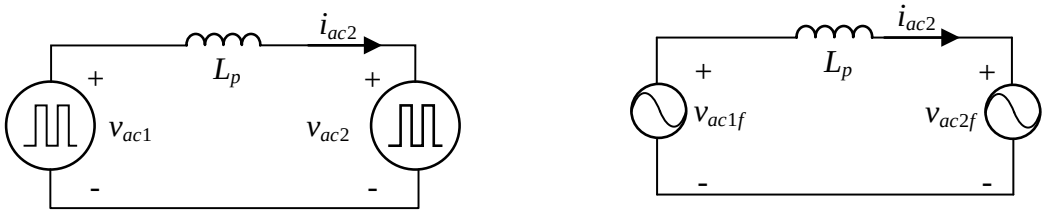


(a) (b)

Fig. 3.24 Plot of (a) $G_{R2O}(s)$ and (b) $Z_o(s)$ with the predictive current control under 1kW.

3.3.3 Stationary current control

As discussed above, FFCC and predictive current controls require the sampling of the high frequency transformer current, which brings in extra hardware cost. A stationary current control is proposed by *D. Nguyen et al.* [82], [83]. Instead of using a current sensor, the transformer current is estimated in the stationary frame. The stationary current control is developed based on the Fundamental Harmonic Approximation (FHA) method [60], [96].



(a) (b)

Fig. 3.25 DAB transformer stage (a) full harmonic and (b) FHA circuits.

As shown in Fig. 3.25, the square wave transformer terminal voltages v_{ac1} and v_{ac2} are replaced by their fundamental harmonic components v_{ac1f} and v_{ac2f} which are expressed as:

$$v_{ac1f}(t) = \frac{4}{\pi} V_{HV1} \cos(\omega_s t) = \mathrm{Re}[\frac{4}{\pi} V_{HV1} e^{j\omega_s t}] \tag{3. 83}$$

$$v_{ac2f}(t) = \frac{4}{\pi} V_{HV2} \cos(\omega_s t - 2\pi D_f) = \mathrm{Re}[\frac{4}{\pi} V_{HV2} e^{j(\omega_s t - 2\pi D_f)}] \tag{3. 84}$$

In the stationary frame, v_{ac1f} and v_{ac2f} are projected on to d-q axis as:

$$v_{ac1f_dq} = v_{ac1f_d} + jv_{ac1f_q} \tag{3. 85}$$

$$v_{ac2f_dq} = v_{ac2f_d} + jv_{ac2f_q} \tag{3. 86}$$

, where

$$\begin{cases} v_{ac1f_d} = \frac{4}{\pi} V_{HV1} \\ v_{ac1f_q} = 0 \end{cases}, \quad \begin{cases} v_{ac2f_d} = \frac{4}{\pi} V_{HV2} \cos 2\pi D_f \\ v_{ac2f_q} = -\frac{4}{\pi} V_{HV2} \sin 2\pi D_f \end{cases} \tag{3. 87}$$

The transformer current can be therefore calculated as:

$$\begin{cases} i_{ac2f_d} = \mathrm{Re}[\frac{v_{ac1f_dq} - v_{ac2f_dq}}{j\omega_s L_p}] = \frac{\frac{4}{\pi} V_{HV2} \sin 2\pi D_f}{\omega_s L_p} \\ i_{ac2f_q} = \mathrm{Im}[\frac{v_{ac1f_dq} - v_{ac2f_dq}}{j\omega_s L_p}] = \frac{\frac{4}{\pi} V_{HV1} - \frac{4}{\pi} V_{HV2} \cos 2\pi D_f}{-\omega_s L_p} \end{cases} \tag{3. 88}$$

The power from the primary source is calculated as in (3. 89). Assuming the input terminal voltage is constant, the active power is only relevant to the transformer current in the stationary frame d axis i_{ac2f_d}.

$$P = v_{ac1f_dq} \bullet i_{ac2f_dq} = v_{ac1f_d} i_{ac2f_d} = \frac{4}{\pi} V_{HV1} i_{ac2f_d} \tag{3. 89}$$

The power can also be expressed as:

$$P = V_{HV1} < i_{HV1} >_{T_s} \tag{3. 90}$$

According to (3. 89) and (3. 90), transformer current in the stationary frame d axis can be estimated by:

$$i_{ac2f_d} = \frac{\pi < i_{HV1} >_{T_s}}{4} \tag{3. 91}$$

, where the input terminal DC side bridge current is measured, and can be calculated as:

$$< i_{HV1} >_{T_s} = \frac{V_{HV2}}{f_s L_p} D_f (1 - 2D_f) \tag{3. 92}$$

Hence, the diagram of the stationary current control is illustrated in Fig. 3.26. Cascaded PI controllers are employed. The outer loop controller regulates the load voltage while the inner loop controls the stationary current.

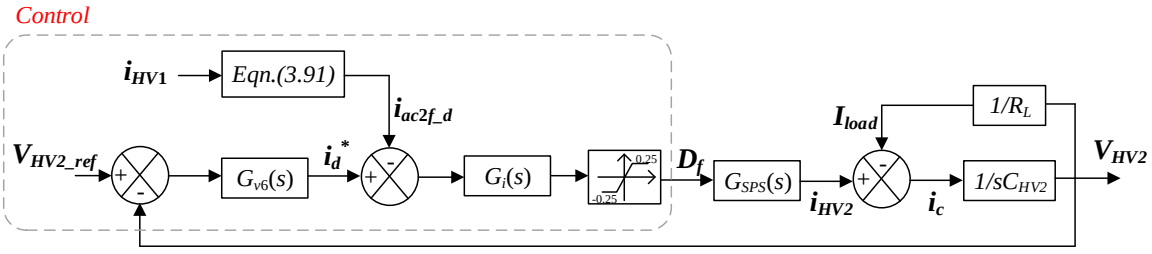


Fig. 3.26 The stationary current control with resistive load R_L [82], [83].

Linearization on the equation (3. 91) is conducted as:

$$G_{vi}(s) = \frac{\partial i_{ac2f_d}}{\partial V_{HV2}} = \frac{\pi}{4 f_s L_p} \overline{D_f} (1 - 2\overline{D_f}) \tag{3. 93}$$

$$G_{di}(s) = \frac{\partial i_{ac2f_d}}{\partial D_f} = \frac{\pi V_{HV2}}{4 f_s L_p} (1 - 4\overline{D_f}) \tag{3. 94}$$

The control block diagram of the stationary current control can be therefore presented as in Fig. 3.27.

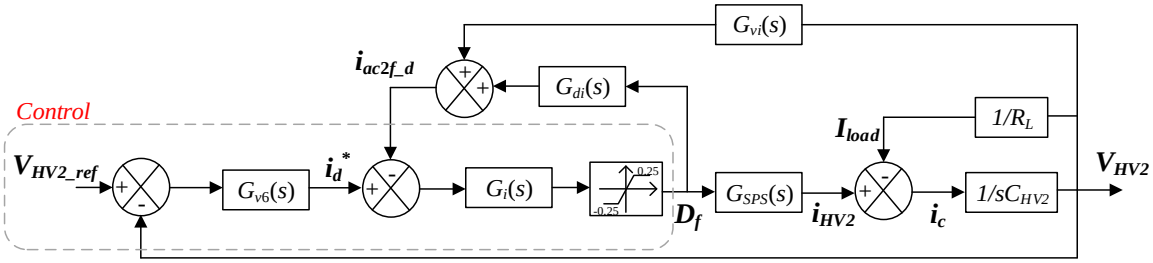


Fig. 3.27 The stationary current control block diagram with resistive load R_L.

It is worth mentioning that Fig. 3.27 shows two non-touching loops. The reference to output transfer function $G_{R2O}(s)$ is therefore derived based on Mason's formular:

$$G_{R2O}(s)=\frac{V_{HV2}}{V_{HV2_ref}}=\frac{G_{v6}(s)G_i(s)G_{SPS}(s)\,{}^{1}\!/_{sC_{HV2}}}{1-[T_1(s)+T_2(s)+T_3(s)+T_4(s)]+T_2(s)T_3(s)} \tag{3.95}$$

, where loop gains are calculated as:

$$T_1(s)=-G_{v6}(s)G_i(s)G_{SPS}(s)\,{}^{1}\!/_{sC_{HV2}} \tag{3.96}$$

$$T_2(s)=-\frac{1}{sC_{HV2}R_L} \tag{3.97}$$

$$T_3(s)=-G_{di}(s)G_i(s) \tag{3.98}$$

$$T_4(s)=-G_{vi}(s)G_i(s)G_{SPS}(s)\,{}^{1}\!/_{sC_{HV2}} \tag{3.99}$$

The output impedance of the DAB with the stationary current control can be derived by replacing the resistive load with current disturbance I_{load} as shown in Fig. 3.28.

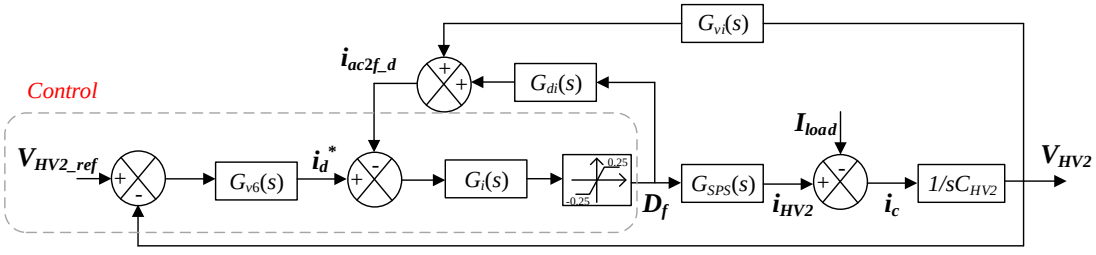
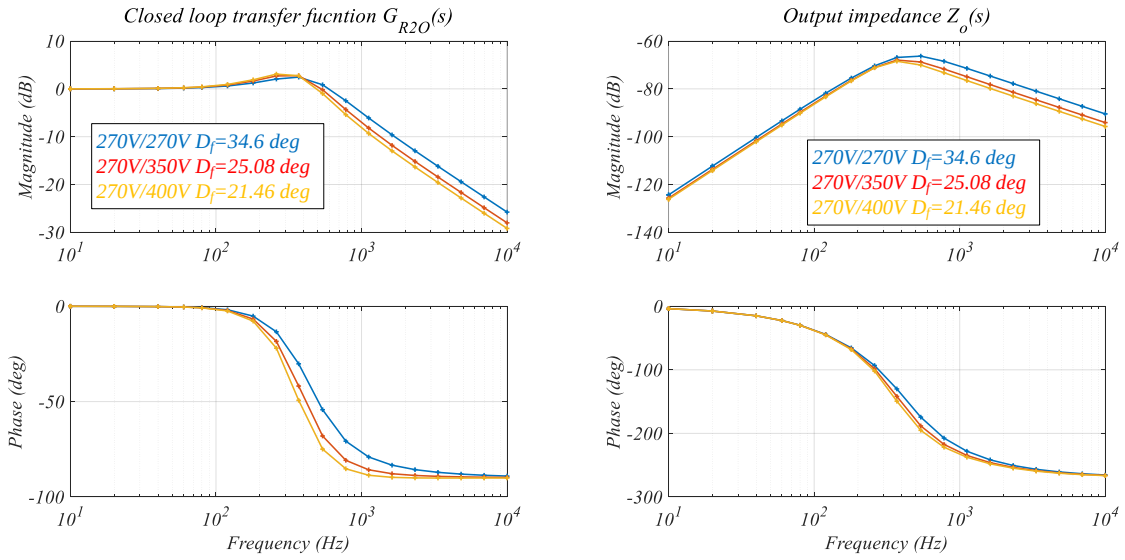


Fig. 3.28 The stationary current control block diagram with load disturbance I_{load}.

The output impedance is calculated as:

$$Z_o(s) = \frac{V_{HV2}}{I_{load}} = \frac{-1/sC_{HV2}}{1-T_1(s)-T_3(s)-T_4(s)} \tag{3. 100}$$

If the outer voltage control parameters for $G_{v6}(s)$ are set as $k_{pv6} = 0.9746$, $k_{iv6} = 2213.8$ to make the crossover frequency at 600Hz for 270V270V 1kW; the inner current control PI parameters for $G_i(s)$ are set as $k_{pi} = 60$, $k_{ii} = 10^5$. Input voltage is 270V while the load voltage varies from 270V to 400V. The load power stays at 1kW. The transfer function expression (3. 95) and output impedance expression (3. 100) are utilized for the plot Fig. 3.29. It is shown in the figure that the plots show smaller changes over terminal voltage variation compared to the FFCC. The inner current control loops T_3 (3. 98) and T_4 (3. 99) help to significantly reduce the output impedance.



(a) (b)

Fig. 3.29 Plot of (a) $G_{R2O}(s)$ and (b) $Z_o(s)$ with the stationary current control under 1kW.

3.4 Linearization control

A linearized control method is proposed by *A. Tong et al.* [84] to eliminate the nonlinear terms in the discrete time circuit model [76], [92], [95]. The control can reduce the sensitivity of system stability to the load condition and reference voltage and help to enlarge the stable margin. In this section, the same control concept has been applied on the reduced order model.

According to Chapter 2 section 2.3.1, the relationship between the phase shift duty and the secondary DC bridge current is:

$$< i_{HV2} >_{T_s} = \frac{V_{HV1}}{f_s L_p} D_f (1 - 2|D_f|) \tag{3. 101}$$

Assuming the voltage PI output is i^*_{HV2}. Similar to the hybrid control, the calculation from i^*_{HV2} to D_f can be derived as:

$$D_f = \begin{cases} \frac{1}{4} - \sqrt{\frac{1}{16} - \frac{f_s L_p < i^*_{HV2} >_{T_s}}{2V_{HV1}}} & i_{HV2} \geq 0 \\ \frac{1}{4} + \sqrt{\frac{1}{16} - \frac{f_s L_p < i^*_{HV2} >_{T_s}}{2V_{HV1}}} & i_{HV2} < 0 \end{cases} \tag{3. 102}$$

The linearization control diagram is shown in Fig. 3.30 where the calculation of the equation (3. 102) is conducted in the control platform.

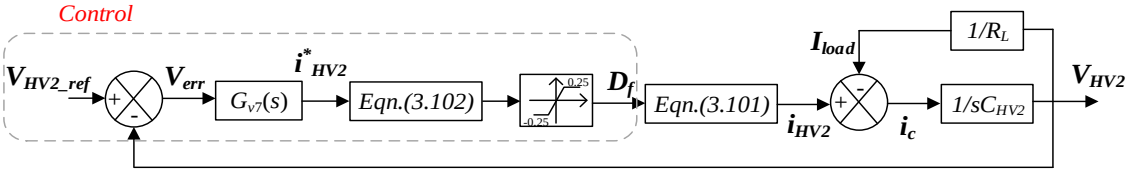


Fig. 3.30 Linearization control diagram with resistive load R_L [84].

Based on the above discussion, if the inductance used in the control equals the practical inductance value and the input terminal voltage sampling is correct, condition $i_{HV2} = i^*_{HV2}$ holds true. The equivalent control block diagram of the linearization control becomes Fig. 3.31.

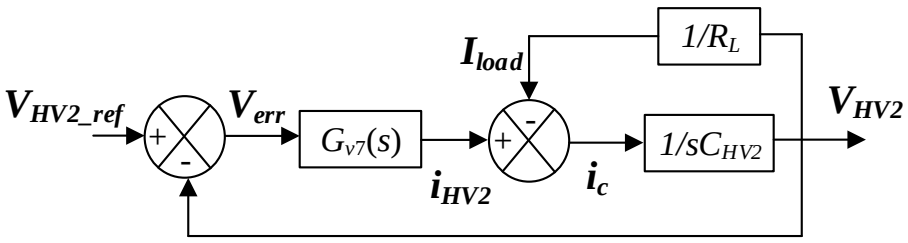


Fig. 3.31 Equivalent linearization control block diagram with resistive load R_L.

Therefore, the reference to the output transfer function $G_{R2O}(s)$ is:

$$G_{R2O}(s)=\frac{V_{HV2}}{V_{HV2_ref}}=\frac{G_{v7}(s)\,{}^{1}\!/\!_{sC_{HV2}}}{1-T_1(s)-T_2(s)} \tag{3. 103}$$

, where the loop gains are calculated as:

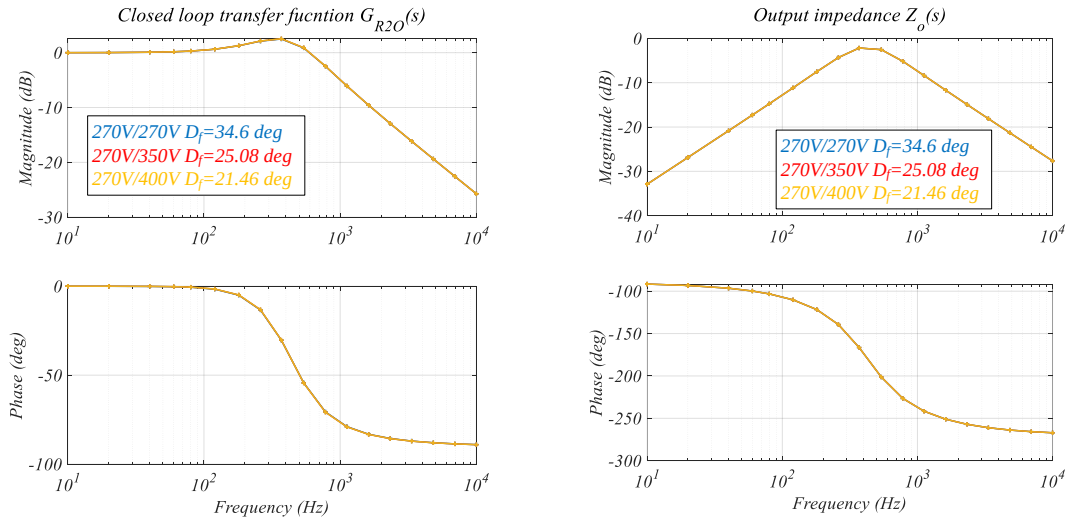
$$T_1(s)=-G_{v7}(s)\,{}^{1}\!/\!_{sC_{HV2}} \tag{3. 104}$$

$$T_2(s)=-\frac{1}{sC_{HV2}R_L} \tag{3. 105}$$

Replace the resistive load R_L with current disturbance I_{load}, and the output impedance $Z_o(s)$ can be calculated as:

$$Z_o(s)=\frac{V_{HV2}}{I_{load}}=\frac{-\,{}^{1}\!/\!_{sC_{HV2}}}{1-T_1(s)} \tag{3. 106}$$

If the voltage control parameters for $G_{v7}(s)$ are set the same as the PI control where k_{pv7} = 1.2468, k_{iv7} = 2.77*10^3, the crossover frequency is 600Hz. The input voltage is 270V while the load voltage varies from 270V to 400V. The load power stays at 1kW. The transfer function expression (3. 103) and output impedance expression (3. 106) are utilized for the plot Fig. 3.32. It is shown in the figure: both $G_{R2O}(s)$ and $Z_o(s)$ do not vary with the change of terminal voltage.



(a) (b)

Fig. 3.32 Plot of (a) $G_{R2O}(s)$ and (b) $Z_o(s)$ with the linearization control under 1kW.

In practice, the inductance L_p can hardly keep consistent with the value in control. Assuming the inductance value in the circuit L_{p_p} is α times larger than the value in control algorithm L_{p_c}:

$$L_{p_p} = \alpha L_{p_c} \tag{3. 107}$$

Therefore, according to (3. 102), the derivative of D_f to i^*_{HV2} is:

$$G_i(s) = \frac{dD_f}{di^*_{HV2}} = \begin{cases} \frac{f_s L_{p_c}}{4V_{HV1}}\left(\frac{1}{16} - \frac{f_s L_{p_c}\overline{i^*_{HV2}}}{2V_{HV1}}\right)^{-\frac{1}{2}} & i^*_{HV2} \geq 0 \\ -\frac{f_s L_{p_c}}{4V_{HV1}}\left(\frac{1}{16} - \frac{f_s L_{p_c}\overline{i^*_{HV2}}}{2V_{HV1}}\right)^{-\frac{1}{2}} & i^*_{HV2} < 0 \end{cases} \tag{3. 108}$$

The equilibrium point value $\overline{i_{HV2}}$ is calculated as:

$$\overline{i^*_{HV2}} = \frac{P}{\overline{V_{HV2}}} \tag{3. 109}$$

The model of the DAB circuit becomes:

$$G_{SPS}(s) = \frac{V_{HV1}(1-4\overline{D_f})}{f_s L_{p_p}} = \frac{V_{HV1}(1-4\overline{D_f})}{\alpha f_s L_{p_c}} \tag{3. 110}$$

The product of $G_i(s)$ and $G_{SPS}(s)$ becomes:

$$G_{SPS}(s)G_i(s) = \frac{(1-4\overline{D_f})}{4\alpha} \frac{1}{\sqrt{\frac{1}{16} - \frac{\overline{D_f}(1-2\overline{D_f})}{2\alpha}}} \neq 1 \quad (\alpha \neq 1) \tag{3. 111}$$

Therefore, the linearization control block diagram is shown in Fig. 3.33.

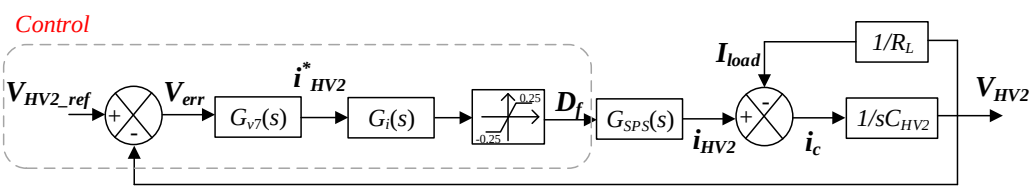


Fig. 3.33 Linearization control block diagram with resistive load R_L [84].

Therefore, the reference to output transfer function $G_{R2O}(s)$ is:

$$G_{R2O}(s)=\frac{V_{HV2}}{V_{HV2_ref}}=\frac{G_{v7}(s)G_i(s)G_{SPS}(s)\,{}^{1}\!/\!_{sC_{HV2}}}{1-T_1(s)-T_2(s)} \tag{3. 112}$$

, where the loop gains are calculated as:

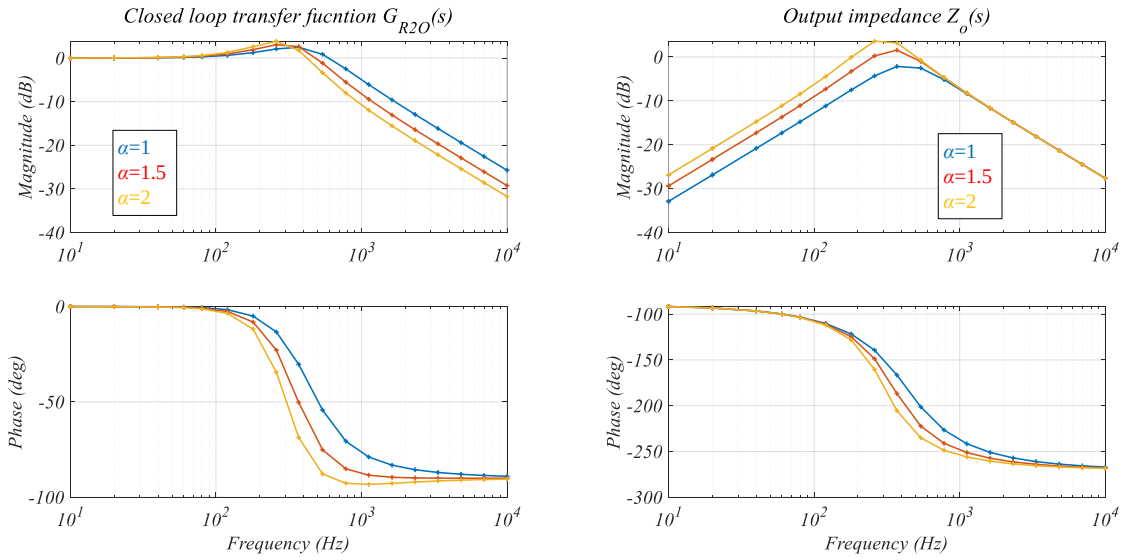
$$T_1(s)=-G_{v7}(s)G_i(s)G_{SPS}(s)\,{}^{1}\!/\!_{sC_{HV2}} \tag{3. 113}$$

$$T_2(s)=-\frac{1}{sC_{HV2}R_L} \tag{3. 114}$$

Replace the resistive load R_L with current disturbance I_{load}, the output impedance $Z_o(s)$ can be calculated as:

$$Z_o(s)=\frac{V_{HV2}}{I_{load}}=\frac{-\,{}^{1}\!/\!_{sC_{HV2}}}{1-T_1(s)} \tag{3. 115}$$

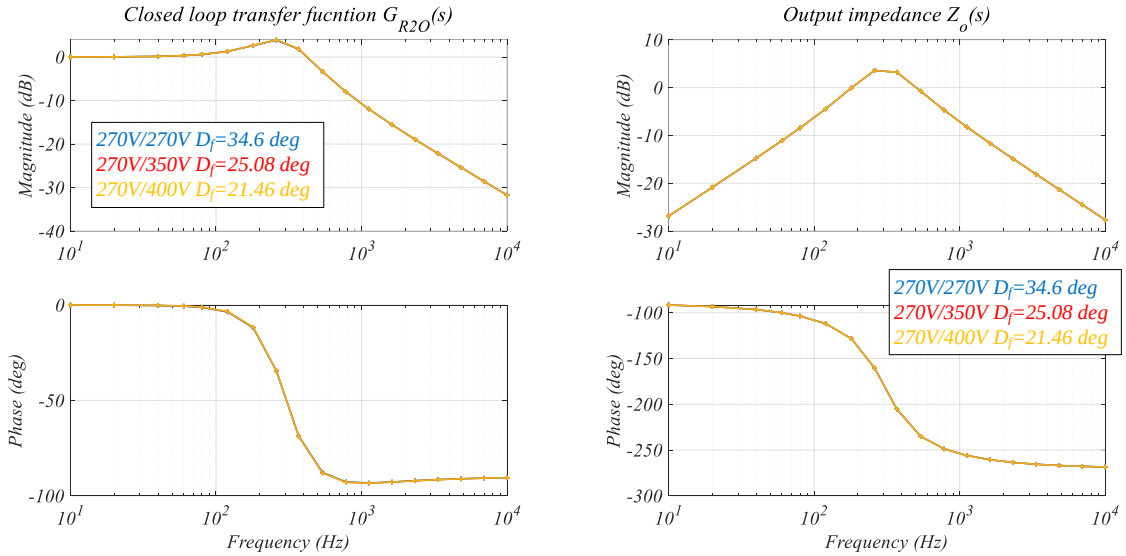
The transfer function expression (3. 112) and output impedance expression (3. 115) are utilized for the plot Fig. 3.34. It is shown in the figure that both $G_{R2O}(s)$ and $Z_o(s)$ are affected by factor α.



(a) (b)

Fig. 3.34 Plot of (a) $G_{R2O}(s)$ and (b) $Z_o(s)$ with the linearization control under 270V/270V 1kW.

Yet with a large difference between L_{p_c} and L_{p_p} (α equals to 2), both $G_{R2O}(s)$ and $Z_o(s)$ can still keep their shape with different terminal voltages as shown in Fig. 3.35. This feature makes linearization control attractive for applications where the terminal voltages vary constantly.



(a) (b)

Fig. 3.35 Plot of (a) $G_{R2O}(s)$ and (b) $Z_o(s)$ with the linearization control under 270V/270V 1kW and α=2.

3.5 Sliding mode control

Small-signal models and analysis have been widely used in power electronics for the assessment of stability. However, they fail to predict the stability of some converters in presence of large transients. Worse still, the small-signal model fails to reveal any stability information of the converter over the entire operating region [97]. In works [98], [99], it is shown that even though stable operation is concluded from the small-signal analysis, the system can still be unstable. The main advantage of a system with sliding mode control characteristics is that it has guaranteed stability and robustness against parameter uncertainties [100].

The sliding mode control has been applied in the DAB converter in [85] based on the average model and in [86] based on the reduced order model. It has been addressed in [92] that the reduced order model presents reasonably good accuracy to the practical full order switching

model. Therefore, the sliding model control is introduced with the reduced order model in this section. In general, assuming the dynamic equation of a system is:

$$\frac{dx}{dt} = f + g \cdot u \tag{3. 116}$$

, where x is the state variable. f and g are functions of x. u is the discontinuous control action expressed as:

$$u = \begin{cases} U^{+} & if \;\; S(x,t) > 0 \\ U^{-} & if \;\; S(x,t) < 0 \end{cases} \tag{3. 117}$$

, where U^{+} and U^{-} are either scalar values or scalar functions of x. $S(x,t)$, usually called the sliding surface, is the instantaneous feedback tracking trajectory of the system and is a predetermined function of the state variable [97]. Typically, $S(x,t)$ is chosen as a linear combination of the weighted values of the state variables, as given as:

$$S(x,t) = \sum_{i=1}^{m} \alpha_i x_i \tag{3. 118}$$

The ideal sliding mode action described in (3. 117) is similar to the on and off bang-bang control [101]–[103] which results in high-frequency oscillation/chattering within the vicinity of the sliding surface while moving towards the origin. Alternatively, equivalent control has been used to replace (3. 117). The equivalent control action u_{eq} is obtained by solving (3. 119. This is called the invariance condition [97].

$$\frac{dS(x,t)}{dt} = 0 \tag{3. 119}$$

The difference between the ideal sliding mode control and the equivalent sliding mode control resembles that of the finite control set - model predictive control [42], [104]–[106] and the continuous control set - model predictive control [107]–[109]. The steady state error that occurs with the ideal sliding mode control (3. 117) can be minimized by comprising an integral term of the state variable into the sliding surface [110]. This approach is called integral sliding mode control. However, the integral sliding mode control becomes less effective when the equivalent

control action is implemented [111]. Therefore, *S. C. Tan et al.* [112] proposed an additional double-integral term of the state variables for construction of the sliding surface when the equivalent sliding mode control is utilized. In the DAB converter, state variables are chosen to be:

$$x = [x_1, x_2, x_3]^T = [V_{err}, \int_0^t V_{err} dt, \int_0^t x_2 dt]^T \tag{3. 120}$$

, where V_{err} is the error between the load voltage reference and the load voltage:

$$V_{err} = V_{HV2_ref} - V_{HV2} \tag{3. 121}$$

According to Fig. 3.1, the state equation can be written as:

$$\frac{dV_{HV2}}{dt} = -\frac{V_{HV2}}{C_{HV2} R_L} + \frac{V_{HV1}}{C_{HV2} f_s L_p} D_f (1 - 2|D_f|) \tag{3. 122}$$

According to the double integration approach [112], the sliding surface is therefore constructed as:

$$S(x,t) = \sum_{i=1}^{3} \alpha_i x_i \tag{3. 123}$$

According to the invariance condition (3. 119), the equivalent control law can be derived as:

$$D_f = \begin{cases} \frac{1}{4} - \sqrt{\frac{1}{16} - \frac{f_s L_p I_{SM}}{2V_{HV1}}} & I_{SM} \geq 0 \\ \frac{1}{4} + \sqrt{\frac{1}{16} - \frac{f_s L_p I_{SM}}{2V_{HV1}}} & I_{SM} < 0 \end{cases} \tag{3. 124}$$

, where

$$I_{SM} = \frac{V_{HV2}}{R_L} + C_{HV2} \frac{\alpha_2}{\alpha_1} V_{err} + C_{HV2} \frac{\alpha_3}{\alpha_1} \int_0^t V_{err} dt \tag{3. 125}$$

Compared with (3. 102), it can be concluded that I_{SM} is the virtual current generated by (3. 125). Based on (3. 124) and (3. 125), the control diagram is as shown in:

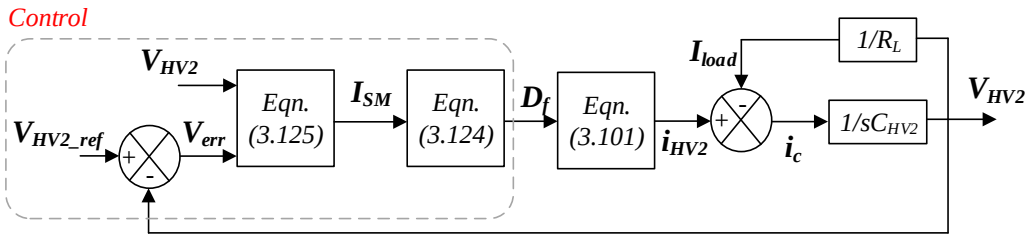


Fig. 3.36 Double integral sliding mode control diagram with resistive load R_L [86].

In order to carry out a fair comparison with other control methods mentioned in the chapter, the sliding mode control discussed above is linearized. For unidirectional power flow, small signal models are derived:

$$G_{di}(s)=\frac{dD_f}{dI_{SM}}=\frac{1}{\sqrt{\frac{1}{16}-\frac{f_s L_p \overline{I_{SM}}}{2\overline{V_{HV1}}}}}\frac{f_s L_p}{4\overline{V_{HV1}}} \tag{3. 126}$$

, where

$$\overline{I_{SM}}=\frac{P}{\overline{V_{HV2}}} \tag{3. 127}$$

According to (3. 126) and (3. 2), condition (3. 128) holds true if the inductance L_p can keep consistent with the value in control.

$$G_{di}(s)G_{SPS}(s)=1 \tag{3. 128}$$

The control block diagram is therefore shown in Fig. 3.37 where k_{i8} and k_{p8} equals to $C_{HV2}\alpha_3/\alpha_1$ and $C_{HV2}\alpha_2/\alpha_1$.

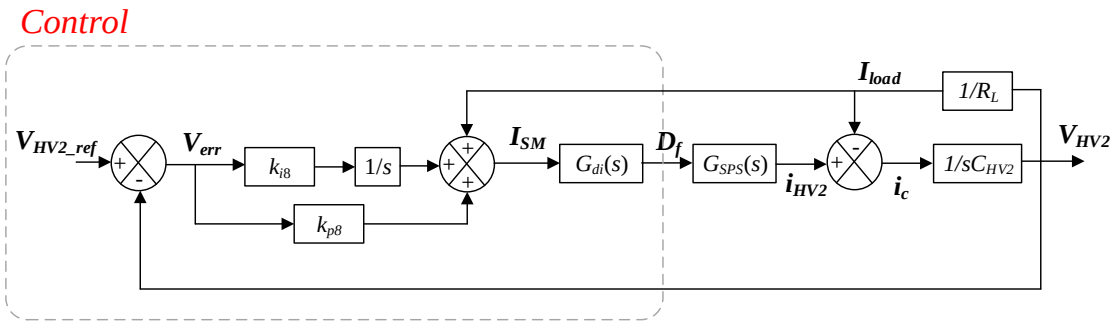


Fig. 3.37 Double integral sliding mode control block diagram with resistive load R_L.

The control to output transfer function $G_{R2O}(s)$ is derived as:

$$G_{R2O}(s)=\frac{V_{HV2}}{V_{HV2_ref}}=\frac{G_{di}(s)G_{SPS}(s)\,1/sC_{HV2}\,(k_{p8}+\frac{k_{i8}}{s})}{1-T_1(s)-T_2(s)-T_3(s)-T_4(s)} \tag{3. 129}$$

, where the loop gains are calculated as:

$$T_1(s)=-k_{p8}G_{di}(s)G_{SPS}(s)\,1/sC_{HV2} \tag{3. 130}$$

$$T_2(s)=-k_{i8}G_{di}(s)G_{SPS}(s)\,1/s^2C_{HV2} \tag{3. 131}$$

$$T_3(s)=G_{di}(s)G_{SPS}(s)\,1/sC_{HV2}R_L=1/sC_{HV2}R_L \tag{3. 132}$$

$$T_4(s)=-\frac{1}{sC_{HV2}R_L} \tag{3. 133}$$

Replacing the resistive load R_L with current disturbance I_{load}, the control block diagram becomes Fig. 3.38.

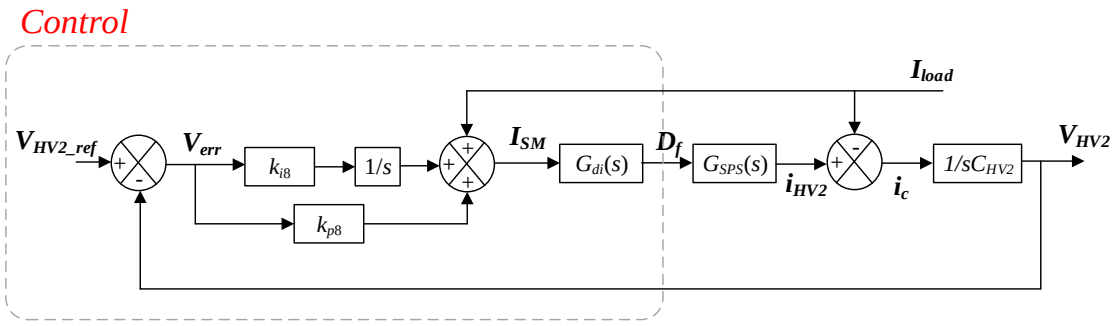


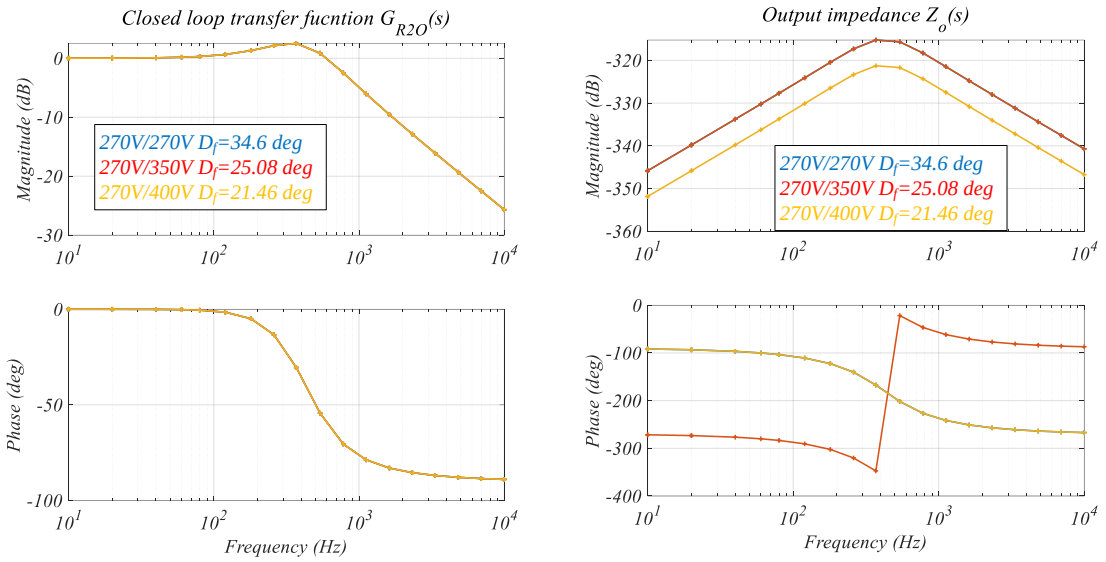
Fig. 3.38 Double integral sliding mode control block diagram with load current disturbance I_{load}.

The output impedance $Z_o(s)$ can be calculated as:

$$Z_o(s)=\frac{V_{HV2}}{I_{load}}=\frac{(G_{di}(s)G_{SPS}(s)-1)\,1/sC_{HV2}}{1-T_1(s)-T_2(s)} \tag{3. 134}$$

It can be concluded that $Z_o(s)$ is ideally zero. The sliding mdoe becomes similar to the hybrid control described in section 3.2.1. Set the control parameters k_{p8} and k_{i8} to 1.2537, 2.7287*10^3, respectively to make the crossover frequency at 600Hz for 270V/270V 1kW. The transfer

function expression (3. 129) and output impedance expression (3. 134) are utilized for the plot Fig. 3.39. It can be seen from Fig. 3.39 that both $G_{R2O}(s)$ and $Z_o(s)$ do not change with load voltage. However, when (3. 128) is not satisfied the same as the hybrid control and Linearization control, the output impedance cannot be constant from load voltage variations. This phenomena has been addressed in section 3.2.1 and 3.4. Therefore, it is omitted here.



(a) (b)

Fig. 3.39 Plot of (a) $G_{R2O}(s)$ and (b) $Z_o(s)$ with the double integral sliding mode control under 1kW.

3.6 Model predictive control

Model predictive control is often considered in power electronics converters for several advantages it can provide, such as fast dynamics, easy inclusion of constraints, and simple digital implementation. In particular, Finite-Control-Set Model-Predictive-Control (FCS-MPC) has been investigated in AC power conversion [113]–[115]. In contrast, the application of model predictive control in DC/DC power converters has not been so intensively reported.

A Finite-Control-Set Model Predictive Control (FCS-MPC) has been proposed in the boost converter by *P. Karamanakos et al.* [41] and *B. Wang et al.* [42] to enhance the dynamic performance. However, these approaches resulted in variable switching frequency and larger inductor current ripples than a conventional method. Moreover, it demanded heavy computational burdens. In contrast, *F. M. Oettmeier et al.* [109] proposed a Continuous-

Control-Set Model-Predictive-Control (CCS-MPC) in a boost converter, which featured fixed switching frequency and fast transition. However, it is hard to include multiple-control objectives and constraints in this control. *P. Akter et al.* [116] presented a MPC for the bidirectional isolated DC-DC converters which were operated at 100kHz switching frequency with only 4kHz nominal transformer current. This fell into the category of application of MPC in AC power conversions [113] where switching frequency was much higher than fundamental current. In this thesis, the control approach is investigated for DAB converters operating with a transformer current frequency, equal to the switching devices. The authors in [62] include switching losses and transformer current Root-Mean-Square (RMS) value into the cost function, which is evaluated for different modulation techniques. This approach can optimize operating efficiency, but it relies still on conventional PI controller for load voltage regulation. To the best knowledge of the author, there is no existing work that successfully applies MPC in DAB conveters to date.

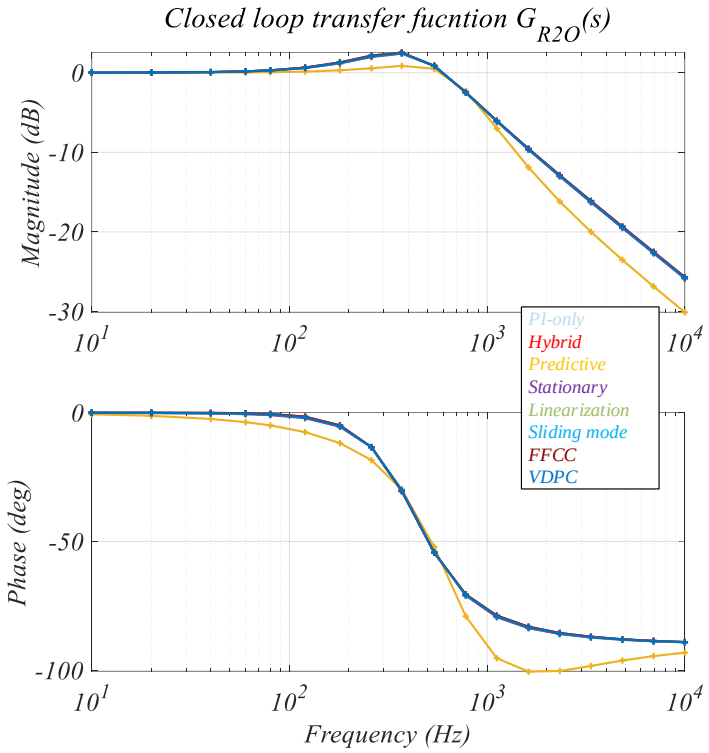
3.7 Comparisons of control methods

In this section, the control methods described in section 3.1-3.5 are compared. The common design rule for all the mentioned controllers are to achieve 600Hz crossover frequency. The control parameters are summerized in Table 3.2.

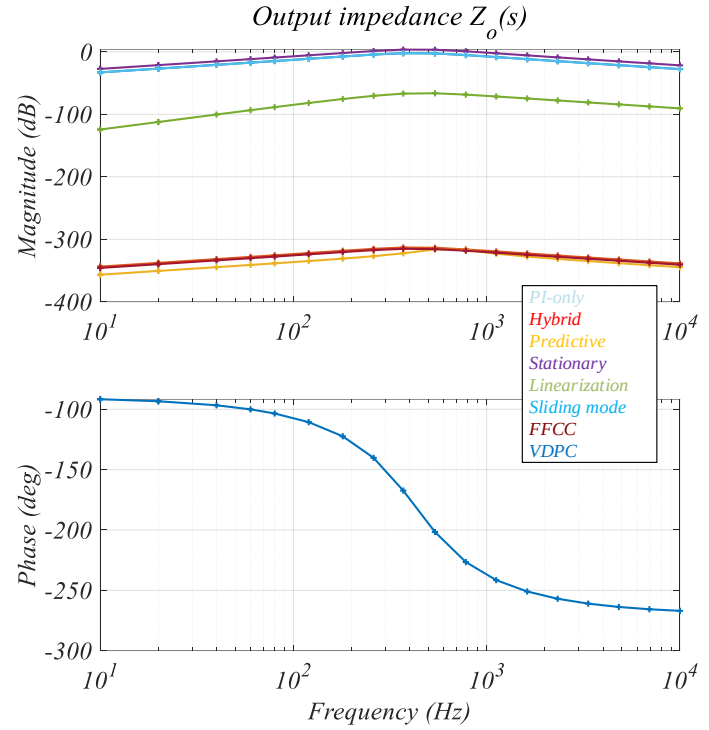
TABLE 3.2 CONTROL PARAMETERS WITH THE SAME CROSSOVER FREQUENCY @ 600HZ

Type	Control parameters
PI[78]	k_{p1}=0.0425, k_{i1}=94.4536
Hybrid [73]	k_{p2}=0.0427, k_{i2}=92.9285
VDPC [79]	k_{p3}=511.6613, k_{i3}=1.1629*10^6
FFCC [80]	k_{p4}=1.2135, k_{i4}=9.8083*10^3
Predictive [81]	k_{p5}=1.9923, k_{i5}=4.7227*10^3
Stationary[6]	k_{p6}=0.9746, k_{i6}=2.2138*10^3
Linearization[84]	k_{p7}=1.2468, k_{i7}=2.7735*10^3
SM [86]	k_{p8}=1.2537, k_{i8}=2.7287*10^3

The Reference to output transfer function $G_{R2O}(s)$ and the output impedance $Z_o(s)$ are compared in Fig. 3.40 where the inductances are kept the same both in control and hardware.



(a)



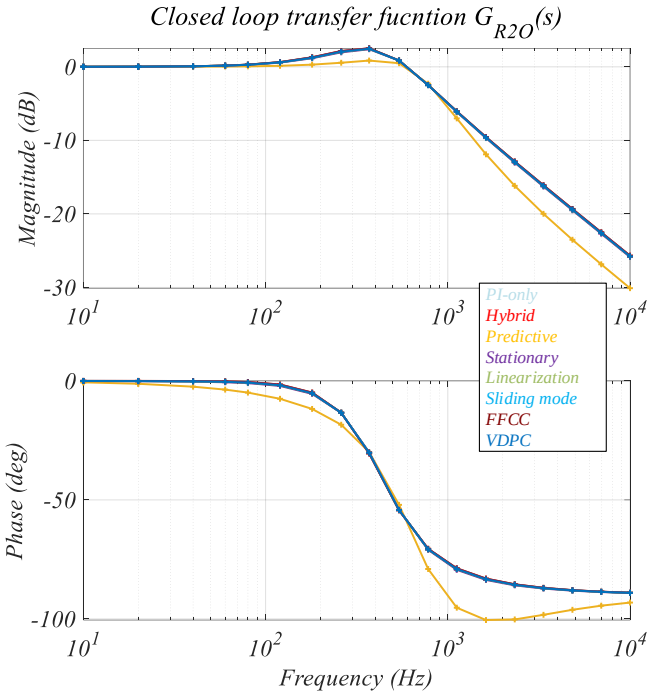
(b)

Fig. 3.40 Plot of (a) $G_{R2O}(s)$ and (b) $Z_o(s)$ under 270V/270V 1kW with consistant inductance in control and circuit.

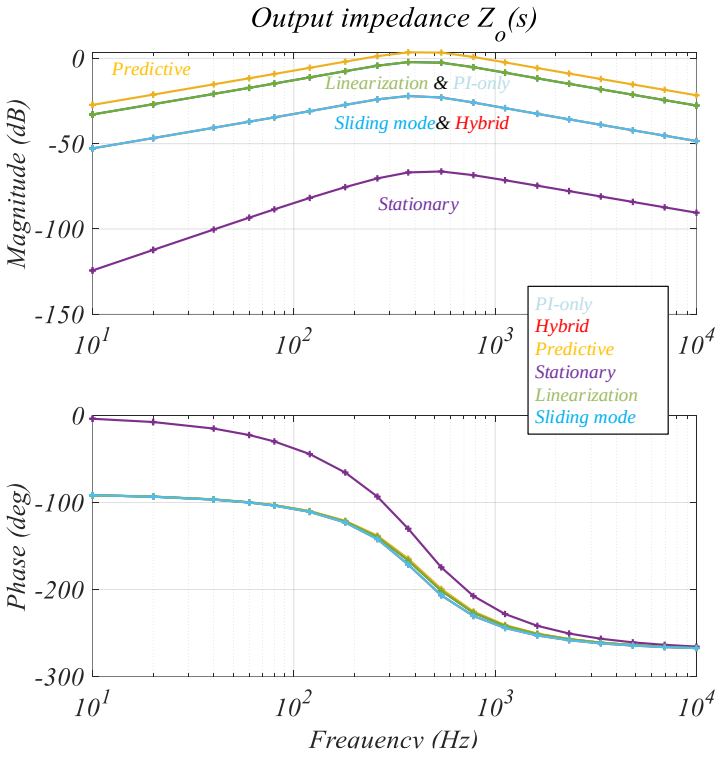
When the inductance in control is 10% larger than the hardware parameter, plots are shown below in Fig. 3.41. Note that VDPC and FFCC are not included for the plot of impenace as they remain ideally zero.

Four aspects have been looked into when comparing those control methods. The regulation describes the ability to reject load disturbance; $V\&P$ and L_p robustness describes the ability to maintain the performance with varying terminal voltage, power and the circuit parameter. Simplicity considers both control algorithm and hardware implementation difficulty.

The PI only control approach shows medium dynamic performance, however, it is the simplest and the most applied approach in practice. The hybrid control, VDPC and FFCC approaches show ideally zero output impedance indicating excellent load voltage regulation in presence of load disturbance. However, their performance are deteriorated under the conditions when L_p, power and voltage ratio vary in hybrid, VDPC and FFCC, respectively. Alternatively, the predictive control shows robust performance over voltage and circuit parameter variation. The drawback for the predictive control is the implementation complexity, the demand for fast computation and bad load disturbance rejection performance. The stationary control are easy to implement while also presenting medium regulation performance and robustness. The sliding mode control can ensure global stability in theory and provide excenllent disturbance rejection when the value L_p is accuate in the algorithm. The linearization control shows robustness with varying power and terminal voltages.



(a)



(b)

Fig. 3.41 Plot of (a) $G_{R2O}(s)$ and (b) $Z_o(s)$ under 270V/270V 1kW with inductance in control 10% larger than in hardware circuit.

The remarks on the mentioned control methods have been summarized in Table 3.3. Since all the controls are designed to have the same crossover frequency, the comparisons are mainly on the output impedance. Regulation is assessed by comparing the output impedance curve. Robustness is assessed by evaluating the variations of output impedance in presence of parameter changes.

In the application for the DAB converter control in the DC distribution system, multiple control objectives are required including the converter stability control, efficiency enhancement and system stabilization. However, none of the control methods mentioned above can easily incorporate theses control objectives.

TABLE 3.3 SUMMARY OF THE CONTROL METHODS IN DAB

Type	Regulation	Robustness		Simplicity	Preferable application
		V&P	L_p		
PI[78]	Low	Medium	Medium	High	Low requirement on dynamics
Hybrid [73]	High	Medium	Low	Medium	Constant permeability core
VDPC [79]	High	Low	High	Medium	Constant power
FFCC [80]	High	Low	High	Low	Fixed terminal voltage
Predictive [81]	Low	High	High	Low	Robust operation
Stationary[6]	Medium	Medium	Medium	Medium	Medium requirement on dynamics
Linearization[84]	Low	High	Medium	High	Voltage/Power variation
SM [86]	High	Medium	Low	High	Large signal stability

3.8 Chapter summary

In this chapter, an indepth literature review on the control methods of DAB converters has been provided. Existing control methods found in the literatures including feedback control, feedforward control, transformer current control, linearization control and sliding mode control are investigated.

The PI-only control is the most widely used control. It can generally satisfy most of the applications. One of the problems with the PI control is its medium robustness against terminal voltages, power and circuit parameter variations. Moreover, the load regulation performance with the PI controller is relatively low. In order to improve the dynamic performance, a so-called hybrid control has been introduced. The hybrid control employs a load current feedforward structure which drastically improve the dynamic performance. Ideally, the output impedance with the hybrid control is zero. However, when the circuit parameter in the practical

converter does not agree with the value used in the algorithm, the peroformance of the hybrid control gets deteriorated. Therefore, another approach VDPC has been presented to address the rubustness issue with circuit parameter in hybrid control. In the VDPC, all the calculations have avoided using the value of the power transfer inductance, resulting in excellent robustness againt circuit parameter variation. Unfortunately, this feature of VDPC comes at the price of low robustness again the power variation. Similarly, FFCC tried to address the same issue that happends in hybrid control by involving the transformer current. The analysis results have shown that FFCC presents good rubustnees against the variations of circuit parameter and power but not with varying terminal voltages. Eventually, the final solution with respect to the overall robustness against the variations of terminal voltage, power and ciruit parameter has been discussed. The method is called the predictive current control. The major drawback of the predictive control is the relatively bad load regulation performace and complexity in implementation. The stationary current control adopted a cascaded control structure which results in a good trade-off for all aspects. Linearization control is preferable in the application for its rubustness in variant terminal voltages and power. The sliding mode control is similar to the hybrid control in terms of performance, but ganrantees large signal stability.

Chapter 4 Mono-dimensional MDCS-MPC

The control of TPS is barely addressed in the existing literature due to its complexity. There are many different operating modes associated with TPS as illustrated in Chapter 2. Each operating mode has a different small signal model, which requires the linear controllers to be designed and tuned with a large number of equilibrium points. Otherwise the performance will deteriorate. Therefore, it is challenging to maintain good performance throughout the terminal voltage and power range with conventional linear controllers for TPS. To address the above issue, in this chapter, a mono-dimensional Moving Discretized Control Set – Model Predictive Control (MDCS-MPC) tailored for DAB converters is introduced. The MDCS-MPC is inspired by the well-known Finite Control Set – Model Predictive Control (FCS-MPC) [113]–[115]. In comparison with FCS-MPC, MDCS-MPC utilizes discretised active duties or the phase shift duty rather than voltage vectors.

The mono-dimensional MDCS-MPC has only one control output. Since SPS has only one control variable, as discussed in Chapter 2 section 2.3, it is feasible to apply the mono-dimensional MDCS-MPC in SPS. However, when TPS is considered, there are three independent control variables as discussed in Chapter 2 section 2.4. The number of control variables in TPS can be reduced down to one by carrying out the offline optimization described in Chapter 2 section 2.4.2. The mono-dimensional MDCS-MPC can then be applied with offline optimized TPS. The proposed MDCS-MPC has the merits listed as follow:

- Circuit parameters, terminal voltages and operating modes of TPS are embedded in the prediction model. Therefore, control parameters designed for MDCS-MPC can maintain good performance throughout the power and terminal voltage range.
- The proposed approach enables flexible multi-objective optimization. Detailed exploration of this feature is going to be addressed in Chapter 6.
- Large signal stability can be guaranteed with the introduced mono-dimensional MDCS-MPC.

- Compared with previous applications of FSC-MPC in DC-DC converters [41], [42], MDCS-MPC utilizes only two prediction horizons and a small number of calculating points in each switching period. Therefore, the computational burden is relatively low.

In this chapter, the MDCS-MPC has been applied on both SPS and TPS. In section 4.1, the mono-dimensional MDCS-MPC is introduced. The large signal stability and small signal analysis are provided in section 4.2 and 4.3, respectively. Finally, the practical results are given.

4.1 Control introduction

The term model predictive control designates an ample range of controls that use the models of a plant to obtain the optimal control output by minimizing the cost function. The MDCS-MPC belongs to the model predictive control family and obeys the same operating principle. Therefore, the introduction of the mono-dimensional MDCS-MPC starts with the derivation of the discretised model of both SPS and TPS.

4.1.1 Discretized model

The MDCS-MPC functions are based on the utilization of average models. It has been demonstrated in Chapter 2 section 2.5 that the reduced order average model of DAB shown in Fig. 4.1 presents a good compromise between simplicity and accuracy.

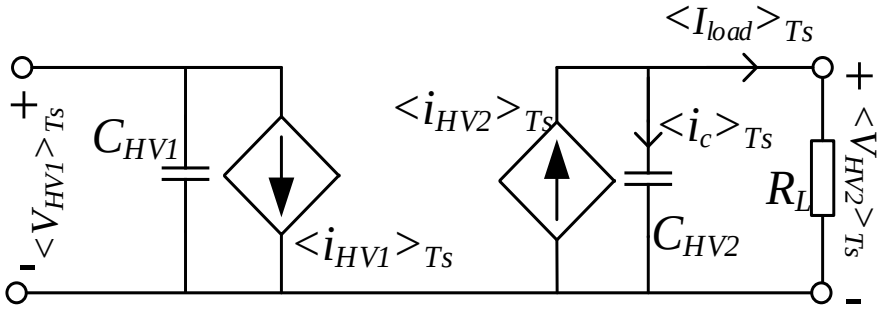
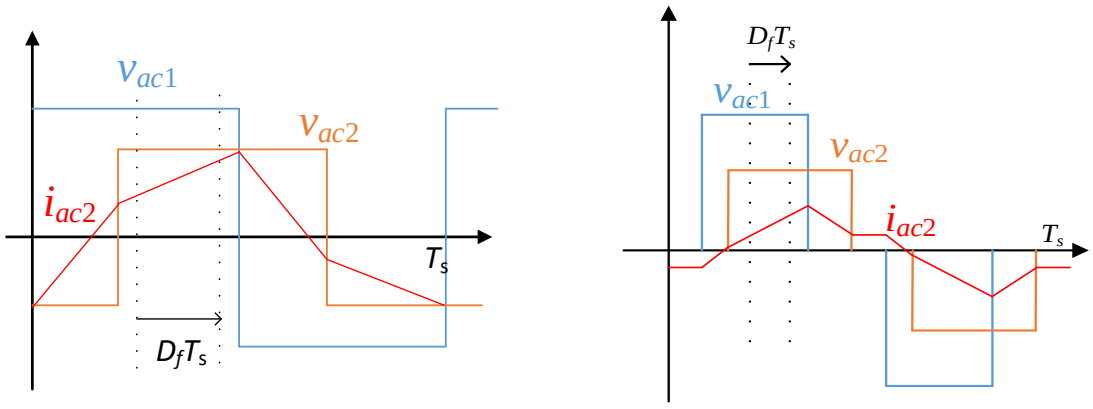


Fig. 4.1 The reduced order model of the DAB.

Therefore, this average model is utilized in this chapter for mono-dimensional MDCS-MPC. In this section, the models of DAB connected with resistive loads are derived for both SPS and

TPS. The same approach also applies to the scenario where DAB is connected with other types of load. Typical waveforms of SPS and TPS are as in Fig. 4.2.



(a) SPS (b) TPS

Fig. 4.2 Generic waveforms of SPS and TPS.

According to the reduced order model in Fig. 4.1, the differential equation of the output voltage is developed as follow:

$$C_{HV2}\frac{d<V_{HV2}>_{Ts}}{dt}=<i_{HV2}>_{Ts}-<I_{load}>_{Ts} \tag{4. 1}$$

Discretizing (4. 1) using forward approximation yields:

$$V_{HV2}[k+1]=\frac{i_{HV2}[k]-I_{load}[\mathrm{k}]}{C_{HV2}f_s}+V_{HV2}[k] \tag{4. 2}$$

Assuming load current does not vary in two sampling periods:

$$I_{load}[k]=I_{load}[k+1]=I_{load}[k+2] \tag{4. 3}$$

The prediction for output voltage at time instance k+2 is:

$$V_{HV2}[k+2]=\frac{i_{HV2}[k+1]-I_{load}[\mathrm{k}]}{C_{HV2}f_s}+V_{HV2}[k+1] \tag{4. 4}$$

Substituting $V_{HV2}[k+1]$ in (4. 2) to (4. 4), yields

$$V_{HV2}[k+2]=\frac{i_{HV2}[k+1]-I_{load}[\mathrm{k}]}{C_{HV2}f_s}+V_{HV2}[k+1] \tag{4. 5}$$

According to Chapter 2 section 2.3.1, the power expression of SPS is:

$$P_{SPS} = \frac{< V_{HV1} >_{T_s} < V_{HV2} >_{T_s}}{f_s L_p} D_f (1 - 2|D_f|) \tag{4. 6}$$

Therefore, the controlled current $< i_{HV2} >_{Ts}$ of SPS is calculated as:

$$< i_{HV2} >_{T_s} = \frac{P_{SPS}}{< V_{HV2} >_{T_s}} = \frac{< V_{HV1} >_{T_s}}{f_s L_p} D_f (1 - 2|D_f|) \tag{4. 7}$$

According to Chapter 2 section 2.5.1, when TPS is applied, $i_{HV2}[k]$ can be found in Table 4.1.

TABLE 4.1 THE CONTROLLED CURRENT IN THE REDUCED ORDER MODEL WITH TPS

Mode	$<i_{HV2}>_{Ts}$
I	$\frac{32MD_f^{\,2}}{1-M}$
II	$\frac{-8(M^2+1)D_f^{\,2} + 4(2M^2 - M + 1)D_f - (M-1)^2}{M^2}$
III	$\frac{32D_f^{\,2}}{M-1}$
IV	$-16(M^2 - 2M + 2)D_f^{\,2} + 8(M^2 - 2M + 2)D_f - (M-1)^2$

In order to evaluate how realistic the assumption made in (4. 3) is, and how accurate the prediction in (4. 5) is, the prediction error has been defined in (4. 8) as an esteem indicator.

$$V_e = |V_{HV2}[k+2] - V_{HV2_s}[k+2]| \tag{4. 8}$$

, where $V_{HV2_s}[k+2]$ is the sampled load voltage at time instance $k+2$. A sinusoidal controlled current source is connected to the load terminal with a fixed amplitude but varying frequency as shown in Fig. 4.3. Circuit parameters are listed in Chapter 2 section 2.7.

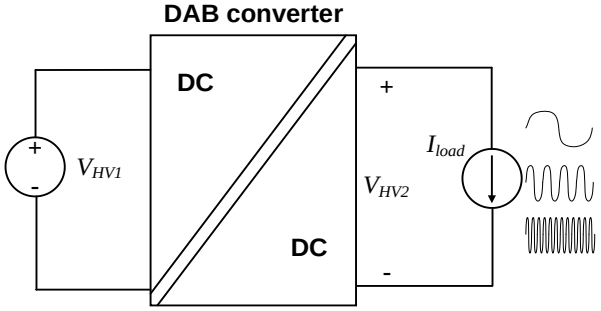


Fig. 4.3 Prediction error assessment circuit

In (4. 3), the load current is assumed to be constant within two sampling periods. Therefore, when the load current changes slowly, this assumption is more likely to hold true. Results shown in Fig. 4.4 have verified this statement. When the load current has a frequency of 1kHz, the maximum prediction error is 0.293V. With the decreasing of the frequency down to 10Hz, the maximum prediction error is reduced to 0.008V. The error in the prediction will not necessarily cause problems. Since 1kHz is already above the bandwidth, 0.293V error is only 0.09% of rated voltage. Therefore, the assumption made in (4. 3) has been deemed reasonable in our study.

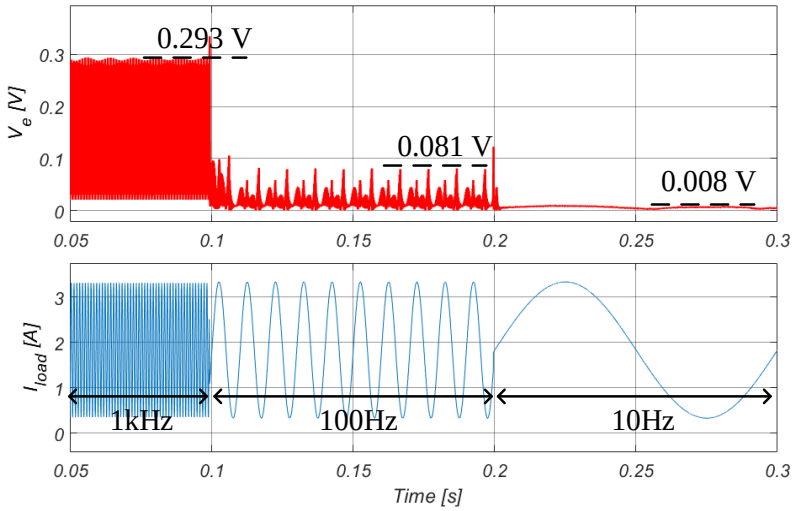


Fig. 4.4 Voltage prediction error evaluation.

4.1.2 Operating principle

Taking into account the computational delay, the MDCS-MPC has a prediction step of two sampling periods. A preliminary cost function is proposed as in (4. 9) with the only purpose of regulating the voltage V_{HV2} to reference V_{HV2_ref}. It is worth mentioning that (4. 9) is not the finalized cost function, but a first step meant to help illustrate the operating principle of the mono-dimensional MDCS-MPC.

$$ct = (V_{HV2_ref} - V_{HV2}[k+2])^2 \tag{4. 9}$$

The control variable D_f is continuous in nature. However, in digital control, D_f needs to be discretized. The discretization precision is subjected to the control platform applied. Δ_f is defined (4. 10) as the smallest phase shift value that can be achieved in a digital control platform.

$$\Delta_f = \frac{f_s}{f_c} \tag{4. 10}$$

Fig. 4.5 presents the generation of the PWM signals in the digital control platform, where f_c is the peripheral clock frequency of the digital control platform.

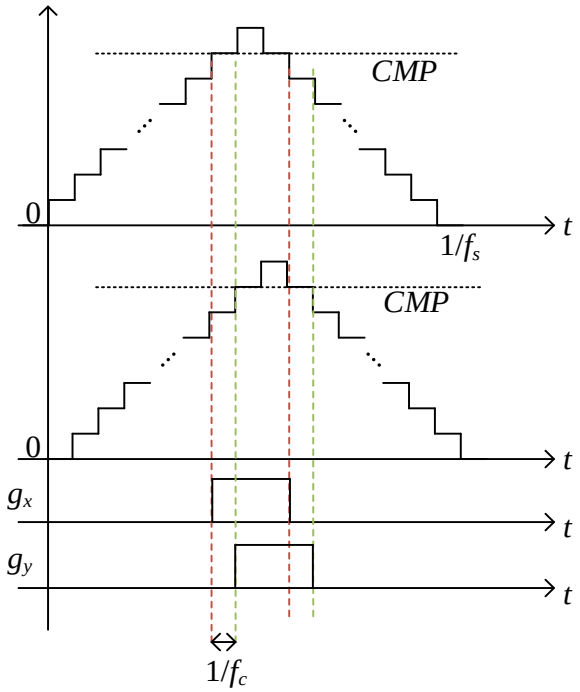


Fig. 4.5 Demonstration of the smallest phase shift value in PWM modules.

For unidirectional power flow, DAB works predominately in the range:

$$D_f \in [0, 0.25] \tag{4. 11}$$

(4. 11) is further discretized into μ_m (=0.25/Δ_f+1) elements as described in array (4. 12).

$$D_f \in \{0, \Delta_f, 2\Delta_f, \cdots, 0.25\} \tag{4. 12}$$

In order to implement a control algorithm that is feasible on standard commercial microcontrollers, the proposed MDCS-MPC evaluates a reduced number of values in each sampling period. In one sampling period, μ ($\mu \leq \mu_m$) number of points are assessed. They are centred at the previous working point.

An intuitive illustration of the proposed MDCS-MPC is depicted in Fig. 4.6. In the control interval k to k+1, μ=3 points are evaluated centred at the previous working point $D_f[k] = a$.

When $D_f[k+1]$ equals to a-Δ_f, a and a+Δ_f, the output voltage V_{HV2} is predicted as $V_{HV2}^{(1)}[k+2]$, $V_{HV2}^{(2)}[k+2]$ and $V_{HV2}^{(3)}[k+2]$. The superscript represents the index of an element in the moving discretized control set.

The moving discretized control set during the period k to $k+1$ is $\{a$-Δ_f, a, a+$\Delta_f\}$. According to the illustration in Fig. 4.6, when $D_f[k+1]= a+\Delta_f$, the predicted output voltage $V_{HV2}^{(3)}[k+2]$ is the closest to V_{HV2_ref}. This results in the smallest cost function defined in (4. 9). Therefore, the value $a+\Delta_f$ is applied at time instance $k+1$ to D_f. In the next control interval, the same process is repeated. However, the moving discretized control set has changed. It has become $\{a, a+\Delta_f, a+2\Delta_f\}$. The control set is moving with the working point within the domain of (4. 12). In this control interval, $D_f[k+3] = a$ results in the smallest cost function. Therefore, this value is applied at the time instance $k+2$. This process continues.

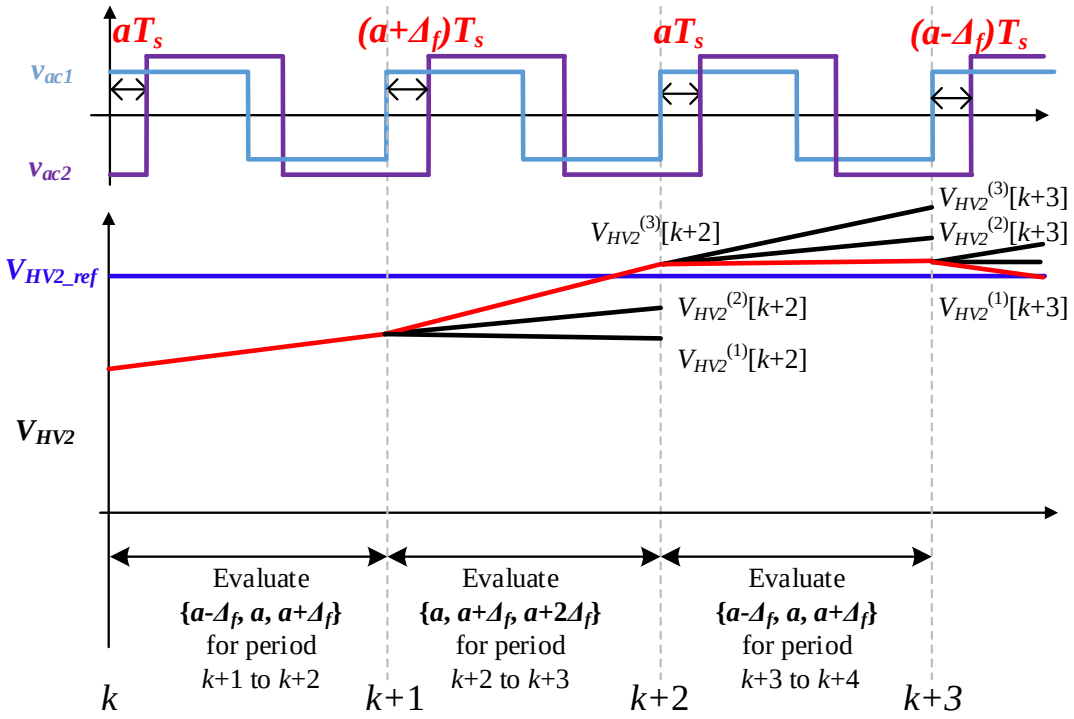
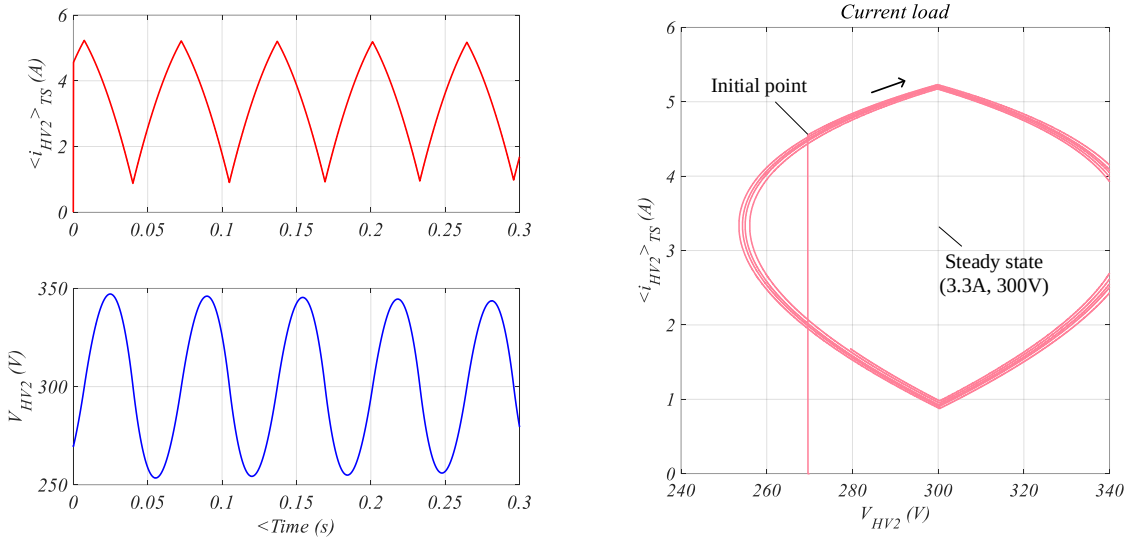


Fig. 4.6The operating principle of the mono-dimensional MDCS-MPC for DAB. μ is set to be 3 for illustration.

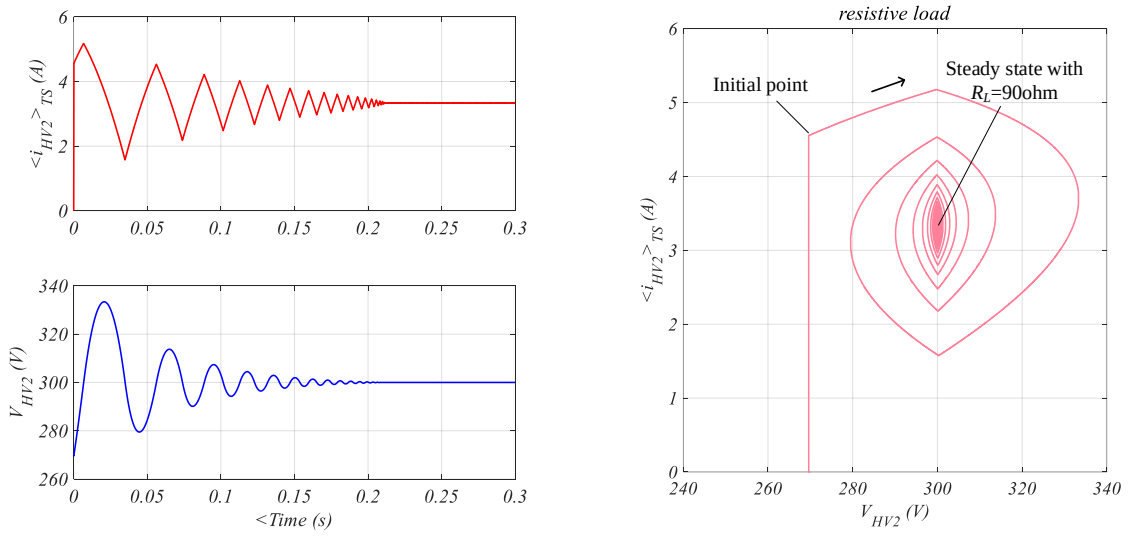
Assessments on the mono-dimensional MDCS-MPC described in Fig. 4.6 are conducted with circuit parameters listed in Chapter 2 section 2.7. SPS is chosen. When the constant current load is connected I_{load}=3.3A, as shown in Fig. 4.7, the operating point ($<i_{HV2}>_{Ts}$, V_{HV2}) cannot quickly converge to the steady state point (3.3A, 300V).



(a) Time domain (b) Phase portrait

Fig. 4.7 Simulation results with constant load current I_{load} = 3.3A. μ = 3, V_{HV1}=300V,V_{HV2_ref}=300V.

However, when the converter is connected with resistive load R_L=90ohm, the operating point ($<i_{HV2}>_{Ts}$, V_{HV2}) shows a relatively faster converging speed. The explanation for the above mentioned phenomena with both constant current/resistive loads and detail analysis on the converter stability with mono-dimensional MDCS-MPC are addressed in section 4.2.



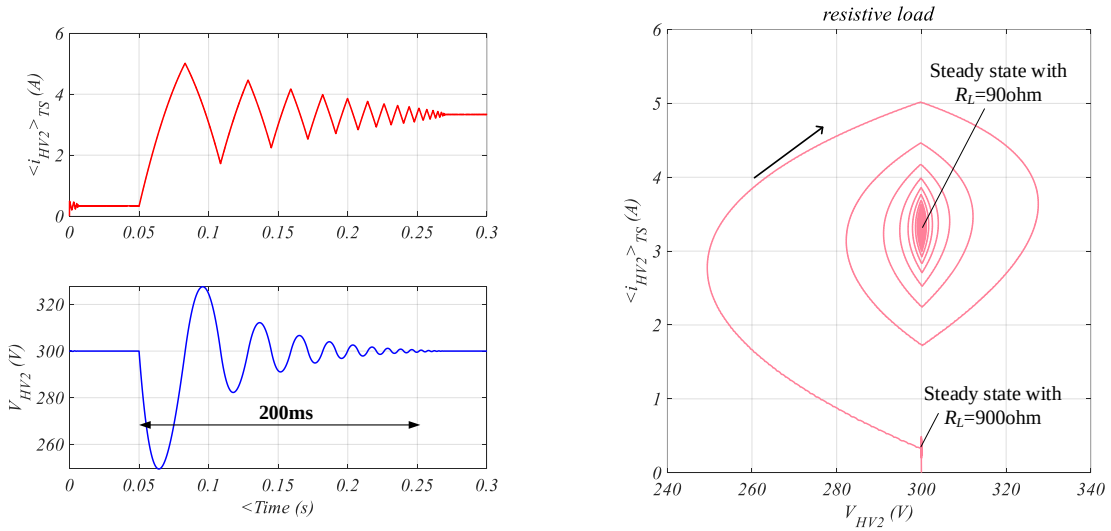
(a) Time domain (b) Phase portrait

Fig. 4.8 Simulation results with constant load R_L = 90ohm. μ = 3, V_{HV1}=300V, V_{HV2_ref}=300V.

4.1.3 Dynamic enhancement

Apart from the stability issue with the scheme described in Fig. 4.6, the dynamic performance is assessed. Dominant factors that affect the dynamic performance are identified.

Simulation on load step up transition has been conducted. The load resistance R_L is decreased from 900ohm to 90ohm at time instance 0.05. Results are shown in Fig. 4.9. It takes 200ms for the converter to adjust the load voltage back to the reference point after the load disturbance at time instance 0.05s. The operating point converges much faster than that of the constant current loads shown in Fig. 4.8. Even so, the dynamic is still rather slow when compared to a converter with switching frequency as high as 20kHz.

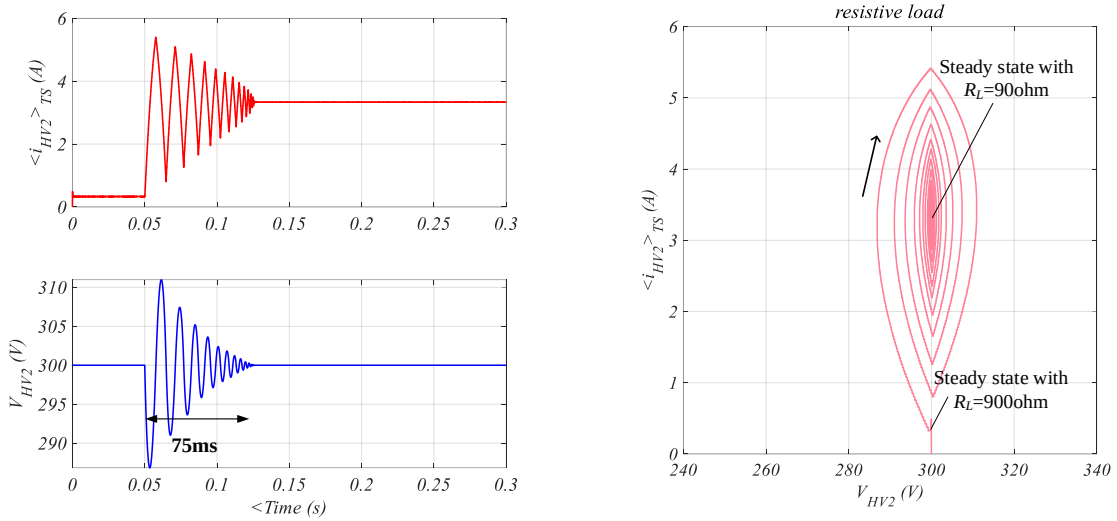


(a) Time domain (b) Phase portrait

Fig. 4.9 R_L decreases from 900ohm to 90ohm at time instance 0.05s with μ = 3, V_{HV1}=300V, V_{HV2_ref}=300V.

4.1.3.1 Increase μ

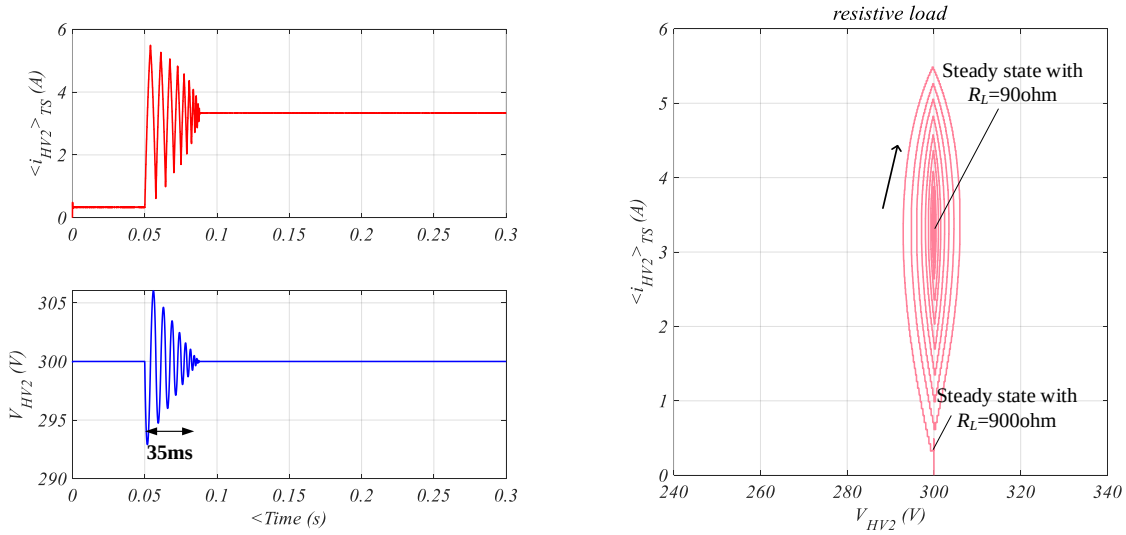
A straight forward way to enhance the dynamic performance is to increase the number of points μ calculated in one sampling period. Simulations are conducted with μ increased to 11, 21 and 201. As can be observed from the results shown in Fig. 4.10, Fig. 4.11 and Fig. 4.12, the dynamic performance increases with the increasing of μ. The transition time decreases from 200ms when μ is 3 to 1.5ms when μ is 201.



(a) Time domain (b) Phase portrait

Fig. 4.10 R_L decreases from 900ohm to 90ohm at time instance 0.05s with μ = 11, V_{HV1}=300V, V_{HV2_ref}=300V.

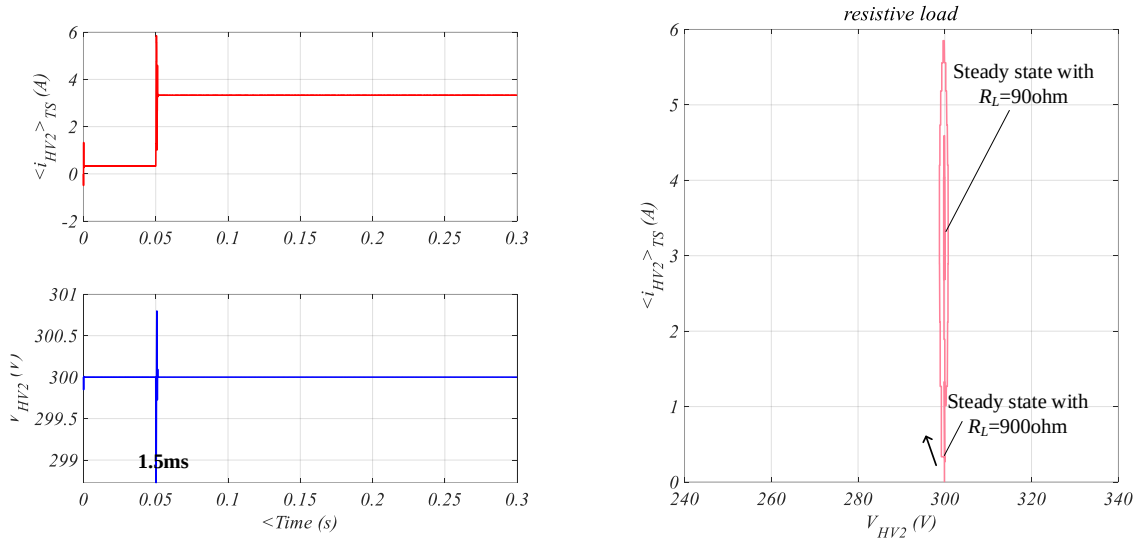
In light of the comparisons of Fig. 4.9(b), Fig. 4.10(b), Fig. 4.11(b) and Fig. 4.12(b), larger values of μ make the shape of the phase portrait contract in X axis and expand in Y axis.



(a) Time domain (b) Phase portrait

Fig. 4.11 R_L decreases from 900ohm to 90ohm at time instance 0.05s with μ = 21, V_{HV1}=300V, V_{HV2_ref}=300V.

Larger values of μ can increase the dynamic, but it aggravates the computational burden on the real-time digital controller. Therefore, instead of increasing the number of points calculated in each sampling period, an adaptive step approach can be used to replace the fixed Δ_f.



(a) Time domain (b) Phase portrait

Fig. 4.12 R_L decreases from 900ohm to 90ohm at time instance 0.05s with μ = 201, V_{HV1}=300V, V_{HV2_ref}=300V.

4.1.3.2 Adaptive step

An adaptive step approach for D_f is adopted instead of the smallest search step Δ_f. Defining the adaptive step Δ_{adp} as (4. 13), (4. 14). The adaptive step Δ_{adp} changes with the difference between the load voltage and the reference. When V_{HV2} is far from the reference, Δ_{adp} becomes large. In contrast, when V_{HV2} equals to the reference, Δ_{adp} contracts to Δ_f. As a consequence, the control accuracy remains in steady state.

$$V_{\Delta} = \begin{cases} \left|V_{HV2_ref} - V_{HV2}[k]\right|, & \left|V_{HV2_ref} - V_{HV2}[k]\right| < V_m \\ V_m, & \left|V_{HV2_ref} - V_{HV2}[k]\right| > V_m \end{cases} \quad (4.\ 13)$$

$$\Delta_{adp} = \Delta_f (1 + \lambda V_{\Delta}^{\ 2}) \quad (4.\ 14)$$

, where V_m is the limiter voltage which is set as 10V. λ is a constant coefficient. The block diagram of the adaptive step is shown in Fig. 4.13.

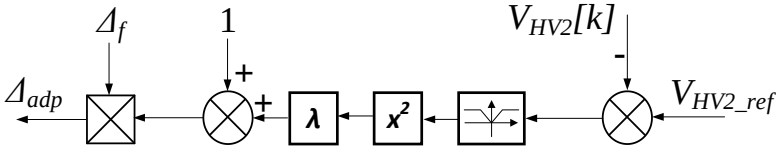
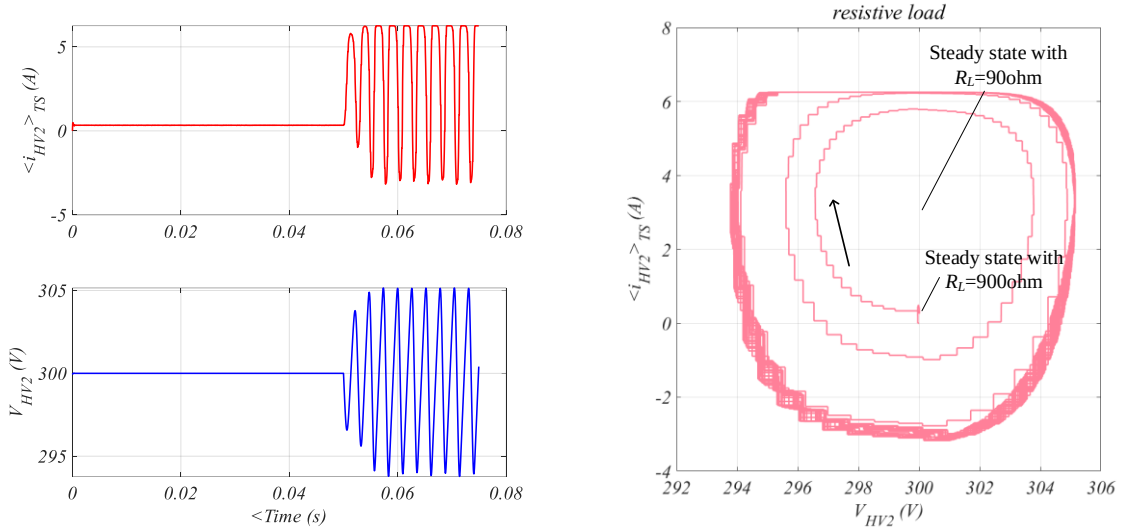


Fig. 4.13 Block diagram of the adaptive step.



(a) Time domain (b) Phase portrait

Fig. 4.14 R_L decreases from 900ohm to 90ohm at time instance 0.05s with μ = 11, V_{HV1}=300V, V_{HV2_ref}=300V, and λ=1.

The evaluation on the adaptive step has been carried out, resulting in waveforms Fig. 4.14. As shown in the figure, the operating point does not converge with the adaptive step. The operating trajectory starts with the initial point (0.3A, 300V). The oscillation amplitudes of both load voltage and controlled current increase until saturation. This phenomena that happens with the adaptive step will be analysed in detail in section 4.2.

4.1.4 Cost function

In order to guarantee the large signal stability of DAB with the mono-dimensional MDCS-MPC, another term G_2 is proposed in the cost function as follows:

$$ct = \alpha_1 G_1 + \alpha_2 G_2 \tag{4. 15}$$

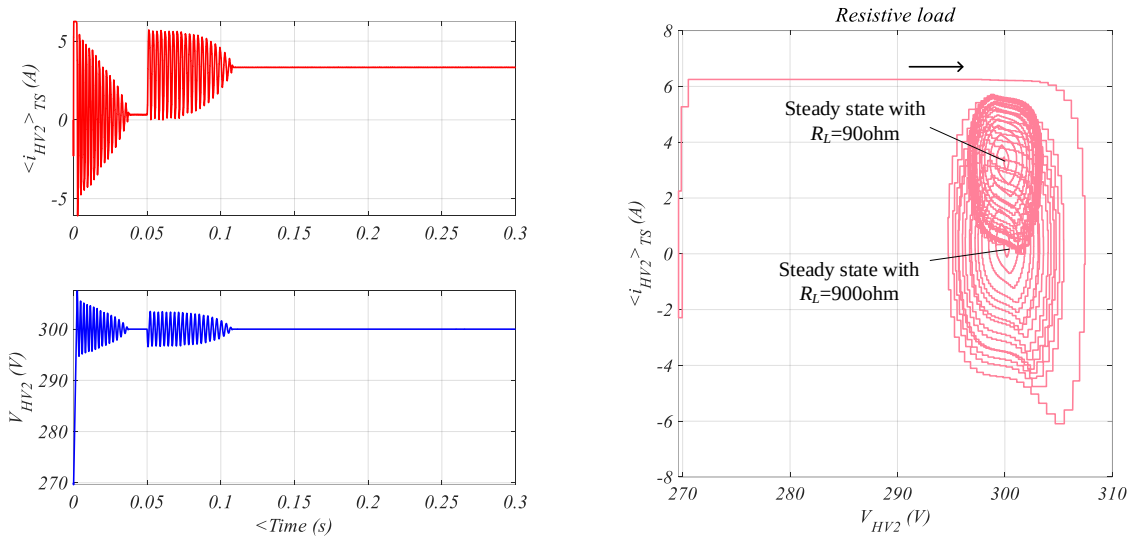
, where

$$\begin{cases} G_1 = (V_{HV2_ref} - V_{HV2}[k+2])^2 \\ G_2 = (V_{HV2}[k+2] - V_{HV2}[k])^2 \end{cases} \tag{4. 16}$$

The first term G_1 is responsible for regulation of the load voltage V_{HV2} to the reference value V_{HV2_ref} while the second term G_2 takes charge of the operating stability.

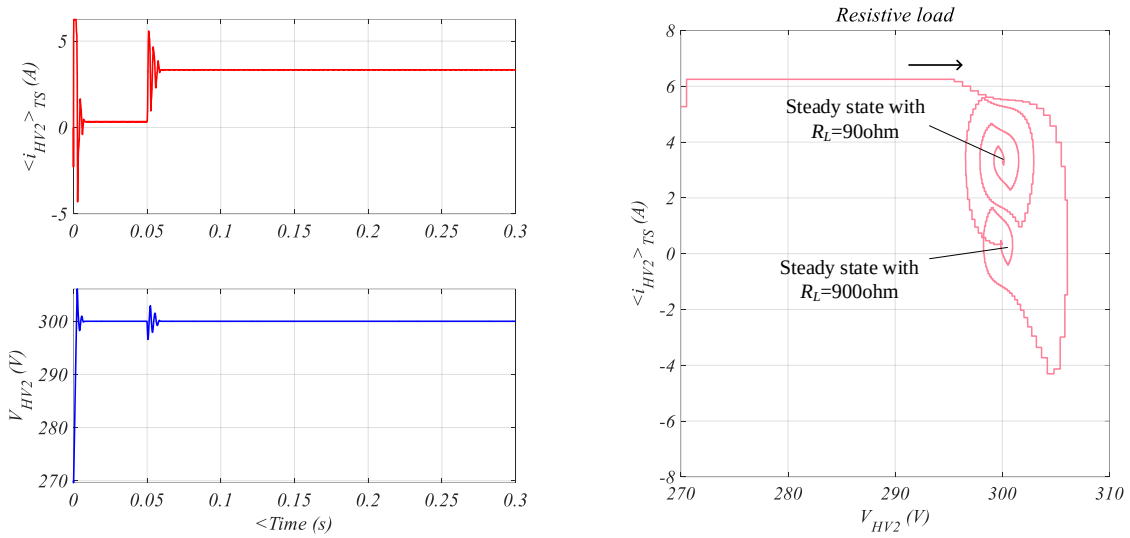
With the adaptive step discussed in section 4.1.3, when α_2 is zero the operating point does not converge according to Fig. 4.14. When α_2 is increased to1.2, the operating point converges even with the adaptive step as shown in Fig. 4.15. The oscillation time gets reduced by further increasing the value of weighting factor α_2 as in Fig. 4.16. When α_2 is increased to four as shown in Fig. 4.17, both controlled current and load voltage do not oscillate, and the operating point converges to the steady states. The dynamic performance shown in Fig. 4.17 gets pretty close to Fig. 4.12 where 201 points are calculated in one switching period. Therefore, it has been demonstrated that the adaptive step approach can boost the dynamic performance with a much lighter computational burden.

In the observation of Fig. 4.15 - Fig. 4.17, the value of α_2 has a positive effect on the system stability. However, α_2 cannot be set too large because it has negative impact on the steady state error. This will be addressed in section 4.1.5.



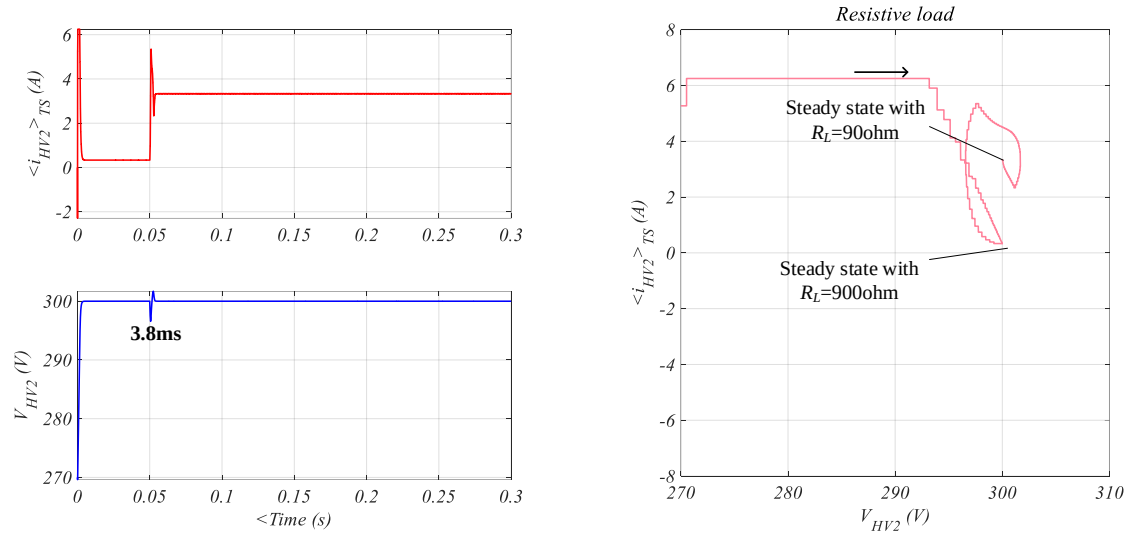
(a) Time domain (b) Phase portrait

Fig. 4.15 R_L decreases from 900ohm to 90ohm at time instance 0.05s with μ = 11, V_{HV1}=300V, V_{HV2_ref}=300V, λ=1 and α_2=1.2.



(a) Time domain (b) Phase portrait

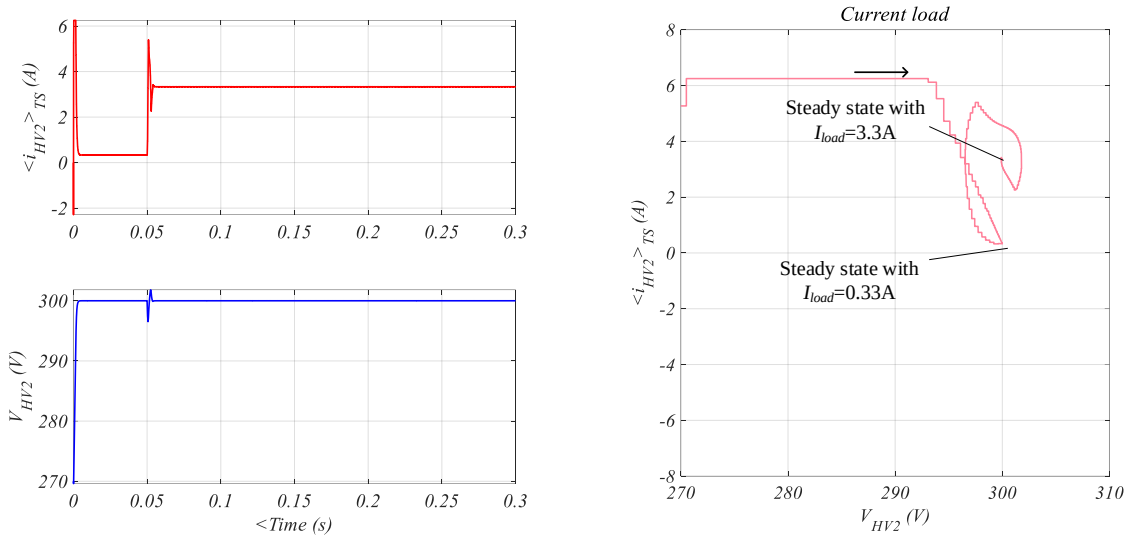
Fig. 4.16 R_L decreases from 900ohm to 90ohm at time instance 0.05s with μ = 11, V_{HV1}=300V, V_{HV2_ref}=300V, and λ=1 and α_2=2.5.



(a) Time domain (b) Phase portrait

Fig. 4.17 R_L decreases from 900ohm to 90ohm at time instance 0.05s with μ = 11, V_{HV1}=300V, V_{HV2_ref}=300V, and λ=1 and α_2=4.

As shown in Fig. 4.7, when a constant load is connected to DAB with the mono-dimensional MDCS-MPC, the converter operating point can hardly converge. Another examination is conducted to verify the effectiveness of G_2 in the scenario with constant current loads. As presented in Fig. 4.18, the converter is stable with G_2 enabled. In fact, Fig. 4.18(b) shows a very similar trajectory with Fig. 4.17(b). Detailed explanations on theses phenomena is addressed in section 4.2.



(a) Time domain (b) Phase portrait

Fig. 4.18 I_{load} increases from 0.3A to 3.3A at time instance 0.05s with μ = 11, V_{HV1}=300V, V_{HV2_ref}=300V, and λ=1 and α_2=4.

4.1.5 Steady state error

There are two reasons for the steady state error in the above discussed mono-dimensional MDCS-MPC. The first reason is the prediction error from the ideal model. As stated in Chapter 2, the accurate modelling of the DAB which considers the copper and core losses from the high frequency is rather complicated. The simplified reduced order model enables relatively easier implementation, however, it also brings prediction error in $<i_{HV2}>_{Ts}$. The second reason is the contradiction between G_1 and G_2. When V_{HV2} nears to V_{HV2_ref}, G_1 becomes very small. The predicted step change ($V_{HV2}[k+2]$-V_{HV2}[k]) is higher than the steady state error (V_{HV2_ref}-$V_{HV2}[k+2]$). In this case, the decreasing of $\alpha_1 G_1$ does not compensate for the increasing of $\alpha_2 G_2$. As a result, (V_{HV2_ref}-$V_{HV2}[k+2]$) cannot be controlled to zero, therefore causing the steady state error.

4.1.5.1 Prediction error

The error of the ideal prediction model can be corrected by a compensation term defined as I_{comp} in (4. 17). I_{comp} is calculated as the difference between the observed output current value i_{HV2_r} and the predicted value i_{HV2}.

$$I_{comp}[k] = i_{HV2_r}[k-1] - i_{HV2}[k-1] \tag{4. 17}$$

, where

$$i_{HV2_r}[k-1] = \frac{C_{HV2}}{T_s}(V_{HV2}[k] - V_{HV2}[k-1]) + I_{load}[k-1] \tag{4. 18}$$

The correction of the prediction model can eliminate the steady state error for the output voltage. However, due to the calculation of i_{HV2_r} in (4. 18) involves a derivative of V_{HV2}. In presence of sampling noise, the compensation term I_{comp} could deteriorate the dynamic performance of MDCS-MPC. I_{comp} is designed solely for the purpose of steady state error correction. A Low Pass Filter (LPF) can be applied for I_{comp}. Therefore, the predicted output voltage is modified as in (4. 19). A diagram of the compensation for the prediction error is shown in Fig. 4.19. A moving average filter is used as the LPF.

$$V_{HV2}[k+2] = \frac{i_{HV2}[k+2] + i_{HV2}[k+1] + 2I_{comp_f}[k] - 2I_{load}[k]}{C_{HV2} f_s} + V_{HV2}[k] \tag{4. 19}$$

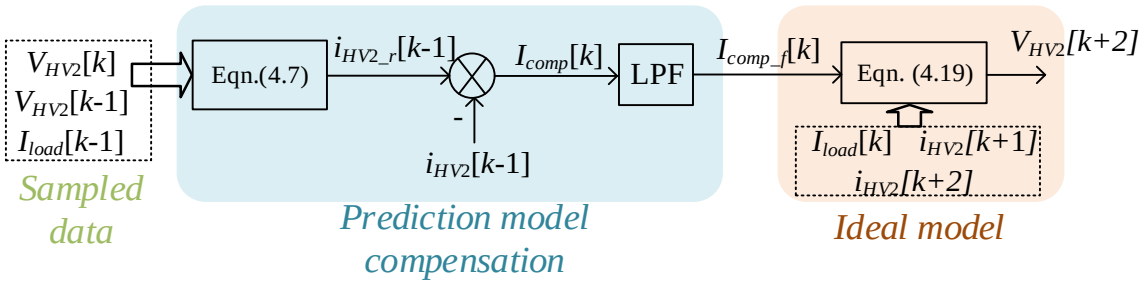


Fig. 4.19 The compensation diagram for the prediction error

4.1.5.2 Error caused by α_2

The steady state error caused by the weighting factor α_2 is analysed as shown in Fig. 4.20. Assuming the converter reaches steady state at time instant k, the assessment on the behaviour of the mono-dimensional MDCS-MPC has been investigated.

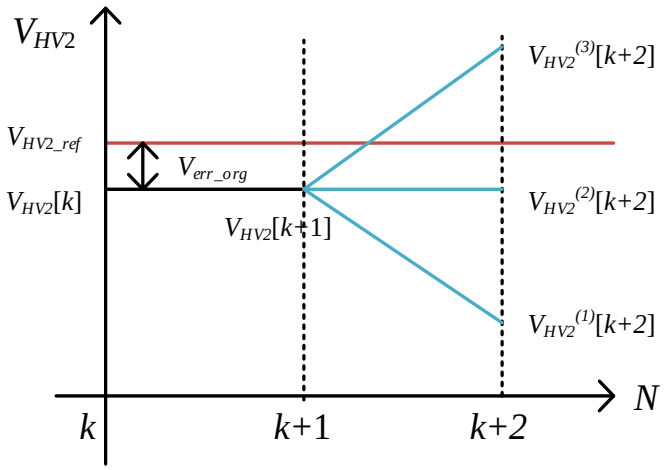


Fig. 4.20 Illustration of the steady state error

To start with, consider the initial cost function in (4. 9) without G_2 and assume that the converter has already been in the steady state:

$$V_{HV2}[k] = V_{HV2}[k+1] \tag{4. 20}$$

$$I_{load}[k] = i_{HV2}[k] = i_{HV2}[k+1] \tag{4. 21}$$

, where the steady state error V_{err_org} is defined as:

$$V_{err_org} = V_{HV2_ref} - V_{HV2}[k] \tag{4. 22}$$

Substitute the conditions (4. 21) and (4. 22) into the prediction model (4. 5). The prediction value for the output voltage $V_{HV2}^{(3)}[k+1]$ in Fig. 4.20 is:

$$V_{HV2}[k+2] = \frac{i_{HV2}[k+2] - i_{HV2}[k+1]}{C_{HV2} f_s} + V_{HV2_ref} - V_{err_org} \tag{4. 23}$$

Equation (4. 23) can be further modified as:

$$V_{HV2}[k+2] = \frac{\Delta_{adp}}{C_{HV2} f_s} \frac{di_{HV2}}{dD_f}\Big|_{Df=\overline{Df}} + V_{HV2_ref} - V_{err_org} \tag{4. 24}$$

The cost functions with voltage predictions $V_{HV2}^{(2)}[k+2]$ and $V_{HV2}^{(3)}[k+2]$ are:

$$ct^{(2)} = V_{err_org}{}^2 \tag{4. 25}$$

$$ct^{(3)} = \left(\frac{\Delta_{adp}}{C_{HV2} f_s} \frac{di_{HV2}}{dD_f} |_{Df=\overline{Df}} - V_{err_org} \right)^2 \tag{4. 26}$$

Due to the steady state assumption, (4. 27) has to hold true.

$$ct^{(2)} < ct^{(3)} \tag{4. 27}$$

Therefore, the maximum prediction error $V_{err_org_max}$ can be obtained in (4. 28).

$$V_{err_org} < \frac{\Delta_{adp}}{C_{HV2} f_s} \frac{di_{HV2}}{dD_f} |_{Df=\overline{Df}} = V_{err_org_max} \tag{4. 28}$$

Now, consider the cost function defined in (4. 15) with the second term G_2 enabled. Set α_1=1. The cost functions with the voltage prediction $V_{HV2}^{(2)}[k+2]$ and $V_{HV2}^{(3)}[k+2]$ become:

$$ct^{(2)} = V_{err_mod}{}^2 \tag{4. 29}$$

$$ct^{(3)} = \left(\frac{\Delta_{adp}}{C_{HV2} f_s} \frac{di_{HV2}}{dD_f} |_{Df=\overline{Df}} - V_{err_mod} \right)^2 + \alpha_2 \left(\frac{\Delta_{adp}}{C_{HV2} f_s} \frac{di_{HV2}}{dD_f} |_{Df=\overline{Df}} \right)^2 \tag{4. 30}$$

, where V_{err_mod} is the steady state error with the term G_2 enabled. Due to the steady state assumption, substitute (4. 28), (4. 29) and (4. 30) in (4. 27). The maximum prediction error $V_{err_mod_max}$ becomes:

$$V_{err_mod} < V_{err_org_max} (1 + \alpha_2) = V_{err_mod_max} \tag{4. 31}$$

The steady state error is dependent on the working points of the converter such as the power and the terminal voltage ratio. Conclusion can be drawn from (4. 28) that smaller step Δ_{adp}, bigger output capacitor C_{HV2} and higher switching frequency f_s are conducive for the reduction on the voltage steady state error. It also can be concluded from (4. 31) that the existence of α_2 increases the steady state error. Compared with only G_1 in the cost function, the error has been increased by (1+α_2) times of $V_{err_org_max}$. Higher values of α_2 introduces better system convergence. However, it also causes steady state load voltage error. In applications where large output capacitors and high switching frequency are required, the error is small enough to

be neglected. In some cases where high voltage precision is required, the adaptive weighting factor design proposed by *T. Dragicevic* [117] can be adopted to address the issue.

4.1.6 Algorithm flow chart

The flow chart of the mono-dimensional MDCS-MPC is presented in Fig. 4.21. It shows the calculation process in the control period k to k+1. The output of the control is the optimal control variable to be applied at time instance k+2. μ (=3) elements are utilized for illustration purposes.

The evaluation process starts with the calculation of the adaptive step Δ_{adp}. It determines the step distance between two near values in the control set. The control set slides in the range described in (4. 12) centred at the control value $D_f[k+1]$ which is applied at time instance k+1. Then the following iteration starts for the mono-dimensional MDCS-MPC:

- The load voltage is predicted with three elements in the control set.
- Each voltage prediction is corrected by the compensation loop illustrated in Fig. 4.19.
- Cost functions are calculated with each corrected voltage prediction value

The element achieving minimal *ct* is then stored in $D_f[k+2]$ which is applied at time instance k+2.

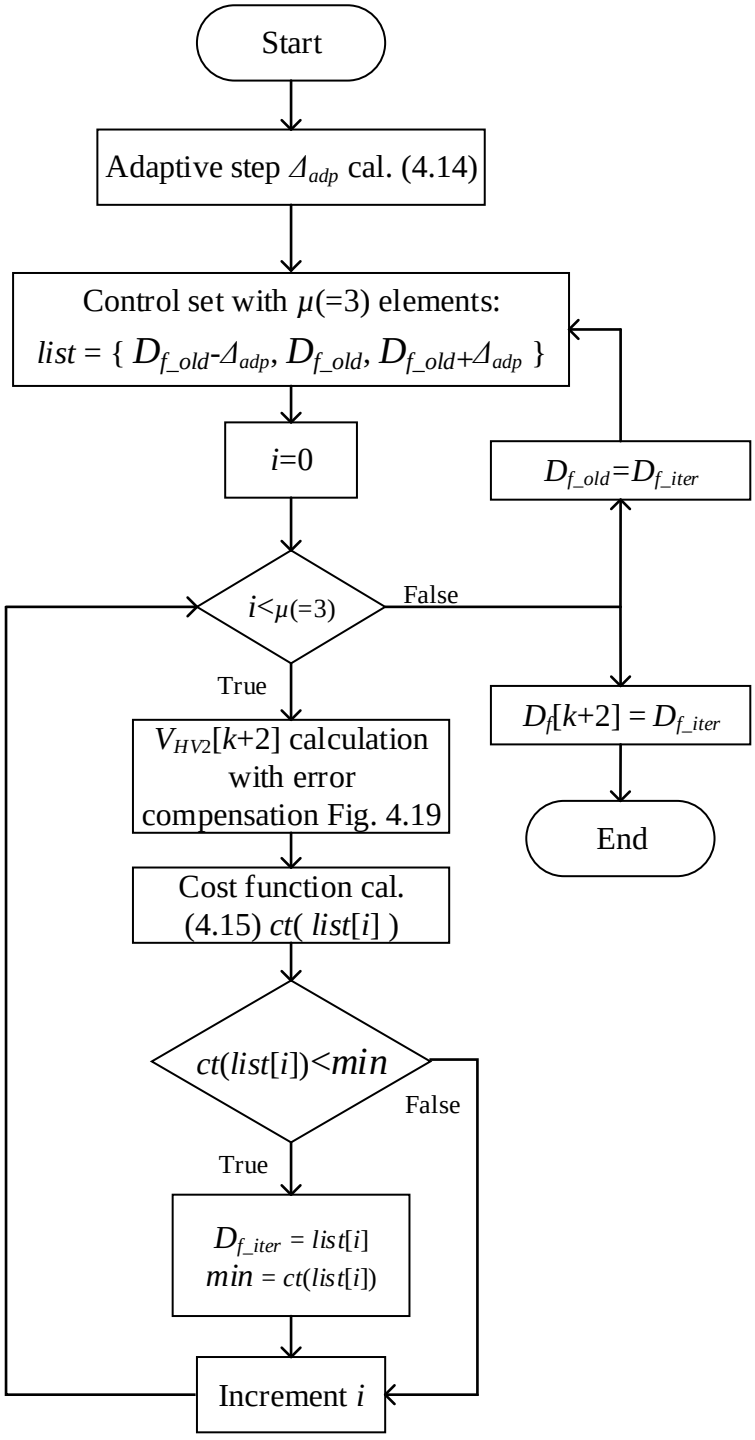


Fig. 4.21 The flow chart of MDCS-MPC

4.2 Large signal stability analysis

In section 4.1, the concept of the mono-dimensional MDCS-MPC has been introduced. However, there are several unexplained phenomena including:

- The operation point converges to the steady state with resistive loads much faster than with constant current loads as shown in Fig. 4.7 and Fig. 4.8.
- The converter becomes unstable with the adaptive step irrelevant to the type of load as shown in Fig. 4.14.
- The converter is stable when G_2 is enabled in the cost function as shown in Fig. 4.17 and Fig. 4.18. The oscillation decreases with the increase of the weighting factor α_2.

All the phenomena mentioned above relate to the stability issue of DAB with mono-dimensional MDCS-MPC. In this section, the large signal stability of DAB is analysed based on the reduced order model in Fig. 4.1. The stability issue will be intuitively explained and mathematically prooven.

4.2.1 Phase portrait analysis method

Three statements that underpin further stability analysis are presented here. The statements are generally true irrelevant to the circuit parameters and control methods used in DAB. The phase portrait plot with controlled current $<i_{HV2}>_{Ts}$ as Y axis and load voltage V_{HV2} as X axis as shown in Fig. 4.22 is the main analysis tool. In the following text, notation $<i_{HV2}>_{Ts}$ is replaced by I_{HV2} for simplicity.

Two curve lines l_1 and l_4 are drawn in Fig. 4.22. Line l_4 starts with the horizontal line i_x where line l_1 also ends upon.

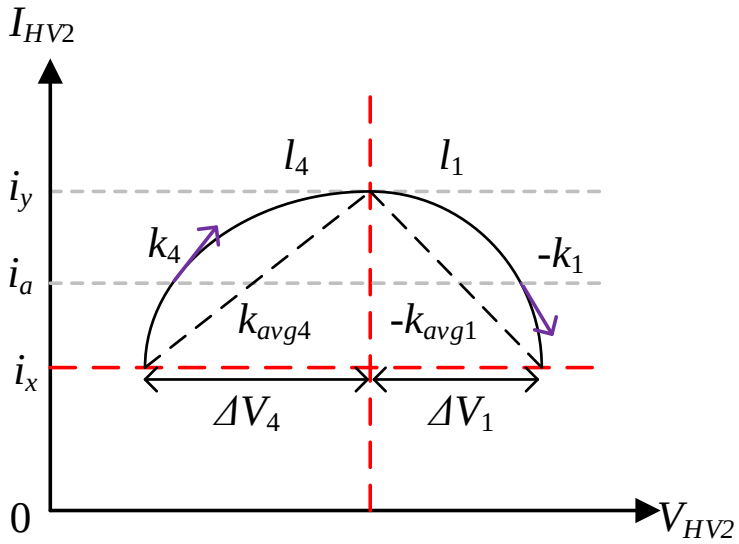


Fig. 4.22 The general phase portrait of DAB

The trajectory functions for l_1 and l_4 are assumed to be:

$$I_{HV2} = f_1(V_{HV2}) \tag{4. 32}$$

$$I_{HV2} = f_4(V_{HV2}) \tag{4. 33}$$

The slopes of l_1 and l_4 when intersecting with horizontal i_a are $-k_1$ and k_4:

$$k_1(i_a) = -[\frac{1}{f_1^{-1}(i_a)}]' \tag{4. 34}$$

$$k_4(i_a) = [\frac{1}{f_4^{-1}(i_a)}]' \tag{4. 35}$$

The average slopes for l_1 and l_4 are defined as $-k_{avg1}$ and k_{avg4}:

$$k_{avg1} = \frac{i_y - i_x}{\Delta V_1} = \frac{i_y - i_x}{\int_{i_y}^{i_x}[f_1^{-1}(I_{HV2})]' dI_{HV2}} = \frac{i_y - i_x}{\int_{i_x}^{i_y} \frac{dI_{HV2}}{k_1(I_{HV2})}} \tag{4. 36}$$

$$k_{avg4} = \frac{i_y - i_x}{\Delta V_4} = \frac{i_y - i_x}{\int_{i_x}^{i_y}[f_4^{-1}(I_{HV2})]' dI_{HV2}} = \frac{i_y - i_x}{\int_{i_x}^{i_y} \frac{dI_{HV2}}{k_4(I_{HV2})}} \tag{4. 37}$$

Based on the above information, it is straight-forward to conclude that:

Hypothesis: In the second period of oscillation, there is no saturation in the controlled current I_{HV2}. In other words, except for the slope at the point intersecting the V_{HV2_ref} line, k_1 and k_4 are not zero.

- **Statement 1 –** The sufficient and necessary condition for (4. 38) to hold true is the satisfaction of (4. 39).

$$\Delta V_4 < \Delta V_1 \tag{4. 38}$$

$$k_{avg1} = \frac{i_y - i_x}{\int_{i_x}^{i_y} \frac{dI_{HV2}}{k_1(I_{HV2})}} < k_{avg2} = \frac{i_y - i_x}{\int_{i_x}^{i_y} \frac{dI_{HV2}}{k_4(I_{HV2})}} \tag{4. 39}$$

- **Statement 2 -** The sufficient condition for (4. 38) to be true is the satisfaction of (4. 40).

$$k_1 = -[\frac{1}{f_1^{-1}(I_{HV2})}]' < k_4 = [\frac{1}{f_4^{-1}(I_{HV2})}]' \tag{4. 40}$$

- **Statement 3 -** If either (4. 41) or (4. 42) is true, ΔV_1 equals ΔV_4.

$$k_1 = k_4 \tag{4. 41}$$

$$k_{avg1} = k_{avg4} \tag{4. 42}$$

4.2.2 Benchmark control

The phase portrait plane is divided into two parts as shown in Fig. 4.23. In the green area, the load voltage is smaller than its reference. In the red area, the load voltage is larger than its reference.

A benchmark control is assumed when the operating point is in the red area, D_f will be decreased at a rate as (4. 43), otherwise D_f will be increased by the same rate.

$$\frac{dD_f}{dt} = \Delta_f f_s \tag{4. 43}$$

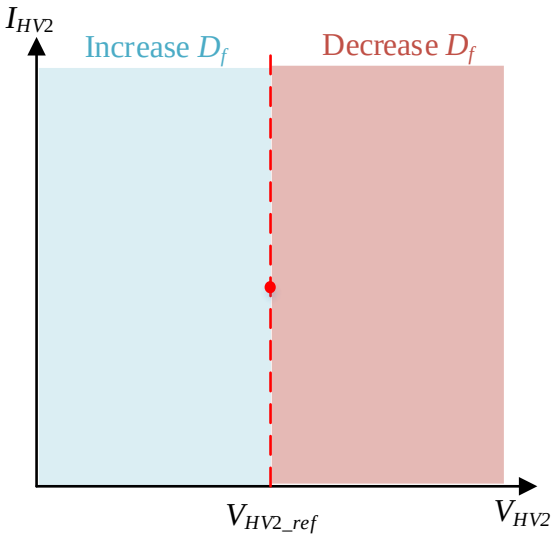


Fig. 4.23 Different control behaviours.

Note that the benchmark control is very similar but not the same as the mono-dimensional MDCS-MPC. To facilitate a better explanation, the stability analysis is first carried out with the benchmark control.

4.2.2.1 Current load

With above benchmark control, stability analysis is carried out with constant current load. The circuit is as shown in Fig. 4.24.

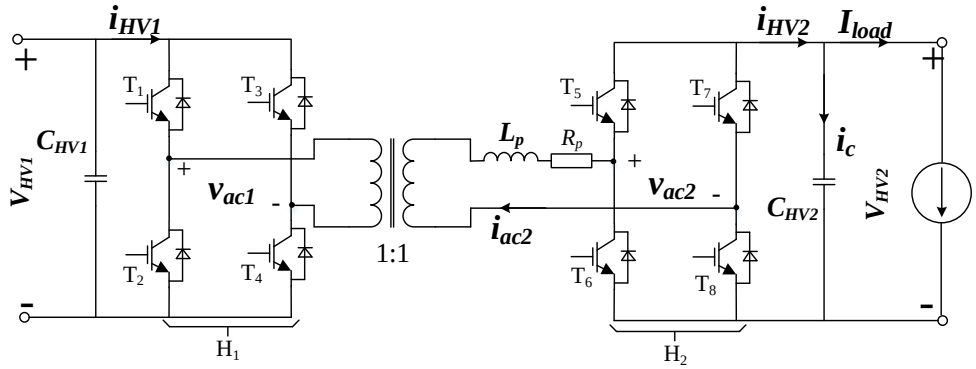


Fig. 4.24 DAB with constant current load

The analysis is conducted on SPS. Therefore,

$$I_{HV2} = \frac{V_{HV1}}{f_s L_p} D_f (1 - 2D_f) = g(D_f) \tag{4. 44}$$

$$\frac{dI_{HV2}}{dt} = \frac{V_{HV1}}{f_s L_p}(1-4D_f)\frac{dD_f}{dt} = \frac{V_{HV1}}{f_s L_p}[1-4g^{-1}(I_{HV2})]\frac{dD_f}{dt} \tag{4. 45}$$

The load voltage dynamic equation is:

$$C_{HV2}\frac{dV_{HV2}}{dt} = I_{HV2} - I_{load} \tag{4. 46}$$

According to (4. 44), I_{HV2} and D_f are positively correlated within the range (0, 0.25), the increase/decrease of D_f results also in the increase/decrease of I_{HV2}. According to (4. 46), when the controlled current I_{HV2} is higher/lower than the load current I_{load}, the load voltage will increase/decrease. With the benchmark control assumed in Fig. 4.23, dynamic behaviours in each quadrant are summarized as follow:

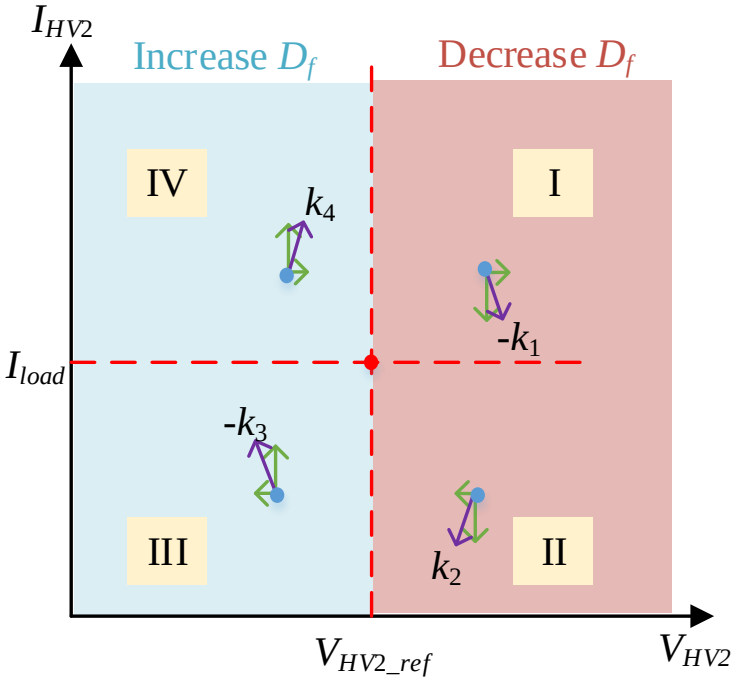


Fig. 4.25 Control behaviours.

- When the operating point is in quadrant I, the load voltage is higher than the reference voltage and the controlled current I_{HV2} is higher than the load current I_{load}. The operating point moves in the right and down direction where the slope $-k_1<0$.
- When the operating point is in quadrant II, the load voltage is higher than the reference voltage and the controlled current I_{HV2} is lower than the load current I_{load}. The operating point moves in the left and down direction where the slope $k_2>0$.

- When the operating point is in quadrant III, the load voltage is lower than the reference voltage and the controlled current I_{HV2} is lower than the load current I_{load}. The operating point moves in the left and up direction where the slope $-k_3<0$.
- When the operating point is in quadrant IV, the load voltage is lower than the reference voltage and the controlled current I_{HV2} is higher than the load current I_{load}. The operating point moves in the right and up direction where the slope $k_4>0$.

Assuming a phase portrait as Fig. 4.26 with constant current load. Operating points P_1 and P_4 have the same current i_a while points P_2 and P_3 have the same current i_b.

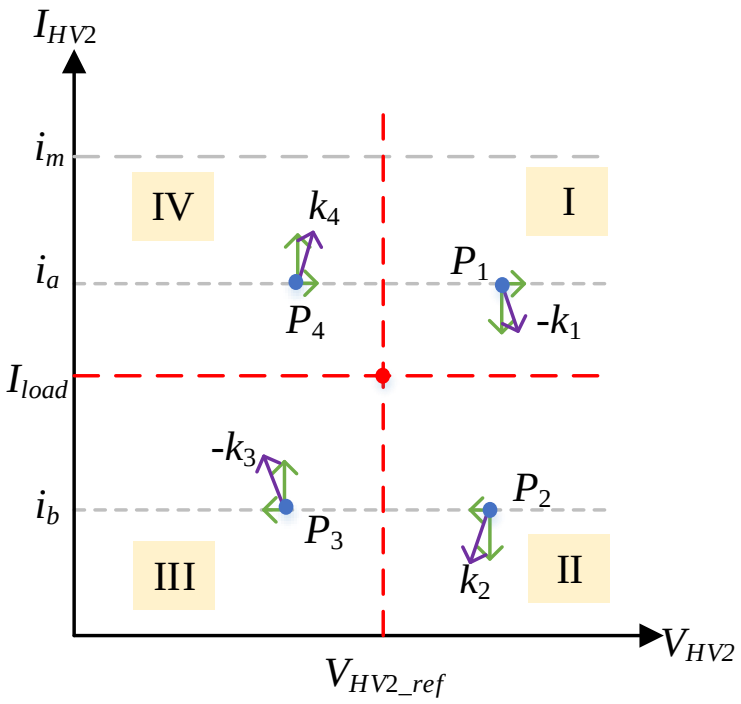


Fig. 4.26 Four quadrant for constant current load

Generally, the absolute value of the slope in the phase portrait can be calculated as:

$$k=\frac{dI_{HV2}}{dV_{HV2}}=\frac{dI_{HV2}/dt}{dV_{HV2}/dt}=\frac{\frac{C_{HV2}V_{HV1}}{f_sL_p}[1-4g^{-1}(I_{HV2})]\frac{dD_f}{dt}}{I_{HV2}-I_{load}} \\ =\frac{C_{HV2}V_{HV1}\Delta_f}{L_p}\frac{1-4g^{-1}(I_{HV2})}{I_{HV2}-I_{load}} \quad (4.47)$$

Based on the equation (4. 47), the slopes at points P_1-P_4 are as follow:

$$k_1 = \frac{C_{HV2} V_{HV1} \Delta_f}{L_p} \frac{1 - 4g^{-1}(i_a)}{i_a - I_{load}} \tag{4. 48}$$

$$k_2 = \frac{C_{HV2} V_{HV1} \Delta_f}{L_p} \frac{1 - 4g^{-1}(i_b)}{i_b - I_{load}} \tag{4. 49}$$

$$k_3 = \frac{C_{HV2} V_{HV1} \Delta_f}{L_p} \frac{1 - 4g^{-1}(i_b)}{i_b - I_{load}} \tag{4. 50}$$

$$k_4 = \frac{C_{HV2} V_{HV1} \Delta_f}{L_p} \frac{1 - 4g^{-1}(i_a)}{i_a - I_{load}} \tag{4. 51}$$

According to (4. 48) - (4. 51), equations (4. 52) and (4. 53) can be concluded.

$$k_1 = k_4 \tag{4. 52}$$

$$k_2 = k_3 \tag{4. 53}$$

According to Statement 3 in section 4.2.1, with the constant current load, the operating point cannot converge to the steady state. The phase portrait for the DAB converter with the constant current load is shown in Fig. 4.27.

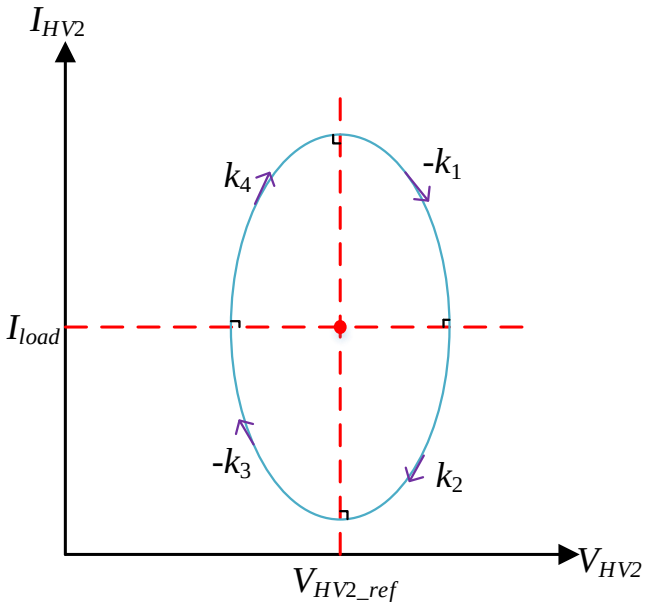


Fig. 4.27 Phase portrait with constant current load using the benchmark control.

4.2.2.2 Resistive load

Similar analysis is conducted on DAB with resistive load. The circuit is shown in Fig. 4.28.

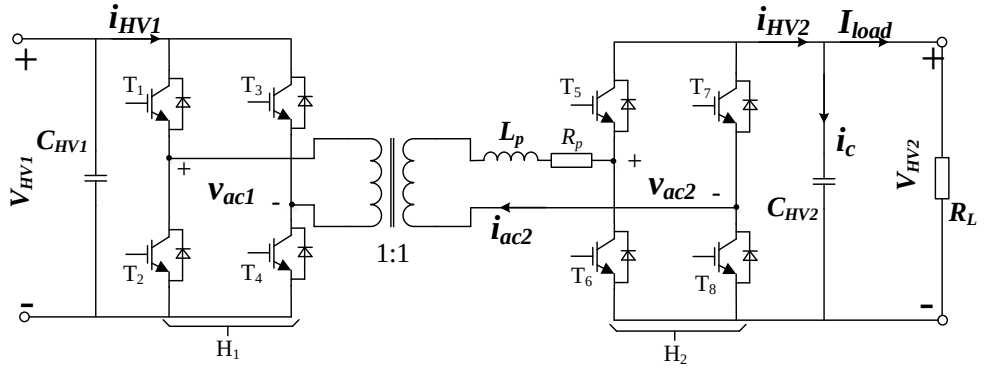


Fig. 4.28 DAB with constant resistive loads.

The load voltage dynamic equation becomes:

$$C_{HV2}\frac{dV_{HV2}}{dt} = I_{HV2} - \frac{V_{HV2}}{R_L} \tag{4. 54}$$

Due to that the load current varies with the load voltage, the phase portrait is divided into four quadrants as shown in Fig. 4.29 different from that of constant current loads in Fig. 4.26. But, the slopes in each quadrant has the same direction as in Fig. 4.26.

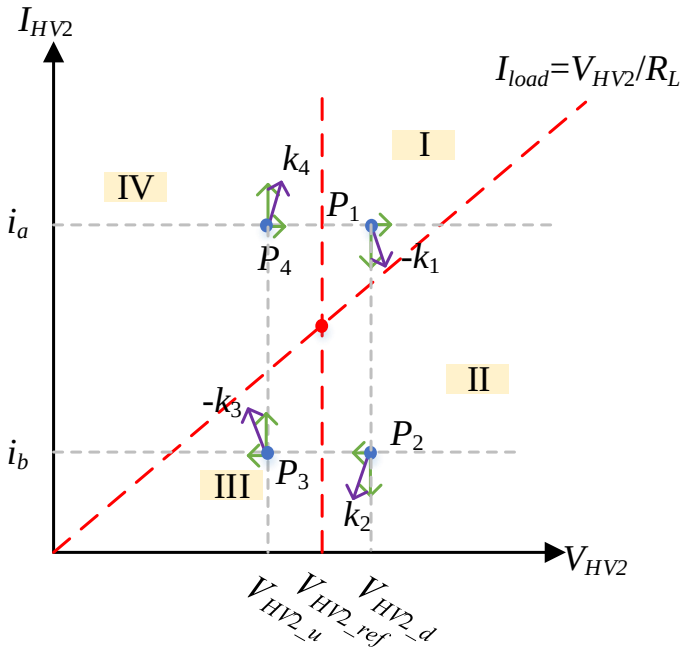


Fig. 4.29 Four quadrants with resistive loads.

According to (4. 47), the slope at each points P_1-P_4 can be calculated as:

$$k_1 = \frac{C_{HV2} V_{HV1} \Delta_f}{L_p} \frac{1 - 4g^{-1}(i_a)}{i_a - \frac{V_{HV2_d}}{R_L}} \tag{4. 55}$$

$$k_2 = \frac{C_{HV2} V_{HV1} \Delta_f}{L_p} \frac{1 - 4g^{-1}(i_b)}{i_b - \frac{V_{HV2_d}}{R_L}} \tag{4. 56}$$

$$k_3 = \frac{C_{HV2} V_{HV1} \Delta_f}{L_p} \frac{1 - 4g^{-1}(i_b)}{i_b - \frac{V_{HV2_u}}{R_L}} \tag{4. 57}$$

$$k_4 = \frac{C_{HV2} V_{HV1} \Delta_f}{L_p} \frac{1 - 4g^{-1}(i_a)}{i_a - \frac{V_{HV2_u}}{R_L}} \tag{4. 58}$$

Due to

$$V_{HV2_u} < V_{HV2_d} \tag{4. 59}$$

According to (4. 55) - (4. 59), the relationship between slopes -k_1 and k_4, also k_2 and -k_3 are:

$$k_1 > k_4 \tag{4. 60}$$

$$k_2 < k_3 \tag{4. 61}$$

Therefore, according to Statement 2 made in section 4.2.1, (4. 62) can be concluded where voltage differences are illustrated in Fig. 4.30.

$$\Delta V_4 > \Delta V_1 > \Delta V_2 > \Delta V_3 > \Delta V'_4 \tag{4. 62}$$

Considering the direction of movement in each quadrant as illustrated in Fig. 4.29, the phase portrait with resistive loads is presented as in Fig. 4.30. The operation with resistive loads is stable with the benchmark control.

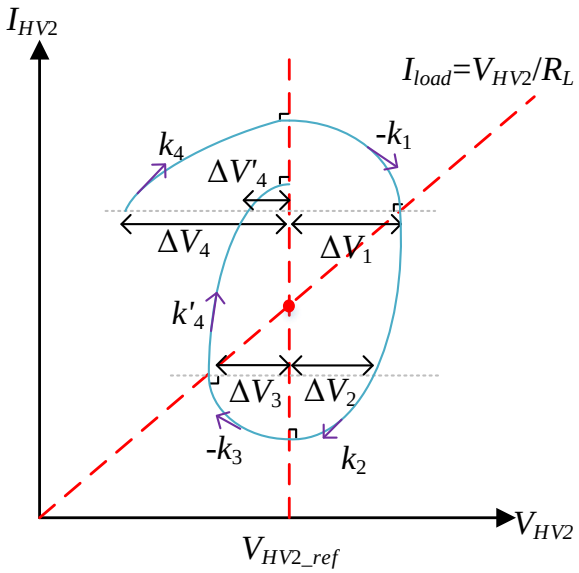


Fig. 4.30 Phase portrait with constant resistive load using the benchmark control.

4.2.3 Analysis on I_{HV2} saturation

The analysis carried out above in Fig. 4.30 demonstrated that the operation is stable using the benchmark control with resistive loads. However, the conclusion is only true when the hypothesis of the three statements are satisfied. If saturation happens during the transition, the operation might not be stable. The impact of controlled current saturation is addressed herein.

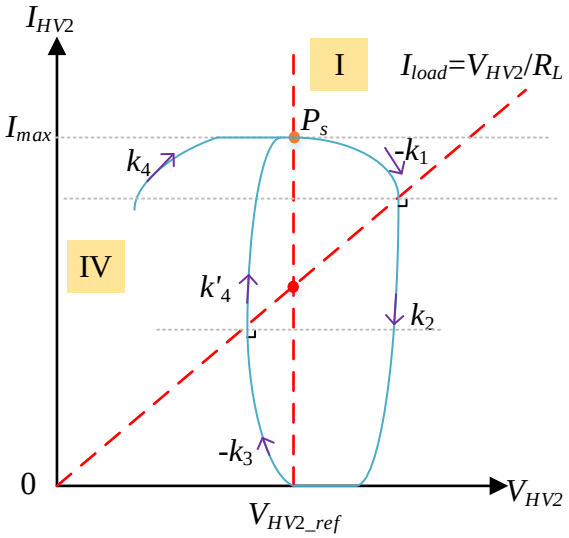


Fig. 4.31 Phase portrait with I_{HV2} saturation using the benchmark control.

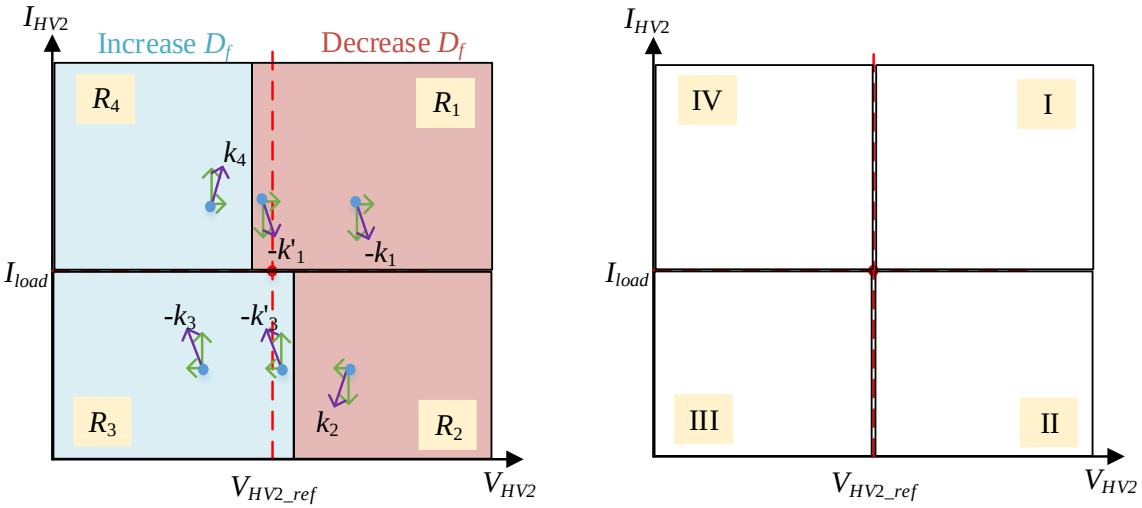
Consider unidirectional power flow, when the controlled current I_{HV2} saturates to its limits I_{max} and 0, the phase portrait will be as in Fig. 4.31. Due to the saturation, the starting point will

always be P_s when the trajectory moves from quadrant IV in to I. The oscillation starts and ends at the same point P_s.

It can be therefore concluded that if the controlled current I_{HV2} is still saturated in the second period of oscillation, the operation will not be stable with the benchmark control.

4.2.4 Analysis on MDCS-MPC

When the mono-dimensional MDCS-MPC with μ=3 and without the adaptive step and G_2 is considered, the control behaves slightly different from that of the benchmark control in Fig. 4.25.



(a) divided by four regions (b) divided by four quadrants

Fig. 4.32 mono-dimensional MDCS-MPC behaviours.

As shown in Fig. 4.32(a), the phase portrait plane is divided into four regions R_1-R_4. The descriptions for those regions are given as follow:

- When the operating point is in R_1, the load voltage is higher than the reference voltage and D_f is decreasing. The operating point moves in the right and down direction where the slope $-k_1<0$.
- When the operating point is in R_2, the load voltage is higher than the reference voltage and D_f is decreasing. The operating point moves in the left and down direction where the slope $k_2>0$.

- When the operating point is in R_3, the load voltage is lower than the reference voltage and D_f is increasing. The operating point moves in the left and up direction where the slope $-k_3<0$.
- When the operating point is in R_4, the load voltage is lower than the reference voltage and D_f is increasing. The operating point moves in the right and up direction where the slope $k_4>0$.

The mono-dimensional MDCS-MPC will decrease D_f before the operating point reaches the $V_{HV2}=V_{HV2_ref}$ in quadrant IV and increase D_f before the operating point reaches the same line in quadrant II.

The reason for the difference between the benchmark control and mono-dimensional MDCS-MPC is analysed here. The four operating points shown in Fig. 4.33 are defined as follows:

- $Q[k]$ in quadrant IV with co-ordinate ($I_{HV2}[k]$, $V_{HV2}[k]$) is the operating point two steps ahead of the $V_{HV2}=V_{HV2_ref}$ line crossing where $D_f[k]=m$ is applied.
- $Q[k+1]$ in quadrant IV with co-ordinate ($I_{HV2}[k+1]$, $V_{HV2}[k+1]$) is the operating point one step ahead of the $V_{HV2}=V_{HV2_ref}$ line crossing where $D_f[k+1]=m+\Delta_f$ is applied.
- $Q[k+2]$ in quadrant I with co-ordinate ($I_{HV2}[k+2]$, $V_{HV2}[k+2]$) is the first operating point after crossing the $V_{HV2}=V_{HV2_ref}$ line where $D_f[k+2]=m$ is applied.
- $Q'[k+2]$ in quadrant I with co-ordinate ($I'_{HV2}[k+2]$, $V_{HV2}[k+2]$) is the first operating point after crossing the $V_{HV2}=V_{HV2_ref}$ line where $D_f[k+2]=m+2\Delta_f$ is applied.

As illustrated in Fig. 4.33, the operating point will move from $Q[k+1]$ to $Q'[k+2]$ by increasing D_f. Instead, the operating point will end up from $Q[k+1]$ to $Q[k+2]$ by decreasing D_f.

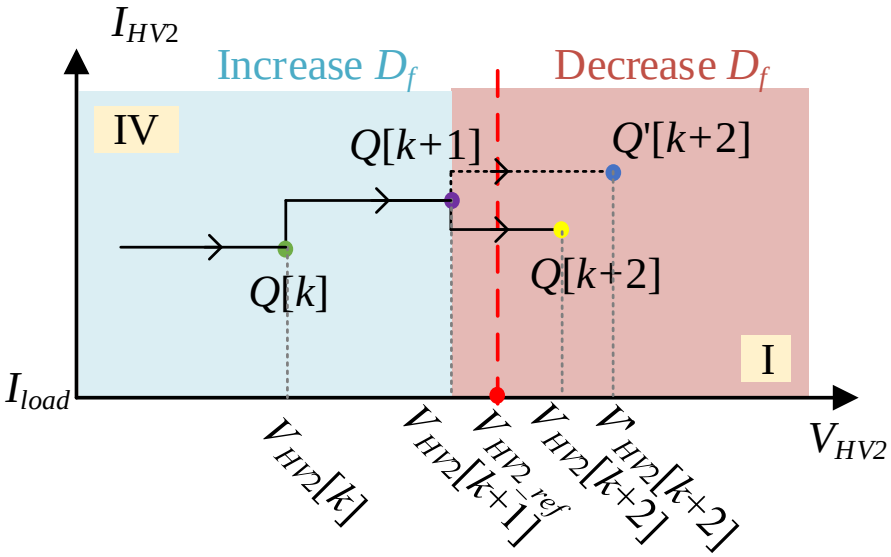


Fig. 4.33 Explaination on the mono-dimensional MDCS-MPC behaviours.

The operating principle of mono-dimensional MDCS-MPC described in Fig. 4.6 states that value $D_f[k+2]$ is determined in the control period k to $k+1$. During this control period, according to (4. 44) and (4. 46), (4. 63) can be concluded.

$$I_{HV2}[k+2] < I'_{HV2}[k+2] \ \& V_{HV2}[k+2] < V'_{HV2}[k+2] \tag{4. 63}$$

Therefore, based on the cost function defined in (4. 9), $D_f[k+2] = m$ presents a smaller ct. The mono-dimensional MDCS-MPC will always decrease D_f one step before crossing the $V_{HV2}=V_{HV2_ref}$ line when the operating point moves from quadrant IV to I and increase D_f one step before crossing the $V_{HV2}=V_{HV2_ref}$ line when the operating point moves from quadrant II to III. This control behaviour results in the movement direction of operating points in each region as shown in Fig. 4.32.

4.2.4.1 Current load

Based on the above knowledge, stability analysis can be conducted with current load. The illustration with current load is shown in Fig. 4.34 where the trajectory with MDCS-MPC in the blue line overlaps with that of the benchmark control in the grey line.

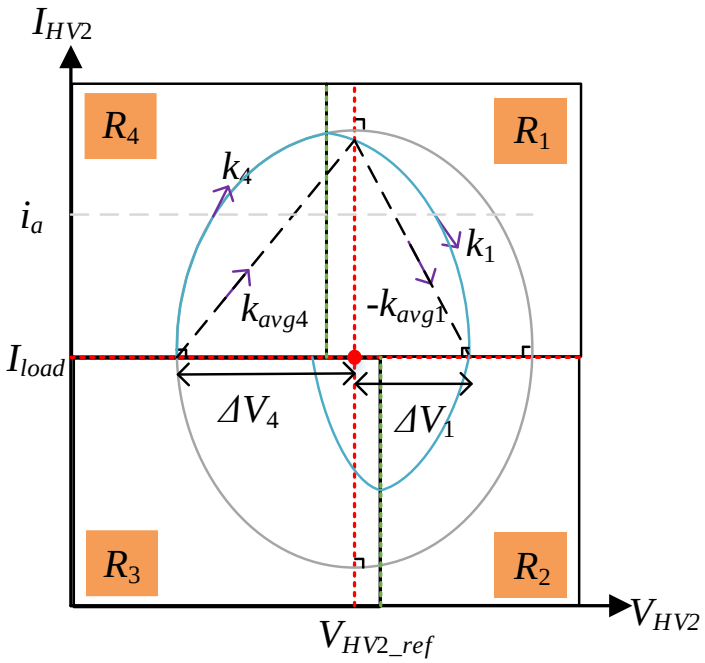


Fig. 4.34 Phase portrait in blue line with constant current load using the MDCS-MPC. Phase portrait in grey line with constant current load using the benchmark control.

According to previous analysis in Fig. 4.27, the blue line is symmetrical about the green dashed line while the grey line is symmetrical about the red dashed line. Referring to the formula (4. 36) and (4. 37), (4. 64) can be concluded when MDCS-MPC is used.

$$k_{avg\,4} < k_{avg1} \tag{4. 64}$$

According to statement 1,

$$\Delta V_1 < \Delta V_4 \tag{4. 65}$$

The same analysis can be carried out for the trajectory in R_3 and R_4. The operating point with constant load current when using MDCS-MPC, is slow, but will eventually converge to the steady state point. The analysis has explained the phenomena which happened in Fig. 4.7 where the current load is connected to DAB with mono-dimensional MDCS-MPC. Fig. 4.7(b) is zoomed in as shown in (4. 35), which verifies the analysis in Fig. 4.34.

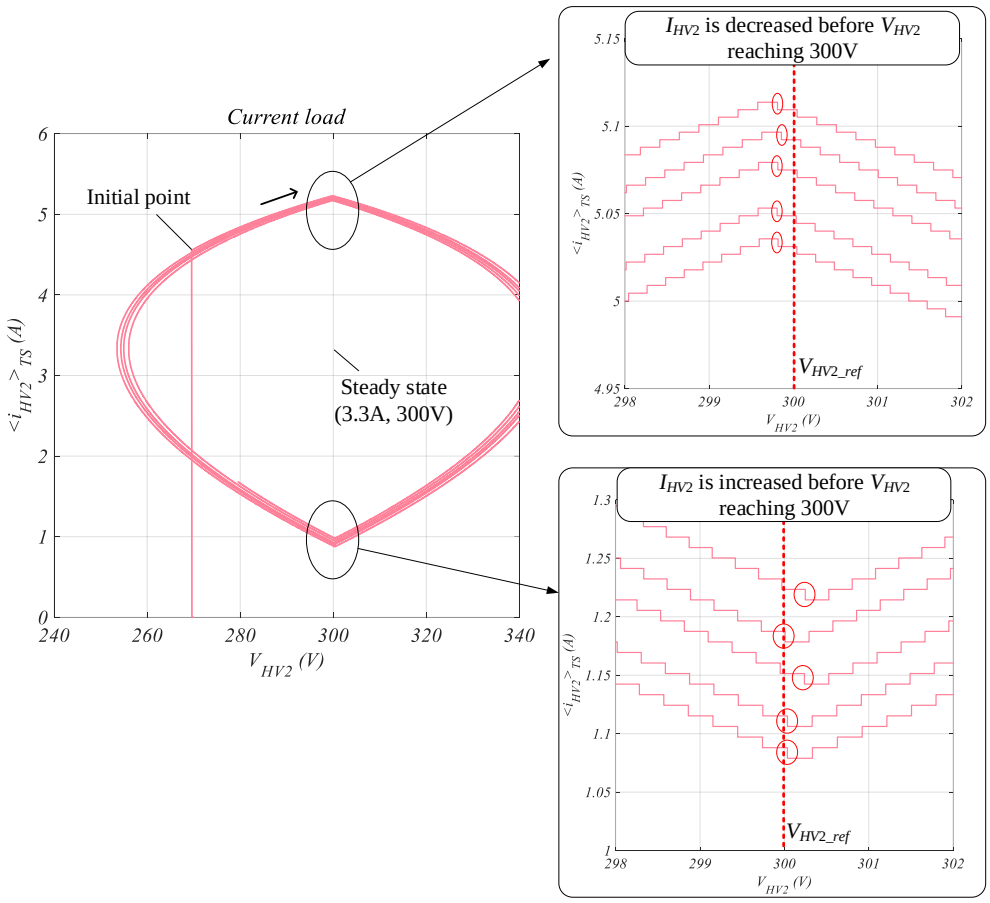


Fig. 4.35 Simulation results with constant load current I_{load} = 3.3A. μ = 3, V_{HV1}=300V,V_{HV2_ref}=300V.

It can be concluded that with the slight difference between the MDCS-MPC in Fig. 4.32 and the benchmark control in Fig. 4.23, the stability changes when the current load is connected.

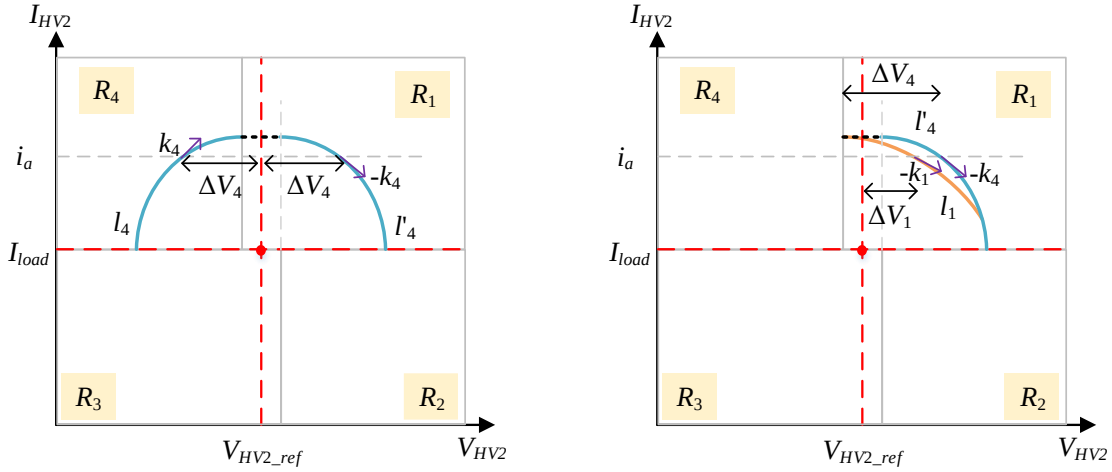
4.2.4.2 Adaptive step

The adaptive step approach introduced in section 4.1.3.2 tells that the adaptive step Δ_{adp} changes with the difference between the load voltage and its reference. When V_{HV2} is far from the reference, Δ_{adp} becomes large. In contrast, when V_{HV2} equals to the reference, Δ_{adp} contracts to Δ_f. When the adaptive step is enabled, the change rate of D_f becomes:

$$\frac{dD_f}{dt} = \Delta_f (1 + \Delta V^2) f_s \tag{4. 66}$$

Assuming l_4 in Fig. 4.36 (a) is the trajectory with adaptive step in region R_4. In order to explain the control behaviour with the adaptive step, V_{HV2}=V_{HV2_ref} is the line of symmetry to l_1 and l'_4.

Assuming l_1 is the trajectory with the adaptive step in region R_1, l_1 and l'_4 are overlapped in Fig. 4.36 (b).



(a) Reflection symmetry l_1 and l'_4 (b) overlap of l_1 and l'_4

Fig. 4.36 Explaination on the mono-dimensional MDCS-MPC behaviour with adaptive step.

According to (4. 47), the slopes in regions R_1 and R_4 are calculated as:

$$k_1 = \frac{C_{HV2}V_{HV1}}{L_p}\frac{1-4g^{-1}(i_a)}{i_a - I_{load}}\Delta_f(1+\Delta V_1^2) \tag{4. 67}$$

$$k_4 = \frac{C_{HV2}V_{HV1}}{L_p}\frac{1-4g^{-1}(i_a)}{i_a - I_{load}}\Delta_f(1+\Delta V_4^2) \tag{4. 68}$$

If

$$\Delta V_1 < \Delta V_4 \tag{4. 69}$$

then

$$k_1 < k_4 \tag{4. 70}$$

According to condition (4. 70), due to the adaptive step, l_1 will have a tendency to move towards l'_4. Once l_1 coincides with l'_4, they will have the same trajectory. Similar analysis can also be conducted for trajectories in R_3 and R_4. In conclusion, if l_1 coincides with l'_4, the operation is not stable. Although the adaptive step can improve the dynamic performance, it is a destabilizing factor to the control, which explains the phenomena in Fig. 4.14.

4.2.4.3 Impact of G_2

In order to guarantee the large signal stability of the mono-dimensional MDCS-MPC with the adaptive step, term G_2 is proposed as in (4. 16). Due to (4. 71), the cost function (4. 15) can also be written as (4. 72).

$$\frac{dV_{HV2}}{dt} = \frac{I_{HV2} - I_{load}}{C_{HV2}} \tag{4. 71}$$

$$ct = \alpha_1 (V_{HV2_ref} - V_{HV2})^2 + \frac{\alpha_2}{f_s{}^2 C_{HV2}^2} (I_{HV2} - I_{load})^2 \tag{4. 72}$$

In light of the mechanism presented in Fig. 4.34, the expansions of region R_2 and R_3 are conducive to the stability. The control behaviours of MDCS-MPC with G_2 are shown in Fig. 4.37.

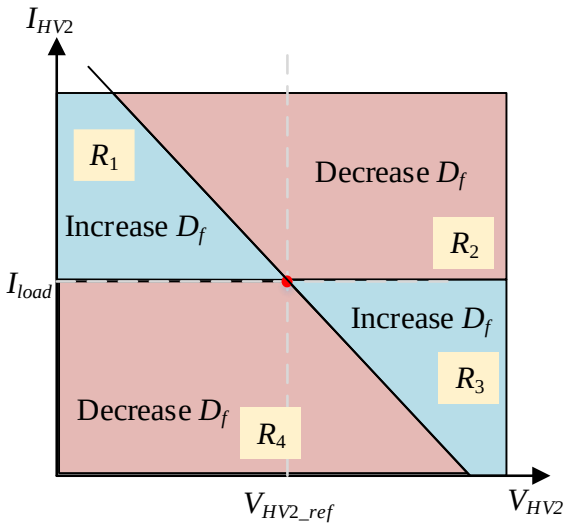


Fig. 4.37 Mono-dimensional MDCS-MPC control behaviours.

In order to explain the control behaviours of Fig. 4.37, Fig. 4.38 is presented. Assume the operating point is in the region R_4 coloured as a green dot in the figure.

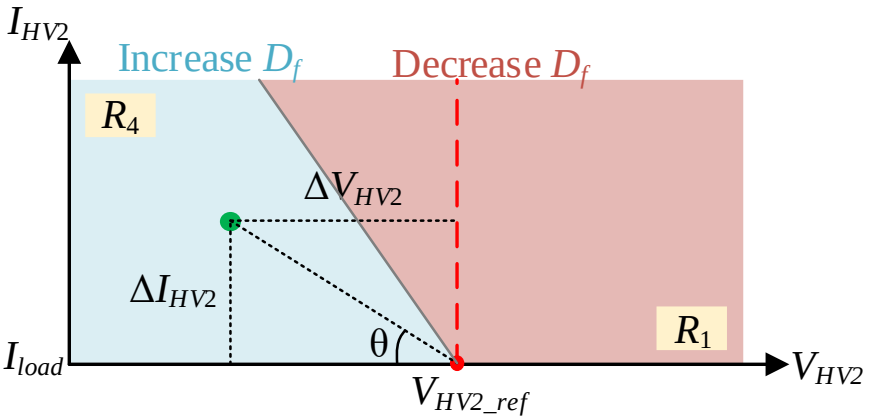


Fig. 4.38 Explaination on the mono-dimensional MDCS-MPC behaviours with G_2.

Based on the definition of *ct* in (4. 72), the derivative of *ct* with respect to the load voltage is calculated as:

$$\frac{\partial ct}{\partial V_{HV2}} = -2\alpha_1 \Delta V_{HV2} + \frac{2\alpha_2}{f_s^{\,2} C^2_{HV2}} \Delta I_{HV2} \tag{4. 73}$$

Therefore, if (4. 74) is satisfied, *ct* will decrease with V_{HV2}. The MDCS-MPC does not change the control behaviour.

$$\frac{\Delta I_{HV2}}{\Delta V_{HV2}} < \frac{\alpha_1}{\alpha_2} f_s^{\,2} C^2_{HV2} \tag{4. 74}$$

However, once (4. 75) is satisfied, *ct* will increase with V_{HV2}. The MDCS-MPC will decrease ΔI_{HV2} to slow down the increase of *ct*. The larger the weighting factor α_2, the smaller the angle θ will be, and the operation will be more stable. This conclusion has explained the phenomena in Fig. 4.15 - Fig. 4.18.

$$\frac{\Delta I_{HV2}}{\Delta V_{HV2}} \geq \frac{\alpha_1}{\alpha_2} f_s^{\,2} C^2_{HV2} \tag{4. 75}$$

4.3 Small signal analysis

In order to provide a quantitative assessment on the small signal dynamic performance of the mono-dimensional MDCS-MPC, the frequency response is utilized. The small signal models of DAB converters are often carried out to analytically derive their frequency response.

However, it is infeasible to describe the DAB converters with non-linear controllers. Another approach is utilized here. If a certain small sinusoidal perturbation signal that is applied to a nonlinear element always excites a sinusoid at the same frequency in the output, then such an element can be represented by its linear "equivalent" frequency response, which is commonly called a describing function (see [118], ch.5). As a result, standard frequency domain techniques can be used to assess the characteristics of the converter which comprises nonlinear elements [119]. As for the analytical method (small signal modelling), the describing function method also needs to have assessments carried out based on a given equilibrium point. Small signal perturbations have been injected into the converter and responses have been measured with the correspondent frequency. This numerical method applies to both linear and non-linear controls.

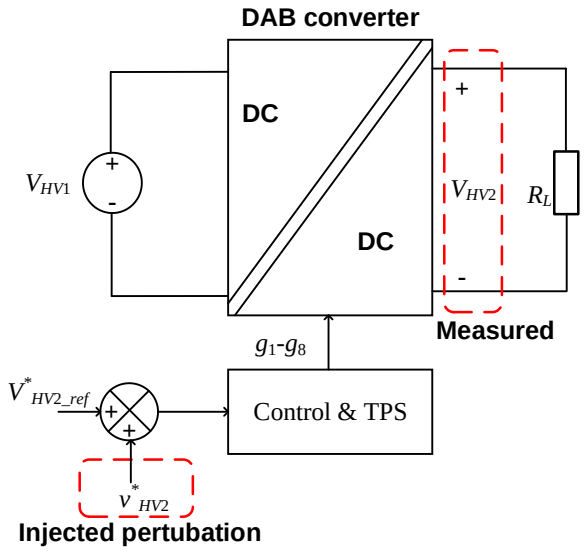


Fig. 4.39 Frequency response sweeping circuit.

The AC sweepings are carried out in the switching model with the equilibrium point 260V/300V 1kW. Perturbations from 10Hz to 10kHz with amplitude of 0.01V are superimposed on the output voltage equilibrium value V_{HV2_ref}=300V as shown in Fig. 4.39. The closed-loop transfer function is defined as in (4. 76).

$$G_{R2O}(f) = \frac{V_{HV2}(f)}{v^*_{HV2}(f)} \tag{4. 76}$$

The results are presented in Fig. 4.40. In the figure, the closed-loop transfer functions in the frequency domain with different values of α_2 and μ are shown. In observation of the solid lines

(α_2=1), μ increases the amplitude of $G_{R2O}(f)$ in the high frequency range. When comparing lines with round markers (μ=3), it can be concluded that α_2 has a negative impact to the amplitude of $G_{R2O}(f)$ in the low to medium frequency range. It can be concluded that parameters α_2 and μ have clear implications on $G_{R2O}(f)$. Comparisons on $G_{R2O}(f)$ between the MDCS-MPC and the PI control discussed in Chapter 2 are also available in the figure. The PI parameters are designed based on the ideal/mathematical model under the equilibrium point 260V/300V 1kW. The control parameters are designed as K_p=0.05, K_i=10. The gain and phase margins are 15.4dB and 72deg, respectively. The crossover frequency is 570Hz. As shown in the figure, the frequency response line of PI sits between the blue and red lines of MDCS-MPC. If tuned with α_2=1 and a μ between 3 and 11, the MDCS-MPC can present very similar frequency responses as the designed PI.

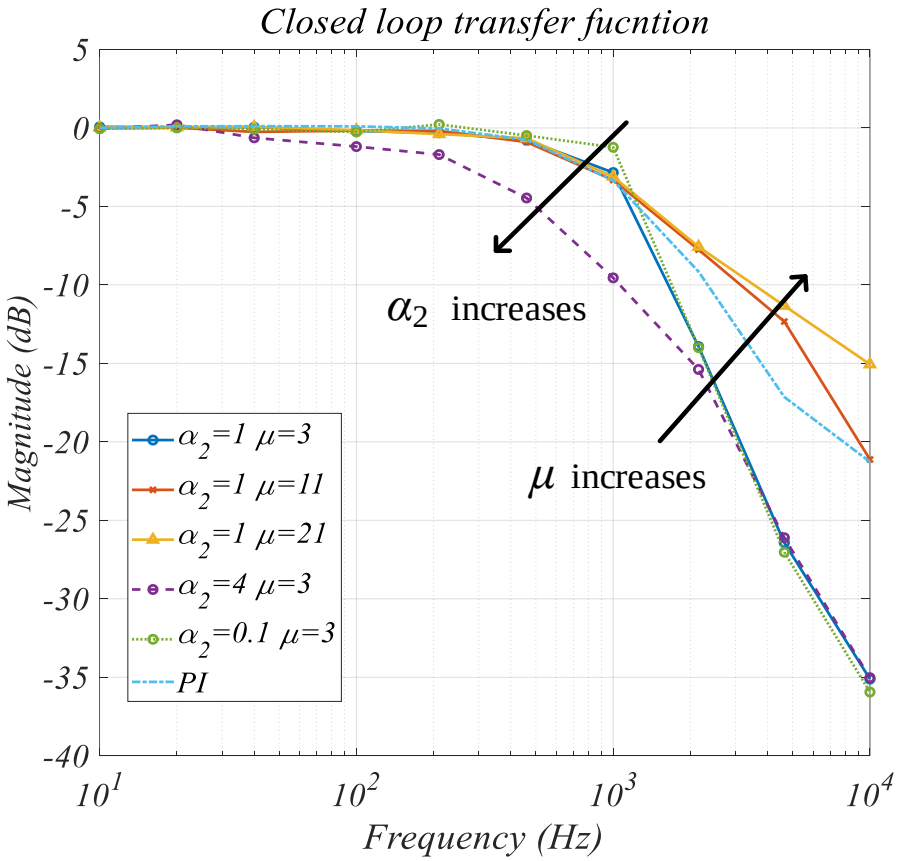


Fig. 4.40 Sweeping results for $G_{R2O}(f)$ in (4. 76) under equilibrium point 260V/300V 1kW

Evaluations on $G_{R2O}(f)$ with different terminal voltages are shown in Fig. 4.41. When MDCS-MPC is used, $G_{R2O}(f)$ can largely be maintained with different terminal voltages. In comparison, the control parameters of the PI have to be designed based on a single equilibrium point. When

the operating point varies, $G_{R2O}(f)$ will change too. As shown in Fig. 4.41, when the input voltage V_{HV1} reduces from 260V (yellow line) to 180V (purple line), the amplitude of $G_{R2O}(f)$ varies significantly with the PI controller.

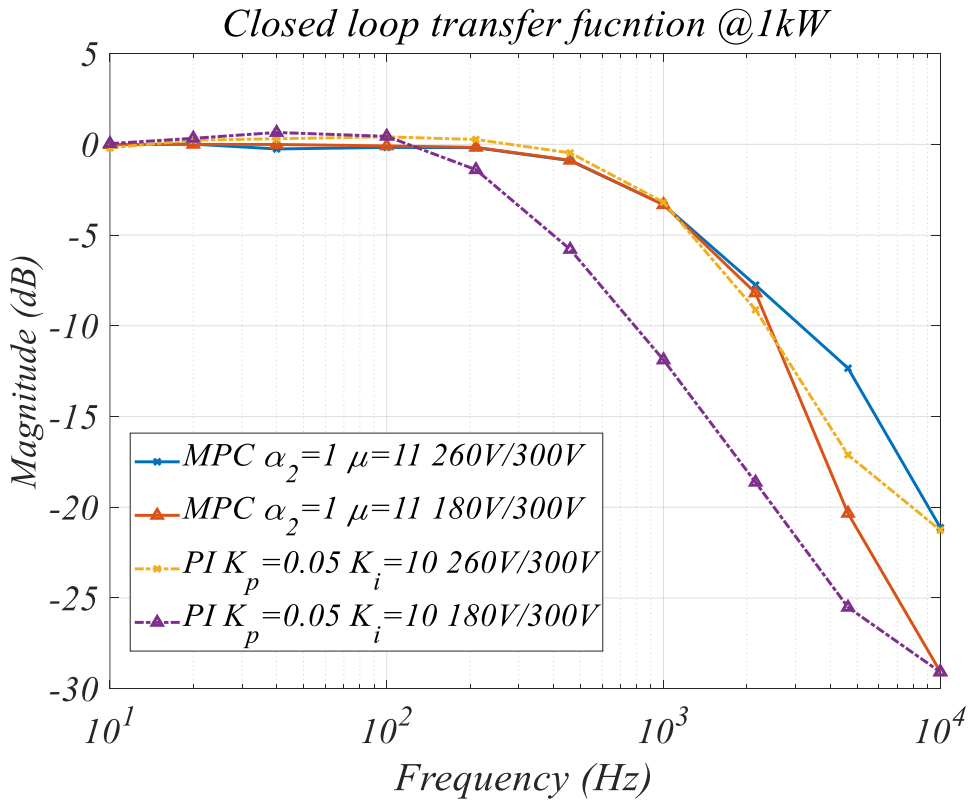


Fig. 4.41 Frequency response with different input voltages in TPS

The reference tracking performance of the PI and the proposed method in the time domain have also been compared. As shown in Fig. 4.42, the load voltage reference changes between 300V and 260V. At time instance t_1, when the proposed control is used, D_3 starts to increase 0.55ms before V_{HV2} reaches reference 260V. In contrast, when PI is used, D_3 can only start to increase once V_{HV2} reaches 260V. A similar phenomena can also be observed at time instances t_3 and t_4. This feature ensures that MDCS-MPC provides better voltage tracking performance, as has also been verified in the experiments section 4.4 Fig. 4.48 and Fig. 4.49.

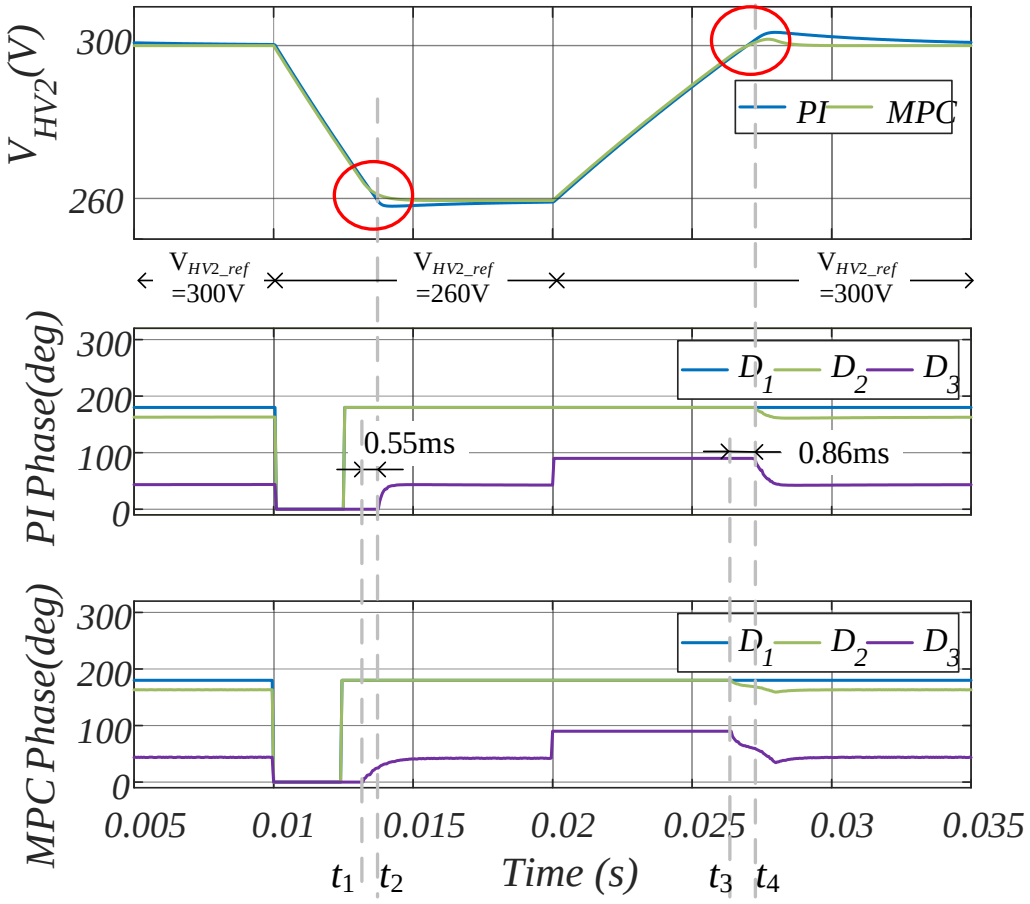


Fig. 4.42 Load voltage reference tracking.

4.4 Practical results

The experiment results are presented in this section. The description of the setup has been presented in Chapter 2 section 2.7.

4.4.1 Stability

Experiments are carried out where both the source voltage V_{HV1} and the load voltage reference V_{HV2_ref} are 300V. The DAB is connected a resistive load, the mono-dimension MDCS-MPC with SPS is used where μ=7, α_2=0, and the adaptive step is not enabled. In the experiment shown in Fig. 4.43, a load step up change is applied. The recovery time is significantly long.

There are two measures to improve the dynamic: increase μ and enable the adaptive step as shown in Fig. 4.44. The same test condition as in Fig. 4.43 is used to obtain the waveforms in Fig. 4.44. It can be seen from the figure that the convergence issue arises when the dynamic is improved. This has been explained in section 4.2.

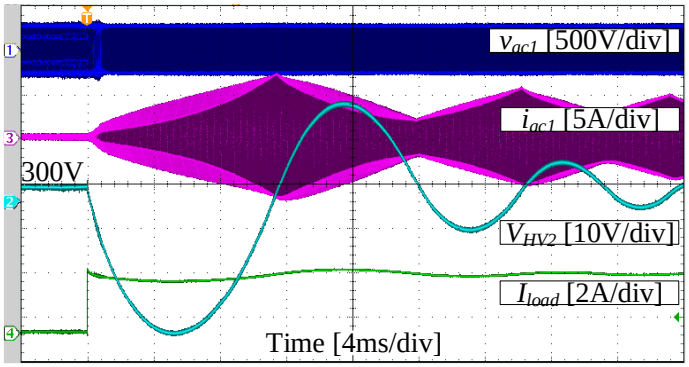


Fig. 4.43 Load step up response with μ=7 and α_2=0

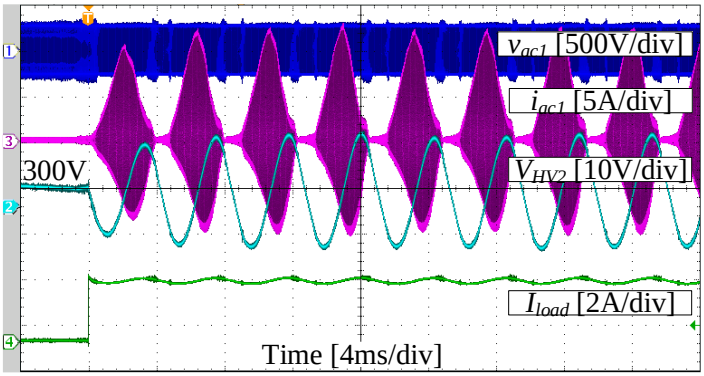


Fig. 4.44 Load step up with adaptive step, μ=7 and α_2=0.

After G_2 is enabled in the cost function, as analysed in section 4.2.4.3, the weighting factor α_2 provides stabilization to the operation of MDCS-MPC as shown in Fig. 4.45.

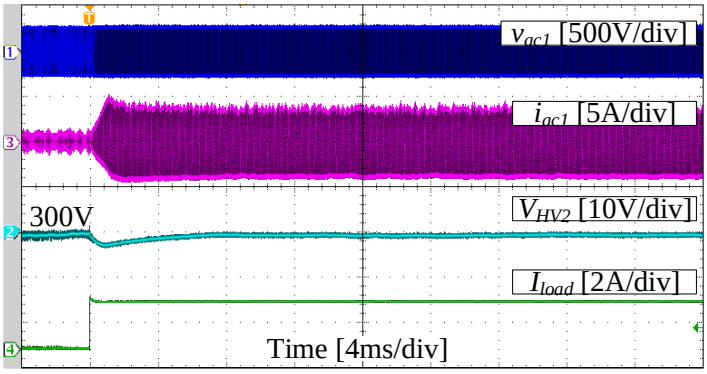


Fig. 4.45 Load step up with adaptive step, μ=7 and α_2=4.

4.4.2 Steady state

The effectiveness of the steady state error compensation loop is verified in experiments with TPS. Waveforms of the MDCS-MPC without compensation are captured in presence of load variation at 20Hz as in Fig. 4.46. Except for the existence of the steady state error, without compensation, the proposed MDCS-MPC demonstrates a superior load disturbance rejection ability in the experiment. There is no oscillation in either transition or steady state. It is clear that there is a difference between the steady state values when changing the load power. When the compensation loop is enabled, the steady error can be much smaller compared to the results without compensations. Fig. 4.47 shows the steady state measurement results of the output voltage mean value.

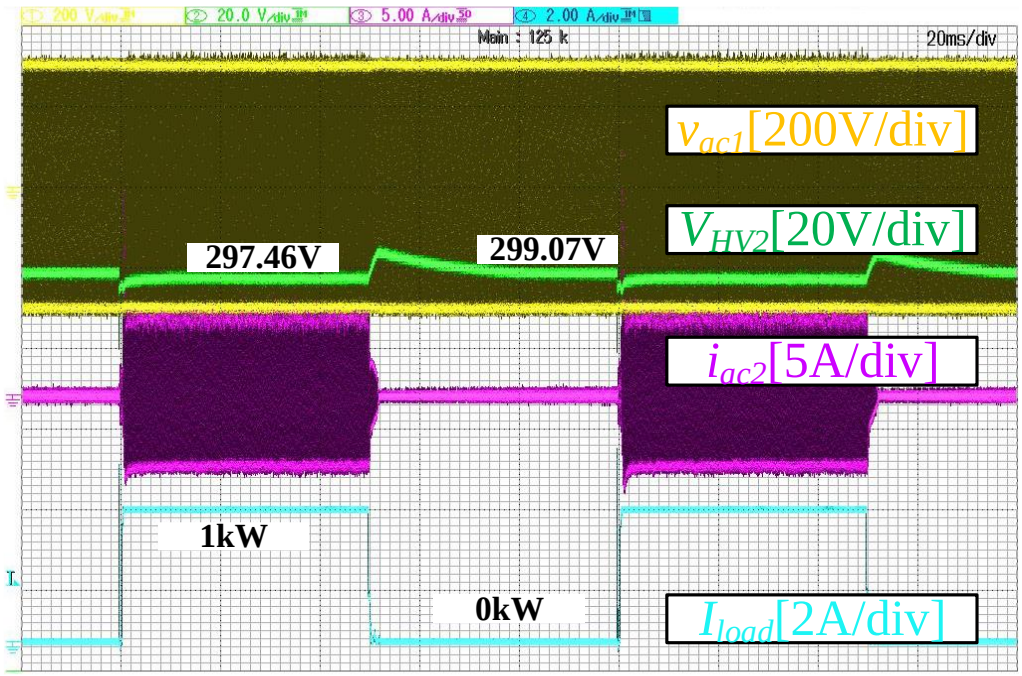


Fig. 4.46 MDCS-MPC controlled DAB loaded with load variations @20Hz. Prediction compensation disabled. V_{HV1}=300V, V_{HV2_ref}=300V.

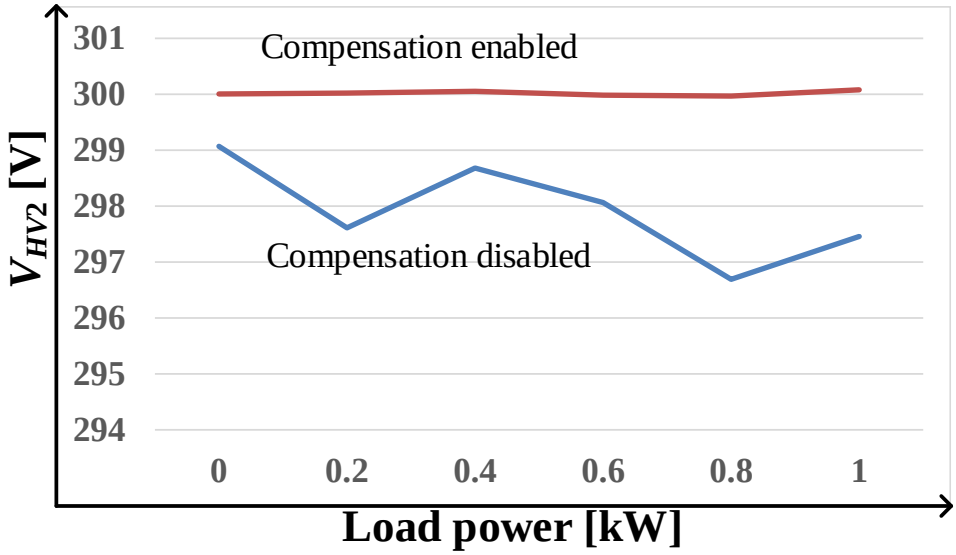
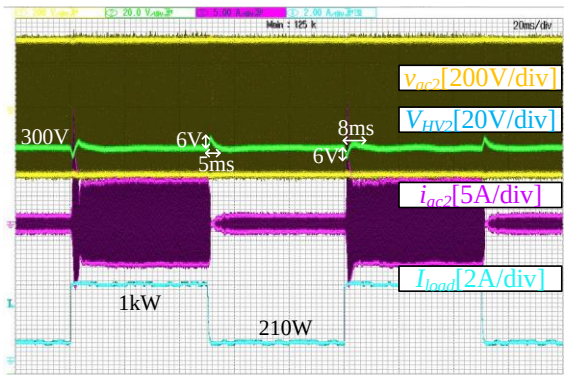


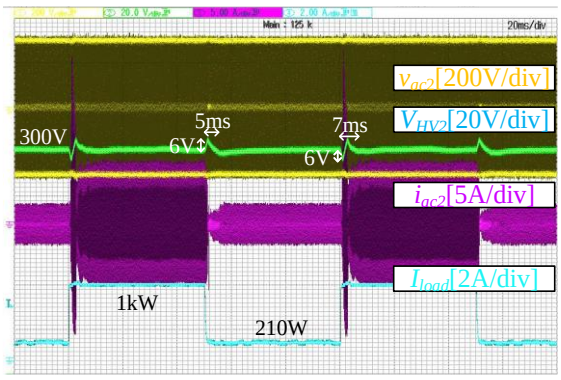
Fig. 4.47 Compensation for the prediction error. Operation under V_{HV1}=300V, V_{HV2_ref}=300V over the whole power range.

4.4.3 Dynamic

Dynamic experiments with MDCS-MPC are conducted in comparison with the PI control designed in Chapter 2 section 2.6. In Fig. 4.48(b) and Fig. 4.49(b), the input voltage is set at 260V, load voltage reference remains at 300V. The load power jumps between 1kW and 210W at a frequency of 20Hz. The performance of TPS deteriorates with the PI controller. In contrast, when MDCS-MPC is used, the performance remains good even when the terminal voltage is changed. The MDCS-MPC has good performance throughout the voltage and power range.

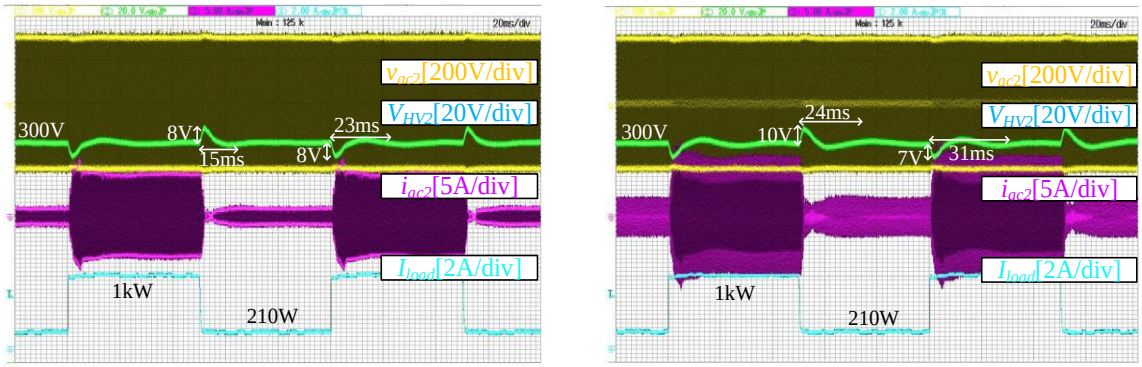


(a) V_{HV1}=300V, V_{HV2_ref}=300V



(b) V_{HV1}=260V, V_{HV2_ref}=300V

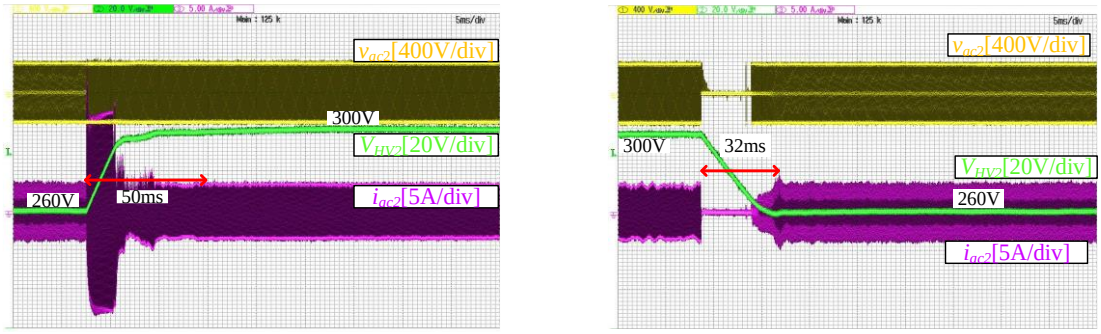
Fig. 4.48 Load step up/down using MDCS-MPC in TPS



(a) V_{HV1}=300V, V_{HV2_ref}=300V (b) V_{HV1}=260V, V_{HV2_ref}=300V

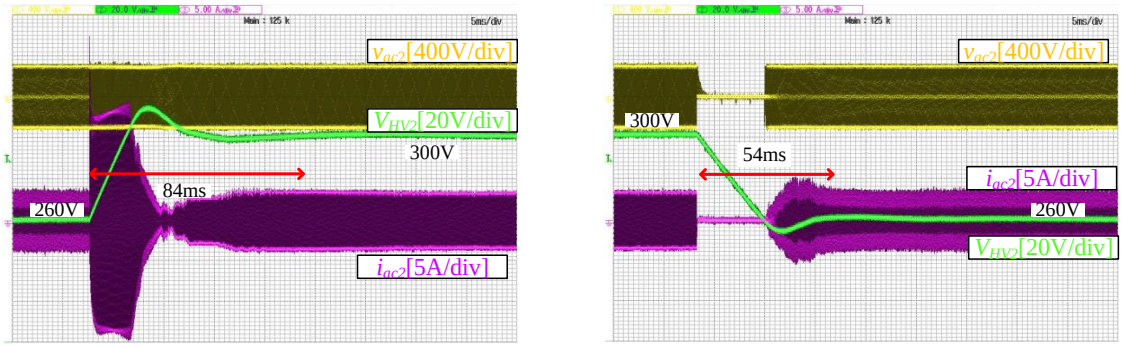
Fig. 4.49 Load step up/down using the PI controller in TPS

Experiments on the step change of the reference voltage are also conducted. The output voltage reference is changed between 260V and 300V. The transition results are presented in Fig. 4.50 and Fig. 4.51. In the experiment with MDCS-MPC, the voltage overshoot/dig is very small, thus ending in fast voltage tracking compared to the PI controller. The results again confirm the superior performance of the proposed MDCS-MPC in the regulation of load voltage. It is worth mentioning that the DC source is uni-directional. So the DAB is controlled uni-directional. When reference steps down, there is a period of time when the energy on the output capacito is only consumed by load.



(a) from 260V to 300V (b) from 300V to 260V

Fig. 4.50 Change of voltage reference V_{HV2_ref} with MDCS-MPC



(a) from 260V to 300V (b) from 300V to 260V

Fig. 4.51 Change of voltage reference V_{HV2_ref} with PI

4.4.4 Computation burden

The computational time of the MDCS-MPC with TPS is evaluated as shown in Fig. 4.52. The PI controller takes 4.2us to run while, in contrast, the time to run MDCS-MPC varies with μ. In the experiment, μ=11 has already demonstrated good performance against the PI controller, and it only takes 18.6us. Since a 20 kHz switching frequency is utilized, 50us is available in one sampling period. Therefore, there is sufficient headroom for implementing A/D sampling, digital filters, MODBUS communication, protections etc.

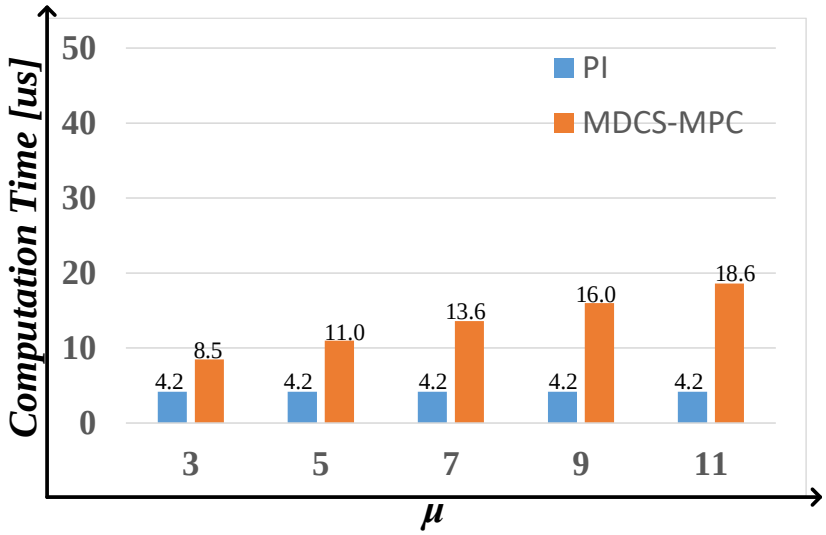


Fig. 4.52 Measurement of computational time.

4.5 Chapter summary

The mono-dimensional MDCS-MPC which provides fast transition and large signal stability is presented in this chapter for DAB. The MDCS-MPC relies on the average model of DAB to derive the optimal control output by minimizing the cost function.

The introduction of MDCDS-MPC begins with the basic operating principle. Two approaches to enhance the transition performance of MDCS-MPC are discussed. A cost function which

provides both reference racking and stability is derived. A compensation approach has been proposed to compensate for the steady state error.

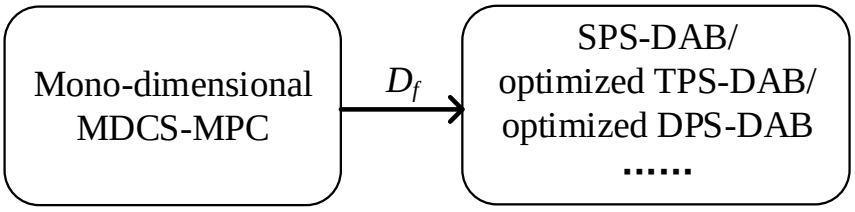
The stability analysis is carried out for MDCS-MPC. The phase portrait has been used as the main analysis tool. Three statements have been proposed to underpin the stability proof. For an easy start, a benchmark control is assumed where stability with current/resistive loads are analysed and proofed. The instability when controlled current saturates is explained. Based on all the above analysis, the stability with MDCS-MPC is addressed. This chapter has explained why the operation with current loads converges slowly, why the adaptive step makes the operation instable and why G_2 can stabilize the operation.

All the theoretical claims in this chapter have been verified by both simulation and practical results.

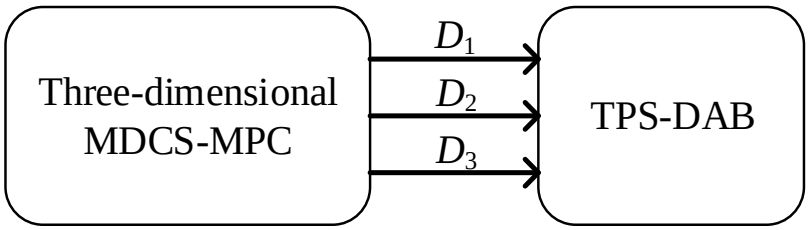
Chapter 5 Multi-dimensional MDCS-MPC

When the mono-dimensional MDCS-MPC is used, as addressed in Chapter 4, there is only one control output. However, modulations such as DPS and TPS have more than one control variable. Therefore, in order to enable those modulations with mono-dimensional MDCS-MPC, the number of control variables has to be reduced down to one by conducting offline optimization as addressed in Chapter 2 section 2.4. The offline optimizations look into only the steady state efficiency improvements, which are not necessarily the optimal for dynamic performance.

In this chapter, multi-dimensional MDCS-MPC is introduced. The multi-dimensional MDCS-MPC has more than one output. A comparison between the mono-dimensional MDCS-MPC and the multi-dimensional MDCS-MPC is shown in Fig. 5.1. The optimization is conducted online with the multi-dimensional MDCS-MPC, which gives greater freedom to achieve faster dynamics whilst maintaining steady state efficiency compared to offline optimizations.



(a) Mono-dimensional MDCS-MPC with SPS or offline optimized modulations



(b) Three-dimensional MDCS-MPC with TPS

Fig. 5.1 Mono-dimensional and multi-dimensional MDCS-MPC.

In this chapter, aiming to facilitate a clearer illustration, a two-dimensional MDCS-MPC with DPS shown in Fig. 5.2 is used to explain the theory that is also applicable to higher dimensional MDCS-MPC. The motivation of implementing online optimizations on advanced modulations with multi-dimensional MDCS-MPC is addressed in section 5.1. In section 5.2, the discretised

model of DPS is derived where two independent control variables are involved. The two-dimensional MDCS-MPC utilizes the derived discretised model to predict future values of the load current, based on which calculations of the cost function are re-iterated. The operating principle of a two-dimensional MDCS-MPC resembles the description in Chapter 4 section 4.1.2. However, differences are addressed in section 5.3 including the extension of the discretised control set and the use of two-dimensional searching method. In section 5.4, a cost function with a current stress minimization term is proposed. Performance evaluations of the two-dimensional MDCS-MPC are provided in section 5.5. Section 5.6 concludes this chapter.

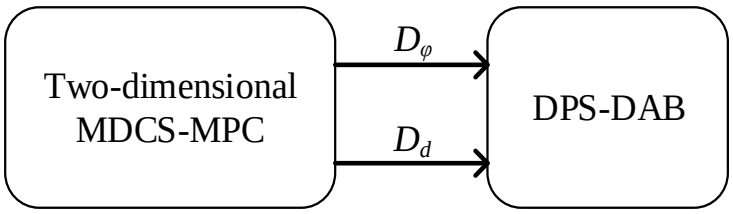


Fig. 5.2 Two-dimensional MDCS-MPC with DPS

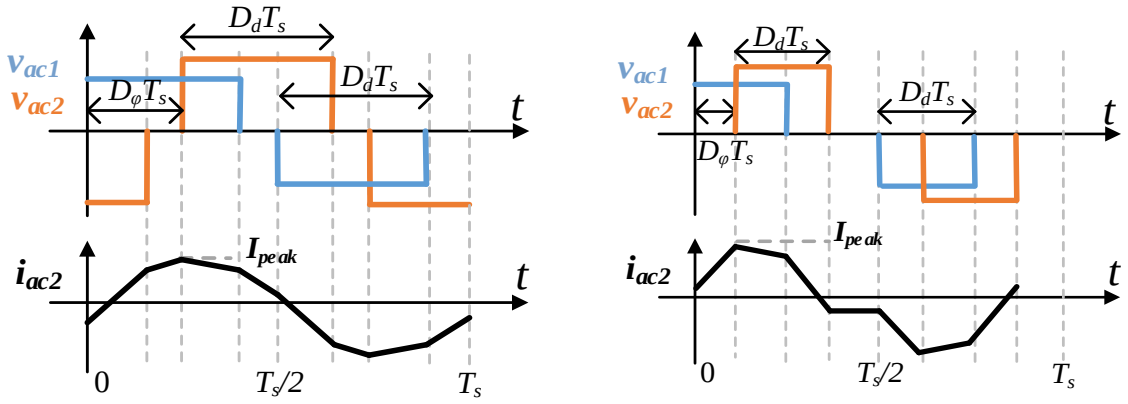
5.1 Online v.s. offline optimization

The advantage of carrying out the online optimization with multi-dimensional MDCS-MPC over the offline optimization is explained in this section. As introduced in Chapter 2 section 2.2, active duties D_1 and D_2 are kept equal as D_d while the phase shift duty D_φ is controlled independently from D_d in the DPS. Both variables range from 0 to 0.5.

According to the relationship between D_φ and D_d, there are four operating modes in DPS. They are identified as Mode I – Mode IV as in (5. 1). Each mode correspondends to a different expression for calculating the operating power. DPS predominately works in Mode I and Mode II depending on the load power [44]. Mode I can transfer more power than Mode II. Therefore, in the following discussion, only Mode I and Mode II of DPS are involved.

$$\begin{cases} Mode\ I:\ D_\varphi < D_d < 0.5 - D_\varphi \\ Mode\ II:\ 0.5 - D_d < D_\varphi < D_d \\ Mode\ III:\ 0.5 - D_\varphi < D_d < D_\varphi \\ Mode\ IV:\ D_d < D_\varphi < 0.5 - D_d \end{cases} \quad (5.\ 1)$$

The generic transformer voltage and current waveforms for DPS Mode I and Mode II are shown in Fig. 5.3. The transformer peak current is designated as I_{peak}.



(a) Mode I: $0.5\text{-}D_d<D_\varphi<D_d$ (b) Mode II: $0<D_\varphi<Min\{0.5\text{-}D_d,D_d\}$

Fig. 5.3 Generic waveforms for predominant operating modes in DPS.

The offline minimization on the transformer peak current I_{peak} has been conducted by *L. Chen et al.* [44]. Results are given as in (5. 2).

$$D_d = \begin{cases} \dfrac{2(2M+1)}{2M-1} D_\varphi, & D_\varphi < \dfrac{2M-1}{8M} \ \&\ M > 0.5 \\ 2(2M-1)D_\varphi + \dfrac{3-2M}{2}, & D_\varphi > \dfrac{2M-1}{8M} \ \&\ M > 0.5 \\ \dfrac{2(1+2M)}{1-2M} D_\varphi, & D_\varphi < \dfrac{1-2M}{4} \ \&\ M < 0.5 \\ \dfrac{1-2M}{M} D_\varphi + \dfrac{6M-1}{4M}, & D_\varphi > \dfrac{1-2M}{4} \ \&\ M < 0.5 \end{cases} \quad (5.\ 2)$$

, where

$$M = \frac{V_{HV2}}{V_{HV1}} \tag{5. 3}$$

The trajectories of (5. 2) are plotted in Fig. 5.4. According to Table 2.4 in Chapter 2 section 2.4.1, power contours of DSP-DAB are represented by black lines in the figure[44]. Lines with other colours stand for operating trajectories with different values of terminal voltage ratio M. D_φ can be calculated by (5. 2) with the value of D_d generated from the controller. It can be seen from the figure that the operating trajectories have to follow predefined paths.

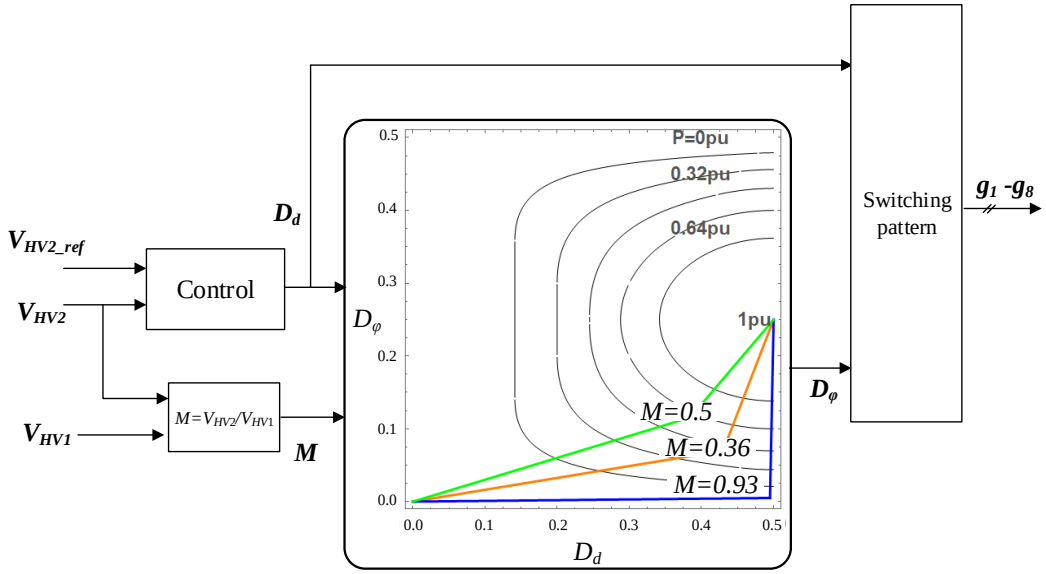
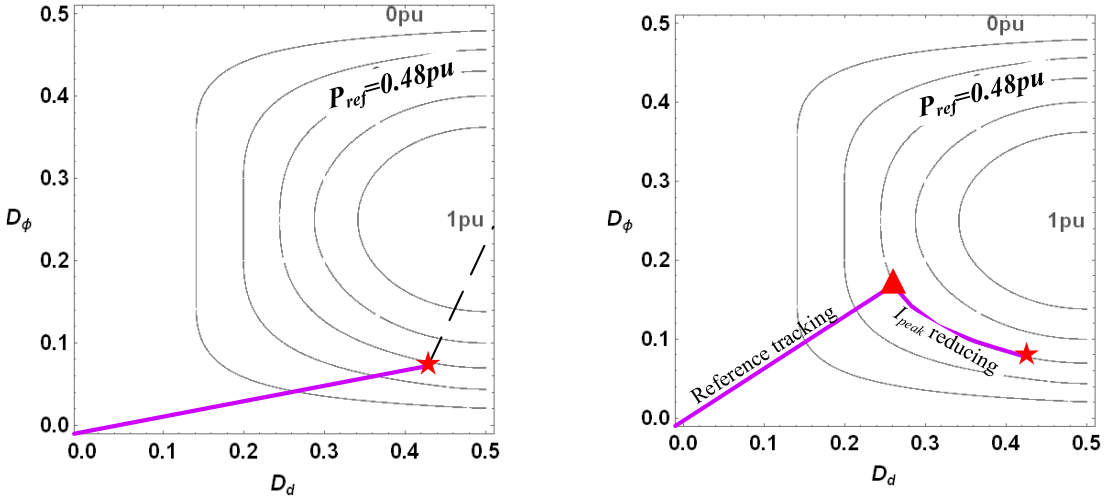


Fig. 5.4 Minimum transformer current stress trajectories with different terminal voltage ratio M.

In this chapter, a two-dimensional MDCS-MPC is proposed to break the restriction defined in (5. 2). For example, as shown in Fig. 5.5(a), assuming the power reference is 0.48pu, if the offline operating optimization is used, the operating point moves from the origin to the steady state (marked with a red star) based on a predefined path. D_φ increases linearly with D_d.

Alternatively, another trajectory in Fig. 5.5(b) breaks down the process into two phases. In the first phase, the operating point moves from the origin to the reference power following the trajectory perpendicular to the power contour line. In such a way, the operating power reaches its reference by the shortest path. In the second phase, the operating point slides on the 0.48 power contour line until it reaches the same red star as in Fig. 5.5(a). During the second phase, the operating power remains fixed while only the transformer peak current is being reduced.

The operating trajectory described in Fig. 5.5(b) allows the converter to achieve both fast transition performance and minimum steady state transformer peak current. In the following sections, the implementation of the trajectory described in Fig. 5.5(b) based on the two-dimensional MDCS-MPC is explained.



(a) Predefined trajectory (b) Ideal trajectory

Fig. 5.5 Tracking trajectory comparison

5.2 Mathematical model

The control objectives in this chapter are to regulate the load current and to minimize the transformer peak current. The two-dimensional MDCS-MPC relies on the discretized model of DAB to obtain the optimal control output (D_d, D_φ) by minimizing the cost function. In this section, the discretized model is developed based on the reduced order model which has been addressed in Chapter 4. The reduced order model of DAB is shown in Fig. 5.6.

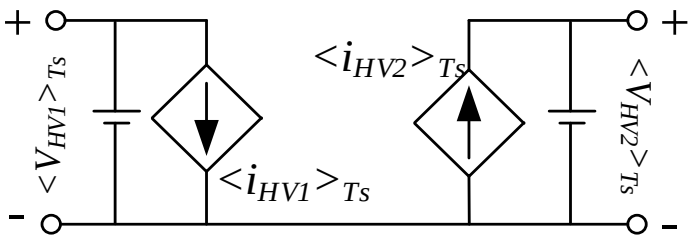


Fig. 5.6 The reduced order model.

Defining a function $\varepsilon(t)$ representing the polarity of the voltage v_{ac2} as:

$$\varepsilon(t)=\begin{cases}1, & v_{ac2}>0\\ -1, & v_{ac2}<0\end{cases} \tag{5. 4}$$

When DPS is used, the controlled current $<i_{HV2}>_{Ts}$ on the secondary side can be calculated as:

$$<i_{HV2}>_{T_s}=\frac{1}{T_s}\int_{T_s}\varepsilon(t)i_{ac2}(t)dt \tag{5. 5}$$

, where i_{ac2} is the transformer secondary side current. The results of (5. 5) are presented in Table 5.1.

TABLE 5.1 THE AVERAGE MODEL OF DPS

Mode	$<i_{HV2}>_{Ts}$
I	$\frac{<V_{HV1}>_{Ts}[D_\varphi-2D_\varphi^{\,2}-(D_d-0.5)^2]}{L_p f_s}$
II	$\frac{<V_{HV1}>_{Ts} D_\varphi(2D_d-D_\varphi)}{L_p f_s}$

5.2.1 Challenge with PI

For convenience, $<i_{HV2}>_{Ts}$ is replaced by i_{HV2} in the following descriptions. The small signal model of the transfer function from D_d to i_{HV2} is obtained numerically by using the circuit parameters in Chapter 2 section 2.7. The sweeping diagram is shown as Fig. 5.7. Sinusoidal small perturbations are injected and superimposed on the steady state value of $\overline{D_d}$. Correspondent frequency components of the load current are measured. The control to output transfer function can be then calculated based on the measured data.

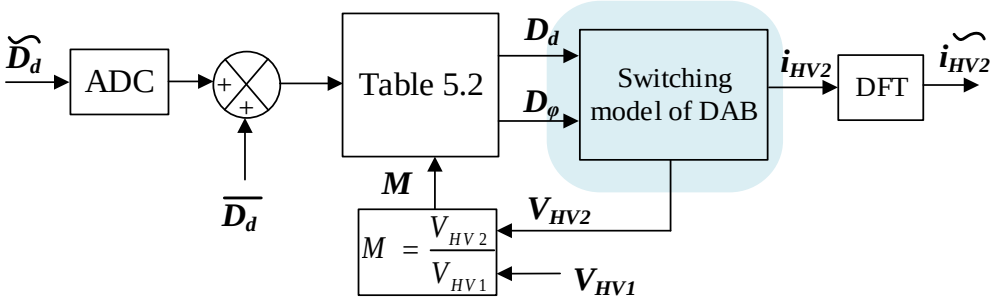


Fig. 5.7 Sweeping diagram of the transfer function $G_{DPS}(s)=i_{HV2}(s)/D_f(s)$.

Results are shown in Fig. 5.8 for two equilibrium points where $\overline{D_d}$ equals 30 degrees and 170 degrees. There exists roughly 20dB difference in magnitude posing difficulty for the design of PI controllers. However, when the MDCS-MPC is used, the terminal voltage information and the circuit model are embedded in the control algorithm. The control parameters associated with MDCS-MPC are expected to work in the full terminal voltage and power range. Detailed implementation of the two-dimensional MDCS-MPC is going to be addressed in sections 5.3 and 5.4 in the chapter.

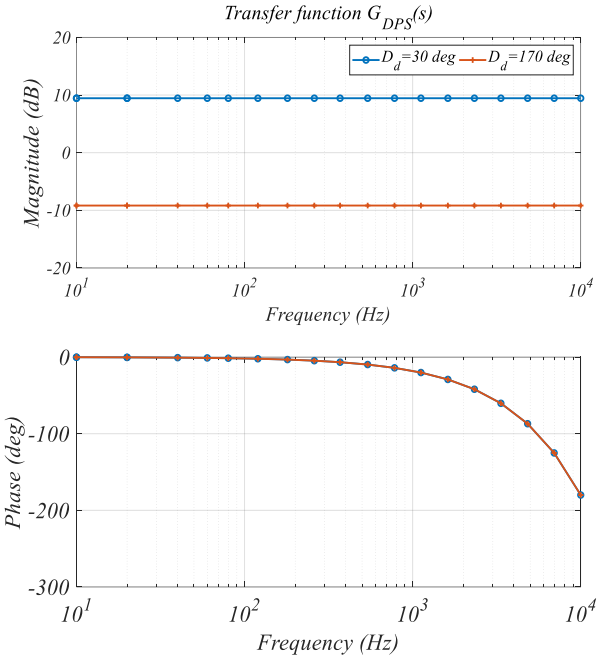


Fig. 5.8 Sweeping results of two equilibrium points. The transfer function $G_{DPS}(s)=i_{HV2}(s)/D_f(s)$ is tested under 250V/270V terminal voltage condition.

5.2.2 Error correction

In practice, the calculation of i_{HV2} in Table 5.1 has errors due to the dead time, copper losses and core losses etc. Therefore, the load current prediction may not be accurate enough in Table 5.1. In order to address this issue, a compensation current I_{comp} is introduced and defined as in (5. 6). I_{comp} is calculated as the difference between the measured load current value i_{HV2_m} and the predicted value i_{HV2}.

$$I_{comp}[k] = i_{HV2_m}[k-1] - i_{HV2}[k-1] \tag{5. 6}$$

, where $i_{HV2_m}[k+1]$ is the measured load current at time instance k-1. The compensated load current prediction value at k+1 can be calculated as:

$$i^*_{HV2}[k+1] = i_{HV2}[k+1] + I_{comp}[k] \quad (5.\ 7)$$

5.3 Operating principle

A preliminary cost function is given in (5. 8). It regulates the load current i^*_{HV2} to its reference i_{ref}. It is worth mentioning that ct in (5. 8) is not the finalized cost function, but one meant to help illustrate the operating principle of the two-dimensional MDCS-MPC.

$$ct = (i_{ref} - i^*_{HV2}[k+1])^2 \quad (5.\ 8)$$

Two control variables D_d and D_φ are continuous in nature, however, in the digital control, D_d and D_φ need to be discretized. As with the mono-dimensional MDCS-MPC, the smallest phase shift value Δ_f that can be achieved in a digital control platform is calculated as:

$$\Delta_f = \frac{f_s}{f_c} \quad (5.\ 9)$$

, where f_c is the peripheral clock frequency of the digital control platform. f_s is the switching frequency. In this section, f_c=100Mhz, f_s=20kHz. Therefore, Δ_f equals 0.0002. Each of D_d and D_φ has been discretized into 0.5/Δ_f+1 elements for unidirectional power flow. Arrays in (5. 10) describe the discretised control sets for DSP-DAB.

$$D_\varphi, D_d \in \{0, \Delta_f, 2\Delta_f, \cdots, 0.5\} \quad (5.\ 10)$$

In the digital control, the power contour plot has a discretised axis as shown in Fig. 5.9. The operating point in the contour plot is written as (D_d, D_φ). There are, in total, (0.5/Δ_f+1)^2 points to be calculated in this plot.

Calculating all of the possible operating points in one switching period is not practical on most standard microcontrollers. Therefore, similarly to the mono-dimensional MDCS-MPC introduced in Chapter 4, a reduced number of points is assessed in one switching period. In the

example shown in Fig. 5.10, μ(=9) points consist a control set that is assessed centred at the previous operating point (a, b).

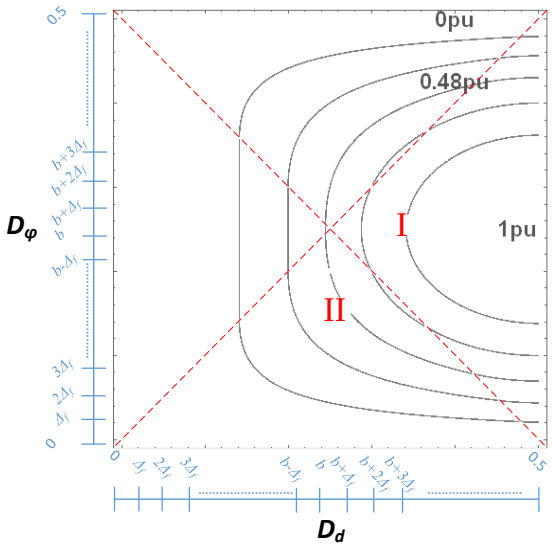


Fig. 5.9 Discretised control variables in DPS.

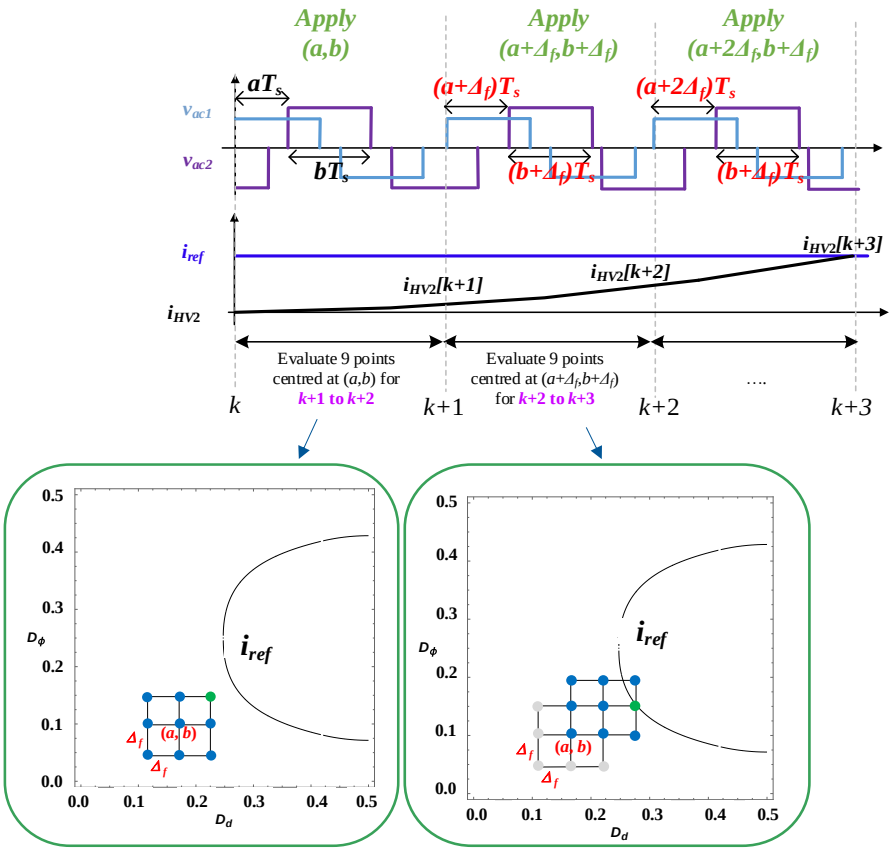


Fig. 5.10 A conceptual process of the 2D MDCS-MPC

Fig. 5.11 describes how the control set moves with the operation illustrated in Fig. 5.10. During the control interval k to k+1 as shown in Fig. 5.11(a), nine points are evaluated centred at (a,b). According to the illustration in Fig. 5.10, the point ($a+\Delta_f$, $b+\Delta_f$) has the shortest distance to the reference contour resulting in the minimum ct. Therefore, this point is applied at time instance k+1. In the next control interval k+1 to k+2 as shown in Fig. 5.11(b), another nine points are evaluated centred at ($a+\Delta_f$, $b+\Delta_f$). According to the illustration in Fig. 5.10, the point ($a+2\Delta_f$, $b+\Delta_f$) results in the smallest ct. Therefore, this point is applied at time instance k+2, the control set becomes as shown in Fig. 5.11(c). This process continuous. The discretised control set moves with the operating point.

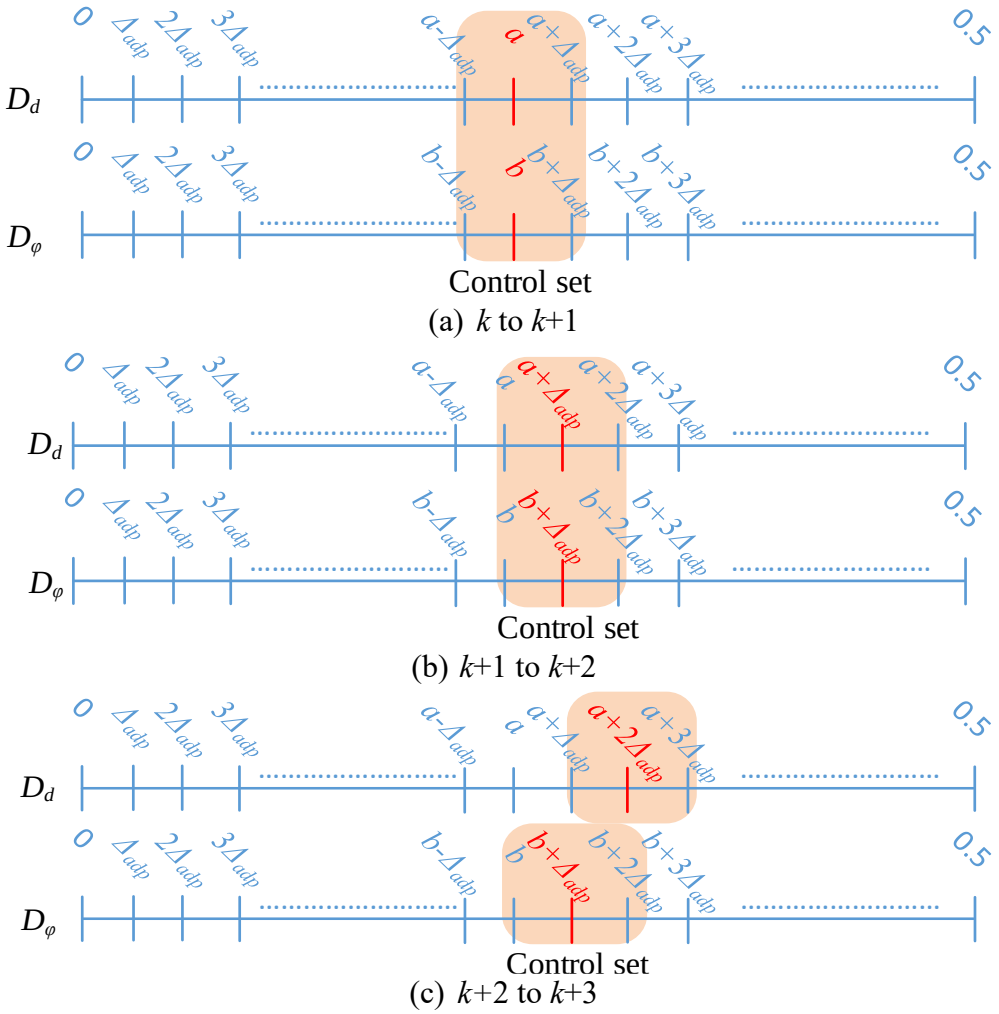


Fig. 5.11 The two-dimensional moving discretised control set.

As demonstrated in Chapter 4 section 4.1.3, increasing the number of points calculated in each switching period results in improvement of dynamic performance, but is a heavy computational

burden. A similar adaptive step approach as described in the mono-dimensional MDCS-MPC can be used to reduce the computational burden while maintaining dynamic performance. Detailed analysis on the adaptive step is addressed in Chapter 4 section 4.1.3.2, which is omitted here. The adaptive step for the two-dimensional MDCS-MPC addressed in this chapter is defined as in (5. 11) and (5. 12).

$$I_{\Delta} = \begin{cases} \left|i_{ref} - i_{HV2}[k]\right|, \left|i_{ref} - i_{HV2}[k]\right| < I_m \\ I_m \qquad\qquad\qquad , \left|i_{ref} - i_{HV2}[k]\right| > I_m \end{cases} \tag{5. 11}$$

$$\Delta_{adp} = \Delta_f (1 + \lambda I_{\Delta}{}^2) \tag{5. 12}$$

5.4 Cost function

Taking into account the computational delay, two-dimensional MDCS-MPC has a prediction horizon of two sampling periods. The cost function is thus proposed as:

$$ct = \alpha_1 G_1 + \alpha_2 G_2 \tag{5. 13}$$

, where

$$G_1 = (i_{ref} - i^*_{HV2}[k+2])^2 \tag{5. 14}$$

$$G_2 = \left(\frac{\Delta D_d}{\Delta D_\varphi}\Big|_{P=P_{const}} - \frac{\Delta D_d}{\Delta D_\varphi}\Big|_{I_{peak}=I_{peak_const}}\right)^2 \tag{5. 15}$$

The first term G_1 is responsible for regulation of the load current to its reference value. When i^*_{HV2} is far from its reference, G_1 plays a dominant role in the cost function. The second term G_2 minimizes the transformer peak current online. Depending on the value of the weighting factor α_2, the trajectory from the initial point to the steady state has different shapes. When α_2 is small, the trajectory behaves like Fig. 5.5(b). When α_3 is large, the trajectory behaves like Fig. 5.5(a). Details about the term G_2 is going to be addressed in this section.

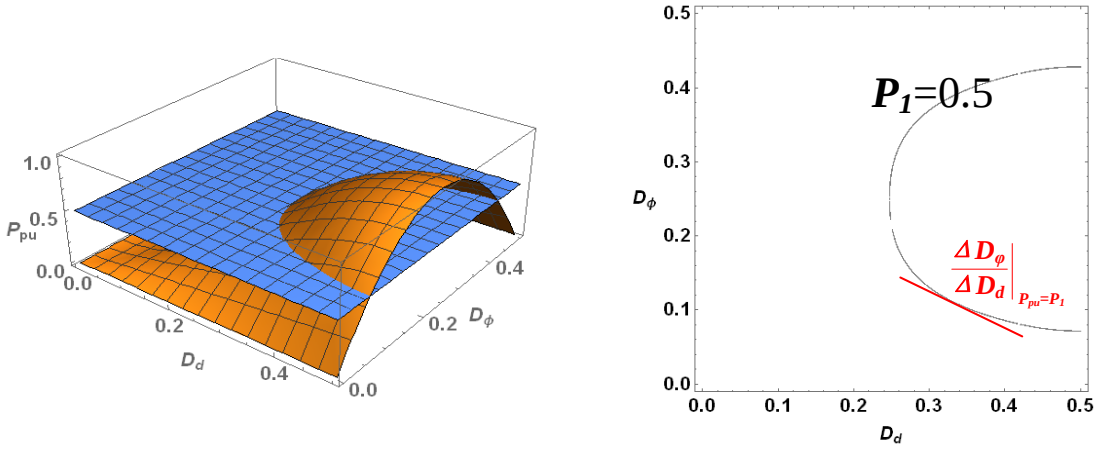
According to Table 2.4 and Table 2.5 in Chapter 2, expressions of the unified transformer peak current are derived as in (5. 16) [44].

$$I_{peak}=\begin{cases}4V_{HV1}D_{\phi}-2V_{HV1}D_d+2V_{HV2}D_d, & M>1\\ 4V_{HV2}D_{\phi}-2NV_{HV2}D_d+2V_{HV1}D_d, & M<1\end{cases} \tag{5. 16}$$

The unity base is written as in (5. 17).

$$I_{base}=\frac{1}{4f_sL_p} \tag{5. 17}$$

The operating power is plotted as Fig. 5.12(a) in the form of a three dimension plot against two control variables of DPS. The constant power plane 0.5 intersects with the power surface, resulting in a line illustrated as Fig. 5.12(b).



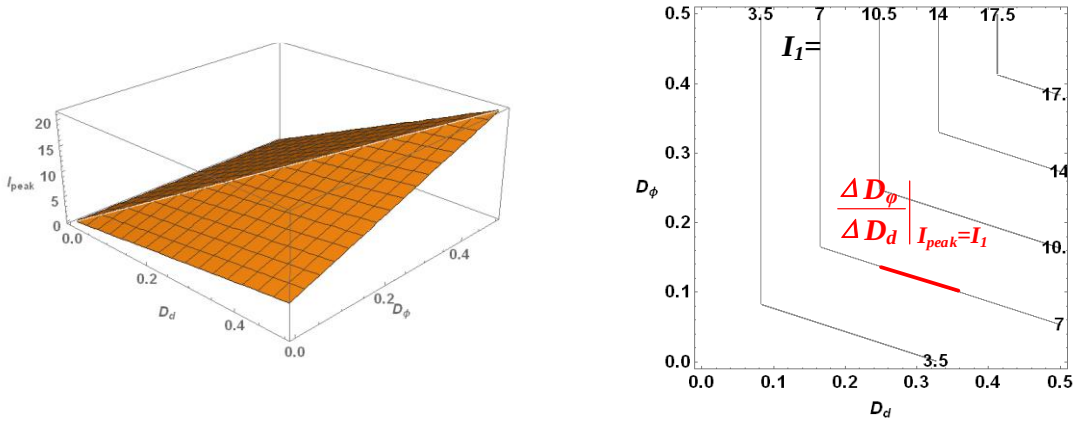
(a) (b)

Fig. 5.12 Power 3D plot and its contour plot.

The slope of the tangent line illustrated in Fig. 5.12(b) is calculated as (5. 18).

$$\frac{\Delta D_d}{\Delta D_\varphi}\Big|_{P=P_{const}}=\begin{cases}\dfrac{1-D_d}{2D_\varphi-1} & ,Mode\ I\\ \dfrac{D_\varphi}{D_\varphi-D_d} & ,Mode\ II\end{cases} \tag{5. 18}$$

Similarly, according to the expression (5. 16), transformer peak current I_{peak} is plotted in Fig. 5.13(a).



(a) (b)

Fig. 5.13 Transformer peak current 3D and its contour plot

Formula (5. 19) calculates the slopes of the tangent line in Fig. 5.13(b).

$$\left.\frac{\Delta D_d}{\Delta D_\varphi}\right|_{I_{peak}=I_{peak_const}} = \begin{cases} 0.5(1-\frac{1}{M}), M<1 \\ 0.5(1-M), M>1 \end{cases} \tag{5. 19}$$

In light of the observation from both formulae (5. 18) and (5. 19), compared with the power expression and peak current formulas in (5. 16), the slopes in (5. 19) and (5. 18) are independent from the circuit parameters. They are relevant to only terminal voltages (V_{HV1}, V_{HV2}) and operating points (D_d, D_φ). Contour plots of both power and transformer peak current overlaps in Fig. 5.14.

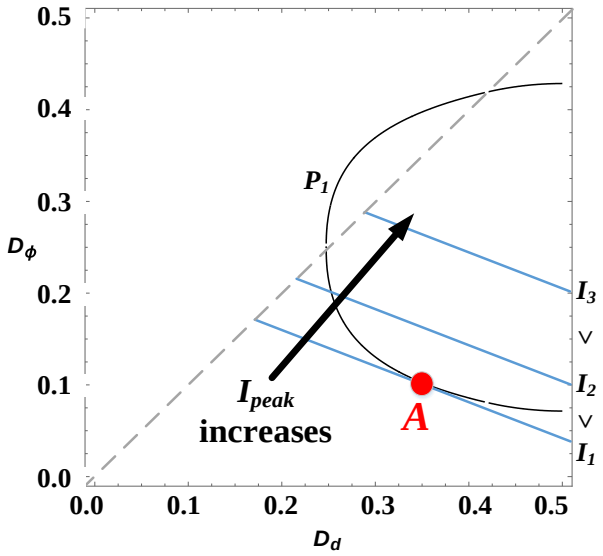


Fig. 5.14 Overlapping of power and peak current contour plots

In the area of interests, if condition (5. 20) is satisfied, under the required operating power, the minimal transformer peak current point can be found. Hence G_2 is defined as (5. 15) based on (5. 20).

$$\frac{\Delta D_\varphi}{\Delta D_d}\Big|_{P=P_{const}} = \frac{\Delta D_\varphi}{\Delta D_d}\Big|_{I_{peak}=I_{peak_const}} \tag{5. 20}$$

The calculation of G_2 relies only on the terminal voltages (V_{HV1}, V_{HV2}) and the operating point (D_d, D_φ). Therefore, it does not need any sensors for the transformer current.

5.5 Algorithm flow chart

The flow chart of the two-dimensional MDCS-MPC with DPS modulation is presented in Fig. 5.15. It shows the calculation process in the control period k to k+1. The output of the control is the optimal control variable to be applied at time instance k+2. μ (=9) elements are utilized for illustration purpose.

The evaluation process starts with the calculation of the adaptive step Δ_{adp}. It determines the step distance between two near values in the control set. The control set slides as described in Fig. 5.11. Then the following iteration starts for the two-dimensional MDCS-MPC:

- The load current is predicted with nine elements in the control set.
- Each load current prediction is corrected by the compensation loop.
- Cost functions are calculated with each corrected load current prediction value

The elements achieving minimal *ct* are then stored which are going to be applied at time instance k+2.

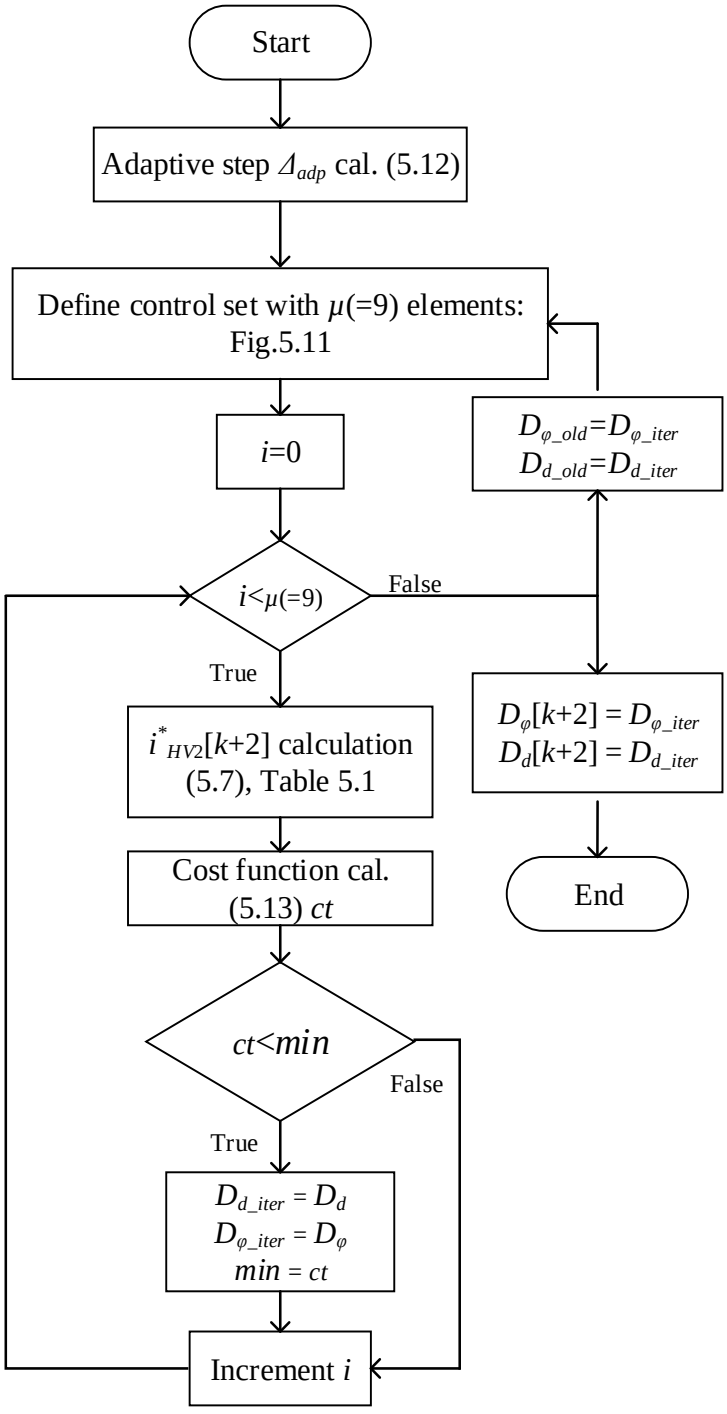


Fig. 5.15 The flow chart of 2-D MDCS-MPC

5.6 Performance evaluations

In this section, the introduced two-dimensional MDCS-MPC for DPS-DAB has been validated using the circuit diagram shown in Fig. 5.16. The DAB is interfaced between two stiff voltage sources V_{HV1} and V_{HV2}. Only the load current i_{HV2} is controlled. Circuit parameters have been listed in Chapter 2 Table 2.9.

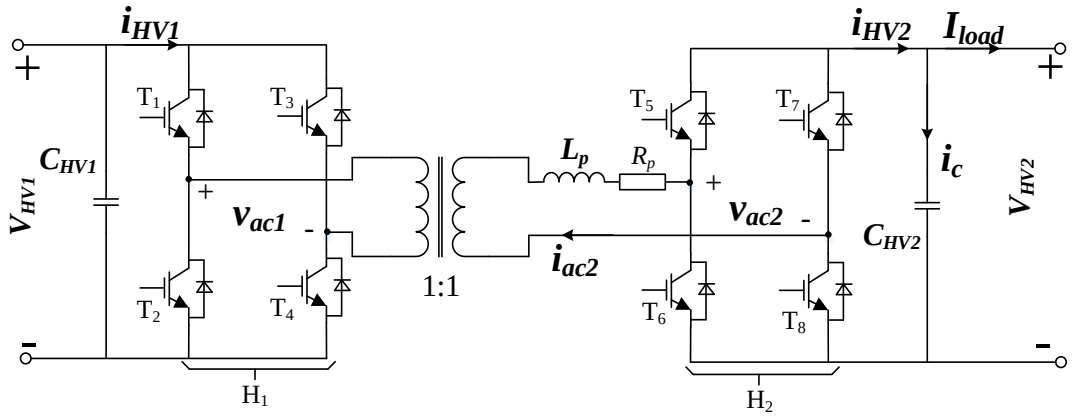


Fig. 5.16 Evaluated circuit

5.6.1 Steady state performance

A comparison on the transformer peak current I_{peak} between the SPS and the DPS is shown in Fig. 5.17 under the terminal voltage condition 150V/320V over the operating power range from 100W to 1kW. DPS shows advantage in the partial load power compared to SPS. When SPS is used D_d is always 0.5 throughout the power range. According to Fig. 5.4, D_d will eventually become 0.5 at full power when DPS is used. This explains the reason for the reduction in difference between the two curves with power.

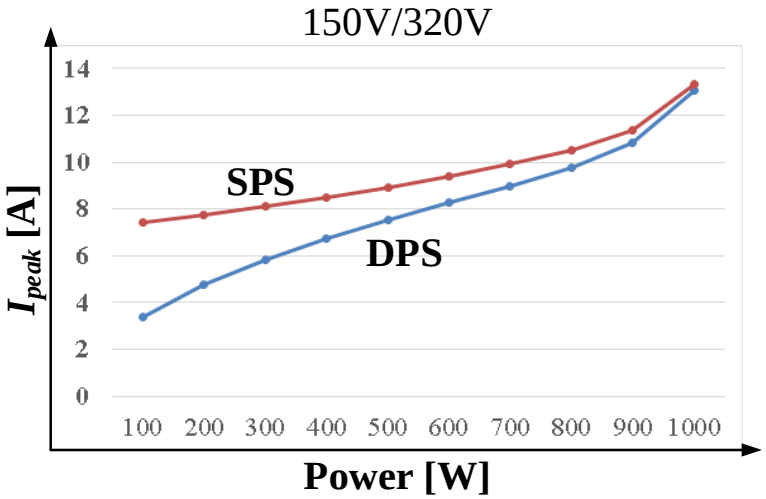
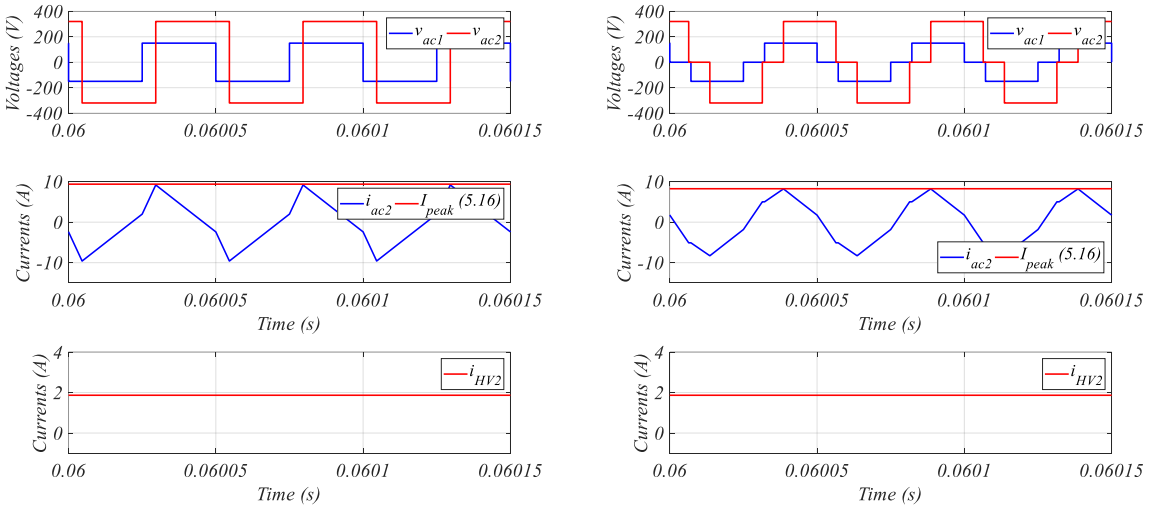


Fig. 5.17 Comparisons on the transformer peak current between SPS and DPS under terminal voltage 150V/320V.

The steady state transformer terminal voltages v_{ac1} and v_{ac2}, transformer secondary current i_{ac2} plus its peak value I_{peak} calculated from (5. 16) and the load current i_{HV2} are shown in Fig. 5.18 under the operating condition 150V/320V 600W. There is a difference of 1.13A between Fig. 5.18(a) and (b) in peak current value I_{peak} due to the employment of the duty phase shift D_d in DPS.



(a) SPS (b) DPS

Fig. 5.18 Time domain waveforms comparison under 150V/320V 600W.

Another comparison on the transformer peak current I_{peak} between the SPS and the DPS is shown in Fig. 5.19 under the terminal voltage ratio close to unity over the same operating power range as Fig. 5.17. DPS has lost the significant advantage compared to Fig. 5.17 where terminal

voltage ratio is far from unity. This is due to the reason that according to (5. 2), under the voltage condition 270V/300V, D_d in DPS is close to 0.5 across the operating power range.

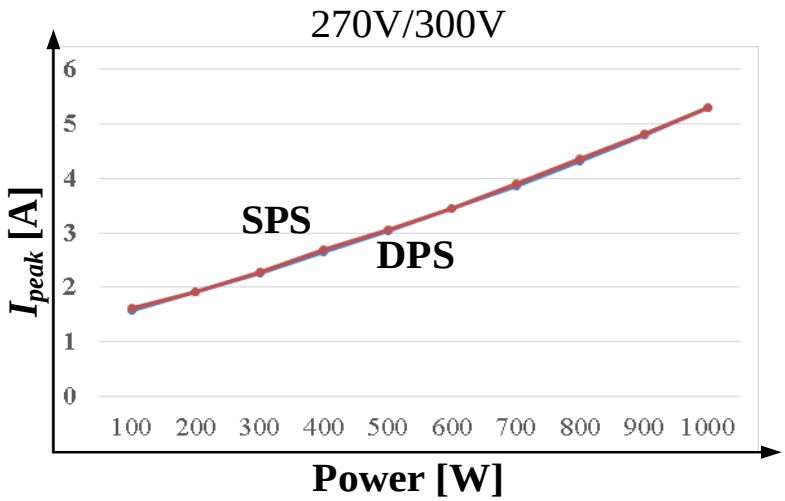
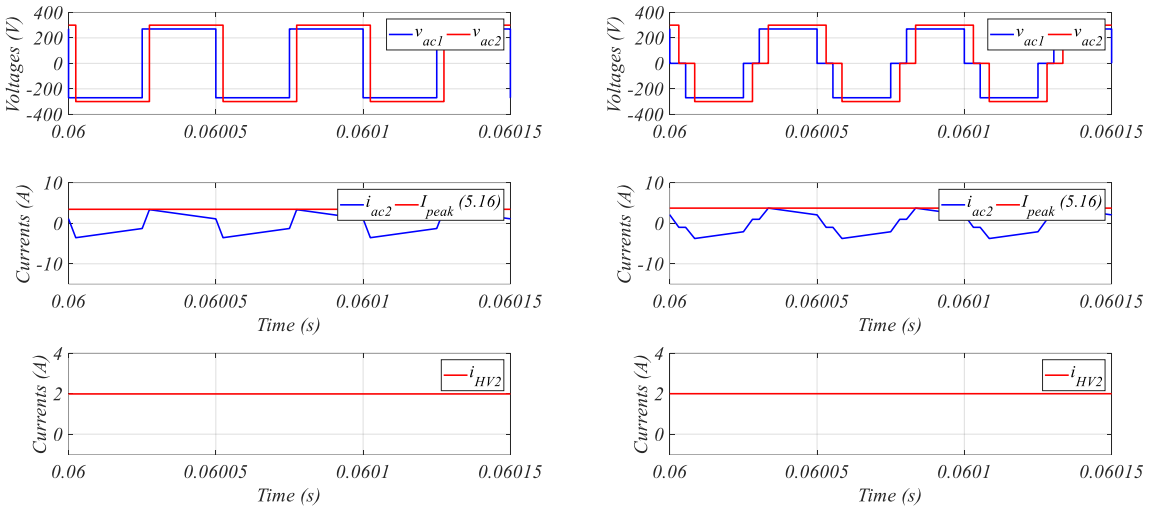


Fig. 5.19 Comparisons on the transformer peak current between SPS and DPS under terminal voltage 270V/300V.

The steady state transformer terminal voltages v_{ac1} and v_{ac2}, transformer secondary current i_{ac2} plus its peak value I_{peak} calculated from (5. 16) and the load current i_{HV2} are shown in Fig. 5.20 under the operating condition 270V/300V 600W. There is a negligible 0.015A difference between Fig. 5.20 (a) and (b) in peak current values I_{peak}.

Based on the above results in Fig. 5.17 and Fig. 5.19, it can be concluded that DPS shows greater advantage in the transformer peak current reduction over the SPS when the terminal voltage ratio varies far from unity. However, as addressed in this chapter section 5.2.1, variations of the small signal model of DPS with different equilibrium points pose difficulty in the linear controller design. Hence the two-dimensional MDCS-MPC is introduced. The control performance of the two-dimensional MDCS-MPC is presented in the following sub-sections.

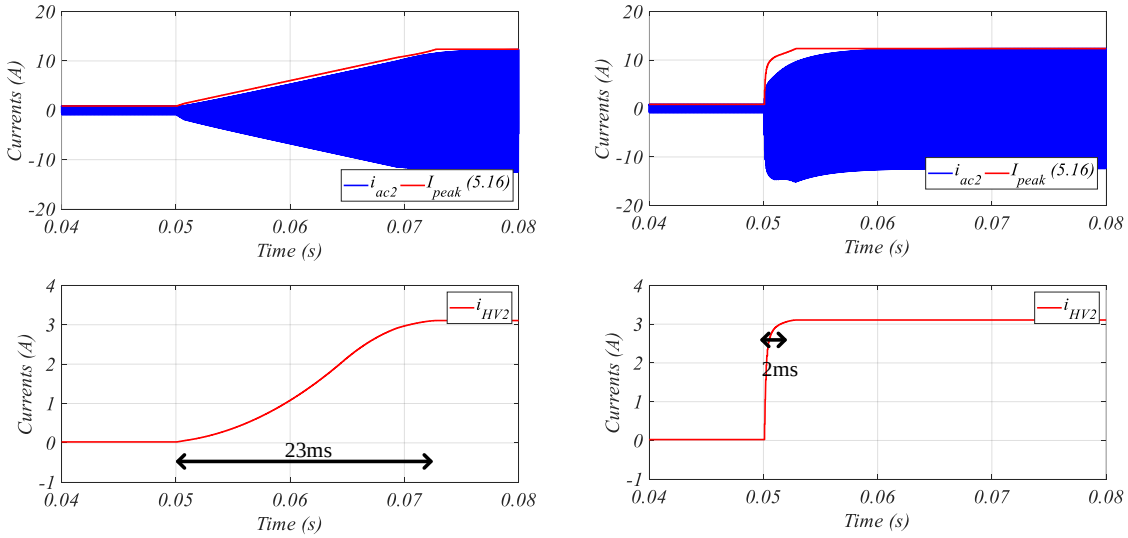


(a) SPS (b) DPS

Fig. 5.20 Time domain waveforms comparison under 270V/300V 600W.

5.6.2 Dynamic performance

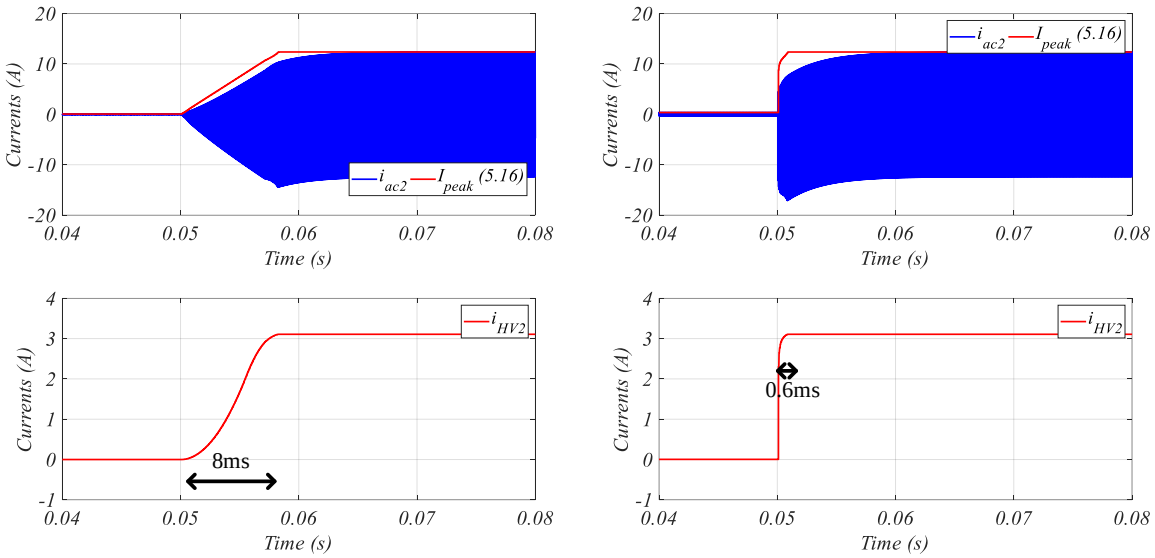
The dynamic performance of the two-dimensional MDCS-MPC is evaluated in this sub-section. Two different measures to increase the transition speed are identified. The first approach to increase the dynamic performance is to increase the number of points μ calculated in one switching period. Load transitions from 0W to 1kW are performed in Fig. 5.21, Fig. 5.22 and Fig. 5.23 at time instance 0.05s.



(a) Adaptive step disabled λ=0 (b) Adaptive step enabled λ=10

Fig. 5.21 Transition from 0W to 1kW Two-dimensional DPS with 3*3 points are calculated in one switching period. α_1=1, α_2=0.1. V_{HV1}=150V, V_{HV2}=300V.

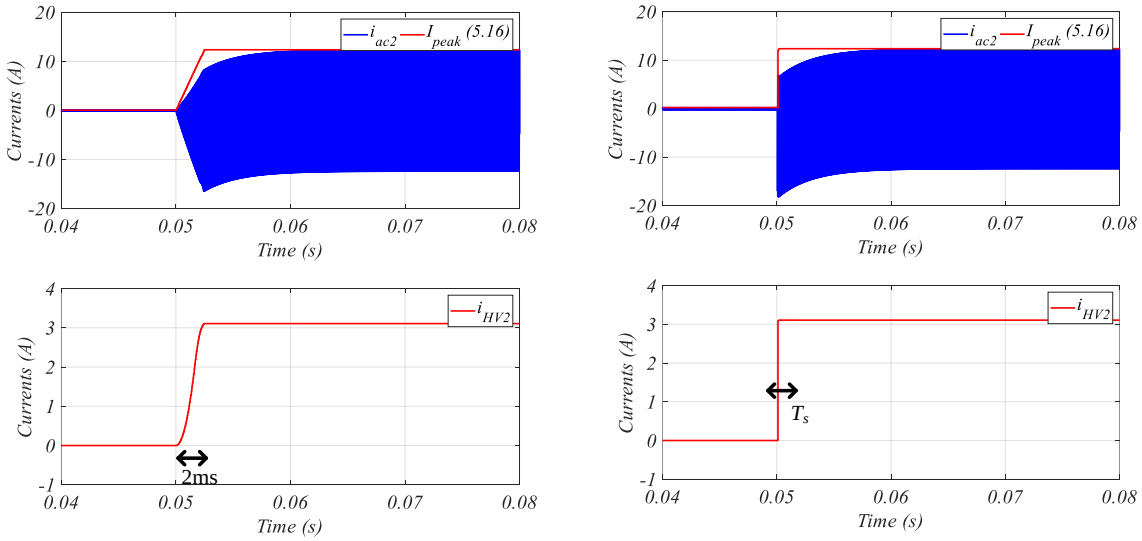
Comparisons among Fig. 5.21(a), Fig. 5.22(a) and Fig. 5.23(a) indicate that the increase of μ from 9 to 441 results in the reduction of the settling time from 23ms to 2ms.



(a) Adaptive step disabled λ=0 (b) Adaptive step enabled λ=10

Fig. 5.22 Transition from 0W to 1kW Two-dimensional DPS with 7*7 points are calculated in one switching period. α_1=1, α_2=0.1. V_{HV1}=150V, V_{HV2}=300V.

Although the increase of μ is conducive to the control performance, the computational burden gets larger. Alternatively, the adaptive step approach as addressed in section 5.3 can be used. Comparisons between Fig. 5.21(a) and Fig. 5.21(b), Fig. 5.22(a) and Fig. 5.22(b) also Fig. 5.23(a) and Fig. 5.23(b) have confirmed its effectiveness.

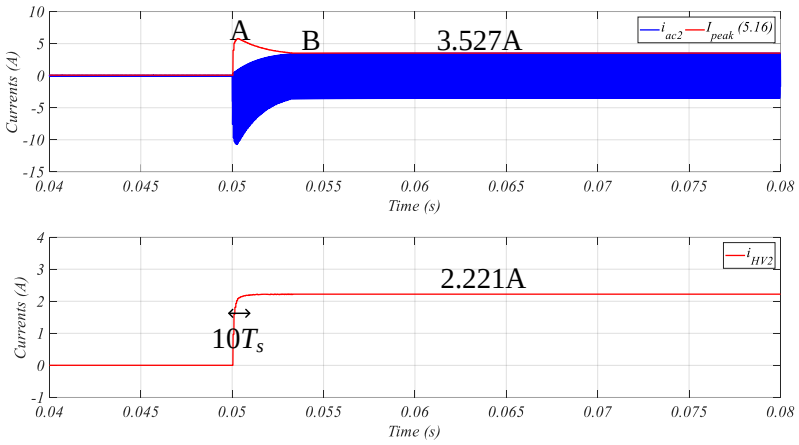


(a) Adaptive step disabled λ=0 (b) Adaptive step enabled λ=10

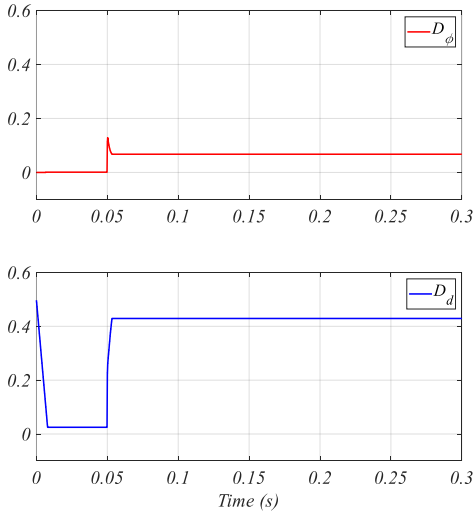
Fig. 5.23 Transition from 0W to 1kW Two-dimensional DPS with 21*21 points are calculated in one switching period. α_1=1, α_2=0.1. V_{HV1}=150V, V_{HV2}=300V. Adaptive step disabled.

5.6.3 Effectiveness of G_2

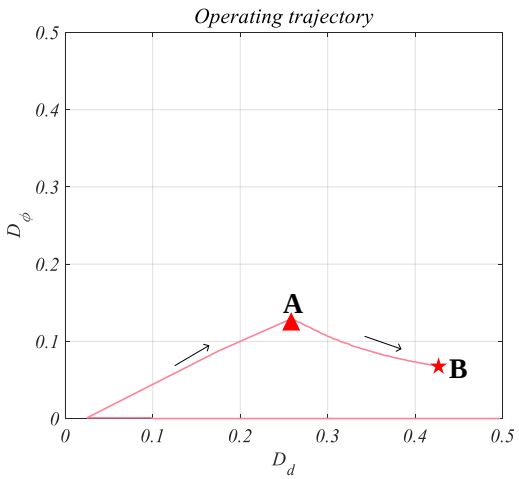
Fig. 5.24 shows a transition from 0W to 600W under voltage condition 250V/270V using the two-dimensional MDCS-MPC. A small value of the weighting factor α_2 (0.1) is used. It can be observed from Fig. 5.24(a) that from point A to point B, the load current i_{HV2} remains constant while the transformer peak current I_{peak} is reduced. Fig. 5.24(b) shows the control variables in time domain. Re-arranging the data D_φ and D_d in Fig. 5.24(b) as Y and X axis, respectively, and the trajectory of the operating point is obtained in Fig. 5.24(c). In the first phase from a point close to the origin to point A, approaching the reference load power/current contour is the priority. From point A to B, reduction of the transformer peak current becomes dominant in the cost function.



(a) transformer and load currents



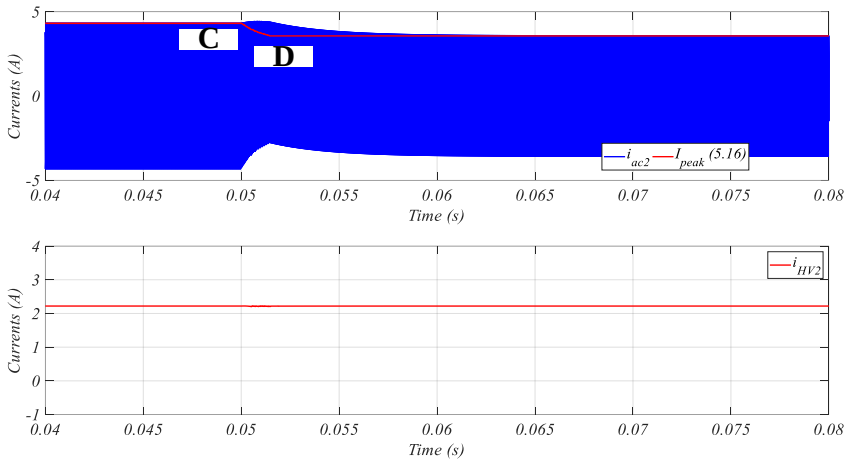
(b) control variables



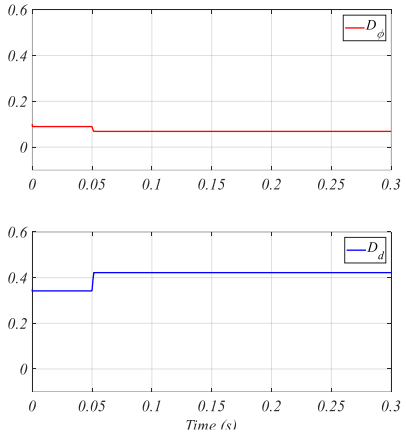
(c) operating trajectory

Fig. 5.24 Two-dimensional DPS with 7*7 points calculated in one switching period. Transition from 0W to 600W. α_1=1, α_2=0.1. V_{HV1}=250V, V_{HV2}=270V.

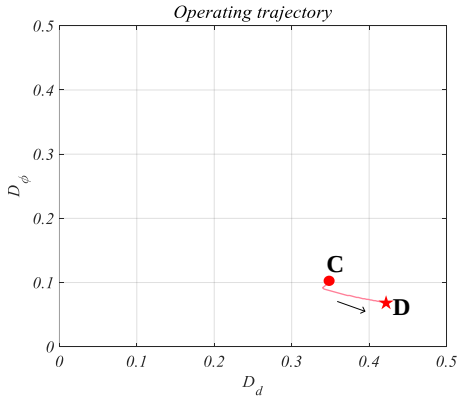
Another evaluation is carried out in Fig. 5.25 where the term G_2 is enabled at time instance 0.05s. A clear peak current reduction is shown in Fig. 5.25(a) after the G_2 is enabled. The steady state operating point has also been altered by G_2 from C to D shown in Fig. 5.25(b) and Fig. 5.25(c).



(a) transformer and load currents



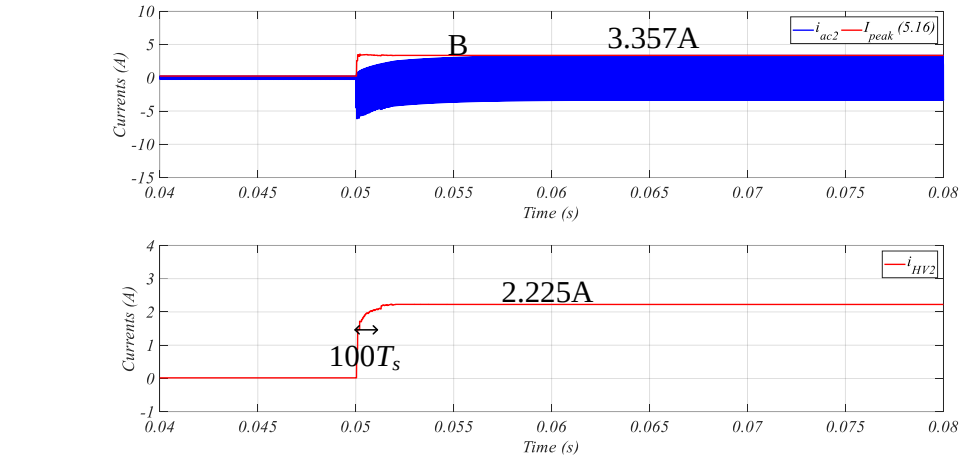
(b) control variables



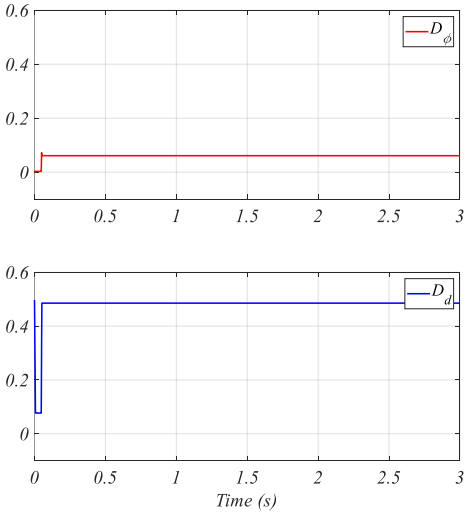
(c) operating trajectory

Fig. 5.25 Two-dimensional DPS with 7*7 points calculated in one switching period. G_2 enabled at 0.05s. α_1=1, α_2=0.1. V_{HV1}=250V, V_{HV2}=270V.

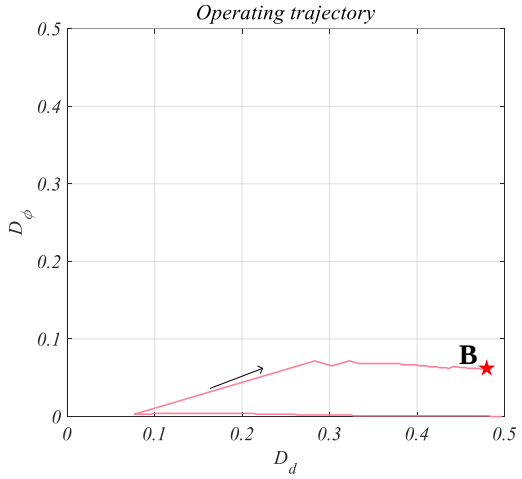
Another assessment with a larger value of weighting factor α_2 has been conducted in Fig. 5.26. A larger value of α_2 (10) gives more leverage on the reduction of transformer peak current when evaluating the cost function. In the steady state, as can be seen from Fig. 5.26(a), I_{peak} is smaller than that of Fig. 5.24(a). However, due to the change of the operating trajectory in Fig. 5.26(c) compared to Fig. 5.25(c), the transition time is also increased from $10T_s$ to $100T_s$.



(a) transformer and load currents



(b) control variables



(c) operating trajectory

Fig. 5.26 Two-dimensional DPS with 7*7 points calculated in one switching period. Transition from 0W to 600W. α_1=1, α_2=10. V_{HV1}=250V, V_{HV2}=270V.

5.7 Chapter summary

Two control objectives need to be achieved with DPS. The first one is the regulation of the load current; the second one is the minimization of the transformer peak current. To achieve the second objective, the optimization can be carried out offline or online.

The advantage of the online over the offline optimization has been addressed. The online optimization breaks the restriction of the predefined path, which brings in greater flexibility to adjust the priority between the two control objectives during transition.

The implementation of the online optimization with two-dimensional MDCS-MPC is introduced. The two dimensional discretised control set and the search method have been illustrated distinguished from the mono-dimensional MDCS-MPC. A cost function, on one hand, regulates the load current. On the other hand, it reduces the transformer peak current value. The priority between the two control objectives can be adjusted by the weighting factors.

The steady state comparisons between the SPS and the DPS are conducted. DPS shows a more significant advantage over SPS in transformer peak current reduction when terminal voltage ratio varies far from unity. The dynamic performance of the introduced two-dimensional MDCS-MPC has been assessed. The increasing of the calculating points in one sampling period enhances the dynamic. However, it aggregates the computational burden. Alternatively, the adaptive step approach can be applied, which enables fast transition even with a small number of calculations. The effectiveness of the transformer peak current reduction term G_2 in the cost function has also been verified in the simulation.

Chapter 6 Stabilization of the DC distribution system

At the current development stage of the More Electric Aircraft (MEA) technology, only roughly 0.5% of the total power is consumed in the form of electricity [120]. *N* multi-phase machines have been implemented for MEA applications [121]. Passive diode multi-phase rectification system is used for its robustness and reliability without posing much torque disturbance to the turbine [122], [123]. The DC distribution system in a typical more electric aircraft is shown in Fig. 6.1 (a). As shown in the figure, an inductor L_f is exploited for smoothing the DC bus voltage v_1. A Dual-Active-Bridge (DAB) converter (Fig. 6.1(b)) is typically used to integrate energy storage elements to the DC bus [9], [13]. In this chapter, the impedance based system stability criteria is introduced first in section 6.1. Conventional stabilization approaches are addressed in section 6.2 and 6.3.

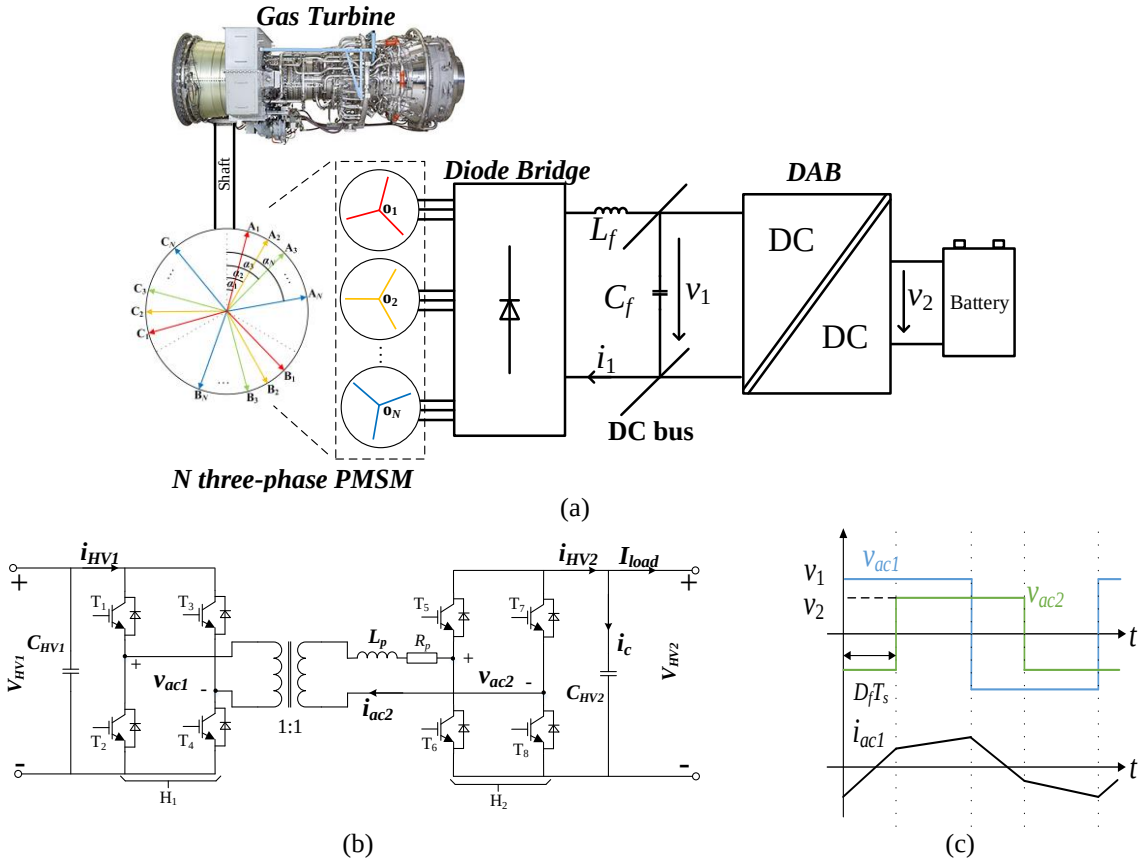


Fig. 6.1 (a) System configuration. (b) Circuit diagram of DAB. (c) Single Phase Shift (SPS) waveforms

6.1 Stability criteria

In the MEA DC distribution electrical power system, a considerable number of tightly regulated AC/DC and DC/DC converters are interconnected on the DC bus [9]. These converters could behave as Constant Power Loads (CPLs) which show negative impedance characteristics. As a consequence, the system phase margin is reduced and oscillation/instability is possible [124]. The impedance model of a single bus multi-generator electrical power system has been evaluated in [125]. Based on the impedance model, stability criteria has been discussed by *J. Sun* [126] on grid-connected inverters and by *R. D. Middlebrook* [127] on voltage regulated DC/DC converters. Similar stability analysis approach is also reported in a MEA DC distribution system [128]. The stabilization controls can then be carried out based on the derived impedance model and the stability criteria.

A simplified system of Fig. 6.1(a) is shown in Fig. 6.2 (a) [129] where prior stages including the diode bridge, PMSM and the gas turbine are replaced by an unidirectional DC source. The impedance model is shown in Fig. 6.2(b). DAB is responsible for regulating the battery current i_{b2} to its reference value i_{b2_ref}.

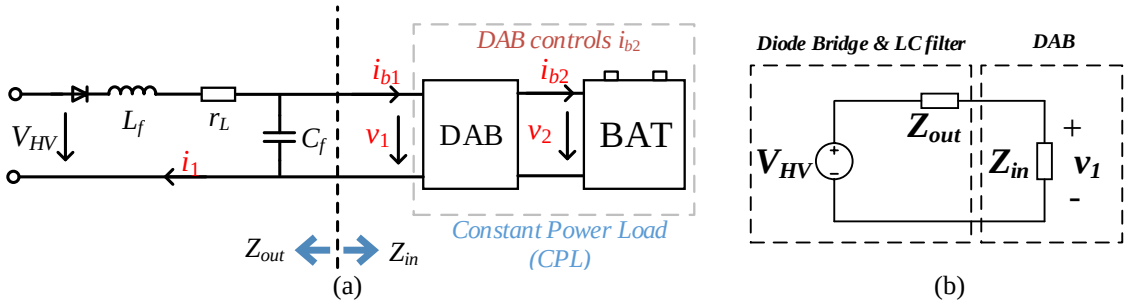


Fig. 6.2 (a) Simplified system. (b) Impedance model

According to the impedance model Fig. 6.2(b), the DC bus voltage v_1 can be expressed as in (6. 1).

$$v_1 = \frac{1}{1+\frac{Z_{out}}{Z_{in}}} V_{HV} \tag{6. 1}$$

Equation (6. 1) represents a closed-loop control system as shown in Fig. 6.3.

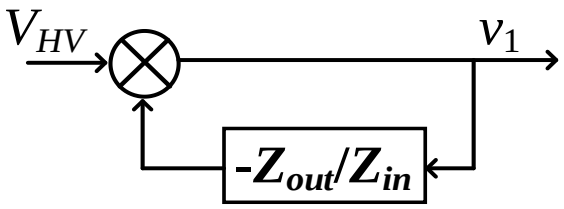


Fig. 6.3 Equivalent close-loop system to (6. 1).

Therefore, according to the classic control theory, the DC bus voltage v_1 is stable only when:

- V_{HV} is stable. When unloaded, the diode bridge output voltage is stable. The stability of V_{HV} is dependent on the PMSM and gas turbine, which is out of the scope of this thesis. Therefore, it is not discussed further.
- The impedance ratio Z_{out}/Z_{in} meets the Nyquist stability criteria [126]. Impedance Z_{out} relates only to the circuit parameters L_f and C_f while Z_{in} is affected by both circuit parameters and control algorithm.

6.2 Passive damping

In this section, stability criteria addressed in section 6.1 is applied to assess the stability of a DC system with the parameters listed in Table 7.2-Table 7.4. A passive damping approach is evaluated to stabilize the system. According to Fig. 6.2 (a), the expression of the *LC* filter output impedance Z_{out} is calculated as (6. 2) where r_L is the sum of the parasitic of inductor L_f and the extra added damping resistors.

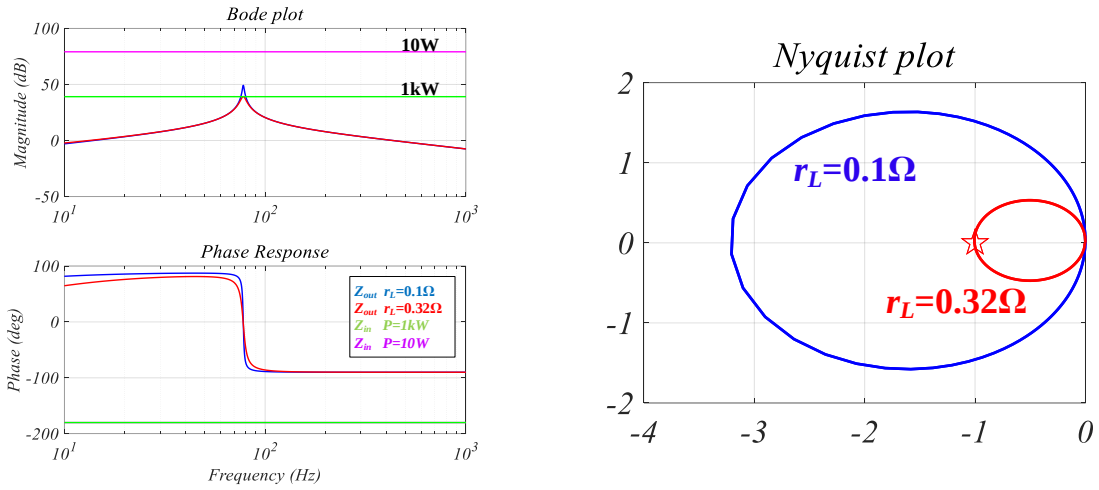
$$Z_{out}(s) = \frac{sL_f + r_L}{L_f C_f s^2 + r_L C_f s + 1} \tag{6. 2}$$

In general, an ideal Constant Power Load (CPL) of Z_{in} is considered as the worst case scenario of system stability [124]. Therefore, a CPL Z_{in} is assumed to be:

$$Z_{in} = -\frac{v_1^2}{P_{const}} \tag{6. 3}$$

, where P_{const} is the constant power consumed by the DAB converter.

The overlapping of both impedances (Z_{in} and $\underline{Z_{out}}$) is plotted in Fig. 6.4(a). According to (6. 3), when the power increases, the amplitude of the impedance Z_{in} decreases. A larger value of r_L renders a lower peak in the amplitude of Z_{out}, thus resulting in the increasing of the Gain Margin (GM). According to Fig. 6.4, it can then be concluded that when r_L equals to 0.32Ω in the example, the amplitude of the impedance Z_{out} is always below the amplitude of the impedance Z_{in} such that the instability of DC bus voltage v_1 can be avoided [130]. Another perspective to appreciate the stability issue is to use the Nyquist plot [129]. The Nyquist plots of the impedance ratio Z_{out}/Z_{in} are shown in Fig. 6.4 (b). With the increasing of value r_L, the loop of the impedance ratio becomes smaller. When r_L equals 0.32Ω, the loop does not encircle the critical point (-1,0), therefore ensuring a stable DC bus.



(a) (b)

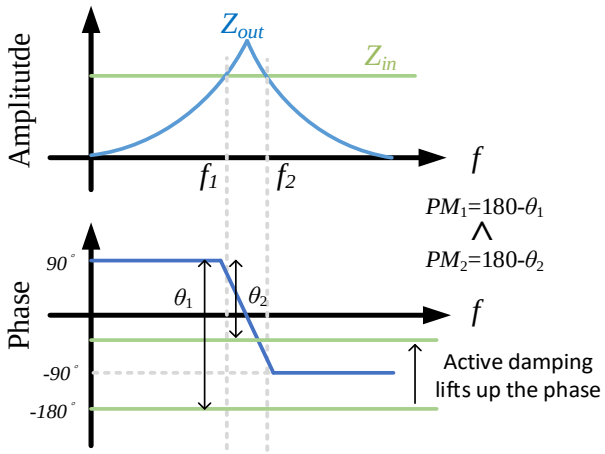
Fig. 6.4 (a) Bode plot and (b) Nyquist plot of the impedance ratio in (6. 1) where v_1=300V, L_p=283uH, C_f=380uF and L_f=11mH.

According to the above analysis, a larger r_L provides better damping to the DC bus voltage. In the meantime, loss is increased. When the rated power is small, as in this case 1kW. A 0.32Ω resistor induces only 3.6W (0.36%) extra conduction loss. However, when the rated power increases to 3kW, a 0.98Ω resistor is required which induces 98W (3.3%) extra conduction loss, projecting a lower efficiency. The proportion of the induced conduction loss increases with the power. Therefore, this passive damping approach is not suitable for high power applications.

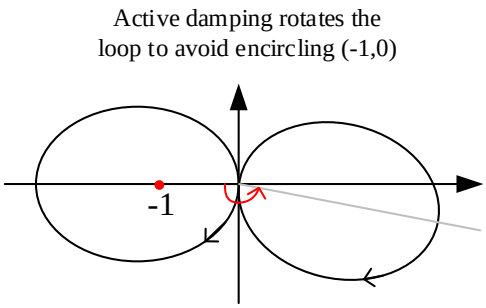
6.3 Active Damping

Conventional active damping controls typically deploy stabilization PI controllers in parallel to the original cascaded PI controllers [129]–[131]. However, this control structure inevitably brings degradation to the load regulation performance. Moreover, the paralleled stabilization PI controllers may incur saturation of the original PI controllers. As a result, the converters end up losing the load regulation ability. This phenomena will be elaborated in this section.

There are two ways to stabilize the system: one is to suppress the amplitude of Z_{out} as analysed in section 6.2 by passive damping; another approach is to shape the impedance of Z_{in} by control without inducing extra losses. Typical active damping approaches change the phase of Z_{in} in order to increase the Phase Margin (PM) [117], [129], [130]. A general illustration on impedance shaping of Z_{in} is shown in Fig. 6.5(a).



(a) Bode plot of Z_{in} and Z_{out}



(b) Nyquist plot of Z_{out}/Z_{in}

Fig. 6.5 A general illustration on the increase of PM by using active damping approaches. Blue line represents Z_{out}. Green line stands for Z_{in}.

The original phase of Z_{in} is lifted up by the active stabilization control from -180 degrees to a value between 90 degrees and -90 degrees. This effectively increases the phase margin which is calculated as (6. 4)

$$PM = 180 - \theta \tag{6. 4}$$

Another perspective in the Nyquist plot is shown as Fig. 6.5(b). The active damping controls stabilize the system by rotating, anti-clock wise, the loop of impedance ratio Z_{out}/Z_{in} in the

Nyquist plot. With sufficient rotation, the critical point (-1,0) can be expelled outside of the enclosed loop, thus ensuring stability.

In this chapter, two active damping approaches are introduced. The first method is based on PI control and the second one is based on mono-dimensional MDCS-MPC. Relevant merits and drawback of those controls in this application are also going to be addressed in the following sections.

6.3.1 PI based stabilization

A PI based active stabilization controller is presented in Fig. 6.6. The stabilization control is implemented by a PI controller $G_d(s)$ which regulates the AC components of the input voltage v_1 to zero. In parallel to the stabilization PI controller, a PI based battery current controller $G_i(s)$ is also implemented.

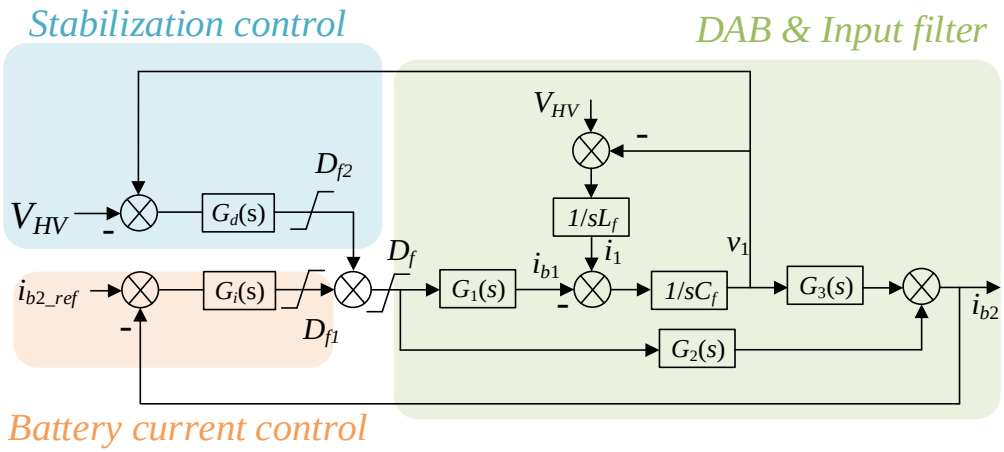


Fig. 6.6 An active damping approach based on the PI controller.

The sum of the two controllers is then fed to the circuit model as the phase shift ratio D_f demonstrated in Fig. 6.6. In this section, the simplified reduced order model is applied [132]. Controllers $G_d(s)$, $G_i(s)$ are defined in (6. 5) where k_{p1}, k_{i1}, k_{p2} and k_{i2} are PI control parameters.

$$G_d(s) = k_{p1} + \frac{k_{i1}}{s},\ G_i(s) = k_{p2} + \frac{k_{i2}}{s} \tag{6. 5}$$

Transfer functions $G_1(s)$, $G_2(s)$ and $G_3(s)$ are derived based on the reduced order model as shown in Fig. 6.7.

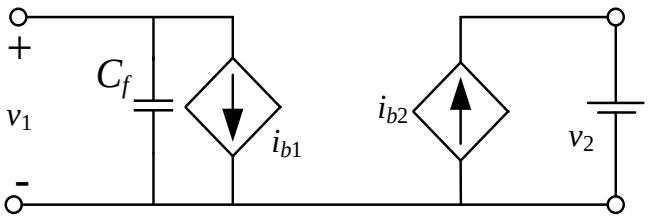


Fig. 6.7 The reduced order model of the DAB.

According to Chapter 2 section 2.3.1, with SPS, the controlled current i_{b1} and i_{b2} can be calculated as:

$$i_{b1} = \frac{v_2}{f_s L_p} D_f (1 - 2|D_f|) \tag{6. 6}$$

$$i_{b2} = \frac{v_1}{f_s L_p} D_f (1 - 2|D_f|) \tag{6. 7}$$

For unidirectional power flow, apply the small signal perturbation to the model (6. 6) based on the equilibrium point yields the transfer function $G_1(s)$ as written in (6. 8) where variables with a bar represents the equilibrium point.

$$G_1(s) = \frac{\overline{v_2}}{f_s L_p} (1 - 4\overline{D_f}) \tag{6. 8}$$

Based on (6. 7), the partial derivative of i_{b2} with respect to D_f and v_1 are the transfer functions $G_2(s)$ and $G_3(s)$, respectively. $G_2(s)$ and $G_3(s)$ are given as follow:

$$G_2(s) = \frac{\overline{v_1}}{f_s L_p} (1 - 4\overline{D_f}) \tag{6. 9}$$

$$G_3(s) = \frac{\overline{D_f}}{f_s L_p} (1 - 2\overline{D_f}) \tag{6. 10}$$

An intuitive explanation on how the DC bus voltage can be stabilized is addressed herein. Fig. 6.8(a) shows conceptually how the currents behave when only battery current control is applied. Since the battery current i_{b2} is tightly regulated to a constant value, the input bridge current i_{b1} equals to P_{const}/v_1. AC components flows into the filter capacitor C_f causing the oscillation in

voltage v_1. When the stabilization PI control loop is enabled, i_{b1} absorbs the AC components of i_1 so that ideally the current i_c remains constant. The stabilization on v_1 is therefore achieved.

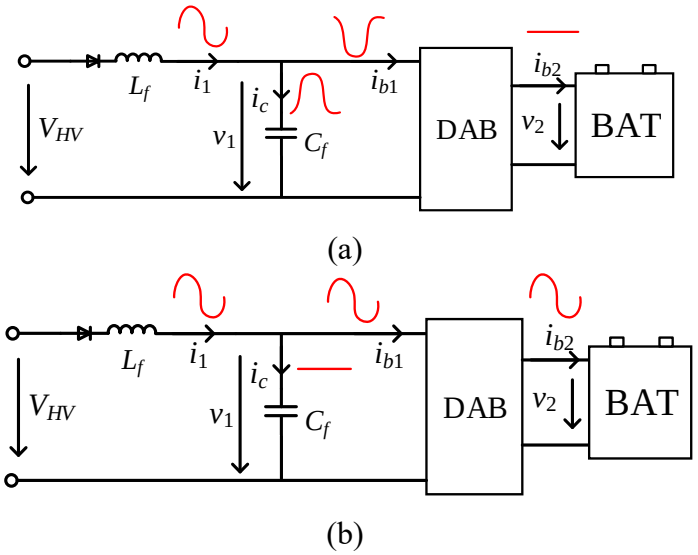


Fig. 6.8 Intuitive explanation on the stabilization. (a) DAB controls only battery current control. (b) Stabilization control is enabled

6.3.1.1 Control evaluation

In order to evaluate how the PI parameters affect the control performance, the input impedance Z_{in} and closed-loop control to output transfer function $G_{R2O}(s)$ of DAB need to be derived. The implications of the stabilization loop and the input LC filter on Z_{in} and $G_{R2O}(s)$ are also going to be identified. To start with, Z_{in} and $G_{R2O}(s)$ are derived without stabilization control loop and the input LC filter. The control block diagram is presented as in Fig. 6.9 where v_1 is the input terminal voltage of DAB.

According to the control block diagram Fig. 6.9, there is only one control loop. From i_{b2_ref} to i_{b2} and from v_1 to i_{b1}, there is only one path for each. Therefore, calculations of Z_{in} and $G_{R2O}(s)$ are presented in (6. 11) and (6. 12).

$$Z_{in} = \frac{v_1}{i_{b1}} = \frac{1 + G_i(s)G_2(s)}{-G_i(s)G_1(s)G_3(s)} \tag{6. 11}$$

$$G_{R2O}(s) = \frac{i_{b2}}{i_{b2_ref}} = \frac{G_i(s)G_2(s)}{1 + G_i(s)G_2(s)} \tag{6. 12}$$

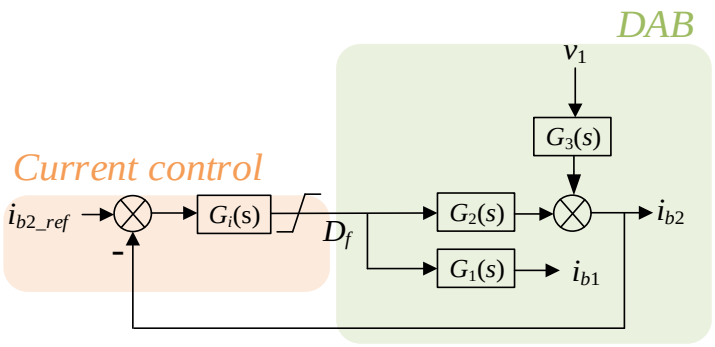
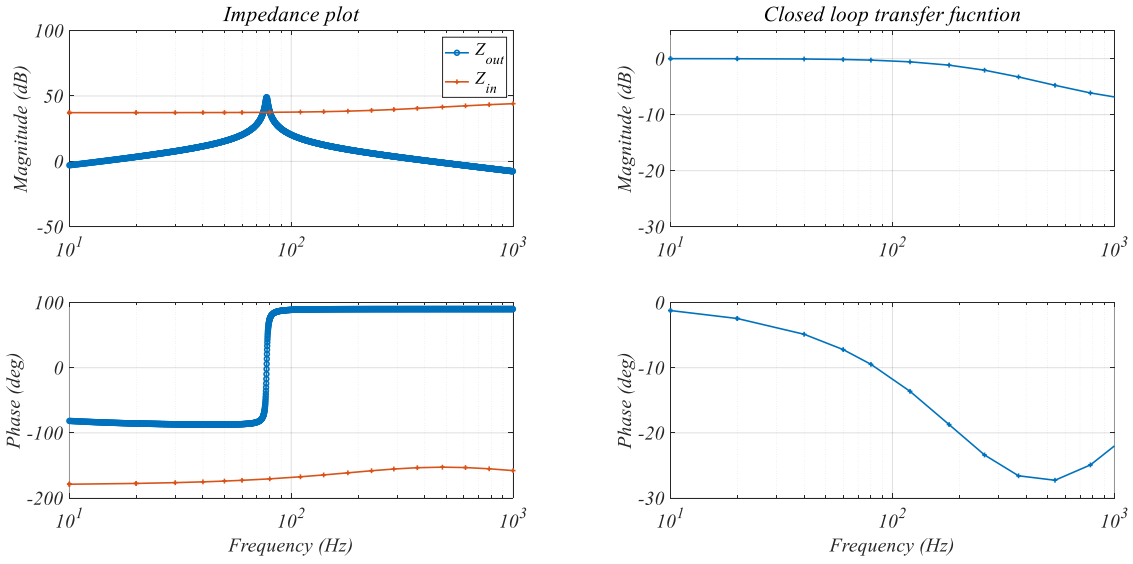


Fig. 6.9 Control diagram without *LC* input filter and stabilization control loop.

The circuit parameters listed in Table 7.2 are applied. Current controller parameters k_{p2} and k_{i2} are set to 0.02 and 100, respectively. The crossover frequency is 576Hz. The plots of Z_{in} and $G_{R2O}(s)$ are presented as Fig. 6.10. According to the stability criteria presented in section 6.1, Fig. 6.10(a) indicates the instability of the DC bus voltage in presence of the *LC* filter (L_f=11mH). The magnitude of $G_{R2O}(s)$ decays at a rate around -10dB/dec after the crossover frequency. In fact, the magnitude of $G_{R2O}(s)$ always decreases after the crossover frequency if a PI controller is used.



(a) (b)

Fig. 6.10 Bode plots of (a) Z_{in} and Z_{out}. (b) $G_{R2O}(s)$ without stabilization control and input *LC* filter.

Another phenomena associated with the bandwidth of the PI controller is shown in Fig. 6.11 where Z_{in} is calculated from both the ideal formula in (6. 3) and the control involved formula in (6. 11). After the bandwidth frequency, Z_{in} calculated based on formula (6. 11) becomes less

"constant" and increases with the frequency while the ideal Z_{in} remains constant in the whole frequency range.

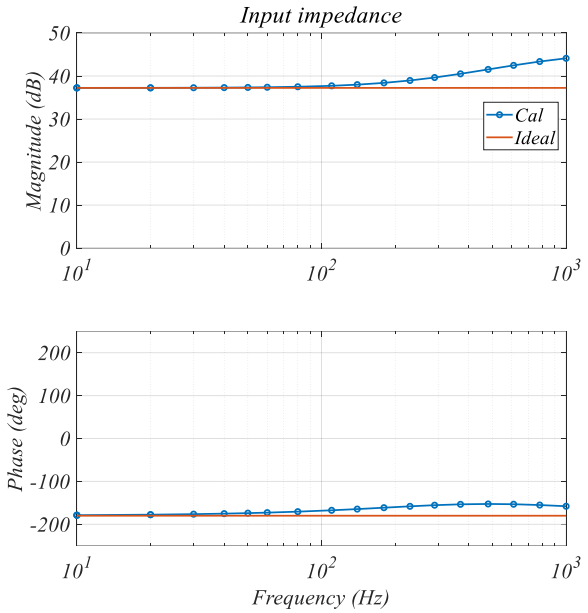
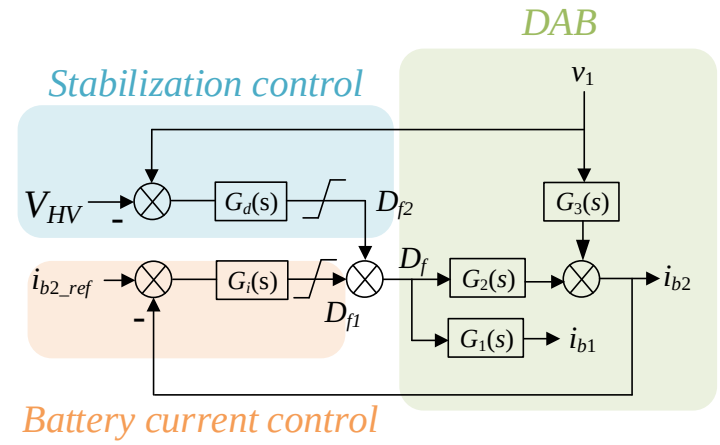
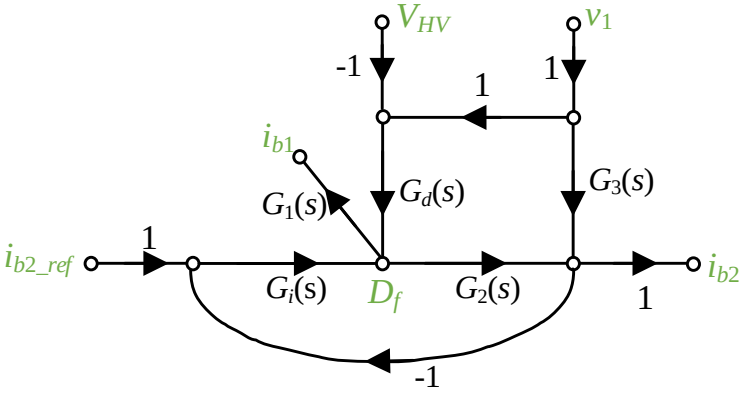


Fig. 6.11 Comparison between the ideal Z_{in} from (6. 3) and calculated Z_{in} from (6. 11).

As discussed above, in order to stabilize the DC bus, a PI based stabilization control can be utilized. The stabilization control loop is expected to lift the phase of Z_{in} as illustrated in Fig. 6.5(a). Since the impedance Z_{in} is an attribute of the converter which is only relevant to the DAB circuit parameters and associated controls. The input LC filter is excluded for now. When the stabilization control loop is enabled without the input LC filter, the control block diagram becomes Fig. 6.12(a). For a system with reasonably complex interrelationships, the block diagram reduction procedure is cumbersome and often quite difficult to complete. An alternative method – signal flow graph diagram for determining the relationship between system variables is used. In Fig. 6.12, both a control block diagram Fig. 6.12(a) and a signal-flow graph diagram Fig. 6.12(b) are presented.



(a) Block diagram



(b) Signal-flow graph model

Fig. 6.12 Control diagram without the input *LC* filter.

According to the signal-flow graph diagram in Fig. 6.12(b), there is still only one loop and one path from i_{b2_ref} to i_{b2}. The loop gain L and the path gain P_1 from i_{b2_ref} to i_{b2} are calculated in (6. 13) and (6. 14).

$$L = -G_i(s)G_2(s) \tag{6. 13}$$

$$P_1 = G_i(s)G_2(s) \tag{6. 14}$$

However, the number of paths from v_1 to i_{b1} is increased by one with the stabilization control. Two path gains P_2 and P_2 are calculated as in (6. 15) and (6. 16).

$$P_2 = G_d(s)G_1(s) \tag{6. 15}$$

$$P_3 = -G_i(s)G_1(s)G_3(s) \tag{6. 16}$$

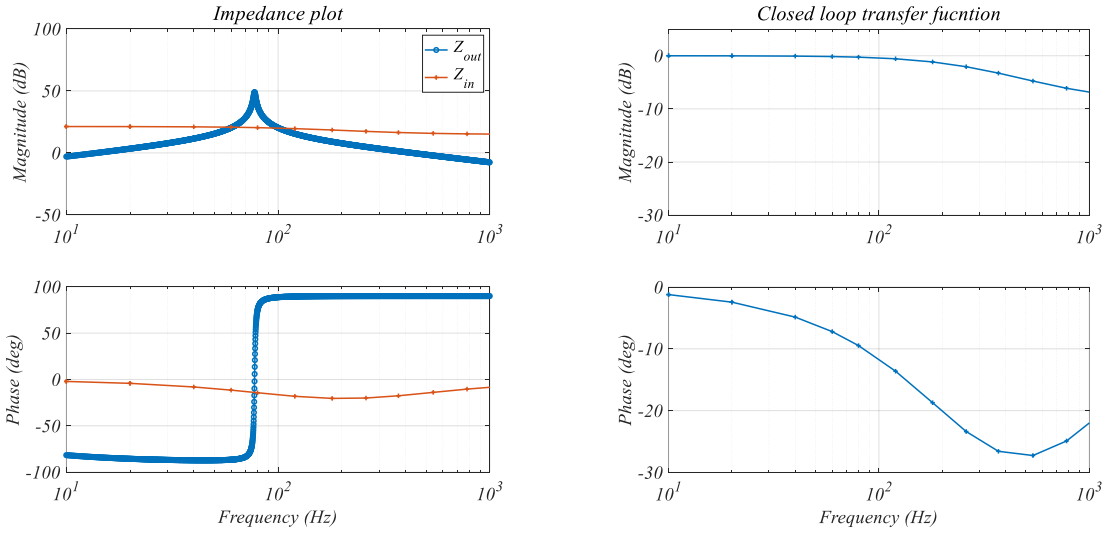
Therefore, according to the Mason's formula, with the stabilization controller $G_d(s)$, the input impedance can be calculated as:

$$Z_{in} = \frac{v_1}{i_{b1}} = \frac{1-L}{P_2 + P_3} = \frac{1+G_i(s)G_2(s)}{-G_i(s)G_1(s)G_3(s)+G_d(s)G_1(s)} \tag{6. 17}$$

The closed-loop transfer function is calculated in (6. 18) which remains unchanged as (6. 12).

$$G_{R2O}(s) = \frac{i_{b2}}{i_{b2_ref}} = \frac{P_1}{1-L} = \frac{G_i(s)G_2(s)}{1+G_i(s)G_2(s)} \tag{6. 18}$$

The circuit parameters listed in Table 7.2 are applied. Current controller parameters k_{p2} and k_{i2} remain at 0.02 and 100, respectively. Stabilization controller parameters k_{p1} and k_{i1} are set at 0.01 and 10, respectively.



(a) (b)

Fig. 6.13 Bode plots of (a) Z_{in} and (b) $G_{R2O}(s)$ with stabilization control but without input LC filter.

As shown in Fig. 6.13(a), the stabilization control loop lifts up the phase of Z_{in} from -180 degrees to a range between -90 degrees and 90 degrees. Therefore, according to the stability criteria discussed in section 6.1, the DC bus voltage is stable. When comparing Fig. 6.10(b) and Fig. 6.13(b), it can be concluded that the close loop transfer function $G_{R2O}(s)$ is not affected by the stabilization control loop when the input LC filter is not included in the main circuit. When the input LC filter is incorporated and with the stabilization control also enabled, the control block diagram has been shown in Fig. 6.6. The gains $G_C(s)$ and $G_L(s)$ are defined as (6. 19) and (6. 20).

$$G_C(s) = \frac{1}{sC_f} \tag{6. 19}$$

$$G_L(s) = \frac{1}{sL_f} \tag{6. 20}$$

The corresponding signal-flow graph diagram shown in Fig. 6.14 becomes much more complicated than the one presented in Fig. 6.12.

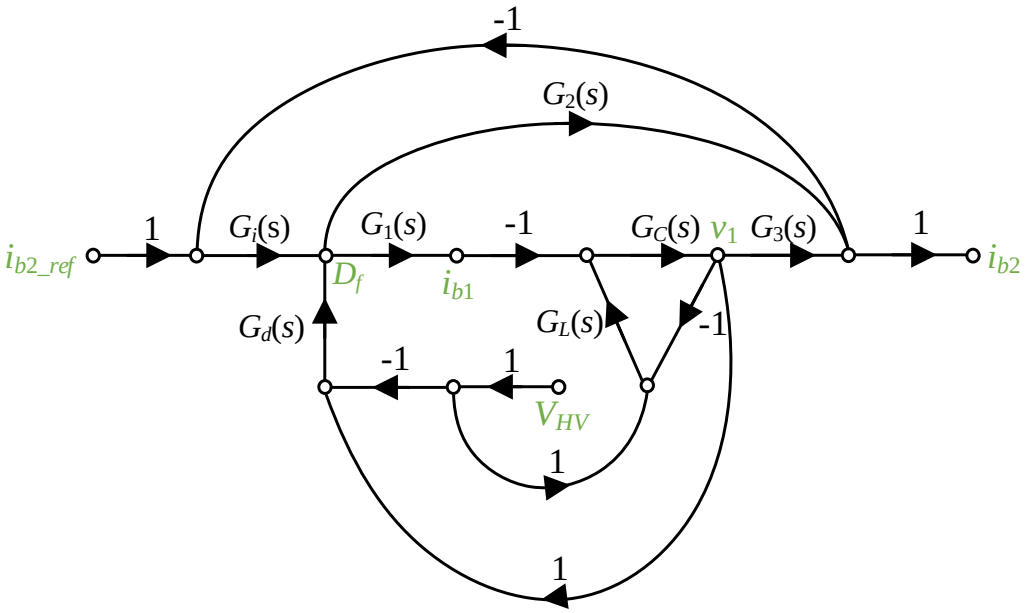


Fig. 6.14 Signal-flow graph model of the control block diagram in Fig. 6.6.

There are four loops L_1-L_4 which can be calculated as in (6. 21)-(6. 24).

$$L_1 = -G_i(s)G_2(s) \tag{6. 21}$$

$$L_2 = -G_C(s)G_L(s) \tag{6. 22}$$

$$L_3 = G_i(s)G_C(s)G_1(s)G_3(s) \tag{6. 23}$$

$$L_4 = -G_d(s)G_C(s)G_1(s) \tag{6. 24}$$

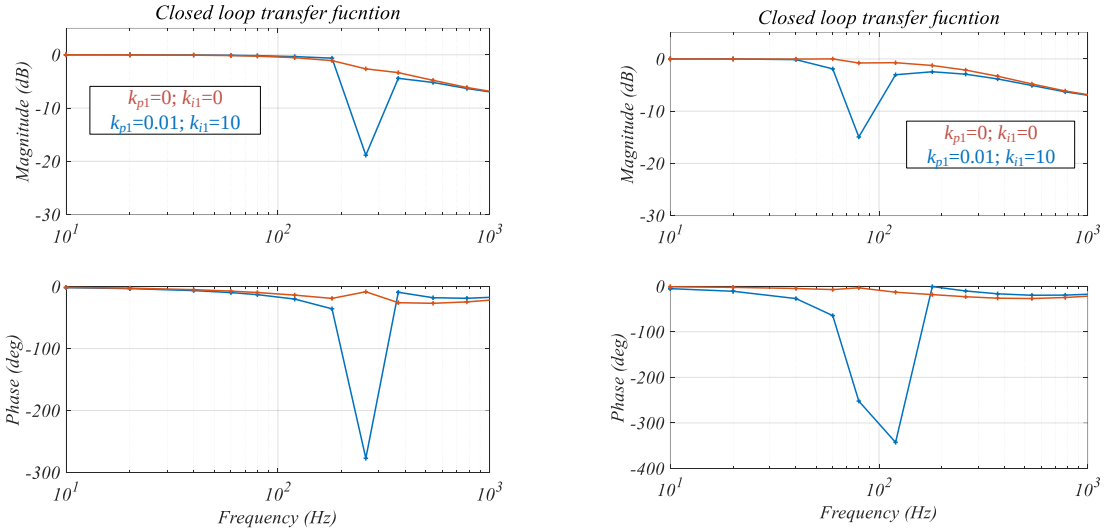
The path gains P_1 and P_4 from i_{b2_ref} to i_{b2} are calculated as in (6. 14) and (6. 25).

$$P_4 = -G_i(s)G_C(s)G_1(s)G_3(s) \tag{6. 25}$$

The closed-loop control to output transfer function $G_{R2O}(s)$ can be then expressed as in (6. 26).

$$G_{R2O}(s)=\frac{i_{b2}}{i_{b2_ref}}=\frac{P_1(1-L_2)+P_4}{1-L_1-L_2-L_3-L_4+L_1L_2} \tag{6. 26}$$

According to (6. 26), the Bode plot of $G_{R2O}(s)$ is shown in Fig. 6.15. In observation of Fig. 6.15(a) and Fig. 6.15(b), it can be concluded that the impedance Z_{out} has impact on $G_{R2O}(s)$. There is an amplitude dip in each figure. The frequency of the amplitude dip is the same as the amplitude peak of Z_{out}. The PI control parameters need to be designed and tuned on a different characteristic of Z_{out} with the information of L_f known.



(a) L_f=1mH (b) L_f=11mH

Fig. 6.15 Bode plot of $G_{R2O}(s)$ with stabilization control and LC filter. k_{p2} and k_{i2} are set as 0.02 and 100.

When the stabilization control parameters are reduced. k_{p1} and k_{i1} are set at 0.001 and 1, respectively. It can be observed that the stabilization loop has negative impacsts on $G_{R2O}(s)$. Therefore, when designing the control parameters, a compromise between the two control objectives has to be considered.

Another observation with the PI controller is that when approaching the current regulation bandwidth, the phase of Z_{in} will increase. This means that the stabilization is less “required” with higher resonance frequency. The stabilization control parameters have to be redesigned and tuned to minimize the impact to current reference tracking performance.

Apart from above mentioned issues, the most vital problem with the PI based stabilization control presented in Fig. 6.6 is the control loop saturation. The saturation of the control loops

will cause the converter to lose the ability to regulate the load current or provide stabilization to the DC distribution system. Details are going to be addressed in section 6.3.1.2.

6.3.1.2 Saturation issue

The PI controller approach presented in Fig. 6.6 has been analysed theoretically without considering the saturation issue. In the application under investigation, the parameters designed in theory with the control structure shown in Fig. 6.6 may not be able to work due to controller saturation. The reason for causing the saturation is explained herein.

Referring to Fig. 6.6, the sum of the control output is D_f as calculated in (6. 27) where D_{f1} and D_{f2} are the outputs of the battery current controller and the stabilization controller.

$$D_f = D_{f1} + D_{f2} \tag{6. 27}$$

Three variables D_f, D_{f1} and D_{f2} are subjected to the same range (6. 28).

$$D_f, D_{f1}, D_{f2} \in [0, 0.25] \tag{6. 28}$$

According to (6. 27) and (6. 28), (6. 29) can be derived.

$$0 < D_{f1} < 0.25\text{-}D_{f2} \tag{6. 29}$$

Defining ΔD_f as

$$\Delta D_f = D_{f1} - D_{f2} \tag{6. 30}$$

Substituting (6. 30) into (6. 29) yields:

$$0 < D_{f1} < \frac{1}{8} - \frac{\Delta D_f}{2} \tag{6. 31}$$

The steady state value of D_{f2} has no influence on the system DC bus stability, However, D_{f2} will reduce the range of D_{f1}. In the worst case, if D_{f2} ends up being 0.25 in the steady state, the current controller loses the ability to adjust the phase shift D_f.

An illustration of this phenomena is shown in Fig. 6.16(a) where circuit parameters in Table 7.2 are used. In phase I, before the stabilization is enabled, $D_{\varphi 2}$ equals to zero. $D_{\varphi 1}$ has the

ability to control the battery current i_{b2}. However, after the stabilization loop is enabled, $D_{\varphi 2}$ becomes even larger than $D_{\varphi 1}$ in the steady state during phase II. In the next phase III, the current reference is changed from 3.7A to 0.37A, $D_{\varphi 1}$ drops to zero hence losing the ability to regulate the battery current in phase III. A faster stabilization loop will even worsen the saturation of $D_{\varphi 1}$ from phase I to phase II. However, this problem can be alleviated by reducing the integrator parameter k_{i1} as shown in Fig. 6.16(b).

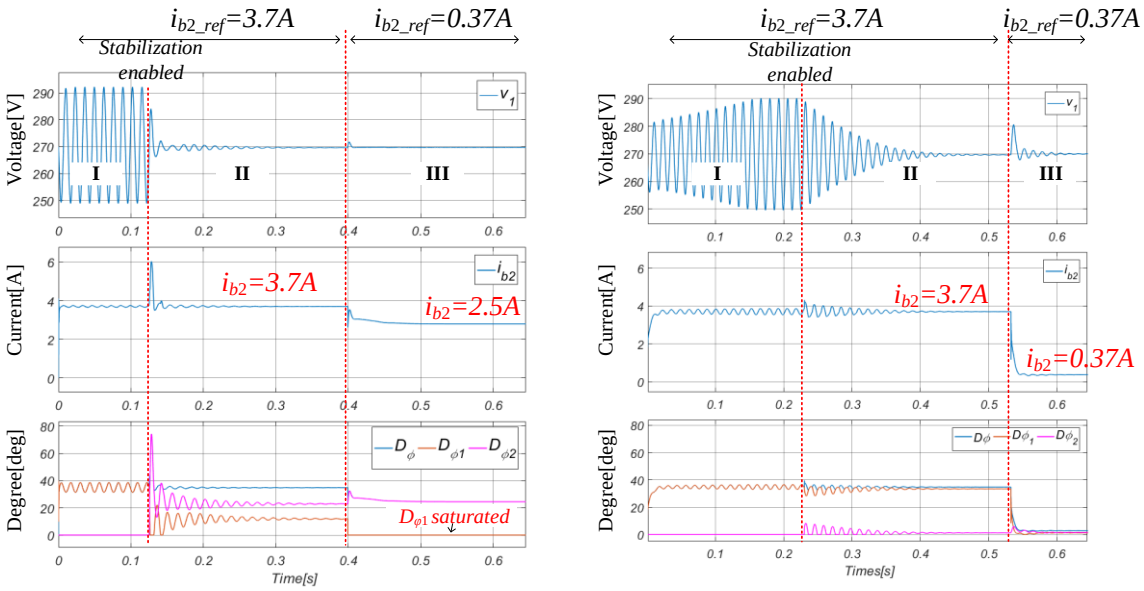


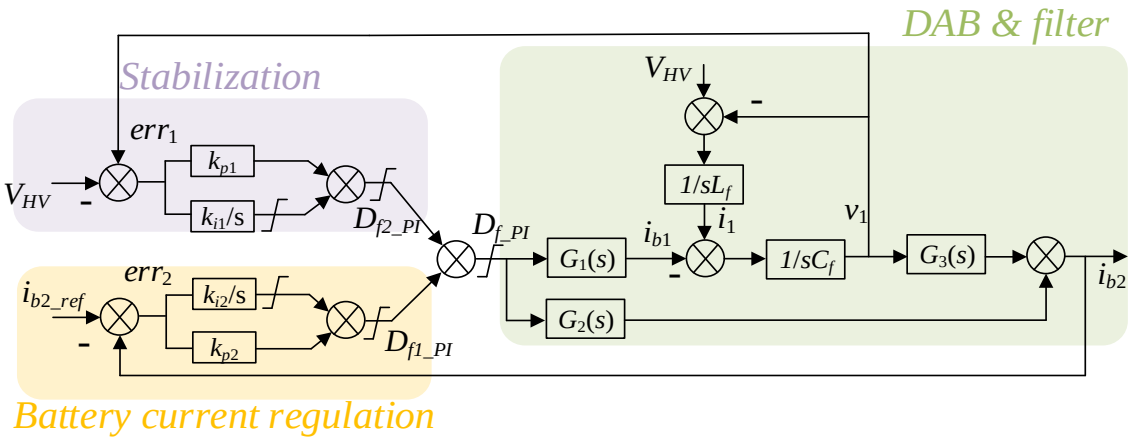
Fig. 6.16 (a) Saturation issue with PI controllers where k_{p1}=0.02, k_{i1}=100, k_{p2}=0.003 and k_{i2}=5. Circuit parameters in Table 7.2 are used. (b) Alleviation of the saturation with a slower stabilization loop where k_{p1}=0.02, k_{i1}=100, k_{p2}=0.001 and k_{i2}=0.1. Circuit parameters are listed in Table 7.2.

6.3.2 Co-ordinated integration

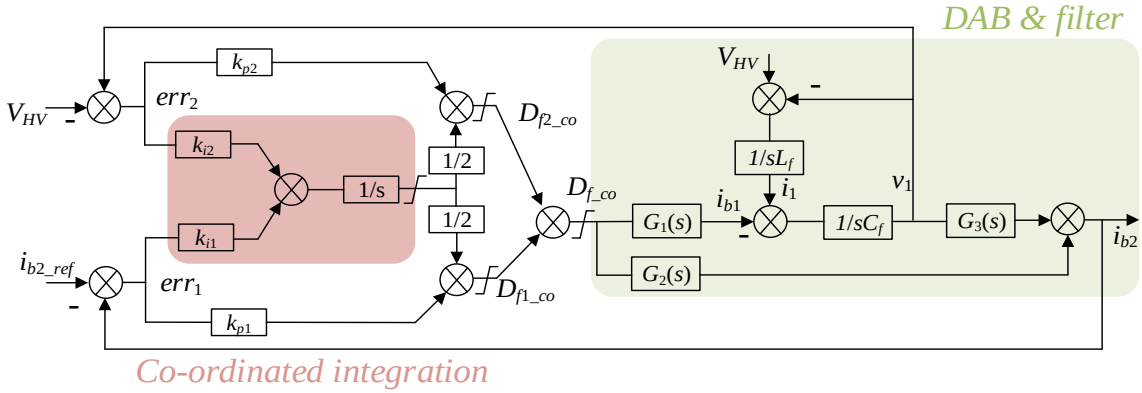
Parallel control structure has been often used where the active damping PI controller is in parallel with other PI controllers [129]–[131]. These PI controllers are independent from each other. This control structure inevitably brings the control loop coordination issue which can result in saturation. The converter may end up losing load power/voltage/current regulation ability.

Aiming to solve this problem, a coordinated integration control is proposed as shown in Fig. 6.17(b). The proposed approach utilizes two linked PI controllers which share their integration history value different from the independent PI control structure as shown in Fig. 6.17(a). The linked integrators provide coordination to control objectives which can effectively avoid the

saturation issue. The coordinated integration control is easy to implemente in digital control platforms.



(a) Independent PI controllers with anti-windup



(b) Co-ordinated integration

Fig. 6.17 PI based active stabilization methods

Mathematical relationship between the proposed control and the conventional PI control is derived as follows:

Assuming the phase shift duty calculated from the conventional PI controls is:

$$D_{f_PI} = D_{f1_PI} + D_{f2_PI} \tag{6. 32}$$

, where

$$D_{f1_PI} = err_1[k]k_{p1} + err_1[k]k_{i1}T_s + his_1[k] \tag{6. 33}$$

$$D_{f2_PI} = err_2[k]k_{p2} + err_2[k]k_{i2}T_s + his_2[k] \tag{6. 34}$$

$err_1[k]$ and $err_2[k]$ are the errors between the references and feedbacks. The integration history values can be expressed as:

$$his_1[k] = k_{i1}T_s\sum_{i=1}^{k-1} err_1[i] \tag{6. 35}$$

$$his_2[k] = k_{i2}T_s\sum_{i=1}^{k-1} err_2[i] \tag{6. 36}$$

Now, the same calculations for the phase shift duty from the coordinated integration control is carried out:

$$D_{f_co} = D_{f1_co} + D_{f2_co} \tag{6. 37}$$

, where

$$D_{f_1_co} = err_1[k]k_{p1} + err_1[k]k_{i1}T_s + {his[k]}/{2} \tag{6. 38}$$

$$his_3[k] = err_1[k]k_{i1}T_s + {his[k]}/{2} \tag{6. 39}$$

$$D_{f_2_co} = err_2[k]k_{p2} + err_2[k]k_{i2}T_s + his_3[k] \tag{6. 40}$$

The shared integration history value is:

$$his[k] = k_{i1}T_s\sum_{i=1}^{k-1} err_1[i] + k_{i2}T_s\sum_{i=1}^{k-1} err_2[i] \tag{6. 41}$$

Based on the calculations in (6. 32) and (6. 37), (6. 42) can be concluded.

$$D_{f_co} = D_{f_PI} + err_1[k]k_{i1}T_s \tag{6. 42}$$

T_s is usually very small. The two control approaches have nearly the same output phase shift duty except that the co-ordination integration approach can avoid the saturation. The control parameters designed in theory can be applied to practice without the worry of the loop saturation.

The same test as in Fig. 6.16 has been conducted with the co-ordinated control. Results are shown in Fig. 6.18. It can be observed from the waveform that D_{f1} and D_{f2} remain close as (6. 43) in the steady state when the stabilization control is enabled.

$$D_{f1} \approx D_{f2},\ D_f \approx 2D_{f2} \tag{6. 43}$$

Therefore, according to (6. 31), the range for D_{f1} is always (0, 0.125) which is mapped to (0, 0.25) for D_f.

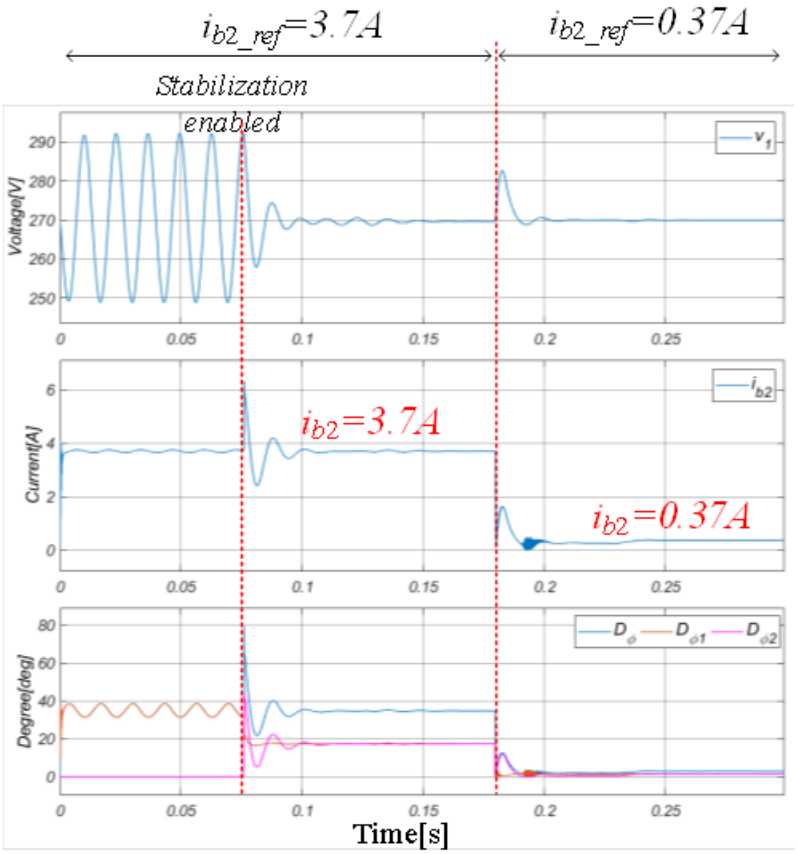


Fig. 6.18 Stabilization with co-ordinated control where PI controllers are set as k_{p1}=0.02, k_{i1}=100, k_{p2}=0.003 and k_{i2}=5. Circuit parameters in Table 7.2 are used

6.4 Chapter summary

A scenario is investigated where the DAB converter is responsible for both load current regulation and DC system stabilization. The impedance stability criteria has been developed. Based on the criteria, the system stability is determined by the impedance ratio. In other words, if both input and output impedances at the connection terminal can be derived, the stability of the bus voltage can be assessed.

Theoretical analysis on the passive damping has been performed. Results have shown that the passive damping approach can stabilize the system, however it brings in extra conduction loss,

the proportion of which increases with the power rating. Therefore, it has been concluded that passive damping approach is not suitable for high power applications.

Active stabilization methods are therefore looked into as alternatives to passive damping approaches. Active stabilization methods are achieved by a control algorithm without inducing physical components. The PI based stabilization control has been addressed. The control has been also analysed by looking into the input impedance and the closed-loop control to output transfer function. It has been concluded that:

- The system impedance has impact on the closed-loop transfer function. The PI control parameters have to be designed with the information of the system impedance.
- The current regulation control loop and the stabilization loop have contradiction in their performance. The stabilization loop inevitably affects the performance of battery current regulation in a wide frequency range.

Apart from the above challenge and issue, the conventional PI based stabilization control presents another vital problem with control loop saturation. The saturation phenomena has been addressed. A solution named co-ordination integration with little changes to the conventional PI control is proposed. The co-ordination links the integration elements of the independent PI controllers, thus preventing saturation for the two controllers.

Chapter 7 MDCS-MPC based system stabilization

Inspired by the shortcomings of the state-of-the-art DC micro-grid stabilization methods mentioned above, a fundamentally different damping approach based on MDCS-MPC is proposed. The two control objectives of load regulation and input bus voltage damping have been incorporated in the cost function. Therefore, with the proper design of the weighting factors [133], the controller will never lose ability in load regulation.

One of the advantages of MDCS-MPC is the flexibility to implement multi-objective control. In Chapter 4, the DAB converter achieves both load voltage regulation and large signal stability with the mono-dimensional MDCS-MPC. In Chapter 5, the DAB converter achieves both load voltage regulation and the transformer peak current minimization with the multi-dimensional MDCS-MPC. In this chapter, another scenario is investigated where the DAB converter is responsible for both load voltage regulation and DC system stabilization. Although both mono-dimensional and multi-dimensional MDCS-MPC can be applied in this scenario to achieve multi-objective control, mono-dimensional MDCS-MPC with SPS (Fig. 6.1(c)) is chosen as an example to showcase the theory.

The objectives of the mono-dimensional MDCS-MPC are, on one hand, to regulate the battery current i_2 and, on the other hand, to stabilize the DC bus voltage v_1. MPC is inherently a good choice for multi-objective optimization problems. In this section, the mono-dimensional MDCS-MPC with SPS is introduced for system stabilization control. The mono-dimensional MDCS-MPC discretizes the only control variable - D_f into piecewise elements to fit into the principle of the well-known FCS-MPC. It enables the predictive stabilization approach in DAB converters. The discretised difference equation of the battery current i_{b2} is developed as in [132]:

$$i_{b1_p}[k] = \frac{v_2[k]}{f_s L_p} D_f[k](1-2\left|D_f[k]\right|) \tag{7. 1}$$

$$i_{b2_p}[k] = \frac{v_1[k]}{f_s L_p} D_f[k](1-2\left|D_f[k]\right|) \tag{7. 2}$$

, where $i_{b1_p}[k]$ and $i_{b2_p}[k]$ are the predicted terminal currents. $v_1[k]$ and $v_2[k]$ are the sampled terminal voltages. The input voltage v_1 can also be predicted in the form of a difference equation as:

$$v_{1_p}[k+1] = v_1[k] + \frac{T_s}{C_f}(i_1[k] - i_{b1_p}[k]) \tag{7. 3}$$

, where $v_{1_p}[k+1]$ is the predicted DC bus voltage. $i_{b1_p}[k]$ is the predicted terminal current from (7. 1). $i_1[k]$ is the sampled input current as demonstrated in Fig. 6.2(a).

Taking into account the computational delay, MDCS-MPC has a prediction step of two sampling periods. The cost function is proposed as in (7. 4). v_{1dc} is the DC component of v_1, processed by a low pass filter.

$$ct = \alpha_1 G_1 + \alpha_2 G_2 \tag{7. 4}$$

, where

$$G_1 = (i_{b2_ref} - i_{b2_p}[k+2])^2 \tag{7. 5}$$

$$G_2 = (v_{1dc} - v_{1_p}[k+2])^2 \tag{7. 6}$$

An intuitive perspective on how the cost function term G_2 provides stabilization to the bus voltage v_1 is explained. Fig. 6.8(a) shows conceptually how the currents behave when only G_1 is included in the cost function. Since the battery current i_{b2} is tightly regulated to a constant value, the input bridge current i_{b1} equals P_{const}/v_1. AC components flows into the filter capacitor C_f causing oscillation in voltage v_1. After G_2 is enabled, and dominants ct. If v_{1dc} is larger than $v_{1_p}[k+2]$, according to (7. 3), the current i_{b1_p} tends to be reduced in order to increase $v_{1_p}[k+2]$. If v_{1dc} is smaller than $v_{1_p}[k+2]$, for the same reason, the current i_{b1_p} tends to be increased in order to reduce $v_1[k+2]$. As a result, i_{b1} absorbs the AC components of i_1 so that ideally the current i_c remains constant. The stabilization on v_1 is therefore achieved. Practically, G_1 and G_2 contradict each other. Their priorities in ct are influenced by the weighting factors, α_1 and α_2.

The same operating principle, adaptive step and error compensation discussed in Chapter 4 can be applied also in this chapter. Sections 6.3.2.1 will briefly address those techniques to underpin further explanations on mono-dimensional MDCS-MPC based stabilization

7.1 Operating principle

The variable D_f is continuous in nature. Compared to the MATLAB aided numerical method reported in [109], the mono-dimensional MDCS-MPC provides an online simplified optimization to the cost function in (7. 4). To implement MDCS-MPC, D_f is discretized. The discretization precision is subjected to the control platform applied. Δ_f is defined in (7. 7) as the finest phase shift value that can be achieved in a digital control platform.

$$\Delta_f = \frac{f_s}{f_c} \tag{7. 7}$$

, where f_s is the switching frequency and f_c is the peripheral clock frequency of the digital control platform. DAB works predominately in the range (7. 8) for bidirectional power flow.

$$D_f \in [-0.25, 0.25] \tag{7. 8}$$

(7. 8) is further discretized into μ_m (=0.5/Δ_f+1) elements as described in array (7. 9).

$$D_f \in \{-0.25, \cdots, -\Delta_f, 0, \Delta_f, 2\Delta_f, \cdots, 0.25\} \tag{7. 9}$$

In order to implement a control algorithm that is feasible on standard commercial microcontrollers, the mono-dimensional MDCS-MPC evaluates a reduced number of values in each sampling period. In one sampling period, μ ($\mu \leq \mu_m$) number of points are assessed. They are centred at the previous working point.

In order to explain the working principle of the MDCS-MPC, we assume the DAB is connected to a stiff voltage source. An intuitive illustration of the mono-dimensional MDCS-MPC is depicted in Fig. 7.1. In the control interval k to k+1, μ=3 points are evaluated centred at the previous working point $D_\varphi[k] = a$. When $D_\varphi[k+1]$ equals a-Δ_f, a and a+Δ_f, the load current i_{b2} is predicted as $i_{b2}^{(1)}[k+2]$, $i_{b2}^{(2)}[k+2]$ and $i_{b2}^{(3)}[k+2]$. The superscript represents the index of an element in the moving discretized control set.

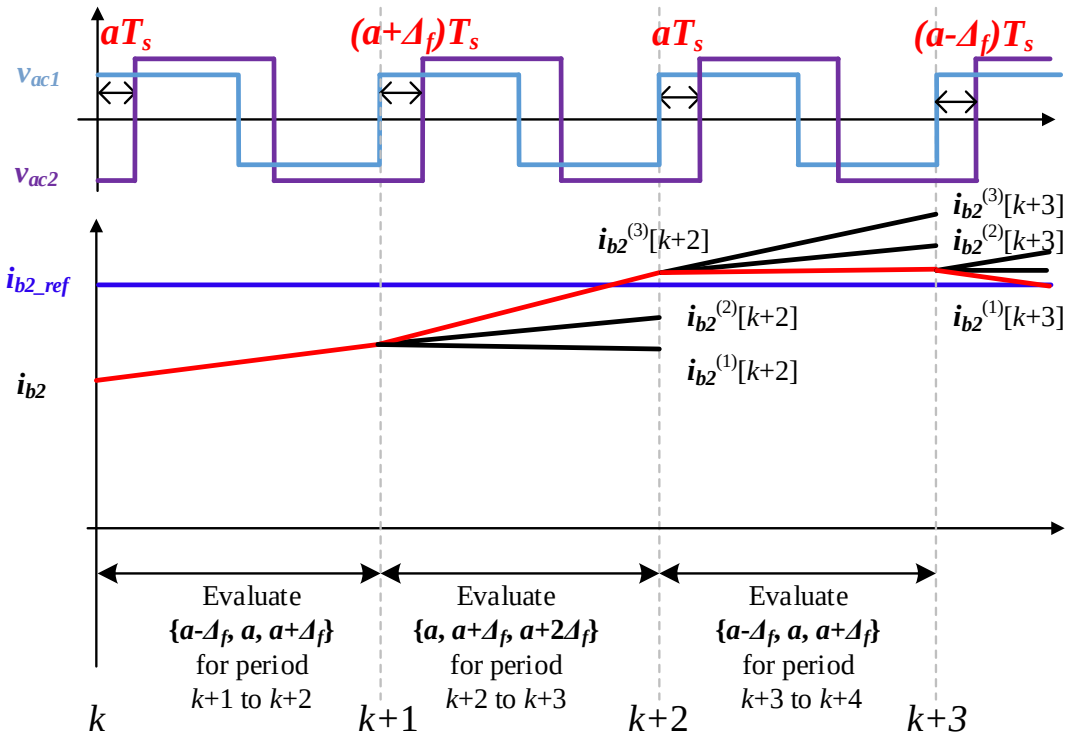


Fig. 7.1 The operating principle of the MDCS-MPC for DAB. μ is set to be 3 for illustration.

The moving discretized control set during the period k to k+1 is $\{a\text{-}\Delta_f, a, a+\Delta_f\}$. According to the illustration in Fig. 7.1, when $D_\varphi[k+1]= a+\Delta_f$, the predicted output voltage $i_{b2}{}^{(3)}[k+2]$ is the closest to i_{b2_ref}. This results in the smallest cost function defined in (7. 4). Therefore, the value $a+\Delta_f$ is applied at time instance k+1 to D_φ. In the next control interval, the same process is repeated. However, the moving discretized control set has changed. It has become $\{a, a+\Delta_f, a+2\Delta_f\}$. The control set is moving with the working point within the domain of (7. 9). In this control interval, $D_\varphi[k+3] = a$ results in the smallest cost function. Therefore, this value is applied at the time instance k+2. This process continues following this procedure.

The evaluation has to be conducted first on the time allowed for implementing a control algorithm in one switching period. The time left for controls determines the value of μ. A larger value of μ can increase the transition dynamics, but it aggravates the computational burden. Therefore, an adaptive step method is proposed as shown in (7. 10) and (7. 11). The adaptive step Δ_{adp} changes with the deviation of the output current to the reference. When i_{b2} is far from the reference, Δ_{adp} grows largely. In contrast, when i_{b2} equals to the reference, Δ_{adp} becomes Δ_f. So, the control accuracy remains.

$$I_{\Delta} = \begin{cases} \left| i_{b2_ref} - i_{b2}[k] \right|, & \left| i_{b2_ref} - i_{b2}[k] \right| < I_m \\ I_m \quad , & \left| i_{b2_ref} - i_{b2}[k] \right| > I_m \end{cases} \tag{7. 10}$$

$$\Delta_{adp} = \Delta_f (1 + \lambda {I_{\Delta}}^2) \tag{7. 11}$$

, where I_m is the saturation. λ is a coefficient related to transition performance which is empirically tuned to achieve required dynamic performance. A larger value of λ increases the current reference tracking speed, however, it may also increase steady state chattering due to sampling noises.

The application of the reduced order model of DAB [132] renders errors in the predictions (7. 1) and (7. 2). However, errors can be corrected by compensation terms defined as I_{comp1} and I_{comp2} in (7. 12) and (7. 13). I_{comp1} and I_{comp2} are calculated as the difference between the observed current values and the predicted values.

$$I_{comp1}[k] = i_{b1_r}[k] - i_{b1_p}[k] \tag{7. 12}$$

$$I_{comp2}[k] = i_{b2_r}[k] - i_{b2_p}[k] \tag{7. 13}$$

, where i_{b1_r} and i_{b2_r} are observed currents at both terminals as calculated in (7. 14) and (7. 15). Due to the direct connection to a battery, i_{b2_r} equals the sampling value.

$$i_{b1_r}[k] = i_1[k] - C_f \, f_s (v_1[k] - v_1[k-1]) \tag{7. 14}$$

$$i_{b2_r}[k] = i_{b2}[k] \tag{7. 15}$$

The control block diagram of the mono-dimensional MDCS-MPC is presented in Fig. 7.2. It shows the process of MDCS-MPC. The output of the control is the phase shift duty D_f depicted in Fig. 6.1(c). μ number of elements are evaluated in the full control set (7. 9). The calculated points can be expanded on request of the particular applications providing enough computational power. The evaluation process starts with the calculation of the adaptive step Δ_{adp}. It determines the step distance between two adjacent values in the control set. The control set slides in the range described in (7. 9) centred at $D_f[k+1]$. Then the iteration starts for the evaluation of *ct*. The bus voltage ($v_{1_p}[k+2]$) and battery current ($i_{b2}[k+2]$) are predicted with μ elements in the control set by (7. 2) and (7. 3). Predictions are corrected by the compensation

terms (7. 12) and (7. 13). The element achieving minimal *ct* is then stored in $D_f[k+2]$ which is going to be applied in the future instance $k+2$.

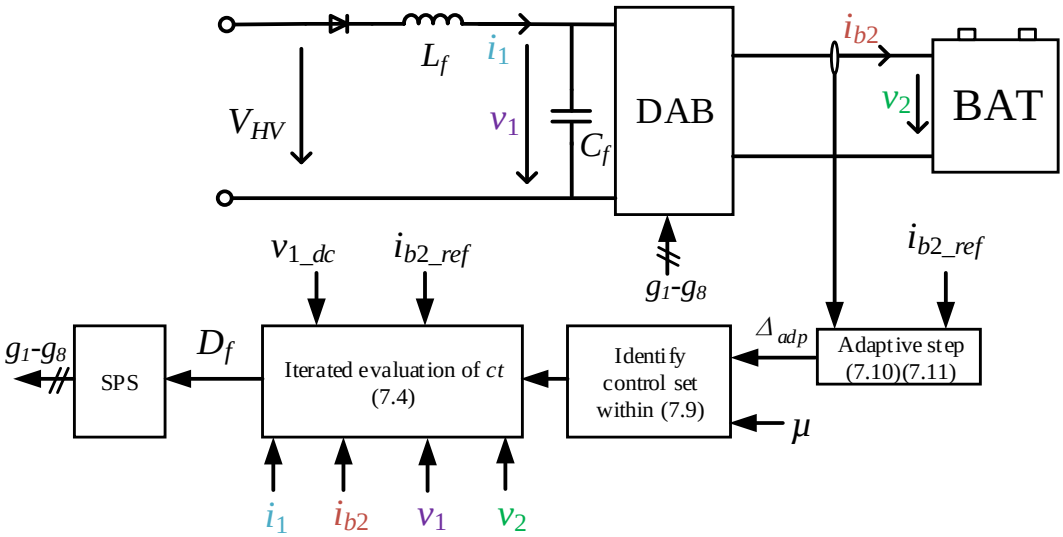


Fig. 7.2 The control block of the MDCS-MPC

7.2 Phase margin assessment

In order to assess the frequency response, the small signal model of DAB converters is often carried out. However, this is infeasible to describe the DAB converters with non-linear controllers. If a certain small sinusoidal perturbation signal that is applied to a nonlinear element always excites a sinusoid at the same frequency in the output, then such an element can be represented by its linear “equivalent” frequency response, which is commonly referred to a describing function (*c.f.* [118], ch.5) As a result, standard frequency domain techniques can be used to approximately assess the stability of the systems which comprise nonlinear elements. Therefore, the standard approach introduced in [134] has been used in this paper. Small signal perturbations have been injected into the converter and responses have been measured with the correspondent frequency. This numerical method applies to both linear and non-linear control systems. Theoretically it equals the analytical method which is based on the small signal modelling in linearization. Both methods need to have their assessments carried out based on a given equilibrium point.

In order to evaluate the performance of the mono-dimensional MDCS-MPC, the describing function approach has been used to sweep the input impedance Z_{in} of the DAB controlled by mono-dimensional MDCS-MPC as shown in Fig. 7.3.

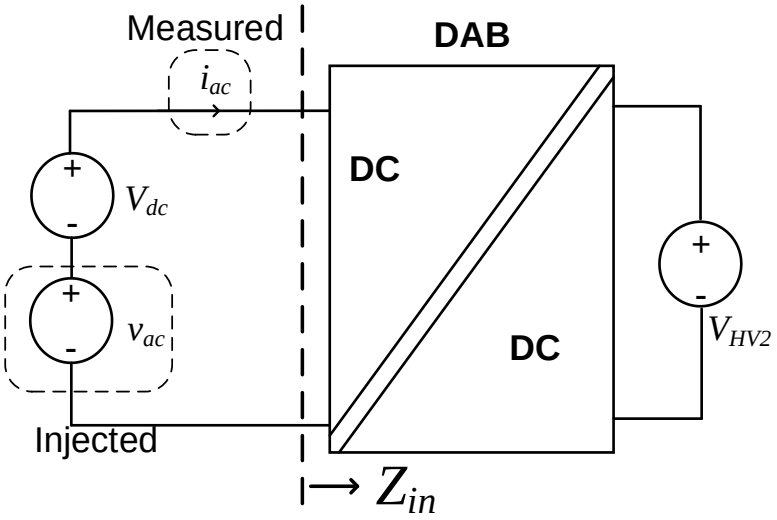
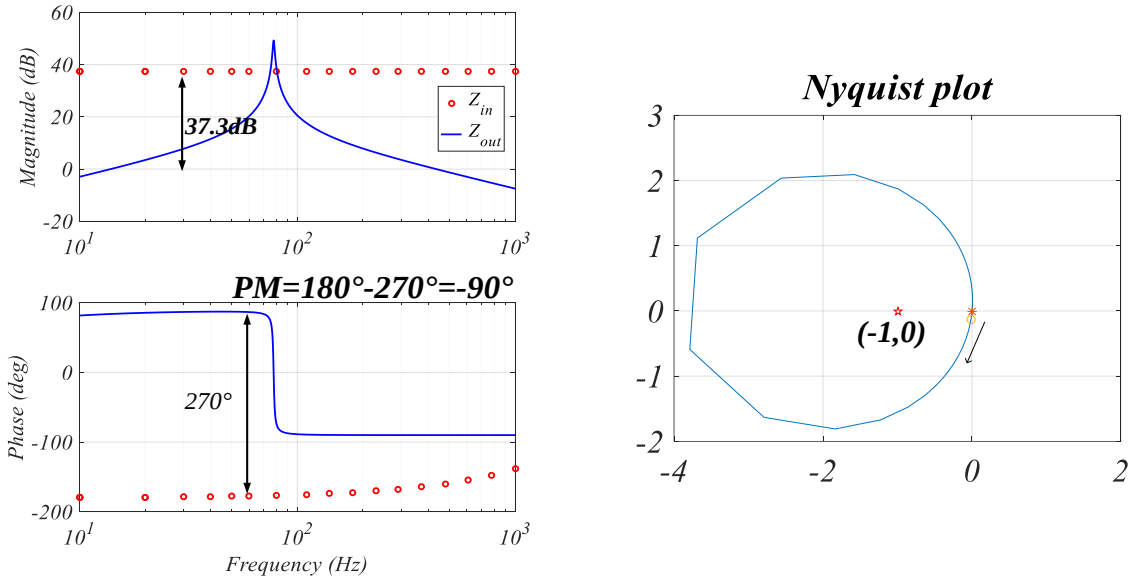


Fig. 7.3 The measurement diagram for the input impedance Z_{in}.

The input impedance can be therefore calculated based on the measured data as

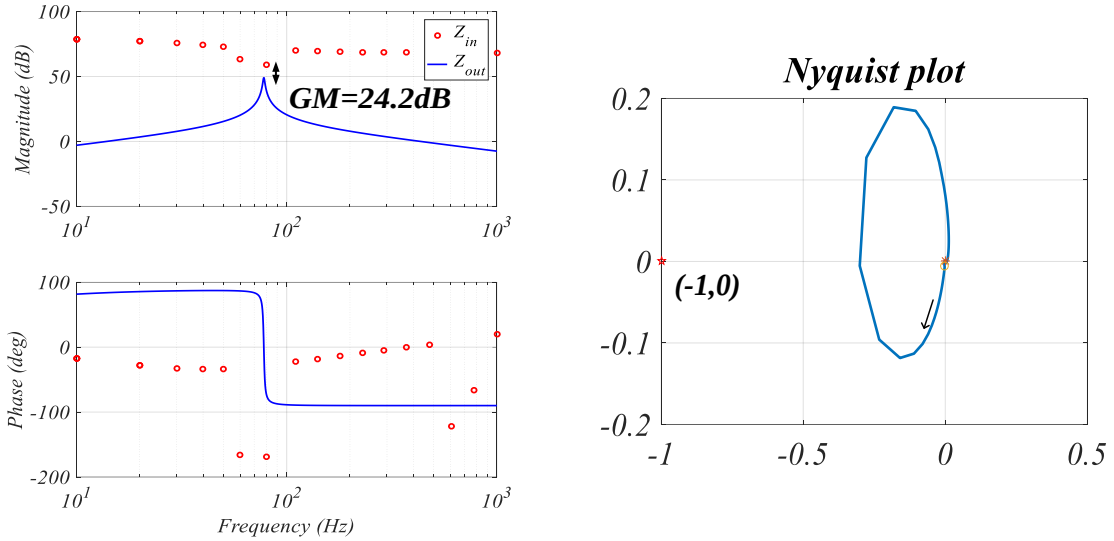
$$Z_{in}(f) = \frac{v_{ac}(f)}{i_{ac}(f)} \tag{7. 16}$$

As shown in Fig. 7.4(a), without the stabilization term G_2 in the cost function, the phase margin is -90 degree indicating that the DC bus voltage is not stable. This has also been confirmed by the Nyquist plot in Fig. 7.4(b). After the stabilization term G_2 is enabled as in Fig. 7.5(a) where α_2 equals to 0.1, the Gain Margin (GM) is 24.2dB indicating that the bus voltage is stable. The Nyquist plot in Fig. 7.5(b) has also supported the same conclusion. However, the GM is subjected to the peak amplitude of the LC resonance. A smaller stray resistance of L_f could reduce the GM. Therefore, the stability is not guaranteed. The phase margin can be greatly improved to 90 degrees by increasing the weighting factor α_2 to 0.3 as in Fig. 7.6(a). This indicates that the bus voltage is stable. The Nyquist plot in in Fig. 7.6(b) has also supported the same conclusion.



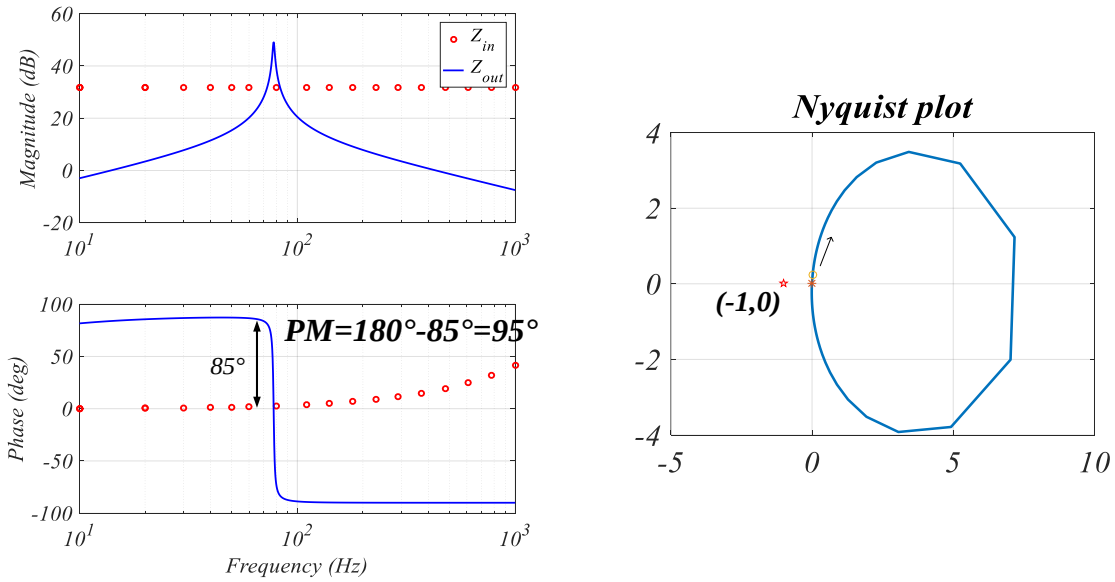
(a) (b)

Fig. 7.4 Stability assessment with mono-dimensional MDCS-MPC α_2=0 @1kW 270V/270V. Circuit and control parameters in Table 7.2 and Table 7.3 are used.



(a) (b)

Fig. 7.5 Stabilization with mono-dimensional MDCS-MPC α_2=0.1 @1kW 270V/270V. Circuit and control parameters in Table 7.2 and Table 7.3 are used.



(a) (b)

Fig. 7.6 Stabilization with mono-dimensional MDCS-MPC α_2=0.3 @1kW 270V/270V. Circuit and control parameters in Table 7.2 and Table 7.3 are used.

7.3 Current regulation performance

The evaluations on the current regulation performance of the mono-dimensional MDCS-MPC and PI controllers have also been carried out using the describing function. Fig. 7.7 describes the sweeping circuit for the close loop transfer function.

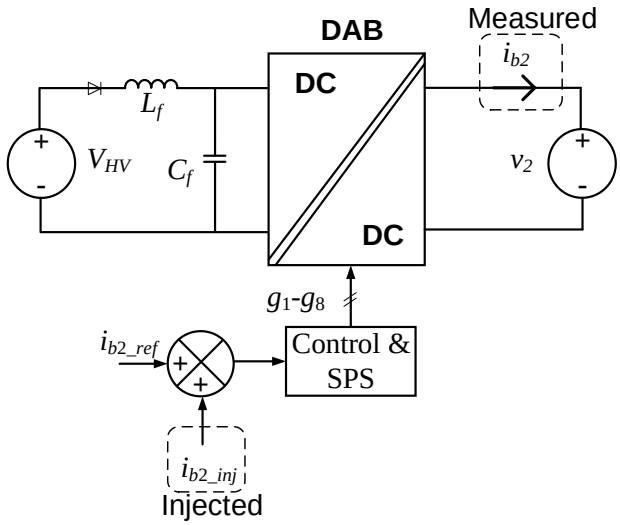
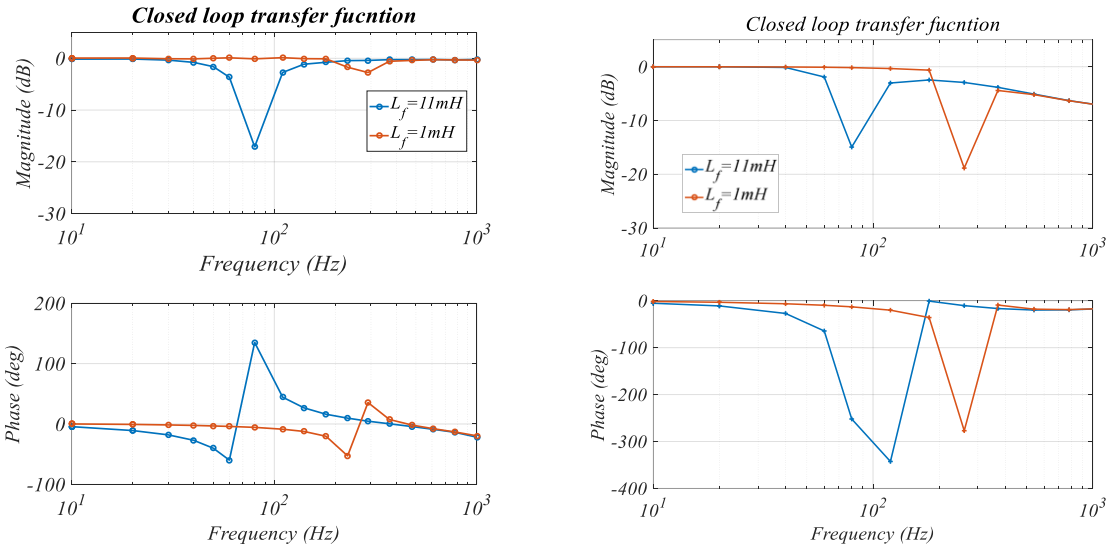


Fig. 7.7 The measurement diagram for the close loop transfer function

Small magnitude sinusoidal signals i_{b2_inj} have been injected on top of the battery current reference value i_{b2_ref}. Battery current i_{b2} has been measured at frequencies correspondent to the injected ones. The close loop transfer function can be therefore calculated based on the measured data as

$$G_{R2O}(f) = \frac{i_{b2}(f)}{i_{b2_inj}(f)} \tag{7. 17}$$

The control parameters from Table 7.3 are used for the comparison. The closed-loop i_{b2_ref} to i_{b2} transfer function has been swept in a resolution of 10Hz as an index to measure the current regulation performance under two different values of L_f. Fig. 7.8 shows the corresponding Bode diagram. When the mono-dimensional MDCS-MPC is used in Fig. 7.8(a). It can be concluded from the figure that the value of L_f affects only the battery current regulation near resonance frequencies. The mono-dimensional MDCS-MPC provides a good regulation of the current in the swept frequency range from 10Hz to 1kHz. In observation from Fig. 7.8(a), the damping term has less influence in the battery current regulation with smaller L_f. When the Co-ordinated integration PI control based stabilization is used as shown in Fig. 7.8(b), the impact on the $G_{R2O}(f)$ remains large for smaller L_f.



(a) MDCS-MPC (b) Co-ordinated integration

Fig. 7.8 Stabilization with mono-dimensional MDCS-MPC α_2=0.1 @1kW 270V/270V. Circuit parameters in Table 7.1, Table 7.2 and Table 7.3 are used.

7.4 Time domain assessments

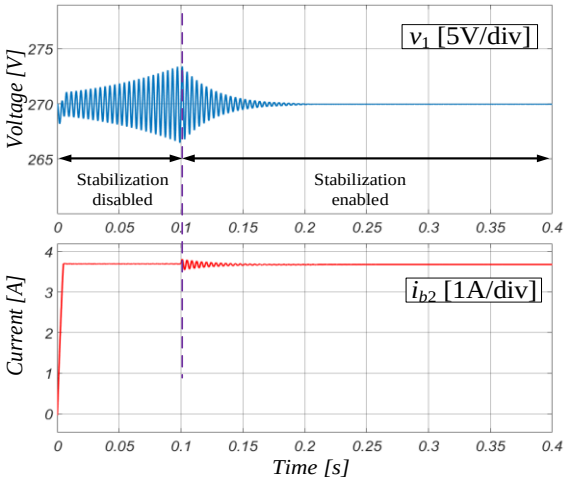
The simulations exam how the conveter behaves in presence of uncertain input *LC* filters with and without stabilization control techiques.Comparisons between the three stabilization control techniques are also highlighted. Time domain assessments are carried out with the control parameters for conventional PI and the co-ordinated integration summarized in Table 7.1. The control parameters for MDCS-MPC are provided in Table 7.3. Circuit parameters in Table 7.2 are used.

TABLE 7.1 CONTROL PARAMETERS FOR TIME DOMAIN ASSESSMENT

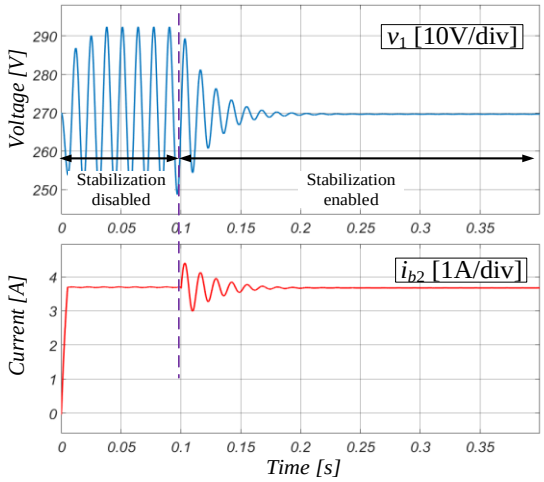
Parameter	PI	Co-ordinated integration
k_{p1}	0.02	0.02
k_{i1}	100	100
k_{p2}	0.001	0.003
k_{i2}	0.1	5

The waveforms in the time domain are presented in Fig. 7.9. When mono-dimensional MDCS-MPC is used, it shows a good compromise between the two control objectives. There are no drastic overshoot in the load current, and the bus voltage is stabilized reasonably fast. It is observed that when different values of Z_{in} applied, the oscillation frequency varies. The mono-dimensional MDCS-MPC is implemented without the knowledge of the input impedance Z_{in}. However, mono-dimensional MDCS-MPC maintains the ability to provide fast stabilization and current regulation.

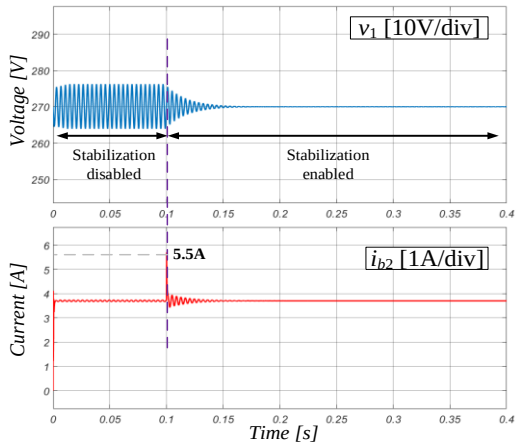
On the contrary, the co-ordinated integration controller has been implemented and tested. The time domain waveforms are presented in Fig. 7.9(c) and (d). The detailed circuit parameter design is presented in chapter 6. The stabilization performace is similar to that of MDCS-MPC. However, there exists significant overshoot in the load current when the stabilization controller is enabled. As discussed in Chapter 6, to avoid control loop saturations, when the conventional PI control is used, slower stabilization loop has to be implemented resulting in slow dynamic shown in Fig. 7.9(e) and (f).



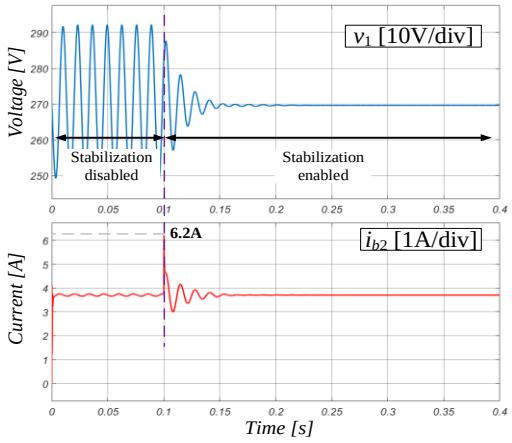
(a) MDCS-MPC L_f=1mH



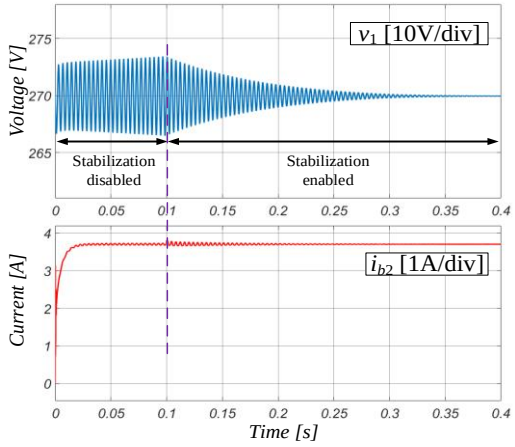
(b) MDCS-MPC L_f=11mH



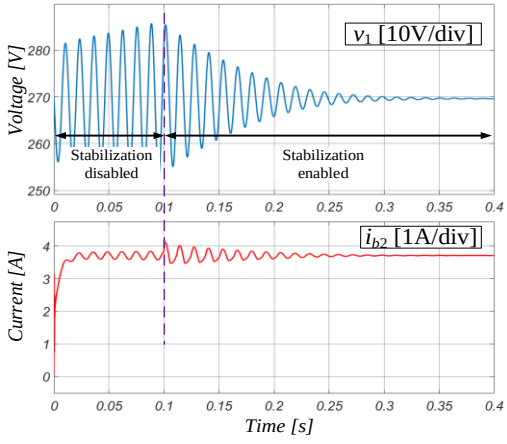
(c) Co-ordinated integration L_f=1mH



(d) Co-ordinated integration L_f=11mH



(e) PI L_f=1mH



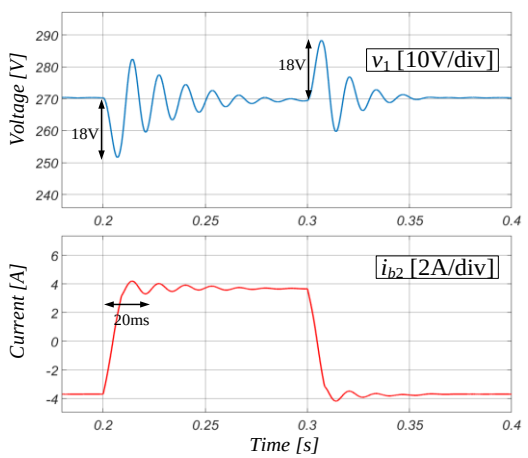
(f) PI L_f=11mH

Fig. 7.9 Time domain stabilization waveforms under different values of L_f.

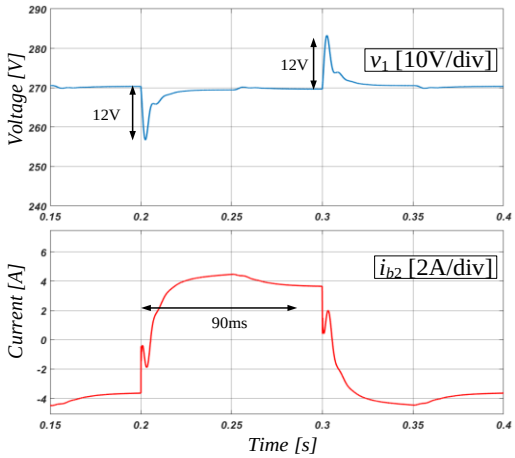
A scenario where diode bridge rectification is used for AC/DC power conversion stage is assumed in our case of study as shown in Fig. 6.1(a). If there are no extra loads connected to the DC bus, bidirectional power flow is not possible. However, in a practical micro-grid

application especially when battery banks are involved, bi-directional operation is inevitable. The transition performance between positive full power and negative full power using the mono-dimensional MDCS-MPC and co-ordinated integration controller have been also simulated. Results are shown in Fig. 7.10 where the diode shown in Fig. 6.2(a) in series with the source V_{DC} has been removed.

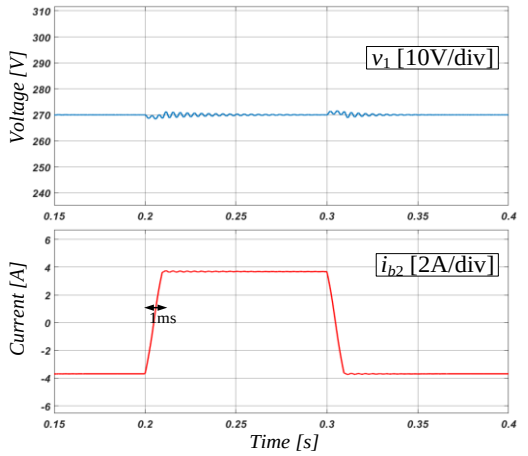
In order to keep a similar current regulation between two controllers under L_f=1mH, the current regulation control paramters for the co-ordinatd integration are set k_{p1}=0.01, k_{i1}=10. It can be observed from Fig. 7.10, the current regulation performace changes drastically with difference LC impendace while MDCS-MPC can effectively mitigate the impact. This verified the effectiveness and superior performance of the proposed controller in both power directions under uncertain grid impedances.



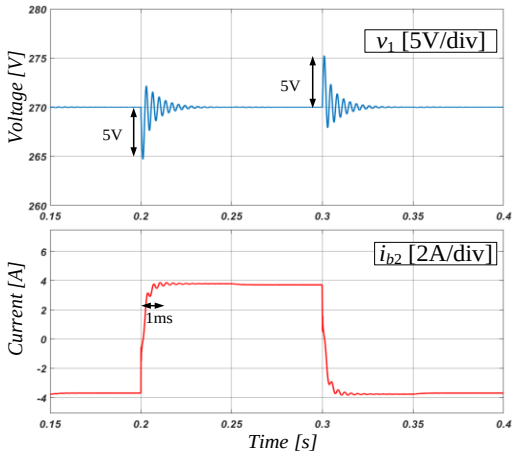
(a)MDCS-MPC L_f=11mH



(b)Co-ordinated integration L_f=11mH



(c)MDCS-MPC L_f=1mH



(d)Co-ordinated integration L_f=1mH

Fig. 7.10 Transition between -1kW and 1kW

7.5 Practical results

The proposed methodology has been validated on a 1kW 20kHz laboratory prototype. The circuit, control and hardware parameters are illustrated in Table 7.2-Table 7.4. Bench power supply EA-PS 9360-40 3U (1 Output, 0 V-360 V, 0 A-40 A) is connected in series with inductor L_f which has a stray resistance of 100mΩ. The electronics load M9715B 0-500V/1800W is used to emulate the battery. The experiment prototype is shown in Fig. 7.11. A TMS320F2837xD evaluation board from Texas Instruments has been adopted as the digital control platform which communicates with a host computer.

TABLE 7.2 CIRCUIT PARAMETERS

Description	Value	Units
Switching frequency f_s	20	kHz
Dead time t_d	1.6	μS
Transformer turn ratio	20:20	/
Primary power inductor L_p	300	μH
Parasitic resistance R_p	50	mΩ
Primary DC capacitor C_f	380	μF
Smoothing inductor L_f	11	mH
Parasitic resistance r_L	0.1	ohm
Rated power	1	kW

TABLE 7.3 MDCS-MPC CONTROL PARAMETERS

Description	Value	Units
Adaptive step saturation I_m	1.5	A
Adaptive step factor λ	1	/
Searching points μ	11	/
Weighting factor α_1	1	/
Weighting factor α_2	0.3	/

TABLE 7.4 HARDWARE COMPONENTS

Component	Description	Parameters
Switching devices	SKM75GB128D	V_{CES}=1200V; I_c=100A
Pri/Sec capacitors	C4DEFPQ6380A8TK	380uF; 400V
Magnetic components	MnZn Ferrites; 3.9mm^2 litz wire	L_m=3mH; L_p=0.3mH
Voltage sensors	LV 25-P	t_r=40us
Current sensors	LA 55-p	BW(-1dB) 200kHz

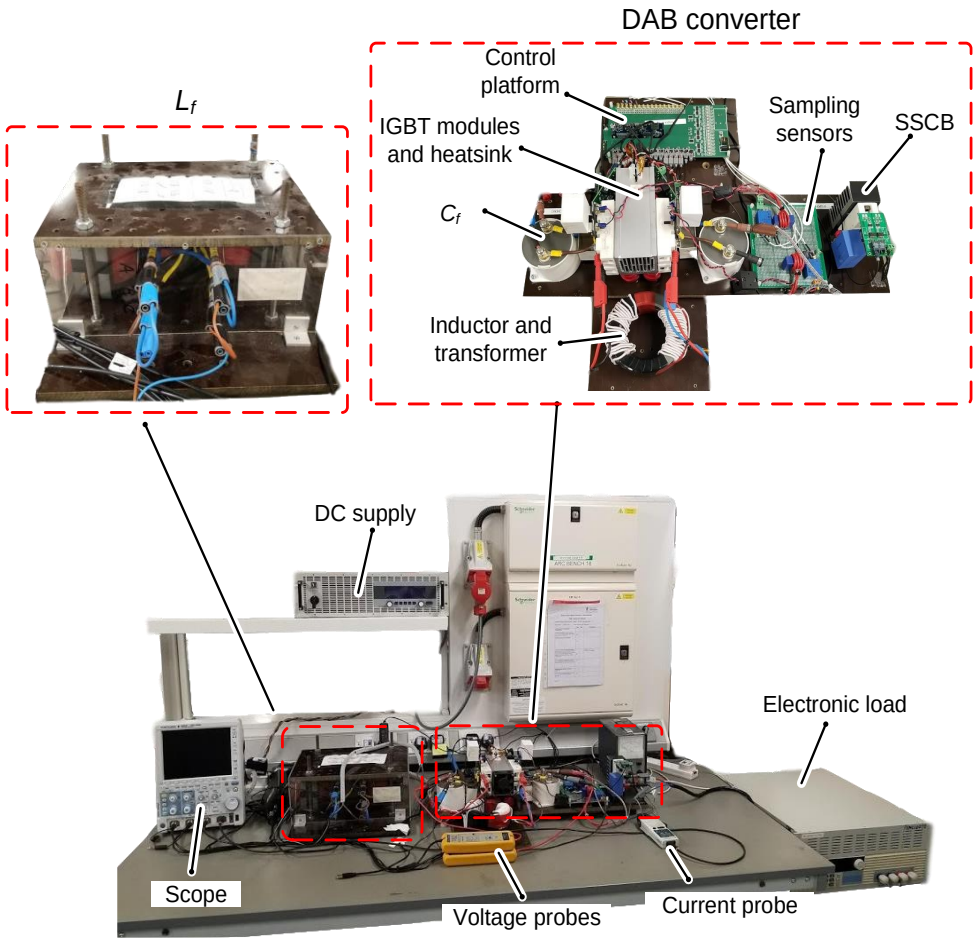
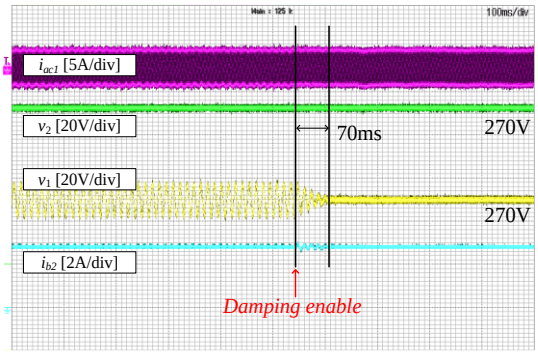


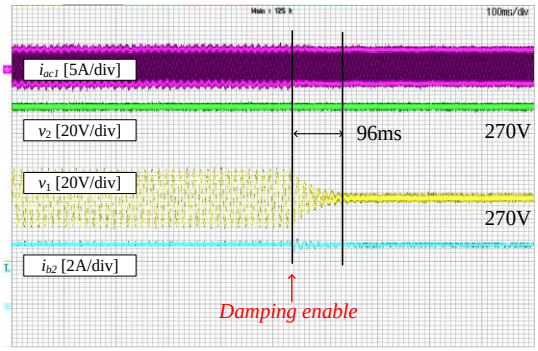
Fig. 7.11 The DAB hardware setup.

7.5.1 Stabilization

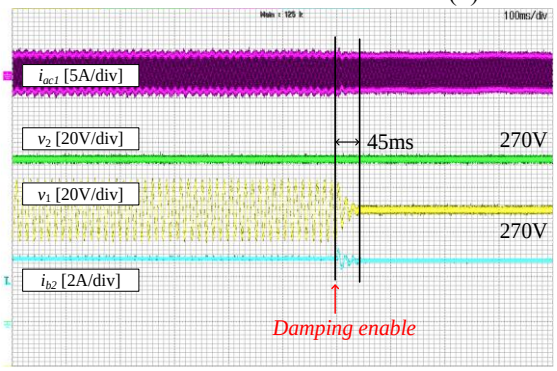
The stabilization performances of the PI controller and MDCS-MPC are compared in Fig. 7.12. The DAB operates at the condition 1kW, 270V/270V. Before the stabilizations are enabled for both PI and MDCS-MPC, the DC bus voltage oscillates as predicted by the Bode and Nyquist plots in Fig. 7.4. It can be noted that when the DC bus voltage is oscillating, both controllers track the reference current well. There is no obvious oscillation in i_{b2}. When the PI stabilizer is activated in Fig. 7.12(a). It takes 70ms to stabilize the DC bus voltage oscillation. While the MDCS-MPC is used, the value of α_2 has a direct impact on the stabilization performance. The stabilizing time is decreased from 96ms to 45ms when the weighting factor α_2 increases from 0.1 to 0.3. The increase of the weighting factor has inevitably incurred a greater disturbance in the current i_{b2} during transition. But it is still reasonably small.



(a) PI controller



(b) MDCS-MPC α_2=0.1

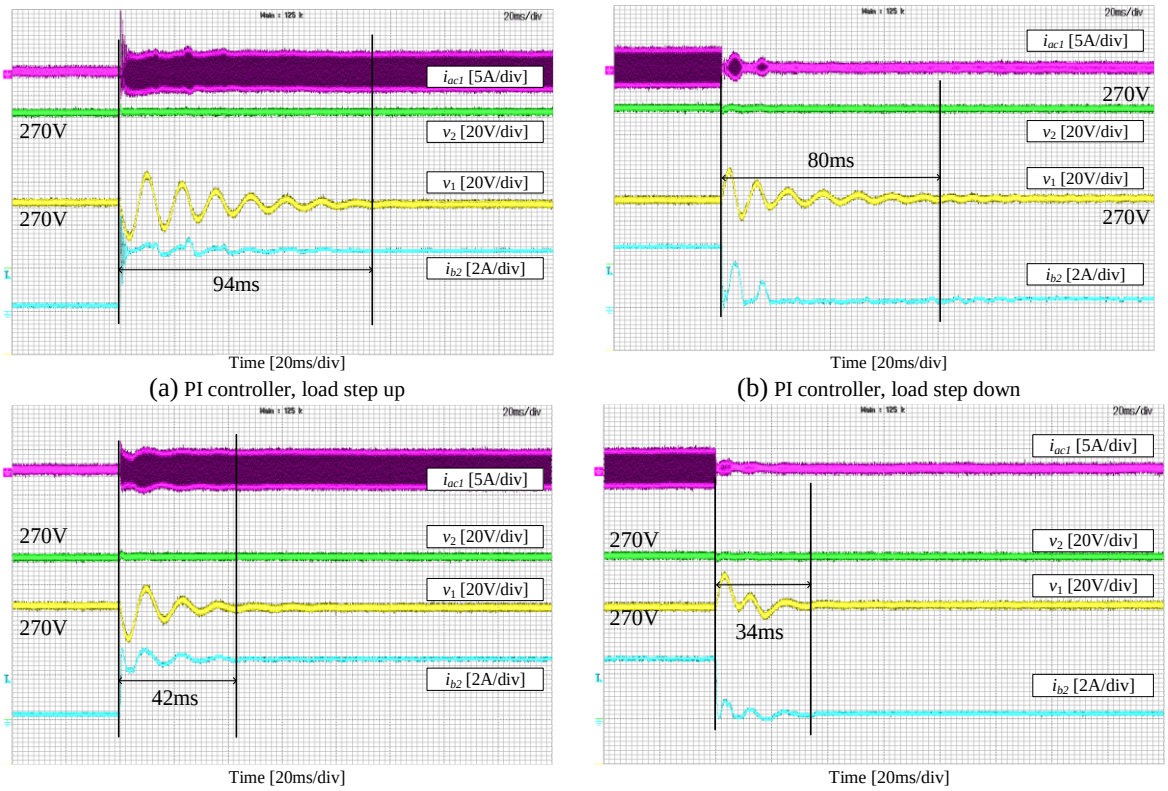


(c) MDCS-MPC α_2=0.3

Fig. 7.12 Stabilization comparisons

7.5.2 Current regulation

Battery current transitions have been performed. In Fig. 7.13(a)(c), the current reference i_{b2_ref} is changed from 0.37A to 3.7A. Stabilization controls have been enabled in both the PI controllers and the MDCS-MPC. It can be observed from Fig. 7.13(a) that at the instance of change in current reference i_{b2_ref}, there is a short period of oscillation in the battery current i_{b2} and overshoot in the transformer current i_{ac1}. However, these phenomena have been avoided in MDCS-MPC due to a better coordination between the two control objectives. The settling times are 42ms and 94ms for the MDCS-MPC and the PI approach, respectively. In Fig. 7.13(b)(d), the current reference i_{b2_ref} is changed from 3.7A to 0.37A. Stabilization controls have also been enabled in both the PI controllers and the MDCS-MPC. Similar conclusion can be drawn. The settling times are 80ms and 34ms for the MDCS-MPC and the PI approach, respectively.



(a) PI controller, load step up

(b) PI controller, load step down

(c) MDCS-MPC α_2=0.3, load step up

(d) MDCS-MPC α_2=0.3, load step down

Fig. 7.13 Load step down transition comparisons with stabilization control enabled

7.6 Chapter summary

A fundamentally different damping approach is established based on the mono-dimensional MDCS-MPC in this chapter. The basic operating principle remains similar to what has been discussed in Chapter 4. The cost function has been modified incorporating a system stabilization term. The impedance based stability analysis has been carried out with describing function. Comparisons between the PI and MDCS-MPC based stabilization control techniques have been presented in both time and frequency domain.

Experiemnts on a pratical DC distribution system are conducted which verify all the theoretical claims. It has been demonstrated that the mono-dimensional MDCS-MPC is inherently a good choice for multi-objective control in DAB. It provides advantages listed as follows:

- The system impedance information is not required for the implementation of MDCS-MPC based stabilization controls.

- Fast stabilization can be achieved while maintaining reasonably good load regulation performance. The stabilization term has only impact on the closed-loop transfer function in a limited frequency range centred at the LC resonant frequency.

All theoretical claims have been confirmed through simulations and experiments.

Chapter 8 Conclusion and future works

8.1 Conclusion

The MPC has been successfully applied in DAB converters. The introduced MDCS-MPC shows the advantages in flexible multi-objective control. This thesis has looked into the applications of the MDCS-MPC concept for DAB converter in three different scenarios.

The mono-dimensional MDCS-MPC which provides fast transition and large signal stability is presented in Chapter 4 for a DAB converter. The MDCS-MPC relies on the average model of DAB converter to derive the optimal control output by minimizing the cost function. The introduction of MDCDS-MPC begins with the basic operating principle. Two approaches to enhance the transition performance of MDCS-MPC are discussed. A cost function which provides both reference racking and stability is derived. A compensation approach has been proposed to compensate for the steady state error. The stability analysis is carried out for MDCS-MPC. The phase portrait has been used as the main analysis tool. Three statements have been proposed to underpin the stability proof. For an easy start, a benchmark control is assumed where stability with current/resistive loads are analysed and proofed. The instability when current saturates is explained. Based on all the above analysis, the stability with MDCS-MPC is addressed. It has been explained why the operation with current loads converges slowly, why the adaptive step makes the operation instable and why G_2 can stabilize the operation.

The concept of MDCS-MPC has been extended into multi-dimensional optimization. In the case study, two control objectives need to be achieved. The first one is the regulation of the load current; the second one is the minimization of the transformer peak current. To achieve the second objective, the optimization can be carried out offline or online. The advantages of the online over the offline optimization have been addressed. The online optimization breaks the restriction of the predefined path, which brings greater flexibility to adjust the priority between the two control objectives during transition. The implementation of the online optimization with two-dimensional MDCS-MPC is introduced. The two dimensional

discretised control set and the search method have been illustrated, distinguished from the mono-dimensional MDCS-MPC. A cost function, on one hand, regulates the load current. On the other hand, it reduces the transformer peak current value. The priority between the two control objectives can be adjusted by the weighting factors. The steady state comparisons between the SPS and the DPS are conducted. DPS shows more significant advantage over SPS in transformer peak current reduction when terminal voltage ratio varies far from unity. The dynamic performance of the introduced two-dimensional MDCS-MPC has been assessed. The increasing of the calculating points in one sampling period enhances the dynamic. However, it aggregates the computational burden. Alternatively, the adaptive step approach can be applied, which enables fast transition even with small number of calculations.

Finally, the mono-dimensional MDCS-MPC has been applied to address the DC system instability issue on MEA. The DAB converter is responsible for both load current regulation and DC system stabilization. Impedance stability criteria has been developed. Based on the criteria, the system stability is determined by the impedance ratio. In other words, if both input and output impedances at the connection terminal can be derived, the stability of the bus voltage can be assessed. The basic operating principle remains the same as discussed in Chapter 4. The cost function has been modified incorporating a system stabilization term. The impedance based stability analysis has been carried out with the describing function approach. It has been demonstrated that the mono-dimensional MDCS-MPC is inherently a good choice for multi-objective control in DAB. It provides several advantages. The system impedance information is not required for the implementation of MDCS-MPC based stabilization controls. Fast stabilization can be achieved while maintaining reasonably good load regulation performance. The stabilization term had only impacts on the close loop transfer function in a limited frequency range centred at the *LC* resonant frequency.

As explained in the chapter 3, to the best knowledge of the author, there found no literatures imposing advanced control methods in DAB with modulation techniques such as DPS and TPS. Comparisons to the PI controllers are conducted throughout this thesis. The summary of the relative advantages and drawbacks of MDCS-MPC over the conventional PI controller is shown in Table 8. 1.

TABLE 8. 1 SUMMARY OF THE RELATIVE ADVANTAGES AND DRAWBACKS

Application		PI control	MDCS-MPC
SPS		Simple implementation with good overall erformance	1. Weighting factor design is important to ensure stability. 2. Computaional burdon is higher
DPS,TPS	Offline optimization	Significant decteriration with different equilibrium points	Good robustness against terminal voltage and power variations
	Online optimization	/	Flexibity in adjusting the priority
Grid stabilization		Not robust to grid impedance variation	Adaptive to uncertain grid impedance

8.2 Future works

This thesis has introduced the MDCS-MPC. Some future work can be carried out based on the theories in this thesis, which are listed as follow:

- Analysis on the feasibility for applying the MDCS-MPC on other power electronics converters. Although this thesis has used DAB convertes as an example for the introduction of MDCS-MPC, the control method can be potentially applied in other power converters [135]. MDCS-MPC is particularly suitable for low order power converters with duty cycle or phase shift modulations.
- Application of the phase portrait stability theory to other topologies and controls. This thesis has proposed and used phase portrait analysis for assessment of the stability when using mono-dimensional MDCS-MPC. The phase portrait approach is also promising in stability analysis for other low order power electronics converters. The application of such method in some simple power converters such as buck, boost and two/three level inverters are worth investigation.
- Extension of the two-dimensional MDCS-MPC into other multi-dimensional MDCS-MPC with different modulation techniques. This thesis has utilized two-dimensional MDCS-MPC with DPS modulation as an example to showcase the theory. However, similar ideas can be applied with modulation techniques which provide more than one control variable such as TPS modulation and modulation techniques involving variable frequency.
- Investigation for the stabilization techniques for MEA DC distribution systems comprising multiple power electronics converters controlled by MPC. Predictive control has been widely investigated generally for its promising features in fast transition, easy inclusion of

non-lienar constraints, straightforward implementation etc. In the future DC distribution system, power converters may use MPC. When there are more than two power electronics converters in a DC system that are required for DC bus stabilization using the MDCS-MPC described in Chapter 7, how those converters stabilize the DC system co-ordinately is an interesting topic.

References

[1] "Fifth Assessment Report — IPCC." [Online]. Available: https://www.ipcc.ch/assessment-report/ar5/. [Accessed: 22-Dec-2019].

[2] "CO_2 and Greenhouse Gas Emissions - Our World in Data." [Online]. Available: https://ourworldindata.org/co2-and-other-greenhouse-gas-emissions. [Accessed: 22-Dec-2019].

[3] "CO2 emissions from commercial aviation, 2018 | International Council on Clean Transportation." [Online]. Available: https://theicct.org/publications/co2-emissions-commercial-aviation-2018. [Accessed: 04-Jan-2020].

[4] J. Lloyd, "Sunday night invited talk: The flight of the Vin Fiz II," 2014, pp. viii–viii.

[5] M. Bentele, *Engine Revolutions*. SAE International, 1991.

[6] "Airbus CEO Enders: Aerospace Industry On Brink Of 'Third Revolution' : The American Institute of Aeronautics and Astronautics." [Online]. Available: https://aviation.aiaa.org/Notebook.aspx?id=15032387008. [Accessed: 04-Jan-2020].

[7] B. Sarlioglu and C. T. Morris, "More Electric Aircraft : Review , Challenges , and Opportunities for Commercial Transport Aircraft," *IEEE Trans. Transp. Electrif.*, vol. 1, no. 1, pp. 54–64, 2015.

[8] P. Wheeler and S. Bozhko, "The More Electric Aircraft," *IEEE Electrif. Mag.*, vol. 2, no. 4, pp. 6–12, 2014.

[9] G. Buticchi, L. Costa, and M. Liserre, "Improving System Efficiency for the More Electric Aircraft: A Look at dc\/dc Converters for the Avionic Onboard dc Microgrid," *IEEE Ind. Electron. Mag.*, vol. 11, no. 3, pp. 26–36, Sep. 2017.

[10] V. Madonna, P. Giangrande, and M. Galea, "Electrical Power Generation in Aircraft: Review, Challenges, and Opportunities," *IEEE Trans. Transp. Electrif.*, vol. 4, no. 3, pp. 646–659, Sep. 2018.

[11] K. Areerak, S. V. Bozhko, G. M. Asher, L. De Lillo, and D. W. P. Thomas, "Stability Study for a Hybrid AC-DC More-Electric Aircraft Power System," *IEEE Trans. Aerosp. Electron. Syst.*, vol. 48, no. 1, pp. 329–347, 2012.

[12] I. Christou, A. Nelms, I. Cotton, and M. Husband, "Choice of optimal voltage for more electric aircraft wiring systems," *IET Electr. Syst. Transp.*, vol. 1, no. 1, pp. 24–30, 2011.

[13] M. Tariq, A. I. Maswood, C. J. Gajanayake, and A. K. Gupta, "Aircraft batteries : current trend towards more electric aircraft," *IET Electr. Syst. Transp.*, vol. 7, no. 2, pp. 93–103, Jun. 2017.

[14] M. Hirst, A. Mcloughlin, P. J. J. Norman, and S. J. J. Galloway, "Demonstrating the more electric engine : a step towards the power optimised aircraft," *IET Electr. Power Appl.*, vol. 5, no. 1, pp. 3–13, 2011.

[15] E. Ganev, "Selecting the best electric machines for electrical power-generation systems: High-performance solutions for aerospace More electric architectures," *IEEE Electrif. Mag.*, vol. 2, no. 4, pp. 13–22, Dec. 2014.

[16] W. Rohouma, P. Zanchetta, P. W. Wheeler, and L. Empringham, “A Four-Leg Matrix Converter Ground Power Unit With Repetitive Voltage Control,” *IEEE Trans. Ind. Electron.*, vol. 62, no. 4, pp. 2032–2040, 2015.

[17] A. Trentin, P. Zanchetta, P. Wheeler, and J. Clare, “Power flow analysis in electro-mechanical actuators for civil aircraft,” *IET Electr. Power Appl.*, vol. 5, no. 1, p. 48, 2011.

[18] M. Villani, M. Tursini, G. Fabri, and L. Castellini, “Electromechanical Actuator for Helicopter Rotor Damper Application,” *IEEE Trans. Ind. Appl.*, vol. 50, no. 2, pp. 1007–1014, 2014.

[19] A. Nothofer, L. Tarisciotti, Q. Zhou, T. Benson, S. Greedy, and C. Christopoulos, “Analysis of conducted emissions from an Electric Nacelle Anti-Ice Power Control System,” *Int. Symp. Electromagn. Compat. - EMC Eur.*, pp. 434–439, 2016.

[20] L. Chédot, G. Friedrich, J. Biedinger, and P. Macret, “Integrated Starter Generator : The Need for an Optimal Design and Control Approach . Application to a Permanent Magnet Machine,” *IEEE Trans. Ind. Appl.*, vol. 43, no. 2, pp. 551–559, 2007.

[21] G. Friedrich and A. Girardin, “Integrated starter generator,” *IEEE Ind. Appl. Mag.*, vol. 15, no. 4, pp. 26–34, 2009.

[22] L. Tarisciotti, A. Costabeber, C. Linglin, A. Walker, and M. Galea, *Evaluation of isolated DC/DC converter topologies for future HVDC aerospace microgrids*. IEEE, 2017, pp. 2238–2245.

[23] D. Izquierdo, R. Azcona, F. J. L. del Cerro, C. Fernández, and B. Delicado, “Electrical Power Distribution System (HV270DC), for Application in More Electric Aircraft,” *IEEE Appl. Power Electron. Conf. Expo.*, no. 1, pp. 1300–1305, 2010.

[24] S. Pugliese, R. A. Mastromauro, and S. Stasi, “270V/28V wide bandgap device-based DAB converter for more-electric-aircrafts: Feasibility and optimization,” in *2016 International Conference on Electrical Systems for Aircraft, Railway, Ship Propulsion and Road Vehicles & International Transportation Electrification Conference (ESARS-ITEC)*, 2016, pp. 1–6.

[25] A. Connaughton, A. P. Talei, K. K. Leong, K. Krischan, and A. Muetze, “Investigation of a Soft-Switching Flyback Converter With Full Secondary Side-Based Control,” *IEEE Trans. Ind. Appl.*, vol. 53, no. 6, pp. 5587–5601, 2017.

[26] M. Forouzesh, Y. P. Siwakoti, S. A. Gorji, F. Blaabjerg, and B. Lehman, “Step-Up DC–DC Converters: A Comprehensive Review of Voltage-Boosting Techniques, Topologies, and Applications,” *IEEE Trans. Power Electron.*, vol. 32, no. 12, pp. 9143–9178, Dec. 2017.

[27] A. Chub, D. Vinnikov, F. Blaabjerg, and F. Z. Peng, “A Review of Galvanically Isolated Impedance-Source DC–DC Converters,” *IEEE Trans. Power Electron.*, vol. 31, no. 4, pp. 2808–2828, 2016.

[28] Xiaodong Li and A. K. S. Bhat, “Analysis and Design of High-Frequency Isolated Dual-Bridge Series Resonant DC/DC Converter,” *IEEE Trans. Power Electron.*, vol. 25, no. 4, pp. 850–862, Apr. 2010.

[29] C. Liu, H. Liu, G. Cai, S. Cui, H. Liu, and H. Yao, “Novel Hybrid LLC Resonant and DAB Linear DC–DC Converter: Average Model and Experimental Verification,” *IEEE Trans. Ind. Electron.*, vol. 64, no. 9, pp. 6970–6978, Sep. 2017.

[30] J. Wu, Y. Li, X. Sun, and F. Liu, “A New Dual-Bridge Series Resonant DC-DC Converter with Dual-Tank,” *IEEE Trans. Power Electron.*, pp. 1–1, 2017.

[31] H. Wu, K. Sun, Y. Li, and Y. Xing, “Fixed-Frequency PWM-Controlled Bidirectional Current-Fed Soft-Switching Series-Resonant Converter for Energy Storage Applications,” *IEEE Trans. Ind. Electron.*, vol. 64, no. 8, pp. 6190–6201, Aug. 2017.

[32] S. Bal, D. B. Yelaverthi, A. K. Rathore, and D. Srinivasan, “Improved Modulation Strategy using Dual Phase Shift Modulation for Active Commutated Current-fed Dual Active Bridge,” *IEEE Trans. Power Electron.*, pp. 1–1, 2017.

[33] F. Z. Peng, H. Li, G.-J. Su, and J. S. Lawler, “A New ZVS Bidirectional DC–DC Converter for Fuel Cell and Battery Application,” *IEEE Trans. Power Electron.*, vol. 19, no. 1, pp. 54–65, Jan. 2004.

[34] G. Spiazzi and S. Buso, “Analysis of the Interleaved Isolated Boost Converter With Coupled Inductors,” *IEEE Transactions on Industrial Electronics*, vol. 62, no. 7. pp. 4481–4491, 2015.

[35] D. Sha, Y. Xu, J. Zhang, and Y. Yan, “Current-Fed Hybrid Dual Active Bridge DC–DC Converter for a Fuel Cell Power Conditioning System With Reduced Input Current Ripple,” *IEEE Trans. Ind. Electron.*, vol. 64, no. 8, pp. 6628–6638, Aug. 2017.

[36] D. Sha, F. You, and X. Wang, “A High Efficiency Current Fed Semi Dual Active Bridge DC-DC Converter for Low Input Voltage Applications,” *IEEE Trans. Ind. Electron.*, pp. 1–1, 2015.

[37] G. Ortiz, L. Fassler, J. W. Kolar, and O. Apeldoorn, “Flux Balancing of Isolation Transformers and Application of ‘The Magnetic Ear’ for Closed-Loop Volt–Second Compensation,” *IEEE Trans. Power Electron.*, vol. 29, no. 8, pp. 4078–4090, Aug. 2014.

[38] B. Zhao, Q. Song, W. Liu, and Y. Zhao, “Transient DC Bias and Current Impact Effects of High-Frequency-Isolated Bidirectional DC–DC Converter in Practice,” *IEEE Trans. Power Electron.*, vol. 31, no. 4, pp. 3203–3216, Apr. 2016.

[39] A. R. Alonso, J. Sebastian, D. G. Lamar, M. M. Hernando, and A. Vazquez, “An overall study of a Dual Active Bridge for bidirectional DC/DC conversion,” *2010 IEEE Energy Conversion Congress and Exposition*. pp. 1129–1135, 2010.

[40] B. Zhao, Q. Song, W. Liu, and Y. Sun, “Overview of Dual-Active-Bridge Isolated Bidirectional DC–DC Converter for High-Frequency-Link Power-Conversion System,” *IEEE Trans. Power Electron.*, vol. 29, no. 8, pp. 4091–4106, Aug. 2014.

[41] P. Karamanakos, T. Geyer, and S. Manias, “Direct Voltage Control of DC–DC Boost Converters Using Enumeration-Based Model Predictive Control,” *IEEE Trans. Power Electron.*, vol. 29, no. 2, pp. 968–978, Feb. 2014.

[42] B. Wang, V. R. K. Kanamarlapudi, L. Xian, X. Peng, K. T. Tan, and P. L. So, “Model Predictive Voltage Control for Single-Inductor Multiple-Output DC–DC Converter With Reduced Cross Regulation,” *IEEE Trans. Ind. Electron.*, vol. 63, no. 7, pp. 4187–4197, Jul. 2016.

[43] Y. Shi, R. Li, Y. Xue, and H. Li, “Optimized Operation of Current-Fed Dual Active Bridge DC-DC Converter for PV Applications,” *IEEE Trans. Ind. Electron.*, vol. 62, no. 11, pp. 6986–6995, Nov. 2015.

[44] L. Chen, L. Tarisciotti, A. Costabeber, Q. Guan, P. Wheeler, and P. Zanchetta, “Phase-Shift Modulation for a Current-Fed Isolated DC-DC Converter in More Electric Aircrafts,” *IEEE Trans. Power Electron.*, vol. 34, no. 9, pp. 8528–8543, 2019.

[45] M. Andresen, K. Ma, G. Buticchi, J. Falck, F. Blaabjerg, and M. Liserre, “Junction Temperature Control for More Reliable Power Electronics,” *IEEE Trans. Power Electron.*, vol. 33, no. 1, pp. 765–776, Jan. 2018.

[46] H. Bai, C. C. Mi, and S. Gargies, “The Short-Time-Scale Transient Processes in High-Voltage and High-Power Isolated Bidirectional DC-DC Converters,” *IEEE Transactions on Power Electronics*, vol. 23, no. 6. pp. 2648–2656, 2008.

[47] G. G. Oggier, G. O. GarcÍa, and A. R. Oliva, “Switching Control Strategy to Minimize Dual Active Bridge Converter Losses,” *IEEE Trans. Power Electron.*, vol. 24, no. 7, pp. 1826–1838, Jul. 2009.

[48] Hua Bai and C. Mi, “Eliminate Reactive Power and Increase System Efficiency of Isolated Bidirectional Dual-Active-Bridge DC–DC Converters Using Novel Dual-Phase-Shift Control,” *IEEE Trans. Power Electron.*, vol. 23, no. 6, pp. 2905–2914, Nov. 2008.

[49] N. Hou, W. Song, and M. Wu, “Minimum-Current-Stress Scheme of Dual Active Bridge DC-DC Converter with Unified Phase-Shift Control,” *IEEE Trans. Power Electron.*, vol. 31, no. 12, 2016.

[50] N. SCHIBLI, “SYMMETRICAL MULTILEVEL CONVERTERS WITH TWO QUADRANT DC-DC FEEDING,” École polytechnique fédérale de Lausanne, 2000.

[51] G. Xu, D. Sha, J. Zhang, and X. Liao, “Unified Boundary Trapezoidal Modulation Control Utilizing Fixed Duty Cycle Compensation and Magnetizing Current Design for Dual Active Bridge DC–DC Converter,” *IEEE Trans. Power Electron.*, vol. 32, no. 3, pp. 2243–2252, Mar. 2017.

[52] F. Jauch and J. Biela, “Combined Phase Shift and Frequency Modulation of a Dual Active Bridge AC-DC Converter with PFC,” *IEEE Trans. Power Electron.*, pp. 1–1, 2016.

[53] C. Mi, H. Bai, C. Wang, and S. Gargies, “Operation, design and control of dual H-bridge-based isolated bidirectional DC-DC converter,” *IET Power Electron.*, vol. 1, no. 4, pp. 507–517, 2008.

[54] S. Shao, M. Jiang, W. Ye, Y. Li, J. Zhang, and K. Sheng, “Optimal Phase Shift Control to Minimize Reactive Power for a Dual Active Bridge DC-DC Converter,” *IEEE Trans. Power Electron.*, pp. 1–1, 2019.

[55] B. Farhangi and H. A. Toliyat, “Piecewise Linear Model for Snubberless Dual Active Bridge Commutation,” *IEEE Trans. Ind. Appl.*, vol. 51, no. 5, pp. 4072–4078, Sep. 2015.

[56] I. Askarian, T. Helmuth, M. Palevani, A. Knight, and S. M. Kaviri, “Hybrid modulation technique for Dual-Active-Bridge DC-DC converters to achieve full ZVS over wide range of operating conditions,” in *2017 IEEE 8th International Symposium on Power Electronics for Distributed Generation Systems, PEDG 2017*, 2017.

[57] Y. Shen, X. Sun, W. Li, X. Wu, and B. Wang, “A Modified Dual Active Bridge Converter with Hybrid Phase-Shift Control for Wide Input Voltage Range,” *IEEE Trans. Power Electron.*, vol. 31, no. 10, pp. 6884–6900, Oct. 2016.

[58] A. Tong, L. Hang, G. Li, X. Jiang, and S. Gao, “Modeling and Analysis of a Dual-Active-Bridge-Isolated Bidirectional DC/DC Converter to Minimize RMS Current with Whole Operating Range,” *IEEE Trans. Power Electron.*, vol. 33, no. 6, pp. 5302–5316, Jun. 2018.

[59] J. Huang, Y. Wang, Z. Li, and W. Lei, “Unified Triple-Phase-Shift Control to Minimize Current Stress and Achieve Full Soft-Switching of Isolated Bidirectional DC-DC Converter,” *IEEE Trans. Ind. Electron.*, vol. 63, no. 7, 2016.

[60] B. Zhao, Q. Song, W. Liu, G. Liu, and Y. Zhao, “Universal High-Frequency-Link Characterization and Practical Fundamental-Optimal Strategy for Dual-Active-Bridge

DC-DC Converter Under PWM Plus Phase-Shift Control," *IEEE Trans. Power Electron.*, vol. 30, no. 12, pp. 6488–6494, Dec. 2015.

[61] Y. Wang, S. W. H. de Haan, and J. A. Ferreira, "Optimal operating ranges of three modulation methods in dual active bridge converters," in *2009 IEEE 6th International Power Electronics and Motion Control Conference*, 2009, pp. 1397–1401.

[62] O. Yade, J.-Y. Gauthier, X. Lin-Shi, M. Gendrin, and A. Zaoui, "Modulation strategy for a Dual Active Bridge converter using Model Predictive Control," in *2015 IEEE International Symposium on Predictive Control of Electrical Drives and Power Electronics (PRECEDE)*, 2015, pp. 15–20.

[63] F. KRISMER, "Modeling and Optimization of Bidirectional Dual Active Bridge DC–DC Converter Topologies," Swiss Federal Institute of Technology Zürich, 2010.

[64] F. Krismer, S. Round, and J. W. Kolar, "Performance optimization of a high current dual active bridge with a wide operating voltage range," in *PESC Record - IEEE Annual Power Electronics Specialists Conference*, 2006.

[65] T. Todorčević, R. Van Kessel, P. Bauer, and J. A. Ferreira, "A Modulation Strategy for Wide Voltage Output in DAB-Based DC-DC Modular Multilevel Converter for DEAP Wave Energy Conversion," *IEEE J. Emerg. Sel. Top. Power Electron.*, vol. 3, no. 4, pp. 1171–1181, Dec. 2015.

[66] M. H. Kheraluwala, R. W. Gascoigne, D. M. Divan, and E. D. Baumann, "Performance characterization of a high-power dual active bridge DC-to-DC converter," *IEEE Trans. Ind. Appl.*, vol. 28, no. 6, pp. 1294–1301, 1992.

[67] J. Li, Z. Chen, Z. Shen, P. Mattavelli, J. Liu, and D. Boroyevich, "An adaptive dead-time control scheme for high-switching-frequency dual-active-bridge converter," in *Conference Proceedings - IEEE Applied Power Electronics Conference and Exposition - APEC*, 2012, pp. 1355–1361.

[68] D. Costinett, R. Zane, and D. Maksimovic, "Automatic voltage and dead time control for efficiency optimization in a dual active bridge converter," in *Conference Proceedings - IEEE Applied Power Electronics Conference and Exposition - APEC*, 2012, pp. 1104–1111.

[69] B. Zhao, Q. Song, W. Liu, and Y. Sun, "Dead-time effect of the high-frequency isolated bidirectional full-bridge DC-DC converter: Comprehensive theoretical analysis and experimental verification," *IEEE Trans. Power Electron.*, vol. 29, no. 4, pp. 1667–1680, 2014.

[70] Y. A. Harrye, K. . Ahmed, G. . Adam, and A. . Aboushady, "Comprehensive steady state analysis of bidirectional dual active bridge DC/DC converter using triple phase shift control," in *2014 IEEE 23rd International Symposium on Industrial Electronics (ISIE)*, 2014, pp. 437–442.

[71] Q. Xiao, L. Chen, H. Jia, P. Wheeler, and T. Dragicevic, "Model Predictive Control for Dual-Active-Bridge in Naval DC Micro-grids Supplying Pulsed Power Loads Featuring Fast Transition and Online Transformer Current Minimization," *IEEE Trans. Ind. Electron.*, pp. 1–1, 2019.

[72] R. W. Erickson and D. Maksimović, *Fundamentals of Power Electronics*. Springer US, 2001.

[73] Hua Bai, Chunting Mi, Chongwu Wang, and S. Gargies, "The dynamic model and hybrid phase-shift control of a dual-active-bridge converter," in *2008 34th Annual Conference of IEEE Industrial Electronics*, 2008, pp. 2840–2845.

[74] K. Zhang, Z. Shan, and J. Jatskevich, "Large- and Small-Signal Average-Value Modeling of Dual-Active-Bridge DC–DC Converter Considering Power Losses," *IEEE Trans. Power Electron.*, vol. 32, no. 3, pp. 1964–1974, Mar. 2017.

[75] Hengsi Qin and J. W. Kimball, "Generalized Average Modeling of Dual Active Bridge DC–DC Converter," *IEEE Trans. Power Electron.*, vol. 27, no. 4, pp. 2078–2084, Apr. 2012.

[76] L. Shi, W. Lei, Z. Li, J. Huang, Y. Cui, and Y. Wang, "Bilinear Discrete-Time Modeling and Stability Analysis of the Digitally Controlled Dual Active Bridge Converter," *IEEE Trans. Power Electron.*, vol. 32, no. 11, pp. 8787–8799, Nov. 2017.

[77] C. Li *et al.*, "A Modified Neutral-Point Balancing Space Vector Modulation Technique for Three-Level Neutral Point Clamped Converters in High Speed Drives," *IEEE Trans. Ind. Electron.*, pp. 1–1, 2018.

[78] H. Qin and J. W. Kimball, "Closed-loop control of DC-DC dual-active-bridge converters driving single-phase inverters," *IEEE Trans. Power Electron.*, vol. 29, no. 2, pp. 1006–1017, 2014.

[79] W. Song, N. Hou, and M. Wu, "Virtual Direct Power Control Scheme of Dual Active Bridge DC–DC Converters for Fast Dynamic Response," *IEEE Trans. Power Electron.*, vol. 33, no. 2, pp. 1750–1759, Feb. 2018.

[80] Z. Shan, J. Jatskevich, H. H.-C. C. Iu, and T. Fernando, "Simplified Load-Feedforward Control Design for Dual-Active-Bridge Converters With Current-Mode Modulation," *IEEE J. Emerg. Sel. Top. Power Electron.*, vol. 6, no. 4, pp. 2073–2085, Dec. 2018.

[81] S. Dutta, S. Hazra, and S. Bhattacharya, "A Digital Predictive Current-Mode Controller for a Single-Phase High-Frequency Transformer-Isolated Dual-Active Bridge DC-to-DC Converter," *IEEE Trans. Ind. Electron.*, vol. 63, no. 9, pp. 5943–5952, Sep. 2016.

[82] D. D. Nguyen, G. Fujita, Q. Bui-Dang, and M. C. Ta, "A reduced-order observer-based control system designed in the frequency domain for dual-Active-bridge converter," in *IEEE International Conference on Sustainable Energy Technologies, ICSET*, 2017, pp. 102–107.

[83] D. D. Nguyen, G. Fujita, Q. Bui-Dang, and M. C. Ta, "Reduced-Order Observer-Based Control System for Dual-Active-Bridge DC/DC Converter," in *IEEE Transactions on Industry Applications*, 2018, vol. 54, no. 4, pp. 3426–3439.

[84] A. Tong, L. Hang, H. S. Chung, G. Li, K. Wang, and Y. He, "Using Sampled-data Modeling Method to Derive Equivalent Circuit and Linearized Control Method for Dual-Active-Bridge Converter," *IEEE J. Emerg. Sel. Top. Power Electron.*, pp. 1–1, 2019.

[85] Y.-C. Jeung and D. C. Lee, "Voltage and Current Regulation of Bi-directional Isolated Dual Active Bridge DC-DC Converters based on Double-Integral Sliding Mode Control," *IEEE Trans. Power Electron.*, pp. 1–1, 2018.

[86] K. Li, Y. Yang, S. C. Tan, and R. S. Y. Hui, "Sliding-Mode-based direct power control of dual-Active-bridge DC-DC converters," in *Conference Proceedings - IEEE Applied Power Electronics Conference and Exposition - APEC*, 2019, vol. 2019-March, pp. 188–192.

[87] O. M. Hebala, A. Aboushady, K. H. Ahmed, and I. A. Abdelsalam, *Generic Closed Loop Controller for Power Regulation in Dual Active Bridge DC/DC Converter with Current Stress Minimization*. 2018, pp. 1–1.

[88] X. Liu *et al.*, "Novel Dual-Phase-Shift Control With Bidirectional Inner Phase Shifts for a Dual-Active-Bridge Converter Having Low Surge Current and Stable Power Control," *IEEE Trans. Power Electron.*, vol. 32, no. 5, pp. 4095–4106, May 2017.

[89] V. M. Iyer, S. Gulur, and S. Bhattacharya, "Hybrid control strategy to extend the ZVS range of a dual active bridge converter," in *Conference Proceedings - IEEE Applied Power Electronics Conference and Exposition - APEC*, 2017, pp. 2035–2042.

[90] D. Segaran, D. G. Holmes, and B. P. McGrath, "Enhanced load step response for a bidirectional DCDC converter," *IEEE Trans. Power Electron.*, vol. 28, no. 1, pp. 371–379, 2013.

[91] S. Tan, P. Lin, C. Hu, L. Chen, and D. Xu, "Interleaved Flyback Micro-inverter with SiC MOSFET," in *2014 International Power Electronics and Application Conference and Exposition*, 2014, pp. 285–290.

[92] F. Krismer and J. W. Kolar, "Accurate Small-Signal Model for the Digital Control of an Automotive Bidirectional Dual Active Bridge," *IEEE Trans. Power Electron.*, vol. 24, no. 12, pp. 2756–2768, 2009.

[93] F. Xue, R. Yu, and A. Q. Huang, "A 98.3% Efficient GaN Isolated Bidirectional DC-DC Converter for DC Microgrid Energy Storage System Applications," *IEEE Trans. Ind. Electron.*, vol. 64, no. 11, pp. 9094–9103, Nov. 2017.

[94] L. Zhu, A. R. Taylor, G. Liu, and K. Bai, "A multiple-phase-shift control for a sic-based EV charger to optimize the light-load efficiency, current stress, and power quality," *IEEE J. Emerg. Sel. Top. Power Electron.*, vol. 6, no. 4, pp. 2262–2272, Dec. 2018.

[95] D. Costinett, R. Zane, and D. Maksimović, "Discrete-time small-signal modeling of a 1 MHz efficiency-optimized dual active bridge converter with varying load," in *2012 IEEE 13th Workshop on Control and Modeling for Power Electronics, COMPEL 2012*, 2012.

[96] W. Choi, K. M. Rho, and B. H. Cho, "Fundamental Duty Modulation of Dual-Active-Bridge Converter for Wide-Range Operation," *IEEE Trans. Power Electron.*, vol. 31, no. 6, pp. 4048–4064, Jun. 2016.

[97] S.-C. Tan, Y.-M. Lai, and C. K. Tse, *Sliding mode control of switching power converters : techniques and implementation*. CRC Press, 2012.

[98] A. R. Brown and R. D. Middlebrook, "Sampled-data modeling of switching regulators," in *PESC Record - IEEE Annual Power Electronics Specialists Conference*, 1981, vol. 1981-January, pp. 349–369.

[99] D. C. Hamill, J. H. B. Deane, and D. J. Jefferies, "Modeling of chaotic DC-DC converters by iterated nonlinear mappings," *IEEE Trans. Power Electron.*, vol. 7, no. 1, pp. 25–36, Jan. 1992.

[100] V. Utkin, J. Guldner, and J. Shi, *Sliding mode control in electro-mechanical systems, second edition*. CRC Press, 2017.

[101] S. Xu, X. Kou, C. Wang, Q. Qian, and W. Sun, "New digital control method for improving dynamic response of synchronous rectified flyback converter with CCM and DCM mode," in *2018 IEEE Applied Power Electronics Conference and Exposition (APEC)*, 2018, pp. 338–343.

[102] W. Fang, X.-D. Liu, and Y.-F. Liu, "A New Digital Control Algorithm for Dual-Transistor Forward Converter," *IEEE Trans. Ind. Informatics*, vol. 9, no. 4, pp. 2074–2081, Nov. 2013.

[103] V. M. Nguyen and C. Q. Lee, “Tracking control of buck converter using sliding-mode with adaptive hysteresis,” in *PESC Record - IEEE Annual Power Electronics Specialists Conference*, 1995, vol. 2, pp. 1086–1093.
[104] M. Preindl and S. Bolognani, “Model Predictive Direct Speed Control with Finite Control Set of PMSM Drive Systems,” *IEEE Trans. Power Electron.*, vol. 28, no. 2, pp. 1007–1015, Feb. 2013.
[105] G. Du, J. Li, and Z. Liu, “The improved model predictive control based on novel error correction between reference and predicted current,” in *2018 IEEE Applied Power Electronics Conference and Exposition (APEC)*, 2018, pp. 3005–3010.
[106] S. Kouro, P. Cortés, R. Vargas, U. Ammann, and J. Rodríguez, “Model predictive control—A simple and powerful method to control power converters,” *IEEE Trans. Ind. Electron.*, vol. 56, no. 6, pp. 1826–1838, 2009.
[107] K. Z. Liu and Y. Yokozawa, “An MPC-PI approach for buck DC-DC converters and its implementation,” in *2012 IEEE International Symposium on Industrial Electronics*, 2012, pp. 171–176.
[108] H. Kinoshita, K. Z. Liu, A. Zaharin, and Y. Yokozawa, “High performance algorithms for the control and load identification of boost DC-DC converters,” in *2010 IEEE Vehicle Power and Propulsion Conference*, 2010, pp. 1–6.
[109] F. M. Oettmeier, J. Neely, S. Pekarek, R. DeCarlo, and K. Uthaichana, “MPC of Switching in a Boost Converter Using a Hybrid State Model With a Sliding Mode Observer,” *IEEE Trans. Ind. Electron.*, vol. 56, no. 9, pp. 3453–3466, Sep. 2009.
[110] P. Mattavelli, L. Rossetto, G. Spiazzi, and P. Tenti, “General-purpose sliding-mode controller for DC/DC converter applications,” in *PESC Record - IEEE Annual Power Electronics Specialists Conference*, 1993, pp. 609–615.
[111] V. M. Nguyen and C. Q. Lee, “Indirect implementations of sliding-mode control law in buck-type converters,” in *Conference Proceedings - IEEE Applied Power Electronics Conference and Exposition - APEC*, 1996, vol. 1, pp. 111–115.
[112] S. C. Tan, Y. M. Lai, and C. K. Tse, “Indirect sliding mode control of power converters via double integral sliding surface,” *IEEE Trans. Power Electron.*, vol. 23, no. 2, pp. 600–611, Mar. 2008.
[113] T. Dragicevic, “Model Predictive Control of Power Converters for Robust and Fast Operation of AC Microgrids,” *IEEE Trans. Power Electron.*, vol. 33, no. 7, pp. 6304–6317, Jul. 2018.
[114] L. Tarisciotti *et al.*, “Model Predictive Control for Shunt Active Filters With Fixed Switching Frequency,” *IEEE Trans. Ind. Appl.*, vol. 53, no. 1, pp. 296–304, Jan. 2017.
[115] L. Tarisciotti, P. Zanchetta, A. Watson, S. Bifaretti, and J. C. Clare, “Modulated Model Predictive Control for a Seven-Level Cascaded H-Bridge Back-to-Back Converter,” *IEEE Trans. Ind. Electron.*, vol. 61, no. 10, pp. 5375–5383, Oct. 2014.
[116] P. Akter, M. Uddin, S. Mekhilef, N. M. L. Tan, and H. Akagi, “Model predictive control of bidirectional isolated DC–DC converter for energy conversion system,” *Int. J. Electron.*, vol. 102, no. 8, pp. 1407–1427, Aug. 2015.
[117] T. Dragicevic, “Dynamic Stabilization of DC Microgrids With Predictive Control of Point-of-Load Converters,” *IEEE Trans. Power Electron.*, vol. 33, no. 12, pp. 10872–10884, Dec. 2018.
[118] J. Slotine and W. Li, *Applied Nonlinear Control*, Vol. 199. Englewood Cliffs, NJ, USA: Prentice Hall, 1991.

[119] T. Dragicevic, "Dynamic Stabilization of DC Microgrids with Predictive Control of Point of Load Converters," *IEEE Trans. Power Electron.*, pp. 1–1, 2018.
[120] P. Wheeler and S. Bozhko, "The More Electric Aircraft: Technology and challenges.," *IEEE Electrif. Mag.*, vol. 2, no. 4, pp. 6–12, Dec. 2014.
[121] X. Wang *et al.*, "Torque Ripple Reduction in Sectored Multi Three-Phase Machines Based on PWM Carrier Phase Shift," *IEEE Trans. Ind. Electron.*, pp. 1–1, 2019.
[122] S. Jordan and J. Apsley, "Diode rectification of multiphase synchronous generators for aircraft applications," in *2011 IEEE Energy Conversion Congress and Exposition*, 2011, pp. 3208–3215.
[123] A. Forsyth, A. Cross, and A. Baghramian, "Approximate, average, dynamic models of uncontrolled rectifiers for aircraft applications," *IET Power Electron.*, vol. 2, no. 4, pp. 398–409, Jul. 2009.
[124] A. Emadi, A. Khaligh, C. H. Rivetta, and G. A. Williamson, "Constant Power Loads and Negative Impedance Instability in Automotive Systems: Definition, Modeling, Stability, and Control of Power Electronic Converters and Motor Drives," *IEEE Trans. Veh. Technol.*, vol. 55, no. 4, pp. 1112–1125, Jul. 2006.
[125] F. Gao, S. Bozhko, A. Costabeber, G. M. Asher, and P. W. Wheeler, "Control Design and Voltage Stability Analysis of a Droop-Controlled Electrical Power System for More Electric Aircraft," *IEEE Trans. Ind. Electron.*, vol. 64, no. 12, pp. 1–1, Dec. 2017.
[126] J. Sun, "Impedance-Based Stability Criterion for Grid-Connected Inverters," *IEEE Trans. Power Electron.*, vol. 26, no. 11, pp. 3075–3078, Nov. 2011.
[127] R. D. Middlebrook, "Input Filter Considerations in Design and Application of Switching Regulators." 1976.
[128] F. Gao *et al.*, "Comparative Stability Analysis of Droop Control Approaches in Voltage-Source-Converter-Based DC Microgrids," *IEEE Trans. Power Electron.*, vol. 32, no. 3, pp. 2395–2415, Mar. 2017.
[129] P. Liutanakul, A.-B. Awan, S. Pierfederici, B. Nahid-Mobarakeh, and F. Meibody-Tabar, "Linear Stabilization of a DC Bus Supplying a Constant Power Load: A General Design Approach," *IEEE Trans. Power Electron.*, vol. 25, no. 2, pp. 475–488, Feb. 2010.
[130] X. Zhang, Q.-C. Zhong, and W.-L. Ming, "Stabilization of a Cascaded DC Converter System via Adding a Virtual Adaptive Parallel Impedance to the Input of the Load Converter," *IEEE Trans. Power Electron.*, vol. 31, no. 3, pp. 1826–1832, Mar. 2016.
[131] Wook-Jin Lee and Seung-Ki Sul, "DC-Link Voltage Stabilization for Reduced DC-Link Capacitor Inverter," *IEEE Trans. Ind. Appl.*, vol. 50, no. 1, pp. 404–414, Jan. 2014.
[132] L. Chen, S. Shao, Q. Xiao, L. Tarisciotti, T. Dragicevic, and P. Wheeler, "Model-Predictive-Control for Dual-Active-Bridge Converters Supplying Pulsed Power Loads in Naval DC Microgrids," *IEEE Trans. Power Electron.*, pp. 1–1, 2019.
[133] T. Dragicevic and M. Novak, "Weighting Factor Design in Model Predictive Control of Power Electronic Converters: An Artificial Neural Network Approach," *IEEE Trans. Ind. Electron.*, pp. 1–1, 2018.
[134] Y. Panov and M. Jovanović, "Practical issues of input/output impedance measurements in switching power supplies and application of measured data to stability analysis," *Conf. Proc. - IEEE Appl. Power Electron. Conf. Expo. - APEC*, vol. 2, pp. 1339–1345, 2005.
[135] L. Chen, L. Tarisciotti, A. Costabeber, P. Wheeler, and P. Zanchetta, "Model Predictive Control for Isolated DC/DC Power Converters with Transformer Peak Current Shaving,"

in *2018 IEEE Energy Conversion Congress and Exposition (ECCE)*, 2018, pp. 5954–5960.